First Annual Report
National Aeronautics and Space Administration
Lewis Research Center
Grant NGR 23-004-068

A STUDY OF THE ROUND-JET/PLANE-WALL FLOW FIELD

prepared by

John F. Foss
Stanley J. Kleis

Division of Engineering Research
MICHIGAN STATE UNIVERSITY
East Lansing, Michigan 48823
October 8, 1971

First Annual Report
National Aeronautics and Space Administration
Lewis Research Center
Grant NGR 23-004-068

A STUDY OF THE ROUND-JET/PLANE-WALL FLOW FIELD

prepared by

John F. Foss
Stanley J. Kleis

Division of Engineering Research
MICHIGAN STATE UNIVERSITY
East Lansing, Michigan 48823
October 8, 1971

ABSTRACT

An exploratory study of the round-jet/plane-wall flow field has been conducted. Impingement angles, between the axisymmetric jet axis and the plane wall, from zero to 15 degrees have been examined for nozzle heights of 0. 75, 1. 0, 1. 5 and 2. 0 diameters and for (i) a fully developed pipe flow and (ii) a relatively uniform exit velocity condition. Velocity measurements have been used to define isotach contours and to determine mass, momentum and energy flux values for the near field (i. e., within five diameters) of the jet. Surface pressure measurements have been used to define surface pressure forces and jet centerline trajectories. The geometric and flow conditions examined and the interpretation of the results have been motivated by the externally blown flap STOL aircraft application.

ACKNOWLEDGMENT

Dr. James A. Albers of the NASA Lewis Research Center has served as the technical adviser for this research project; his guidance and counsel has been of considerable importance in making this study relevant to the externally blow flap application problem. The efforts of Mr. Robert L. Walton in the preparation of data acquisition and processing computer programs and the assistance of Mr. Richard Riel in the experimental program is gratefully acknowledged.

TABLE OF CONTENTS

LIST OF TABLES

LIST OF FIGURES

NOMENCLATURE

C. S.	control surface
C. V.	control volume
d	diameter of nozzle exit
E	energy flux; $\int\int \rho u^3 \, dydz$
F	force
h	height of nozzle centerline above the plane wall
h(x)	$h - x \tan \alpha$
$\hat{i}$	x-component unit vector
J	momentum flux; $\int\int \rho u^2 \, dydz$
J_0	momentum flux based on Q(0), $\rho Q(0)^2 A_o$
$\hat{j}$	y-component unit vector
k	coefficient defined by Equation (8)
$\hat{k}$	z-component unit vector
M	mass flux, $\int\int \rho u \, dydz$
$\hat{n}$	outward drawn unit vector
N	any extensive property
p	pressure
Q	magnitude of the velocity vector, $Q(0) \equiv Q(0, 0, 0)$
r	radius for cylindrical coordinates
R_j	radius of the jet (arbitrarily defined)
u	x-component velocity, $\vec{v} \cdot \hat{i}$, $u(0) \equiv u(0, 0, 0)$
u_s	maximum velocity in a plane of constant x
u_θ	internal energy
v	y-component velocity; $\vec{v} \cdot \hat{j}$
$\vec{v}$	vector velocity
V	volume
w	z-component velocity; $\vec{v} \cdot \hat{k}$
x, y, z	coordinates (see Figure 2)
z_c	jet centerline defined by the center of the circular isotach pattern at a given x location
z_m	jet centerline defined by the moment-of-momentum equation (33)

NOMENCLATURE

C. S.	control surface
C. V.	control volume
d	diameter of nozzle exit
E	energy flux; $\int\int \rho u^3 \, dydz$
F	force
h	height of nozzle centerline above the plane wall
h(x)	$h - x \tan \alpha$
$\hat{i}$	x-component unit vector
J	momentum flux; $\int\int \rho u^2 \, dydz$
J_0	momentum flux based on Q(0), $\rho Q(0)^2 A_o$
$\hat{j}$	y-component unit vector
k	coefficient defined by Equation (8)
$\hat{k}$	z-component unit vector
M	mass flux, $\int\int \rho u \, dydz$
$\hat{n}$	outward drawn unit vector
N	any extensive property
p	pressure
Q	magnitude of the velocity vector, $Q(0) \equiv Q(0, 0, 0)$
r	radius for cylindrical coordinates
R_j	radius of the jet (arbitrarily defined)
u	x-component velocity, $\vec{v} \cdot \hat{i}$, $u(0) \equiv u(0, 0, 0)$
u_s	maximum velocity in a plane of constant x
u_θ	internal energy
v	y-component velocity; $\vec{v} \cdot \hat{j}$
$\vec{v}$	vector velocity
V	volume
w	z-component velocity; $\vec{v} \cdot \hat{k}$
x, y, z	coordinates (see Figure 2)
z_c	jet centerline defined by the center of the circular isotach pattern at a given x location
z_m	jet centerline defined by the moment-of-momentum equation (33)

Superscripts

$\overline{(\ )}$	time average quantity
$(\ )'$	fluctuating quantity

Subscripts

$(\ )_e$	entrainment
$(\ )_j$	pertaining to the jet
$(\ )_o$	condition at the nozzle exit
$(\ )_T$	true value
$(\ )_x, (\ )_z$	x and z component values

Greek Symbols

α	inclination angle of the jet
δ_u, δ_p	error values for velocity and pressure
η	N per unit mass
θ	azimuthal coordinate (r, θ, x)
λ_u, λ_{fd}	momentum flux ratio characterizing the nozzle exit velocity distribution
Λ	diffusion length for the Reichardt theory or (a suitably defined) macro scale of turbulence
ν	kinematic viscosity
ρ	viscosity

1. INTRODUCTION

1.1. STOL Aircraft - The Application Problem

Contemporary transportation requirements have led to considerable interest in STOL aircraft. A recent article by Wick and Kuhn [1] examines the general aspects of these aircraft. STOL aircraft are characterized by the requirement of large lift at low forward speed. The externally blown flap (see Figure 1) has been proposed as a technically feasible scheme to provide this condition. This configuration, initially proposed by NACA personnel, has been extensively investigated via wind tunnel model studies; see e. g., Smith [2].

For the externally blown flap configuration, the engine exhaust is used to provide boundary layer control on the suction side of the flap (or flaps) and to create the high velocity jet sheet from the trailing edge of the flap. The success in obtaining these desired conditions is dependent upon the wing-flap geometry and the flow field which is present at this intersection. The flow field is dependent upon the location and orientation of the engines, the influence of the external stream and the upstream effects of the flap. The design problem is to select the appropriate geometric and flow conditions to obtain optimum take-off, cruise and landing configurations. This is obviously a quite challenging aerodynamic design problem; it has motivated the present study.

Complicated problems such as the selection of the proper location and orientation of the engines for the externally blown flap are often profitably approached via the strategy of reductionism. That is, the complicated problem is simplified in such a manner that the most elementary form of the problem, which retains the basic characteristics of the prototype conditions, is examined. The basic mechanisms which are revealed by such a study are then used to interpret the behavior of the prototype or a more complicated approximation of the desired flow. The study by Albers and Potter [3], in which a two-dimensional analysis of the externally blown flap is presented, provides one example of this general approach. The results of their analysis can be used to determine the desirable characteristics which must be provided by the three-dimensional flow field of the prototype configuration. The present study of the round-jet/plane-wall flow field is based upon this strategy. This flow field, which is shown in Figure 2, has been the subject of a

rather extensive one-year exploratory study; the results of the study are presented in this report.

1. 2. Background

There have been numerous studies of the interaction of a round jet and flat plate but most have been for the condition where the jet is perpendicular to the plate. Tani and Komatsu [4] and Chao and Sandborn [5] have recorded mean and turbulence quantities for such flows. A recent literature evaluation and further experimental results have been reported by Gaunter, Hryack and co-workers [6] and [7]. Obliquely impinging jets for large (nearly perpendicular) angles have been studied less extensively; very little information is available for small angle oblique jets. These two categories are reviewed in the following paragraphs.

Yakovlevskii and Krasheninnikov [8] in a study of a round jet impinging on a flat plate at large angles have indicated that the lower portion of the jet shows some reversed flow at an angle of 30-35 degrees. Their pressure data and velocity data were mainly in support of their interest in the flow at a considerable distance from the impingement point and is too coarse to be of value to the present study. Donaldson and Snedecker [9] have provided a rather extensive documentation of nozzle height, mach number, and large angle (α = 90, 60, 45, 35 degrees) effects on an impinging jet. Because of the reversed flow condition for angles larger than 30-35 degrees (an observation which they substantiate), the majority of their work does not overlap with or contribute directly to the present study. The pertinent features of their study are quoted along with the results presented herein.

Limited data on the interaction of a compressible jet with a plane wall as well as the coalescence of two round jets is given in a paper on jet propulsion by Squire [10]. The results for the round-jet/plane-wall at α = 19. 5 degrees, h/d = 27. 4 indicated that the jet retains an axisymmetric form in the full jet before the plate is reached and in the upper region away from the direct influence of the plate after the interaction has occurred. Velocity data near the plate was apparently not available.

Crow and Champagne [11] have investigated the axisymmetric jet in an effort to determine the possible existence of an orderly structure in the near field. The study was motivated by jet noise considerations and

made use of a loud speaker driven oscillating plenum pressure condition to search for the orderly structure. The volume flux data from this study will be particularly pertinent for the interpretation of the present results.

Alexander, Baron and Comings have reported an extensive series of tests involving free jet flows [12]. They propose that the analytical approach due to Reichardt provides an effective calculation scheme for transport phenomena. As one aspect of this general study, they have recorded a limited quantity of data for two round jets. The data are recorded for the plane defined by the jet axes and the streamwise direction (except for a symmetry plane traverse at x/d = 30). The data is reported for $x/d \geq 10$ and for a jet separation of (approximately) 2.4d. With the observation that the center plane is a plane of symmetry, they indicated that the two-jet flow field will be similar to that with a wall at the plane of symmetry. Their data for the latter case also commence at x/d = 10 and are only for the above indicated planes. The data for the case using the physical plane show somewhat greater velocities near the plane than the completely free condition. This observation, not explained by the authors, may be due to the generation of streamwise vorticity.

A wind tunnel simulation study by Raney and his associates [13] was carried out at the British R. A. E. Farnborough to evaluate the effects of an underslung engine placed in rather close proximity to the support wing. The investigation evaluated a configuration for an airbus, and a straight wing (no flap) was used with jet-to-free-stream velocity ratios between 1 and 2 ($1 \leq u_s/u_{jet} \leq 2$); that is, a condition simulating a high speed forward flight was investigated. The actual engine geometry was simulated and an airfoil with upper and lower surface static taps was used to determine the pressure distribution over the airfoil; these were the object data for the study. An incidence angle (α) of four degrees was employed for the majority of the tests, and h/d values of 0.65 to 0.88 were investigated.

For the geometries and flow conditions evaluated, the upper surface pressure distribution remained unchanged from the condition in which only an airfoil was present. However, the lower surface pressure distribution showed a strong dependence on the spacing (h/d) and velocity

(u_s/u_j) ratio. These dependencies were most pronounced for the minimum and maximum portions of the investigated ranges. The stagnation point of the attachment phenomena was also clearly evident for these extreme conditions of their tests. It should be noted that STOL applications will involve much greater velocity ratios and possibly different engine configurations than those tested. The data of Raney and associates may allow the effects of a non-zero u_s to be evaluated for the round-jet/plane-wall studies.

The near field of an axisymmetric jet has been investigated by Sami et al. [14]. Mean velocity profiles, turbulence intensities, turbulence kinetic energy budgets and turbulence scales are presented for the region $0 < x/d \leq 10$. The mean velocity data of [14] will be used as reference data for the mass and energy flux values for the near field.

1.3. Characteristics of the Round-Jet/Plane-Wall Flow Field

The flow field is determined by the appropriate geometric and flow conditions imposed upon it. The geometric conditions are defined by two parameters, the distance above the plate (h) normalized by the jet exit diameter (d) and the angle between the jet axis and the plate (α). The flow conditions are defined by the flow at the exit plane of the jet and the ambient flow conditions (u_s) if any. The ambient velocity was zero for the present study. The only universally defined exit flow condition is that of a fully developed pipe flow; this case was investigated. A second case, that of a uniform profile with boundary layers on the nozzle wall was also investigated. For the latter condition, it would be necessary to determine the state of the turbulent motion (i.e., the second and higher order correlation functions) in order to characterize the flow conditions. For nearly all jet studies, the mean velocity profile and the longitudinal intensity represent the maximum information reported. Studies by Bradshaw [15] and Flora and Goldschmidt [16] have reported effects on the development of free shear flows due to the initial turbulence structure, but this aspect of the problem is largely unknown at present.

The flow field which results from the interaction of the jet with the plate may be characterized by several phenomena. These several phenomena are identified in the following subsections and are reported in detail in the results section. Other phenomena which also serve to

characterize this flow field will be briefly identified herein and more extensively examined and reported as a part of the second year's activity.

1. 3. 1. The Jet Trajectory

The characteristic of a jet to entrain ambient fluid will influence the location of the intersection of the jet and the plate. The entrainment of ambient fluid from the region between the jet and the plate results in a non-axisymmetric reduced pressure field around the jet and a consequent deflection toward the plate. (This effect is of course not as important for a round jet as compared with a plane jet.)

1. 3. 2. Jet Spreading

As the jet impinges upon the plate, greater than ambient pressures may be expected on and near the plate in the interaction region. The resulting fluid accelerations that are required to balance the pressure gradient and shear effects lead to a three-dimensional flow field near the plate with possibly strong lateral flows (parallel to the plate and perpendicular to the streamwise direction). Strong lateral flows would result in a significant spreading of the jet. It can be expected that the magnitude of this effect will be a strong function of the geometric parameters.

1. 3. 3. Entrainment

In the region between the nozzle exit and the streamwise location where the effect of the plate is felt, the entrainment (i. e., the capture of and the transfer of vorticity fluctuations $\acute{\omega}_i$ to ambient fluid with the consequent increase in the mass flux [17]) is dependent upon the geometry and the nozzle exit conditions. However, once the jet-plate interaction has occurred, the amount of entrainment, as indicated by the mass flux values, will reflect the character of the jet boundary exposed to the ambient fluid. The difference in mass flux values between the free jet and the impinging jet cases will therefore help to characterize the behavior of the jet and also its effect on its environment.

1. 3. 4. Dissipation

The decreasing values for the flux of mean flow kinetic energy reflect the dissipative processes within the jet. (In this sense, the production of turbulent kinetic energy is considered dissipation in that

it represents an energy drain from the mean flow which will ultimately be dissipated by the smaller scale turbulence structure.) Since the flux of mean flow kinetic energy is easily obtained from the present measurements and since it helps to characterize (i.e., provides a quantitative measure of) the velocity field, these values will be presented. Since the production of turbulence kinetic energy will be altered by the jet-plane interaction, the kinetic energy flux values may be instructive regarding the flow characteristics in these regions.

1.3.5. Other Phenomena

The production of mean streamwise vorticity is one of the potentially most important features of this flow field. The production occurs because the dominant mean vorticity in the jet is azimuthal (ω_θ in a streamwise r, θ, z coordinate system) and because in the region of the stagnation point on the plate, the velocity gradients are such as to cause stretching and reorientation of these vortex filaments. Specifically $\partial u/\partial\theta$ is such that $\omega_\theta \, \partial u/\partial\theta > 0$ for $y > 0$ and $\omega_\theta \, \partial u/\partial\theta < 0$ for $y < 0$. This results in a pair of streamwise vortex filaments at a given x location such that a secondary flow toward the plate and away from the center line is created. Figure 3a shows such a development for a characteristic vortex filament; the powder seeded jet of Figure 3b shows the effect of the streamwise vorticity. The significance of this phenomena is related to the desired boundary layer control. If the streamwise vortex filaments could be caused to extend through the flap gap, they would have the effect of energizing the boundary layer on the suction side of the flap by inducing high velocity fluid to be swept down to the flap surface. This would be similar to the effect achieved by the vortex generators which have been installed on certain commercial airliners. Quantitative considerations of this effect will be considered in a separate report.

A stagnation region on the plate will occur where a streamline from the jet intersects the plate. This effect and the stagnation of the entrained fluid as it meets the jet fluid result in rather complex surface static pressure patterns. The integral effects of these pressures, i.e., forces and moments, will be considered in this report. Detailed considerations of the surface pressure patterns will be reported later.

1. 4. Objectives and Scope

The externally blown flap for STOL aircraft provides the technological motivation for the present study; the optimal location and orientation of the engine is the design problem which has directly stimulated this investigation. The round-jet/plane-wall flow field has been identified as one with some of the basic characteristics of the design problem. The objectives of this study are to (i) identify the basic characteristics of the round-jet/plane-wall flow field, and (ii) develop quantitative measures of these characteristics (see 1. 3. 1 - 1. 3. 5 for the characteristics). Subsequent analysis will be able to develop sensitivity coefficients for these measures which will express the influence of the flow and geometric conditions (see 1. 3 for the conditions).

The range of flow and geometric conditions are $0 \leq \alpha \leq 15$ degrees, $0 \leq h/d \leq 2$, $0 \leq x/d \leq 5$ (see Figure 2 for definitions). Flow visualization studies using a powder-seeded jet with planar illumination to observe the jet cross-sectional shape have been conducted to define what cases were of interest. Quantitative data for velocity and plate surface static pressure measurements have been obtained. From these data, the following quantities, which serve as both measures of the flow field characteristics and variables of intrinsic interest, have been computed:

i) isotach contours to provide a visual representation of the jet representation,

ii) a phenomenological model for the description of the axisymmetric portion of the velocity field,

iii) mass, momentum and energy flux ratios,

iv) pressure force exerted on the plate and descriptions of the jet trajectory.

2. ANALYTICAL CONSIDERATIONS

This investigation can be described as an exploratory-experimental study of a three-dimensional turbulent shear flow. The role of analysis for this study is to provide a framework to organize, interpret and present the experimental data. This will be accomplished by using fundamental relationships -- the conservation laws -- and a phenomenological theory -- the Reichardt Hypothesis. These considerations are given in 2. 1 and 2. 2.

2. 1. The Control Volume Formulation of the Conservation Laws

For the round-jet/plane-wall flow field and for nearly all flow fields of engineering interest, the required information is the behavior of the fluid in a region in space and not the behavior of an individual particle (or a collection of particles) passing through the region. However, the laws of mechanics are fundamentally known in terms of individual or collections of particles. For example, the familiar expression, $\vec{F} = \vec{ma}$, clearly involves quantities defined in terms of an identified mass element. Such relationships are described in "material coordinates" whereas information regarding the behavior of the fluid in a region of space requires "spatial coordinates." The control volume formulation provides the formal procedure to transform the material coordinates description of the conservation laws into a spatial coordinate description. The Reynolds transport theorem, which accomplishes this transformation is given by Equation (1) in terms of the extensive (i. e., mass dependent) property N. The other symbols in the equation are η: N per unit mass, ρ: density, V: volume, $\vec{v}$: velocity, $\hat{n}$: an outward drawn unit normal. The time-rate-of-change-of N is given by

$$\frac{DN}{Dt} = \frac{d}{dt}\int_{C.V.} \eta\,\rho dV + \int_{C.S.} \eta\,\rho\vec{v}\cdot\hat{n}\,dA \quad . \qquad (1)$$

The C. V. and C. S. stand for control volume and control surface, respectively. The four conservation laws and their contribution to the present investigation are given in the following subsections. Since this flow field is steady (time independent) the first term on the right hand side is zero. The essence of utilizing this approach for a general fluid mechanics problem is in the selection of the control volume; Figure 4 shows the control volume selected for the round-jet/plane-wall flow field.

2. 1. 1. Conservation of Mass

The mass, M, of a collection of particles is obviously constant; therefore DM/Dt = 0 and η = mass/unit mass = 1. For these conditions, Equation (1) becomes

$$0 = \int_{C.S.} \rho\vec{v}\cdot\hat{n}\,dA \quad . \qquad (2)$$

Entrainment of ambient fluid was one of the phenomena discussed in Section 1. 3. This is quantified by Equation (2) in that the mass efflux at the plane x = x will be greater than that entering from the jet, x = 0, by the amount entrained through the other portions of the control surface. The mass flux from the jet and the exit mass flux from the control volume are obtainable from the experimental data.

2. 1. 2. Conservation of Momentum

The sum of the mass times the (vector) velocity for each particle, N, is the resultant momentum of the collection of particles. The momentum per unit mass, η, is velocity and the net force on the collection of particles, $\vec{F}$, is equal to the time-rate-of-change of the momentum of the fluid particles. The term "conservation" indicates that the momentum of an isolated system, e. g., the universe, is constant. For this steady flow problem

$$\vec{F} = \int_{C.S.} \vec{v}\, \rho \vec{v} \cdot \hat{n}\, dA \quad . \tag{3}$$

The z-component of Equation (3) expresses the primary balance between the net pressure force on the plate and the net change of the z-component momentum flux, J_z, through the control volume; the effects due to entrainment can be expected to be of secondary importance except for negligibly small α values. Since the asymptotic condition is $J_z = 0$ for $x \to \infty$, a zero J_z value will indicate that the plate is effectively infinite in length as regards the turning of the jet. If a zero J_z value is not obtained, then the downstream section of the plate will affect the flow at the local x station and the conditions of the present study may differ from those associated with a finite length of plate. These considerations are discussed in 4. 5.

The x-component equation expresses the balance between the force terms, that is the shear force on the plate and the streamwise pressure gradient effects and the x-component of the momentum flux. It will be shown that the x-component forces are negligibly small, hence the x-component momentum flux can be used as a reference value for the flow field.

2. 1. 3. Conservation of Moment-of-Momentum

A moment-of-momentum can be ascribed to each particle. Let the symbol $\vec{r}$ represent the distance from an arbitrary origin to the particle and N be the moment-of-momentum of the collection of particles. $\vec{M}$ is defined as the net moment on the collection of particles, hence

$$\vec{M} = \int_{C.S.} \rho(\vec{r} \times \vec{v})\, \vec{v} \cdot \hat{n}\, dA \quad . \tag{4}$$

Equation (4) can be used to identify the effective location, i. e., z_m, of the x-component momentum flux as it leaves the control volume. That is, from the measured pressure distribution and the contribution of the pressure to the moment on the control volume and from suitable assumptions regarding the entrainment effects, the distance z_m may be calculated. The relationship of this height to the effective center of the axisymmetric portion of the jet is compared in the results section, 4. 5.

2. 1. 4. Conservation of Energy

The rate of heat transfer, $\dot{Q}$, and the rate of work done by the control volume, $\dot{W}_s$, may be related to the time rate of change of energy in the control volume.

$$\dot{Q} - \dot{W}_s = \int_{C.S.} \rho [u_\theta + v^2/2 + gz + p/\rho]\, \vec{v} \cdot \hat{n}\, dA \tag{5}$$

where u_θ is the internal energy per unit mass. Some subtle arguments are required for the rate of work effects which result in the p/ρ term as part of the flux quantities. For the round-jet/plane-wall flow field, $\dot{W}_s = 0$ and the net flux values for p/ρ and gz are negligible. Consequently, the net flux of kinetic energy through the control volume is balanced by the internal energy and heat flux terms; these latter terms are equal to the dissipation of the mean flow kinetic energy. Consequently, the flux of kinetic energy, which may be readily evaluated from the available velocity data, provides a measure of the dissipative effects in the flow field.

2. 2. The Reichardt Inductive Theory

The equations which describe the point-by-point velocity field for a linearly viscous, incompressible (Newtonian) fluid -- the Navier-Stokes equations -- are well known. These equations describe the instantaneous motion of a laminar or turbulent flow; they may be written in Cartesian tensor form as

$$\frac{\partial u_i}{\partial t} + u_j \frac{\partial}{\partial x_j} u_i = -\frac{1}{\rho}\frac{\partial p}{\partial x_i} + \nu \frac{\partial^2 u_i}{\partial x_j \partial x_j} \quad . \tag{6}$$

For the round-jet/plane-wall flow field, these equations contain far more information than is desired; specifically, they describe the instantaneous velocity and pressure fields. The instantaneous fields may be described as the superposition of the time mean $\overline{u}_i$, $\overline{p}$ and instantaneous $\dot{u}_i$, $\dot{p}$ fields as

$$u_i = \overline{u}_i + \dot{u}_i \quad ; \quad p = \overline{p} + \dot{p} \tag{7a;7b}$$

from which the Reynolds equations may be derived as

$$\frac{\partial \overline{u}_i}{\partial t} + \overline{u}_j \frac{\partial}{\partial x_j} \overline{u}_i = -\frac{1}{\rho}\frac{\partial \overline{p}}{\partial x_i} + \nu \frac{\partial^2 \overline{u}_i}{\partial x_j \partial x_j} - \frac{\partial}{\partial x_j} \overline{\dot{u}_i \dot{u}_j} \quad . \tag{8}$$

The term $-\rho\,(\overline{\dot{u}_i \dot{u}_j})$, which originates in the non-linear acceleration term, is termed the Reynolds stress tensor. The presence of this term has been referred to as the "closure problem" since there are no fundamentally correct universal or special-case formulations to relate it to the mean velocity field; that is, there is no fundamentally correct constitutive equation. There have been several ad-hoc proposals for such a relationship; these are the mixing length for vorticity and momentum, the eddy viscosity and a von Karman technique (to relate the first and second derivatives of the mean velocity) and they are all motivated by more or less reasonable physical arguments which are not sustained in detail when compared to experimental observations. These are examined by Hinze (see Chapter 5 [18]). An alternative hypothesis was advanced by Reichardt [19] which claimed no physical motivation but yielded a diffusion equation for free shear flows and an exponential form for the mean velocity distribution which agreed satisfactorally with

wake, jet and shear layer data. The Reichardt hypothesis was generalized by Baron and Alexander [20] and has most recently received vigorous attention by Sforza and co-workers in a major evaluation and redirection of turbulent mixing engineering research. The most recent report by Mons and Sforza [21] provides an extensive description of both the generalized Reichardt formulation and results of turbulent jet mixing studies by this group.

Briefly, the extended Reichardt hypothesis is (for the instantaneous velocity components)

$$\overline{u\,v} = -\Lambda(x)\,\frac{\partial \overline{u}^2}{\partial r} \tag{9}$$

for which case Equation (6) may be rewritten as (for the time average of u^2)

$$\frac{\partial}{\partial x}\,\overline{u^2} + \Lambda(x)\,\frac{\partial^2 \overline{u}^2}{\partial r^2} = 0 \quad . \tag{10}$$

This is seen to be a parabolic or diffusion equation. Three boundary conditions are required; specifically an initial condition, which is obtained from the exit (or other) profile, and conditions for $\overline{u}^2(r)$ based on the geometry of the problem. For example $\partial \overline{u}^2(o)/\partial r = 0$ and $\overline{u}^2(\infty) = 0$ for a jet. The velocity field of a free shear flow is independent of the initial conditions for sufficiently large downstream distances; this is not the case for the near field. The presence of the initial condition and the available flexibility in the choice of $\Lambda(x)$ provide a format which makes it relatively easy to describe the initial region of a jet via this semi-empirical description. Trentacoste and Sforza [22] report marked success in terms of evaluating the initial velocity fields for different free jets.

The Reichardt hypothesis will be used to compute the axisymmetric portion of the jet which is not influenced by the plate for the round-jet/plane-wall flow field. The availability of this scheme will facilitate interpolation and extrapolation of the data.

3. EXPERIMENTAL FACILITY

3. 1. Flow Systems

3. 1. 1. Flow Visualization

Two flow systems were used for the round-jet/plane-wall studies. A preliminary flow visualization study was performed to establish the gross response of the flow field to changes in the geometric parameters; a separate facility was used to obtain quantitative data.

A schematic description of the flow visualization facility is shown in Figure 5. The air was seeded with powder by using a jet pump shown schematically in Figure 6. The powder flow is induced by the high velocity air stream in the inner tube. This configuration provided a repeatable powder density which was constant over the time required to obtain the photographs. The jet tube is 1/4 in. (0. 635 cm.) in diameter and 10 in. (25. 4 cm.) in length. The exit velocity was approximately 150 ft. /sec. (45. 5 mps). Photographs were taken of the cross-sectional profiles, in x = constant planes, of the seeded jet. The cross-sectional profiles were made visible by illuminating the powder with a thin (. 15 cm.) sheet of light produced by passing the beam of a 500 mw argon laser through a cylindrical lens. A photographic record of the jet's shape was made at each diameter for $0 \leq x/d \leq 5$ (see Figure 3b). The Reynolds number is the only parameter which is required to establish similarity between the visualization and quantitative studies since the geometric parameters are identical and the two flow fields are incompressible. The Reynolds numbers differ by approximately a factor of seven which is not significant since they are large ($u(0)\, d/\nu \cong 10^5$: quantitative; 2×10^4: visualization) and since the bulk of the flow is not directly influenced by viscous shear effects. Characteristic photographs from this portion of the study are presented in Figure 3b.

3. 1. 2. Quantitative Study

The second flow system, shown in Figure 7, was used for quantitative measurements of surface static pressures and mean velocities. High pressure air, produced by means of a multiple stage centrifugal blower was ducted through a counterflow heat exchanger were placed in a separate room in order to ensure constant ambient conditions near the test facility during the course of a run. A plenum

chamber was used to remove the large scale pressure fluctuations from the flow. The fully developed pipe exit condition was obtained by a 12 ft. long, 2 in. (5.08 cm.) I.D. extruded aluminum pipe giving exit velocities of about 120 ft./sec. (36 m/sec.). The pipe was supported such that h/d values between 0 and 2 could be obtained.

The flow system for the uniform exit profile consisted of a 6-inch (15.24 cm.) I.D. extension of the plenum chamber terminated by a short radius contraction to a 12-inch (30.48 cm.) pipe (see Figure 8). This configuration provided a compromise between a uniform exit condition and a geometry which minimized blockage effects (i.e., for entrainment) and allowed small values of h/d and α to be physically obtained.

A large plate, hinged on a base of aluminum channel to provide variable angles α, served as the plane-wall. A portion of the plate was movable and was driven in the y-direction by a stepping motor geared through a precision threaded shaft and follower arrangement. As shown in Figure 9, two rows of surface static pressure taps, parallel to the x-axis and 4 inches (10.16 cm.) apart were used for the static pressure data. The taps in each row were located on 1/4 inch (.635 cm.) centers for six inches (15.24 cm.) and 1/2-inch (1.27 cm.) centers beyond six inches (15.24 cm.). The rows were staggered so that, if symmetry was assumed, a spacing as fine as 1/8 inch (.3175 cm.) in the x-direction could be obtained.

The movable plate section was also used to drive the hot-wire rake support head, (see Figure 10) in the y-direction for the mean velocity traverses. The rake of four hot-wire probes was positioned in x and z and then traversed across in the y-direction at 0.1 inch (.254 cm.) intervals taking readings for 10 seconds at each point.

3.2. Instrumentation and Data Acquisition System

A schematic representation of the data acquisition and recording system is shown in Figure 11. Decker 308 pressure transducers were used for the measurement of the dynamic pressure at the nozzle exit and the static pressures on the plate. Units whose output provided 10 volts for differential pressures of 3 and 0.3 inches of water were used.

In order to make a record of the plate static pressures, two transducers were used to monitor a pair of static taps while the plate was traversed with respect to the jet. In order to gain maximum

efficiency for these measurements, the transducer outputs were monitored by an on-line 1800 computer (real time); continuously up-dated mean values were calculated for each pressure reading and the input signal was sampled until a stationary value was obtained. Upon the attainment of a stationary value, that is when

$$[1/T \int_0^T p'^2 (y)\, dt]^{1/2} \leq .03\, \bar{p}\,(y),$$

a signal was generated in the computer to drive the y-position stepping motor to its new position. Increments of $\Delta y = 0.1$ inch (0.254 cm.) were used. The computer simultaneously recorded the number of readings to obtain a stationary value, the mean and r.m.s. pressure values, as well as the position coordinates for subsequent processing. A transverse span of 4 inches could be covered by this procedure; consequently, the two rows of static taps covered an 8-inch width under the jet flow.

A similar procedure was used for the mean velocity data using a rake of four, vertically-mounted single hot-wire probes. The rake was mounted on a traverse head which allowed positioning in the x and z directions and which was driven by the movable plate in the y-direction.

The analog voltage signal for the mean velocity data was produced by four constant temperature anemometers, two channels, Thermo-Systems, Inc. Model 1054A (linearized), one Disa 55D05 anemometer with a Disa 55D15 linearizer and one Disa 55A01 anemometer with a Disa 55D15 linearizer. These signals were fed to the computer where averages were computed for 10 seconds at a point. This averaging time represents a compromise between the time required for a stationary signal in the outer region of the jet and the total time required for the quantity of data recorded. The acceptable data scatter in the velocity traverses justifies the selection of the averaging time.

4. RESULTS

4.1. Introduction

The round-jet/plane-wall flow field is an idealization of the externally blown flap configuration. The prototype problem involves a more complicated flow field since the air foil is of finite length and the flap will exert some upstream influence. Its more complicated nature

means that 1) the total flow pattern depends on more variables and is more sensitive to these flow and geometric variables and 2) the underlying dominant mechanisms of the flow will be obscured by this complexity in terms of analyzing experimental test results for a prototype condition. Two separate, although not distinct, objectives have been established and pursued for the round-jet/plane-wall flow field: 1) to establish the character of this flow (there is virtually no information in the literature regarding the details of such a flow at small incidence angles) and 2) to identify the primary mechanisms responsible for the character of the flow. That is, the two objectives are to determine the "what" and the "why" of the flow field.

The present report is to provide a characterization of the flow field to achieve maximum relevance to the engine blown flap application to synthesize the considerable amount of primary data generated in the experimental program. A second report, which requires additional special tests and further analysis, will seek to establish the mechanisms which govern this flow field. If these mechanisms can be identified, then the complicating effects of the prototype can be assessed. This will contribute to the analysis of test results for the prototype configuration and allow a more rational design to be effected.

The results communicated in the present report are derived from velocity measurements in planes of constant x or from surface pressure taps located in the plane-wall. The geometric parameters which define this problem are the inclination angle of the jet α and the dimensionless height of the jet axis above the plane-wall h/d. The flow parameters are defined by the condition of the surrounding fluid (namely, quiescent air with the same properties as the jet for the present study) and the fluid dynamic conditions at the nozzle exit. The effect of the nozzle exit condition was examined by using a fully developed pipe flow and a relatively uniform velocity profile as the exit conditions. The exit velocity profiles are indicated on Figures 28 and 29.

The necessity for schemes to synthesize the primary data can be appreciated from the following. Each hot-wire probe of the four wire rake was positioned at 40 locations in a y traverse (-2 in. $\leq$ y $\leq$ 2 in.). Two z positions, and when required a second y traverse of

2 in. $\leq$ y $\leq$ 6 in., were used for the rake at a given x location. The result was a minimum of (40 . 4 . 2 =) 320 data points per x location per geometric condition. Traverses were made at x/d locations of 0 (approximately), 1, 2, 3, 4, 5 for 8 geometric conditions using the uniform nozzle and 7 conditions using the fully developed nozzle. Hence the total number of velocity data points to be interpreted is (320 . 6 . [8 + 7]) $\simeq 3.0 \times 10^4$. In addition, the pressure data usually involved 10 or more traverses per geometric and exit profile condition which contributed an additional 4×10^3 data points.

Four basic synthesizing schemes have been developed. These are presented in the remainder of Section 4 using the following format.

1) Purpose: a description of the scheme and its contribution to establishing the character of the flow.

2) Data Processing: a description of the computations and analysis of the data to convert it from the primary form into that required by the particular scheme.

3) Discussion: a consideration of the results in terms of their contribution to the definition of the flow field characteristics.

4) Relevance: special interpretations not covered in (3) which serve to relate the results of the particular scheme to the engine blown flap configuration.

4. 2. Isotach Contours

4. 2. 1. Purpose

An isotach contour is a curve of constant velocity magnitude; for this study, they have been generated for planes of constant x/d. These contours are to provide a graphical representation of the jet and, by comparing the isotachs between x/d stations or between cases for different geometric or flow conditions, they are to provide a graphical format to show the response of the jet to different conditions. This scheme synthesizes the multiple traverses at a given x location into a single figure and shows the three-dimensional character of the flow field with much greater clarity than would be achieved by a presentation of the u(y) data.

4. 2. 2. Data Processing

The primary data is a 10 second average of the voltage output of a given wire mounted parallel to the z axis and located at x, y, z in the flow field. The computer averaged voltage is converted into a velocity from the calibration table for the linearized wire. (The table is the voltage-velocity relationship stored at 0. 25 fps intervals in the memory of the IBM 1800 computer.) The calibration scheme is quite accurate and the resulting data is sufficiently smooth to justify the 10 second averaging time. However, the interpretation of a single wire in the presence of the strong pitch and yaw effects of the present flow field is rather difficult. Champagne [23] has provided a formalism to interpret the output voltage of a linearized wire in terms of the mean and fluctuating velocity components of the flow. The resulting expression, carried out to third order terms for the fluctuating velocities is quite complicated. In terms of the present study, it serves as a warning that the averaged output of the single wire cannot be accurately interpreted as the velocity except in regions of relatively low intensity. As a first approximation, the recorded velocity can be interpreted as the magnitude of the velocity in the yz plane since

$$\bar{Q}\Big)_{\text{measured}} \cong Q_s \left(\cos^2\beta - \kappa^2 \sin^2\beta\right)^{1/2} \qquad (11)$$

where β is the angle between the time mean streamwise velocity (Q_s) and the normal to the wire and $\kappa \simeq 0.2$. The first correction term is the normal turbulence intensity which can be expressed in the present nomenclature as $(\overline{u}^2 + \overline{v}^2)^{1/2}/Q_s$. Therefore, to the order of Equation (11), the wire responds to $(\overline{u}^2 + \overline{v}^2)^{1/2}$ and the level curves of this function form the isotachs.

The error in neglecting the turbulent fluctuation contribution is dependent upon the relative intensity; hence, a large percentage error is possible at the edge of the jet. However, approximately the same relative errors will occur for the different geometric and flow conditions which facilitates the comparison between cases.

The approximate velocity magnitudes of the present study have been generated by the relatively straight forward techniques described

above. In order to obtain a significant improvement in the accuracy of the values, considerable effort must be expended including a multiple positioned single wire or a dual (x or v) wire configuration combined with appropriate interpretive routines to extract the velocity components. The necessary sophistication and additional effort would have considerably reduced the comprehensiveness of the cases investigated and would have been incompatible with the exploratory nature of this initial study.

The isotachs were defined by a search routine which located the y locations of a given ratio for $u/u(0)$ for a given value of z (i. e., from a y traverse) at a given x value. The y-z locations so identified were recorded and a compass was used to locate the center of the isotachs at a given x. The estimated uncertainty for this process is ±. 03 in.

4. 2. 3. Discussion

The circular patterns of the isotachs (see Figures 12 to 27) near the nozzle exit and for those cases where the jet does not come in close proximity to the plate are to be expected. The regularity of the isotachs indicates that the multiple wire rake and the calibration procedure provide reliable velocity data. This observation indicates the general reliability of the data acquisition and processing techniques; quantitative measures of the techniques are provided by the flux measurements.

A rather striking result is the maintenance of the circular isotach pattern for the upper portion concurrently with a strong deformation of the isotach pattern for the lower portion of the jet. The factors causing a deformation are shear stress and pressure gradient effects. The shear stress is clearly a "near field" effect and can be expected to slowly erode the circular pattern as shown by the data. The pressure field will remain uniform (at the atmospheric value) except in the region near the plate where the streamline curvature effects will result in increased pressure values. The experimental results indicate that the pressure gradients in this region are relatively large, the flow is apparently turned with a relatively small radius of curvature.

The distortion of the lower portion of the isotachs clearly shows the developing secondary flow and the associated production of streamwise vorticity as discussed in Section 1. 3. 5 and as shown schematically in

Figure 3a. The secondary flow carries the high velocity fluid away from the y=0 plane; the magnitude of this transport is shown by the deviation of the isotach contour from the circular arc defined by the upper portion of the jet. An approximate boundary for the region of the secondary flow is indicated by the region of the distorted isotach patterns.

4. 2. 4. Relevance

The major contribution of the isotachs is their ability to graphically communicate the type of flow regime to be expected for a given α, h/d and x/d. Unlike some of the quantitative measures of the jet to be presented in later sections, the isotachs are rather insensitive to the nozzle exit conditions. Since the objective of the externally blown flap is to provide a portion of the fan exhaust to energize the flap, the velocity field presented to the flap gap region is quite important. The isotach contours provide an indication of this; the effect of the finite airfoil and the upstream effect of the flap will, of course, modify these results for the prototype flow field.

The spreading of the jet along the surface of the plate for the small h/d, large α conditions may prove attractive for the STOL application. For this, a deflectable jet, a gimballed nozzle or a solid extension of the air foil followed by the flap(s) might be required to also allow for the desired cruise condition geometry.

4. 3. The Extended Reichardt Hypothesis

4. 3. 1. Purpose

As shown by the isotach contours, the upper portion of the jet retains an axisymmetric character even though the lower portion of the flow is distorted by the jet-plate interaction. The purpose of this section is to evaluate the Reichardt hypothesis with regard to its ability to calculate the free jet profiles and to determine whether the same formulation can be used for the upper portion of the jet. The studies by Sforza and co-workers [21], [22] and Baron and Alexander [20] would indicate that this formulation is quite useful for free jets.

4. 3. 2. Features of the Data Processing

The pertinent equations may be taken from the report by Mons and Sforza [21].

$$\overline{\rho v u} = -\Lambda(x) \frac{\partial(\overline{\rho u u})}{\partial r} \qquad (3)^*$$

$$\frac{\partial}{\partial x}(\overline{\rho u u}) = \frac{\Lambda(x)}{r} \frac{\partial}{\partial r}\left[r \frac{\partial}{\partial r}(\overline{\rho u u})\right] \qquad (5)^*$$

Initial condition

$$\text{at } x=0: \quad \overline{\rho u u} = \begin{cases} f(r') & \text{for } r' < d/2 \\ 0 & \text{for } r' \geq d/2 \end{cases} \qquad (6)^*$$

Boundary conditions

$$\rho u u \to 0 \quad \text{as } r \to \infty, \quad \frac{\partial}{\partial r} uu = 0 \quad \text{at } r = 0. \qquad (7)^*$$

From [21]: "$\Lambda(x)$ is unknown and must be obtained by comparison between theory and experiment. For convenience, we introduce the transformation [24]

$$\chi = \int_0^x \Lambda(x')\, dx' \quad \text{or} \qquad (8)^*$$

$$d\chi = \Lambda(x)\, dx$$

Under the transformation $(8)^*$, Equation $(5)^*$ becomes

$$\frac{\partial(\overline{\rho u u})}{\partial \chi} = \frac{1}{r} \frac{\partial}{\partial r}\left[r \frac{\partial}{\partial r}(\overline{\rho u u})\right] \qquad (9)^*$$

The solution of $(9)^*$ for arbitrary initial conditions [25] is

$$\overline{\rho u u} = \frac{1}{2\chi} \exp -\left\{\frac{r^2}{4\chi}\right\} \int_0^{\frac{d}{2}} \exp -\left\{\frac{r'^2}{4\chi}\right\} I_0\left(\frac{rr'}{2\chi}\right) f_u(r') r' dr' \qquad (10)^*$$

where $I_o\left(\frac{rr'}{2\chi}\right)$ is a modified Bessel function of order zero and has the form $I_o(z) = \sum_{m=0}^{\infty} (1/2\, z)^{2m}/m!\, \Gamma(m+1)$. [26]"

---

*Equation numbers from Mons and Sforza [21].

Two inputs are required for this system of equations, viz., the initial velocity profile f(r') and a functional form for the transfer length. The initial velocity profile is dependent upon the nature of the nozzle and the approach flow conditions; for this analysis, it is considered to be a known function given by experimental data. The diffusion length must be chosen somewhat arbitrarily. Its form does not affect the momentum flux; therefore, it is not constrained by fundamental laws. Its magnitude does affect the effective spread or entrainment rate and conversely the dissipation rate for the jet. For the far downstream region, the χ function behaves as x^2 which results in a self-preserving form for the velocity profile. A series approximation would therefore involve x^2 as the highest power for χ. Motivated by the series expansion form, an expression for χ was formulated as

$$\chi/d = C_o + C_1 x/d + C_2 (x/d)^2 \qquad (12)$$

where $C_o = 0$ since χ results from the integral over x of some function Λ. It should be stressed that this form is arbitrary; fractional or exponential powers of x may be even more suitable to use to approximate this function. The values of C_1 and C_2 were evaluated from the uniform flow data by a trial and error process of calculating a $u(\chi, r)$ distribution for $0 \leq x/d \leq 5$ and obtaining the "best fit" to the experimental data in this x range.

4. 3. 3. Discussion

The exit profile and the data used for the trial and error process were for the uniform nozzle exit condition and $\alpha = 9$ degrees and $h/d = 1$. The values calculated from Equation (9)* and the data of several uniform exit profile conditions is shown in Figure 28. Only the experimental data which demonstrated conservation of the measured momentum flux (that is, reliable data) were used for this figure.

Unlike a functional form to fit experimental data in the self-preserving region, this formulation must determine the absolute value of the velocity, not a fractional value of the (otherwise obtained) center line value. The agreement between the calculated and measured values is considered to be good. The requirement of determining two coefficients is a reasonable input to be expected of a phenomenological theory

especially since one χ formulation for a given class of exit profile conditions should be sufficient for any member of the class.

The data of Figure 28 also show that the analytical formulation is valid for the condition of a disturbed lower portion of the flow field. That is, the formulation provides reasonably good agreement with the data for $\alpha=9$, $h/d=1$ for which significant distortions occur in the lower portion of the jet.

Figure 29 presents a comparison of the solution for Equation (9)* using the fully developed pipe exit condition for $f(r')$ and the same χ function determined for the uniform flow condition. The curves show a consistent trend wherein the experimental data are below the analytical values for small r and above the analytical values for large r. The selection of different C_1 and C_2 values in (12) could be expected to again force agreement between the analytical and experimental values. The purpose of Figure 29 is to show that the transfer length and hence the χ function is dependent upon the character of nozzle exit condition.

4. 3. 4. Relevance

The ability to calculate the velocity field for the upper portion of the jet as it approaches the flap gap would appear to be of considerable utility for the interpretation, if not the prediction, of test results which indicate the jet-flap interaction. For this, the present study indicates that the free jet characteristics of the nozzle exit profile and sufficient downstream profiles to determine $\chi(x)$ will be required.

4. 4. Flux Ratios

4. 4. 1. Purpose

The properly normalized flux of mass, momentum and energy across a given x=constant plane provide a quantitative measure of the entire, three-dimensional, jet field. (These flux values are given by the integrals on the right hand side of Equations 2, 3, and 5 where the area of integration is a plane of constant x and not the control surface. Since these flux ratios depend upon all the velocity data for a given x=constant plane, they also provide a synthesis of the data into a given numerical value for the flux ratio. (Unlike free, axisymmetric jet studies, the data of interest cannot be expressed by a single traverse.)) Hence, in the same manner in which an isotach contour is required instead of a radial traverse, an area, and not a radial, integration is

required for the flux ratio.

The flux ratios can serve to characterize the present jets (in the region where they are not directly affected by the plate) with respect to the near fields of jets reported in the literature. Also, the jet-plate interaction may be assessed in terms of its effect on the flux ratios as compared with their behavior for no direct influence of the plate and the effect of the nozzle exit condition may be assessed in terms of the effect of this flow parameter on the flux values.

4. 4. 2. Data Processing

Extensive data processing considerations were required for the computation and the presentation of the flux ratio values. In addition, flux ratio values were calculated for similar data reported in the literature. These considerations are summarized in this subsection; they are fully reported in Appendix A.

The detailed considerations, regarding the interpretation of the linearized hot-wire voltage in terms of a velocity magnitude, presented in 4. 4. 2. 1 applies directly to the data processing required for the flux ratios. The mass flux requires the integration of $\overline{u}(x_o, y, z)$ over the plane of x_o. Since no corrections for yaw or turbulence intensity effects were made, the indicated mass flux values can be expected to be too large. The magnitude of the error is difficult to estimate; a nominal value of 6 percent for the maximum would seem reasonable. The error is probably relatively constant between different configurations; hence, a comparison based on the relative values will provide a somewhat more reliable measure of the flow field character. The mean velocity yaw effect, $\overline{v}$, and the transverse turbulent velocity $\overline{v}^2$ will cause errors in the evaluation of the momentum flux. The longitudinal intensity term $\overline{u}^2$ is part of the actual momentum flux and therefore does not represent an error in the measured value. The expected error for the momentum flux is smaller than that for the mass flux since the integral is the square of the velocity and $(\overline{v}/\overline{u})^2$ is uniformly much smaller than 1. 0 except in the entrainment region. The evaluation of the energy flux is, for this reason, even more accurate since the third power of the velocity is involved.

It was necessary to establish a cut off criteria in order to exclude the contribution of the entrainment velocity to the flux value, that is

$\vec{v} \cdot \hat{n} = 0$ but $|\vec{v}|\,|\hat{n}| \neq 0$ in the entrainment region. Also, integration schemes to exploit the axisymmetric character of the full or upper portion of the jet were developed. The details of these operations are given in Appendix A.

The accuracy of the flux integrals depend upon the correctness of the local velocity and the ability to form an area integral from separate y traverses. Consequently, some ambiguity must be expected. Two procedures were used to standardize the data for presentation and further processing. The data for the x = constant planes which demonstrated apparently correct isotachs and negligible pressure effects (such that the momentum flux was conserved) were used to define a standard momentum flux as the average J(o) value for the above described cases. This value was normalized by J_o and was only dependent on the nozzle configuration. The values calculated by this process were

$$\lambda_u \equiv J(o)/J_o = 0.809 \quad \text{uniform} \tag{13}$$

$$\lambda_{fd} \equiv J(o)/J_o = 0.676 \quad \text{fully developed} \tag{14}$$

The second procedure made use of the streamwise invariance of the x-component momentum flux J_x as determined by (1) an auxiliary test of the maximum wall shear force magnitude and (2) a calculated estimate for the maximum pressure force acting on a yz plane. Since the J_x value is defined as

$$J_x(o) = J(o) \cos \alpha \tag{15}$$

and since

$$\frac{dJ_x}{dx} = 0 \quad , \tag{16}$$

the measured values of $J_x(x)$ provide an integral check on the accuracy of the data. If the computed value of $J_x \neq J_x(o)$ then some error exists in the velocity data or the integration process. If the error results from the integration process or an irregular velocity error, then no rational procedure to correct the mass and energy flux values is known. If the error is in velocity and if the error recorded is proportional to the

true velocity value (and if the integration schemes are valid), then the mass and energy flux values can be corrected as shown below. The appendix gives a more detailed account of the motivation for and the analytical aspects of this correction procedure.

Let u be the measured x-component velocity and let

$$u = u_T + \delta_u \tag{17}$$

where u_T = the true velocity and δ_u the difference error. If δ_u is proportional to u_T (i.e., $\delta_u \sim u_T$) then the momentum flux is

$$\begin{aligned} J &= k \int \rho u_T^2 \, dA \\ &= k \, J_T \qquad \text{for } \delta_u \sim u_T \end{aligned} \tag{18}$$

where $k = [1 + (\delta_u/u_T)^2]$ and J_T is the value given by (15). Similar considerations lead to

$$E_T = E(x)/k^{3/2} \qquad \text{for } \delta_u \sim u_T \tag{19}$$

$$M_T = M(x)/k^{1/2} \qquad \text{for } \delta_u \sim u_T \tag{20}$$

The normalizing scheme of (19) and (20) is used for the presentation of the flux data. This usage is motivated by the consideration that the correction is valid if $k \cong 1$ and no other rational correction is known if $k \neq 1$. The flux data are presented in two separate plots for each nozzle configuration; the data are separated according to whether or not the computed k value is within the range $|k - 1| \leq 0.03$. If the k value is outside this range and if δ_u is not proportional to u_T, then the data must be considered for their qualitative, not quantitative, value. The trends of the data must serve as the guide for this evaluation.

4.4.3. Discussion

The mass and energy flux ratio values are presented in Figures 30 to 33. Two separate figures have been prepared for each nozzle exit condition; the data for the condition $|k - 1| \leq 0.03$ is separated from the data which fall outside this range. This grouping does not necessarily segregate the data into accurate and inaccurate groupings;

rather, it separates the data into more and less degrees of certainty with regard to its accuracy. That is , to show that the groupings are fallible, it there is proportionality between δ_u and u_T, then the data for $|k - 1| > 0.03$ is as reliable as those cases defined by the three percent error band for the momentum flux. Conversely, the nonlinearity of the momentum flux integrand means that for the condition $\delta_u \neq 0$, $k \approx 1.0$ is possible.

4. 4. 3. 1. The Effect of the Nozzle Exit

The effect of the nozzle exit condition on the mass and energy flux values can be evaluated from those cases of essentially constant momentum flux and negligible direct influence of the plate. These cases have been used to define the (least squares evaluated) straight lines on Figures 30 and 32. These linear variations were not expected; they do facilitate this and other comparisons. It should be noted that neither mass flux curve is constrained to pass through (0, 1). However, the ratio of the maximum to the average velocity for a fully developed pipe flow in the Reynolds number range of the present study is 0.817 which compares very closely with the $(J(0)/J_0)^{1/2}$ value of $(0.6764)^{1/2}$ = 0.8224.

The slope of the mass rate of flow curve is the spatial entrainment rate of ambient fluid. A significant difference between the uniform and fully developed nozzle exit conditions is evidenced by these results. The entrainment rates for the uniform and the fully developed exit conditions were 0.134 and 0.174, respectively. This is a difference of about 30 percent!

The entrainment of ambient fluid is, in the most fundamental sense, a transfer of vorticity by viscous diffusion. The entrainment rate depends upon the contamination rate of ambient fluid which, in turn, is dependent upon the spatial gradient of the vorticity fluctuations and the total surface area available for the transfer. Although the uniform flow case would appear to have steeper velocity gradients and therefore probably larger spatial gradients of vorticity fluctuations, the large scale turbulence structure at the exit of the fully developed nozzle would provide a relatively larger surface area for the diffusion of vorticity. Hence, the larger entrainment rate for the fully developed condition is a reasonable result.

4. 4. 3. 2 Comparisons with Earlier Studies

The computed mass and energy flux values for the earlier studies are presented in Figures 34 and 35 the linear curves defined for the present data are included for reference purposes. The data of Alexander et al. shows a strikingly constant momentum flux and a quite linear M(x) variation. The x=1 data of Sami et al. results in a momentum flux value which is much smaller than the other x stations which show consistent momentum flux values. This pattern would be compatible with a vena contracta effect. This explanation is also supported by pressure measurements x = 1 and by the shape of the nozzle. The relatively large jump in the J value between x = 0 and x/d ≃ 3 for the Mons and Sforza data is not readily explained; the error is apparently caused by the displacement effect associated with an impact tube in a strong velocity gradient [26]. This explanation would be compatible with the decreasing values calculated in [21] for J(x) and the equality of J(0) and J(x) for large x values. If this is the source of the error, then the use of $k^{1/2}$ is not a formally valid correction but will cause the indicated value to tend toward the true value.

The data from these earlier studies are compatible with two intuitive estimates for the effect of the initial and geometric conditions on the near field entrainment rate. The initial conditions have been examined in terms of the present data; specifically, if the flow contains large structure turbulence at the exit plane, then it will probably have a greater entrainment rate as compared with a more quiescent flow. Secondly, if the entrainment can proceed parallel to the jet axis, then the entrainment rate will be greater than the perpendicular entrainment condition of a jet exhausting from a wall. The turbulence structure at the exit plane was not reported for any of these studies; however, it can be estimated that the Alexander et al. investigation involved a rather strongly disturbed exit condition since their 5: 1 (diameter) contraction nozzle was fed by a pipe. The disturbance levels for the Mons and Sforza and the Sami et al. studies are difficult to estimate although the former utilized two banks of settling screens in the plenum ahead of the small radius contraction for the orifice hole (plenum diameter = contraction radius = 0. 625 inches, orifice diameter = 0. 363 inches) and the latter

used a large plenum with a small contraction ratio nozzle.

The data of Crow and Champagne [11] were generated from a nozzle shape quite similar to that of Alexander, et al.; however, the nozzle exit flow condition was quite different for [11]. The intensity of streamwise fluctuations $[\overline{u}^2]^{1/2}/u(0)$ for [11] was approximately 0.005, with a locally large value in the shear layer (0.08) at the location x/d = 0.025. For this condition, the entrainment rate was 0.136 for the first two diameters. Their data showed a gradual increase in the entrainment rate with a (supposed) asymptotic value of 0.292 being attained for $x/d \gtrsim 6$. The rather different behavior of their flow (i.e., a non-linear growth in the mass flux) as compared with the other prior studies and the present data may result from the very thin laminar boundary layer at x = 0 for their study. For the case of 2 percent forcing, i.e. $[\overline{u}^2]^{1/2}/u(0) = 0.02$, the initial entrainment rate was approximately 0.2, for $0 \leq x/d \lesssim 2$, and showed a non-linear behavior resulting in a "final" entrainment rate of approximately 0.27. The trend associated with the forcing condition is compatible with the interpretations of the present study that the near field entrainment rate is dependent upon the disturbance level of the flow at x = 0.

With regard to the entrainment region geometry, the Alexander et al. study and the Crow and Champagne study allowed for basically parallel entrainment; the Mons and Sforza orifice was in a plane 10 diameters larger than itself and the Sami et al. orifice was in an effectively infinite wall. Consequently, both the probable disturbance level and the geometric effects contribute to the large entrainment rate for the Alexander et al. study; the influence of the individual effects are suggested by a comparison between [12] and [11] to show the flow condition effects and between [12] and the fully developed data to show the geometric effects.

The combination of the previous and present experimental results does allow an interesting interpretation about the indirect effect of the infinite plate. Specifically, it appears that the presence of the plate significantly inhibits the mass entrainment even for a condition wherein no direct effect is apparent in the surface pressures or the isotach patterns. A control volume of unit length defined with regard to (x, 0, z_c) as the r = 0 location and with boundaries $R_j \leq r \leq R_L$ and $0 \leq \theta \leq \pi$

(where $\theta = 0$ is parallel to the plane of the plate) is useful for indicating this effect. This is similar to the control volume shown in Figure 4 except that the lower surface is at z_c and not $z=0$. For a steady flow, the flux of mass into the control volume is identical to the flux of mass out of the control volume. This mass flux is equal to the entrainment rate. The area available for entrainment is equal to

$$\text{Entrainment area} = \pi R_L + 2z_c \tag{21}$$

and since $2z_c/\pi R_L \to 0$ as $R_L \to \infty$, the mass entrained in the far field of the upper half plane is approximately the total mass entrainment. Therefore, the entrainment rate for the round-jet/plane-wall flow field (dM/dx) can be expected to be characterized as

$$(1/2)\left.\frac{dM}{dx}\right|_{\text{free jet}} \leq \left.\frac{dM}{dx}\right|_{\text{present}} < \left.\frac{dM}{dx}\right|_{\text{free jet}} \tag{28}$$

This indicates that even though the jet may be displaced a significant distance above the plate, the (effectively) infinite lateral extent of the plate can have a marked effect on the entrainment since the effective entrainment area is reduced compared with that of a free jet.

This analysis suggests that the geometric effects are significant since the disturbance level of the fully developed condition in the present study is probably greater than that in the Alexander et al. investigation. This conclusion should be evaluated experimentally. This was not done for the present study since the traverse device would not accomodate such an evaluation. It will be done for part II of this investigation.

In the "far" downstream region of a free jet, a condition of self-preservation is attained for which the velocity field may be described by the conditions (see Townsend [27] for a more complete discussion of self-preservation):

$$u = u_o f(r/\ell_o) \quad \text{(self-preservation)} . \tag{23}$$

In this region for an axisymmetric turbulent jet,

$$u_o \sim x^{-1} , \quad \ell_o \sim x , \quad \text{and} \quad M(x) \sim x . \tag{24}$$

It has been strongly suggested, but not proved, that the coefficients for the above proportionalities are independent of the nozzle conditions [27]. A very clever study by Ricou and Spalding [28] has identified the coefficient for the mass flux such that

$$\frac{M(x)}{M(0)} = 0.32\, x/d \tag{25}$$

Consequently, if the "independence of origin" hypothesis is valid, the near field entrainment rate for all the cited cases is lower than the asymptotic rate and the initially linear region must possess a non-linear intermediate region of growth to achieve the required growth rate far downstream.

The smaller rate in the near field is reasonable in terms of a relationship between the corrugations of the bounding surface and the net entrainment rate. That is, the scale of the turbulent structure (Λ) is (apparently) an increasing fraction of the jet radius for increasing x until the ratio Λ/ℓ_0 attains a constant value in the self-preserving region.

There is not sufficient information to determine whether or not the asymptotic entrainment rate is independent of the conditions at the origin. If it is not, then an experimental configuration as employed by Ricou and Spalding would necessarily be used for each different nozzle. However, the significantly smaller entrainment rate for the near field and the effect of the initial and geometric conditions is clearly established.

4. 4. 3. 3. The Direct Effect of the Jet-Plate Interaction

The data which are not used to define the characteristics of the uniform and fully developed jet conditions are available to characterize the jet-plate interaction effects. The qualitative trend that the mass flux is reduced is both expected and observed. The corresponding observation that the energy flux decreases at a lesser rate is analytically required since a relative decrease in the integral of u accompanied by the constancy of the u^2 integral requires that the integral of u^3 be

relatively increased. Physically, these observations can be explained in terms of limitation in the area over which entrainment can occur (re the mass flux) and a protection of the high velocity fluid by inhibiting the turbulent shear effects (re the energy flux). The shear effects will be locally greater near the plate for a jet-plate interaction but they will not affect as much fluid as does the free-shear field of the jet. This latter observation is supported by the formulation (see Corrsin [29])

$$\epsilon_M \sim \dot{u}\Lambda \tag{26}$$

where Λ is an integral scale of the turbulence. The influence of the plate is to reduce Λ and hence the magnitude of the turbulent shear effect.

The quantitative effects are not as easily defined because of the ambiguities of the data. The fully developed cases do show a rather consistent and clear trend in which the stronger jet-plate interactions cause deviations from the linear portion of the M(x) curve for smaller x/d values. The apparently greater accuracy in data for the fully developed condition was not expected since a spurious jet temperature effect on the hot-wire readings was identified after the majority of the fully developed data were acquired; that is, the air was heated by approximately 10-15 degrees Fahrenheit in the blower and flow system and this changed the effective overheat value for the wire. A linearized analysis (for small Δ T) showed that such an effect would not alter the zero value but would affect the slope of the linearized hot-wire calibration curve. This correction was made to the data by a computer routine which corrected each hot-wire slope to that value indicated by the measured velocity u_o. This correction procedure is known to contribute some inaccuracy since the mixing of the jet with ambient fluid reduces this temperature error. However, since the $J_x(x)$ value was used for the normalization scheme, the net corrections (apparently) provide reasonably accurate results. The heat exchanger shown in Figure 7 was added before the acquisition of the uniform exit condition data. The irregularities for the uniform exit condition may result from the steeper mean flow gradients for this case which would result in greater

inaccuracies in forming an area integration from discrete, z-location traverses.

4. 4. 4. Relevance

The flux ratios have shown that the exit conditions have a rather marked effect on the entrainment rate for the near field of a jet and the somewhat lesser effect on the energy flux ratios would imply that the primary effect of the nozzle condition is evidenced in the outer portion of the jet. Since the engine blown flap configuration makes use of the near field of a jet and since the outer region of the jet will be important in defining the jet-jet interaction for multiple engines, it is felt that this effect is of importance for the application problem.

Energy flux data for the condition of a direct jet-plate interaction show that the high velocity fluid near the "centerline" of the jet is "conserved;" that is, the velocities above the plate remain relatively large outside of the three-dimensional boundary layer on the plate. This is inferred to be quite significant for the application problem since high velocities near the plate (air foil) are desirable in order to energize the boundary layer on the suction side of the flap via the high velocity fluid passed through the flap gap. This would indicate that a short length before attachment is desirable.

The measured entrainment rates will provide an indication of the entrainment velocities. From these, the effect of the jet entrainment on the modification of the "inviscid" flow around the airfoil can be estimated. The comparison of the M(x) values determined from the earlier studies and the indicated geometric effects on the interpretation of near field jet data provide cause for general caution in the interpretation of experimental data for such flow fields.

4. 5. Results Dependent Upon Surface Pressure Values

4. 5. 1. Purpose

Surface pressure measurements have been made for a wide range of geometric and flow conditions. These data have allowed the determination of (1) surface pressure forces, (2) the magnitude of the z component momentum flux and (3) the location of the effective x-component momentum flux as functions of x for the various conditions.

The surface force provides a measure of the jet-plate interaction and additional aspects of the nozzle exit effects are provided by these

data. The indicated force loadings may also be pertinent for the structural design of the air foil. The z-component momentum flux (J_z) has an asymptotic value of zero for large x. Therefore, the numerical values for this quantity provide a measure of the effective development length of the flow field for a given x location. The measured pressure values and the z-component momentum flux along with certain assumptions regarding the entrainment allow the effective location (z_m) of the x-component momentum flux to be determined from the moment-of-momentum equation. The effective location will be identical with the geometric axis of the nozzle until the lateral force effects of the jet-plate interaction cause the jet to curve. A comparison of the z_m and z_c values allows a comparison between the turning effect on the entire jet (z_m) as compared with the behavior of the center line defined by the upper portion of the jet (z_c).

4. 5. 2. Data Processing

The pressures on the plate were measured in steps of 0. 1 inch for a y traverse and in integer multiples of 1/8 inch as a function of x. (This assumes symmetry of the flow field as noted in Section 3.) These rather fine spacings and the computer averaged values of p(x, y, t) to define $\bar{p}(x, y)$ have resulted in data of considerable reliability. The normalized pressure force (F_p) is defined as

$$\frac{F_p(x)}{J(0)} = \frac{1}{J(0)} \int_0^x \int_{-\infty}^{\infty} p \, dy dx \quad . \tag{27}$$

The z-component of momentum has been calculated using the pressure data and the control volume of Figure 4. For this, the Bernoulli equation is required to relate the entrainment velocity (Q_e) to the pressure outside the jet (p_e) as

$$p_{atm} - p_e = \frac{\rho}{2} (Q_e^2 - Q_{atm}^2) \tag{28}$$

and since the gage pressure is required for the calculation of the pressure force and since $Q_{atm} \equiv 0$, the gage pressure $(p_e)_g$ is

$$(p_e)_g = -\rho \frac{Q_e^2}{2} \tag{29}$$

The z-component momentum equation is

$$\int_{A_p} p\, dA - \int p_e \hat{k} \cdot \hat{n} dA = J_Z(x) + J(0) \sin\alpha + \int_{A_e} \rho \vec{v}_e \cdot \hat{k}\, \vec{v}_e \cdot \hat{n}\, dA \tag{30}$$

where gage pressures are assumed, A_p is the area of the plate, and A_e is the entrainment area (i.e., the dome shape of Figure 4). The assumption is made that

$$\vec{v}_e = - |Q_e| \hat{n}$$

hence

$$(\vec{v}_e \cdot \hat{k}\, \vec{v}_e \cdot \hat{n}) = - Q_e^2 \hat{k} \cdot \hat{n}$$

and the entrainment pressure and flux integrals of (30) can be combined for the general normalized equation as

$$\frac{F_p}{J(0)}(x) = \frac{1}{J(0)} \int_{A_p} p\, dA = \frac{J_z}{J(0)}(x) + \sin\alpha - \frac{1}{2J(0)} \int_{A_e} \rho Q_e^2 \hat{k} \cdot \hat{n}\, dA \,. \tag{31}$$

This equation allows the $J_z(x)/J(0)$ values to be computed from the measured pressure data and the estimated entrainment velocites which are based on the entrainment rates discussed in Section 4. 4. 3.

The moment-of-momentum equation can be used to define the location of the x-component momentum flux (z_m). Using the control volume of Figure 4 and summing moments about the axis of the nozzle at x=0

$$\int_{A_p} p\, x\, dA = (h - z_m) J_x + x J_z - \frac{1}{2} \int_{A_e} \rho(\vec{r} \times \vec{v}_e) \cdot \hat{j}\, \vec{v}_e \cdot \hat{n}\, dA \,. \tag{32}$$

Note that the entrainment integral is zero except for the plane x = 0; hence, its contribution is negligible. This equation can be normalized by using J(0) and d. The effective location of J_x, (i.e., z_m) can be seen to be dependent primarily on the pressure data since J_x is a constant for a given nozzle and J_z is defined in terms of the pressure and Q_e. The normalized equation is

$$\frac{1}{J(0)} \int_{A_p} p\,(x/d)\,dA = \frac{(h-z_m)}{d}\,(\cos\alpha) + \frac{x}{d}\,\frac{J_z}{J(0)}$$

and can be written in a form to emphasize that the pressure effects will result in a positive or negative desplacement from the extended axis of the jet $h(x) = h - x\tan\alpha$. That is,

$$\frac{z_m}{d} = \frac{h}{d} - \frac{1}{J(0)\cos\alpha} \int_{A_p} p\,(\tfrac{x}{d})\,dA + \frac{x}{d}\,\frac{J_z}{J(0)}$$

and using equation (31) for J_z,

$$= \frac{h}{d} - \frac{x}{d}\sin\alpha + \frac{x}{d}\left\{\frac{F_p}{J_o} + \frac{1}{2J(0)} \int_{A_e} \rho Q_e^2\, \hat{k} \cdot \hat{n}\, dA\right\} - \frac{1}{J(0)\cos\alpha} \int_{A_p} p\,\frac{x}{d}\,dA \quad . \tag{33}$$

4. 5. 3. Discussion

4. 5. 3. 1. Pressure Force and z Component Momentum Flux

The pressure force values are shown in Figures 36 to 44. The initial region of each curve involves an essentially zero force value indicating no direct effect of the jet on the plate. The initial region is followed by a region of negative pressure force which is an indication of the entrainment effects. For larger x values, the pressure force increases and approaches the asymptotic limit defined by $J_z \to 0$ for $x \to \infty$ in (31). This asymptotic value can be approximated by neglecting the entrainment effects; for this assumption

$$\frac{F_p}{J(0)} \to \simeq \sin\alpha \qquad \text{for } x \to \infty \quad . \tag{34}$$

This asymptote is shown on the figures for the pressure force.

A general pattern is evidenced by these figures in which the negative portion for the fully developed exit condition is rather pronounced as compared with that for the uniform exit condition. This is compatible with the entrainment rate results of Section 4. 4. 3 which indicated a significantly greater rate for the fully developed exit profile condition.

The approximate asymptotic value for F_p is independent of the nozzle exit condition, however, the figures show that the character of the pressure force is quite dependent upon this flow parameter. Apparently, the slope of the F_p curve is greater for the uniform case if the joint conditions 1) small streamwise distances to the plate and 2) a relatively rapid (not a glancing) approach to the plate are met. The uniform exit condition shows a less steep rise in the pressure force curve if the opposite conditions obtain. The following sequence of cases (designated as α, h/d) are cited in support of the above generalization. Note that 9, 1 provides a condition of nearly identical $F_p(x)/J(0)$ values, that is, it is a reference condition for the terms "small" and "rapid" in (1) and (2) above. The cases are (i) 6, 0.75; (ii) 3, 0.75; (iii) 12, 1.5; (iv) 9, 1; (v) 6, 1; and (vi) 9, 1.5.

The x-location of the maximum slope would also serve to characterize the $F_p(x)$ curve. This x dependence appears to respond to a more complex set of causal factors since no pattern has been identified.

The existence of an approximate asymptotic value for $F_p/J(0)$ allows the magnitude of $F_p(x)/F_p(\infty)$ to be used as a measure of the development length of the flow field; the shape of the curve indicates the rate of development. An alternate representation of the development length is provided by the values of $J_z/J(0)\sin\alpha$ presented in Table 1. (The asymptotic value of J_z is zero, i.e., $J_z(\infty) = 0$.) The tabular format has been prepared to allow an assessment of the effect of the geometric and flow conditions on the development length for a given x/d location.

The development length and the degree of attainment of asymptotic condition is an important factor in assessing the generality of these results. The present study was performed using an effectively infinite plate.[1] When the condition $J_z = 0$ is attained, the flow would be parallel to the plate and the plate would be effectively infinite in length as regards the end condition affecting the upstream flow. If $J_z \neq 0$ at the x location of the plate termination, then the present results could not be considered applicable without further information. For example, if

---

[1] A finite plate would not only introduce an additional geometric parameter; more importantly it would require the specification of the flow condition at the termination of the plate.

the plate exhausts to a relatively high velocity (u_s) streaming flow (i. e., if $\bar{w}(x)/u_s << 1$) then the streaming flow would serve as an extension of the plate and the present results would be applicable. If $u_s = 0$, then the termination of the pressure field will have some upstream effect and the present results would necessarily be applied with caution. The smaller the J_z value in Table 1, the less important are the conditions at the end of a plate of length x/d.

4. 5. 3. 2. Location of x-Component Momentum Flux

The z_m values are presented in three figures, (see 45 to 47) in order to provide a comparison between z_m and z_c for a given nozzle condition and to compare z_m values for the different nozzle conditions. The former plots compare a measure of the jet locations which depend upon the entire jet, i. e. z_m, with one which is only a measure of the upper portion of the jet, i. e. z_c. The vertical scale for these plots is exaggerated to show the small deviations from the geometric axis of the jet defined by h(x). The z_c values have an uncertainty of ±0. 03 in. about the best straight line through the data points. (This accounts for positioning errors in the generation of the original data. The z_m values are not so affected since they are computed from the pressure data.) The probable uncertainty in the z_m values depends upon the thermal drift which occurred between the frequent rezeroings of the transducer. (The transducer is linear to within less than one percent.) Considering the pressure reading to be expressed as $p = p_T + \delta_p$ and examining the maximum percentage error in terms of the deviation of z_m from h(x), one can conclude from (31) that the maximum error will occur at that x location where the pressure terms pass through zero. Since the z_m data agrees quite well with h(x) in this region it is inferred that the probable error in z_m is very small.

The deviation of the z_m values from the h(x) curves is considered to be an accurate measure of the jet turning as a result of the jet-plate interaction. In general, the z_c values tend to follow the geometric axis for a longer streamwise distance. This is reasonable; it confirms the earlier observation that the pressure effects are, in general, confined to the region below the center line of the jet as defined by z_c or h(x).

Figure 47 shows the effect of the nozzle exit on the z_m values; the effect is seen to be quite small with the exception of the region where

$z_m < h(x)$, i. e., where the entrainment causes the jet to approach the plane wall. This observation supports the earlier conclusion that the nozzle condition primarily affects the low velocity fluid near the edge of the jet.

4. 5. 4. Relevance

The importance of the nozzle exit condition on the force distribution and the development length of the flow field provide an indication of factors which can influence the test results from the externally blown flap configuration. The force magnitudes represented by these measurements will also provide order of magnitude estimates and an indication of possible geometric influences for the pressure forces to be expected for a prototype configuration. The definition of the "flow development" measures in terms of $F_p(x)/F_p(\infty)$ and $J_z(x)$ will provide guidelines for the interpretations of these data in terms of the application problem. The agreement between z_c and h(x) supports the use of the Reichardt analysis to compute the upper portion of the jet field.

5. SUMMARY AND CONCLUSIONS

The round-jet/plane-wall flow field investigation reported herein has been motivated by the externally blown flap configuration for STOL aircraft. The study has been primarily experimental; analytical considerations have been used to define measures of the flow field characteristics. This application problem has been used as a guide for the selection of the investigated geometric and flow conditions. The application problem has also served to structure the processing of the experimental data and the measures used to characterize the flow field. The results are presented in a common format which includes the following four elements for each of the four characterizations of the flow field 1) purpose, 2) data processing, 3) discussion (of the results) and 4) relevance (to the externally blown flap application problem).

The following conclusions are supported by the results of this study.

1) The condition of the flow at the exit plane of the nozzle has an apparently significant effect on the jet. This effect is most pronounced for the outside or low velocity portion of the jet. This is shown by the mass flux ratios and by the pressure force values.

2) The x-component of the momentum flux is essentially conserved for all the cases of the present study. The mass and energy flux values show that the jet-plate interaction "protects" the high velocity fluid near the plate surface.

3) The upper portion of the jet is relatively unaffected by the jet-plate interaction. The axis of the jet (defined as the center of isotach pattern) is not appreciably affected by the presence of the plate. The Reichardt analysis can be used to compute the axisymmetric portion of the velocity field even for strong distortions of the lower portion of the jet.

4) Measures for the development length of the flow field show that the jet-plate interaction is still developing at $x/d = 5$ for nearly all of the cases investigated. This must be considered when applying the present results with those generated by an investigation of the prototype.

APPENDIX A

Data Processing for the Flux Ratios

A. 1 INTEGRATION PROCEDURES

Considerable care was required for the computer integration of the data for the flux ratios. Since the individual points were generated in steps of 0. 1 in, a direct application of the Simpson rule was warranted. However, the y traverses were made over a physical distance of $-2 \text{ in} \leq y \leq 2 \text{ in}$ and consequently the wires, in general, recorded transverse entrainment velocities at the extremities of these traverses. In this region, the approximation that $(\overline{u}^2 + \overline{v}^2) \simeq \overline{u}^2$ is clearly in error. (The inclusion of these spurious readings was responsible for errors up to $\approx$ 15 percent in some of the early data processing for this study.) A cut-off condition that could be logically determined by a processing routine was required; the development of this routine is described below. A second possible source of error for the integration of the experimental data was the insufficient number of traverses for large z; that is, the upper isotach patterns were circular but the uppermost z location formed a chord for the circular pattern. Consequently, some velocity data was not directly included in the individual traverses.

The cut-off criterion was established on the basis that the entrainment velocity could be described as cylindrically symmetric and hence

$$(\text{velocity magnitude})\,(r) = K \tag{1A}$$

where r is measured from the isotach center for that x location. The value of K for a given y traverse was determined by proceeding with the computation from the outside of the jet toward the center and evaluating an average K from the individual rQ products. The edge of the jet was defined as the location for which two successive K values deviated by more than 10 percent from the average; two values were required to guard against a spurious velocity value.

The velocity data which was corrected for the cut-off condition was integrated by one of three techniques. These schemes were developed to account for the possibility of incomplete data in the upper portion of the jet and to take advantage of the smoothing effects provided by the axisymmetric assumption.

For those conditions which resulted in negligible distortion of the isotach pattern, the entire flow field was assumed to be axisymmetric. The data points which were stored according to their y location for a traverse at a given z value were converted to an r, θ designation with the r value measured from the center of the isotach circles. A u(r) velocity distribution was then obtained by averaging the contributions from the various traverses. That is,

$$\bar{u}(r) = \frac{1}{N} \sum_{i=1}^{N} u(r, \theta_i) \tag{2A}$$

where $r = [(z-z_c)^2 + y^2]^{1/2}$ and $\theta_i = \tan^{-1}(z_i - z_c)/y_i$. The data in this form allowed a direct integration for the mass, momentum, or energy flux values.

A second technique was used for those cases which exhibited an axisymmetric condition for the upper half ($z > z_c$) but not the full plane. The $\bar{u}(r)$ averaging and the axisymmetric integration were performed for the upper-half plane; these values were added to the results of a cartesian coordinate integration technique utilized for the lower portion of the jet.

The mass flux for the lower portion of the jet will be used as an example of the technique; it can be expressed as

$$M(0 \leq z \leq z_c) = \int_0^{z_c} \int_{-\infty}^{\infty} \rho\, u\, dy dz \quad . \tag{3A}$$

Since the data were available in the form of y traverses at different z locations, it was convenient to integrate the primary data with respect to y to obtain

$$M(z) = \int_{-\infty}^{\infty} \rho\, u\, dy \tag{4A}$$

The integration with respect to z can be constructed by fitting a second order equation to the M(z) values as

$$M(\zeta) = a + b\zeta + c\zeta^2 \tag{5A}$$

and then performing the integration over the area as

$$M(0 \leq z \leq z_c) = \int_{z_1}^{z_2} M_1(\zeta)d\ell + 1/2 \left[\int_{z_2}^{z_3} M_1(\zeta)d\zeta + \int_{z_2}^{z_3} M_2(\zeta)d\zeta \right]$$

$$+ 1/2 \left[\int_{z_3}^{z_4} M_2(\zeta)d\zeta + \int_{z_3}^{z_4} M_3(\zeta)d\zeta \right] + \ldots \int^{z_c} \ldots \tag{6A}$$

where $M_1(\zeta)$ is the second order equation determined by the first three z location traverses, M_2 is determined by the traverses at the second, third and fourth z locations, etc. until all the z traverses in the lower portion of the jet are accounted for.

The third integration technique involves the application of the method described by (3A) to (6A) for the entire flow field. The third technique is used for all cases which do not show a circular isotach pattern for the upper portion of the jet. The isotach data for $\alpha = 12$, $h/d = 1$, uniform shows these three situations. Specifically, the data for $x/d = \simeq 0, 1$ show the condition wherein the full jet is axisymmetric, $x/d = 2, 3$ show the condition wherein the upper portion is axisymmetric and the lower portion is not and $x/d = 4, 5$ show the condition requiring a cartesian integration of the data.

A. 2. Presentation of the Flux Ratios

The integration techniques described in A. 1 represent the most accurate processing scheme given the available data; however, the values so determined may not be accurate as a result of the relatively coarse z spacing of the traverses and because of the inability to determine the velocity magnitude in the high turbulent intensity, strongly three-dimensional regions of the flow. Consequently, an independent evaluation of the probable accuracy or internal consistancy of the flux ratios is desirable.

As shown in the following, the physical effects which lead to a reduction in the magnitude of the x-component momentum flux (J_x)

can be shown to be negligible with respect to $J_x(0)$. Consequently J_x is a constant. Since $J_x(x)$ can be calculated from the velocity traverse data, an integral evaluation of the accuracy of the data is available. The special considerations which show that J_x is constant and an analysis leading to a plausible correction for the data is presented below.

The magnitude of the x-component momentum flux can be reduced by two physical effects: the surface shear stress τ acting over the plate surface and the static pressure force acting on a plane of constant x. The magnitude of the surface shear effect was determined by a special test. A small plate was supported by four light cords such that the fully developed nozzle exit and the conditions $\alpha = 18$ degrees, $h/d = 1$ were obtained. The initial orientation of the plate was such that its plane was perpendicular to the gravitational field. The cords formed a parallelogram as the plate was displaced by a force in its own plane. Consequently, the length of the cords (L), the weight of the plate (W) plus the normal force caused by the pressure on the plate (F_p) and the displacement of the plate (δ) caused by the action of the shear force on the plate (F_s) were sufficient to calculate F_s as a function of the momentum flux of the jet J(0). Specifically,

$$F_s = \frac{\delta}{(L^2 - \delta^2)^{1/2}} (W + F_p) \qquad (7A)$$

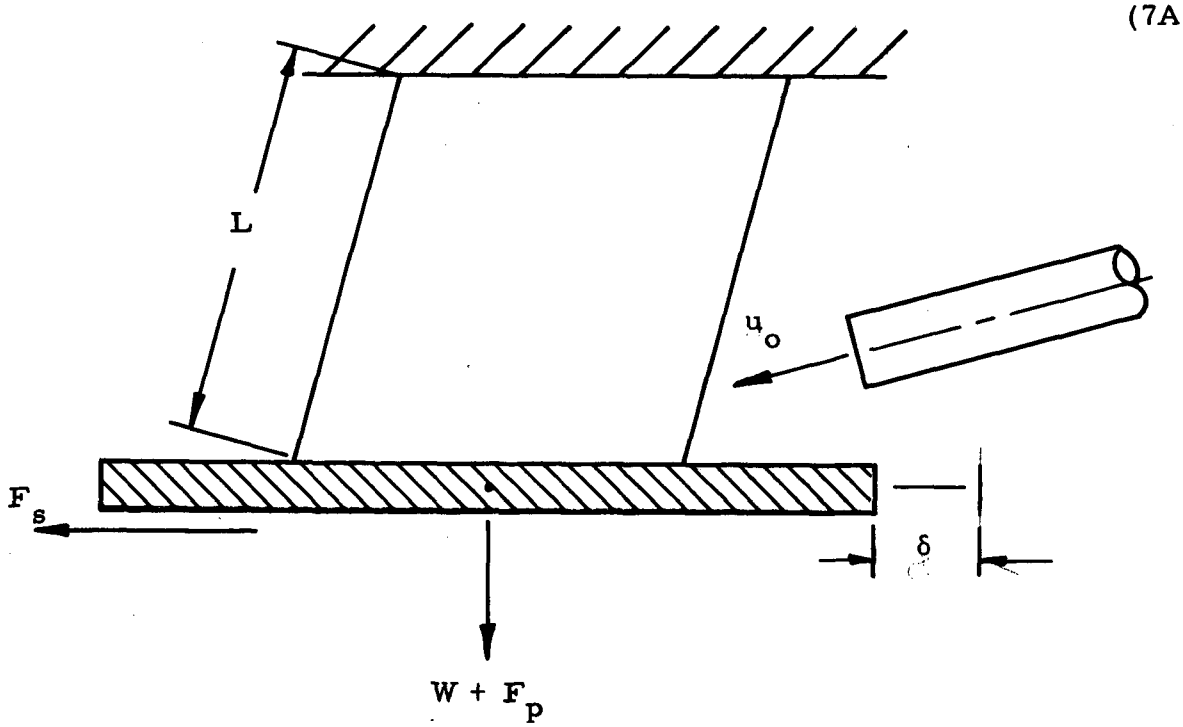

The results of this evaluation, for what was considered to be a worst case, showed that $F_s/J(0) < 1.5$ percent.

The maximum pressure force was estimated from data for the condition $\alpha = 15$ degrees, $h/d = 1$. For this, the pressure distribution at $x/d = 2.625$ was selected (since it possessed the maximum average pressure) and a pressure force was calculated from the assumption that

$$p(y, z) = p(y, 0) - \frac{p(y, 0)}{(z-z_c)} \quad z \quad \text{for } 0 \leq z \leq z_c$$

The pressure force over the plane of constant x (F_{yz}) was then evaluated as

$$F_{yz} = \int_0^{z_c} \int_{-\infty}^{\infty} p(y, z)\, dydz \tag{8A}$$

When this value was normalized on J(0), the pressure force was found to be approximately 2.5 percent of J(0). Unlike the shear force which monotonically increases with x, the pressure force F_{yz} will reach a maximum value and then decrease. Since this value was determined for the most extreme conditions of the present study, it is concluded that the reduction of the x-component momentum flux is negligible for all cases.

The centerline velocity at the nozzle exit u(0) was set at a value in the range $u(0) = 120 \pm 2$ fps for each geometric condition. Since the velocity field is insensitive to Reynolds number for these conditions and the exit velocity is essentially constant, the u(0) may be used to normalize the primary data for a given nozzle exit condition. Also, a unique relationship should exist between a momentum flux defined using this maximum velocity J(0) and the actual momentum flux from the nozzle J(0). (If the exit profile were uniform across the plane of the nozzle exit, the two would be identical.) Since the momentum flux is constant before the jet interacts with the plate, the J(0) value can be evaluated from a large number of measured values, namely those x stations which show a well defined isotach pattern and which do not show an increase in pressure on the plate.

The "true" J(0) value is

$$J(0) = \frac{1}{N} \sum_{i=1}^{N} J_x(\alpha,\ h/d,\ x/d)_i \ \frac{1}{\cos \alpha_i} \qquad (9A)$$

where J_x is the value determined from an integration of the primary data because of the response of the wire (Section 4. 2. 2). This evaluation has resulted in the values

$$J(0)/J_o = 0.809 \qquad \text{for the uniform nozzle} \qquad (10A)$$

and

$$J(0)/J_o = 0.676 \qquad \text{for the fully developed nozzle} \qquad (11A)$$

The normalized momentum flux values $(J_x(x)/J(0)\cos \alpha)$ evaluated at any station in the flow field should be unity; that is

$$\frac{1}{J(0) \cos \alpha} \int_0^{\infty} \int_{-\infty}^{\infty} \rho u^2 \, dydz = 1 \quad . \qquad (12A)$$

A value other than 1. 0 indicates that some sort of error exists in the original data or in the processing routine. The existence of an error in the velocity magnitude can be accounted for by the formulation $u = u_T + \delta_u$ where u_T is the true value of the velocity and u is the measured value. If the error is proportional to the true velocity magnitude, i. e., if δ_u/u_T = constant, then the momentum flux $J_{(x)}$ can be expressed as

$$J_x(x) = kJ_T(x)$$

since

$$\begin{aligned} J &= \int \rho u^2 \, dA \\ &= \int \rho (u_T + \delta_u)^2 \, dA \\ &= (1 + \delta_u/u)^2 \int \rho u_T^2 \, dA \\ &\equiv k \int \rho u_T^2 \, dA \end{aligned} \qquad (13A)$$

Since the true value of the normalized momentum flux is known to be unity, the value of k may be determined from the integration of the experimental data. The mass and energy flux values can be evaluated on the basis of the same assumption for δ_u.

$$M(x) = \int \rho u \, dA$$

$$= \int \rho(u_T + \delta_u) \, dA$$

$$= k^{1/2} \int \rho \, u_T \, dA \qquad (14A)$$

and $E(x) = \int \rho u^3 \, dA$

$$= k^{3/2} \int \rho u_T^3 \, dA \qquad (15A)$$

Consequently, if a given set of data does not provide a normalized momentum flux value of unity and if it is assumed that the velocity error δ_u is proportional to u_T, then the computed mass and energy flux values can be corrected by the use of (14A) and (15A) as

$$M_T(x) = M(x)/k^{1/2} \qquad (16A)$$

$$E_T(x) = E(x)/k^{3/2} \, . \qquad (17A)$$

If the assumption that δ_u is proportional to u_T is not valid, then (16A) and (17A) are not valid and there is no technique to rationally correct the mass and energy flux values.

A proportional error would result if the ambient air at the probe location were different from the air temperature for the calibration condition (this assumes a linear response to the temperature difference and hence a relative small ($\lesssim$ 10° C) temperature change.) A proportional error would also exist if the flow rate from the blower were altered. (This is rather improbable but not impossible; the exit velocity (u(0)) was not checked at the termination of every run.)

The normalizing scheme of (16A) and (17A) is used for the presentation of the data. For the condition of proportionality between u_T and δ_u,

this correction is justified and consistent trends in the data should be in evidence; for the condition $\delta_u = 0$, $J = J_T$ and the correction is irrelevant. For the condition where δ_u is not proportional to u_T no other correction appears to be rational; therefore, the data for such a case can be considered for its qualitative, not quantitative contribution.

A. 3 Evaluation of the Flux Ratios for Previous Studies.

In order to compare the data of the present study to the results of earlier investigations, the normalization scheme involving k must be applied to the earlier studies.

The data of Sami et al. and Mons and Sforza was scaled from the several plots of $\overline{u}(x, r)$ in their papers. Alexander, et al. [12] provided tabular values of $\overline{u}(x, r)$. For these, Simpson Rule integration routines were used to determine the flux and k values.

REFERENCES

[1] B. H. Wick and R. E. Kuhn, "Turbofan STOL research at NASA," Astron and Aeron. 9, 5, (May 1971).

[2] C. C. Smith, "Effect of engine position and high lift devices on aerodynamic characteristics of an external-flow jet-flap STOL model," NASA TN D-6222, (March 1971).

[3] J. A. Albers and M. C. Potter, "Potential flow solution for a STOL wing propulsion system," NASA TN D-6394, (July 1971).

[4] I. Tani and Y. Komatsu, "Impingement of a round jet on a flat surface," Proc. 11th Int. Cong. Appl. Mech., H. Goertler, ed., Springer Verlay, 672-676 (1966).

[5] J. L. Chao and V. A. Sandborn, "Evaluation of the momentum equation for a turbulent wall jet," J. Fluid Mech. 26, 819-828 (1966).

[6] J. W. Gauntner, J. N. B. Livingood and P. Hryack, "Survey of literature on flow characteristics of a single turbulent jet impinging on a flat plate," NASA TN D-5652, (February 1970).

[7] P. Hrycak, D. T. Lee and J. W. Gautner, "Experimental flow characteristics of a single turbulent jet impinging on a flat plate," NASA TN D-5690, (March 1970).

[8] O. V. Yakovlevskii and S. Y. Krasheninnikov, "Spreading of a turbulent jet impinging on a flat surface," Fluid Dynamics 1, 4, (July-August 1966).

[9] C. DuP. Donaldson and R. S. Snedecker, "A study of free jet impingement, Part 1 mean properties of free and impinging jets," J. Fluid Mech. 45, 281 (1971).

[10] H. B. Squire, "Jet flow and its effect on aircraft," Aircraft Eng. 22, 62 (March 1950).

[11] S. C. Crow and F. H. Champagne, "Orderly structure in jet turbulence," J. Fluid Mech. 48, (August 1971).

[12] L. G. Alexander, T. Baron and E. W. Comings, "Transport of momentum, mass and heat in turbulent jets," University of Illinois, Engineering Experiment Station, Bulletin 413, (1953).

[13] D. J. Raney, A. G. Kurn and J. A. Bagley, "Wind tunnel investigation of jet interference for underwing installation of high by-pass ratio engines," ARC-CP-1044 (RAE, Farnborough, 1969). STAR Code N69 38230.

[14] S. Sami, T. Carmody and H. Rouse, "Jet diffusion in the region of flow establishment," J. Fluid Mech. 27, 231 (1967).

[15] P. Bradshaw, "The effect of initial conditions on the development of a free shear layer," J. Fluid Mech. 26, (October 1966).

[16] J. J. Flora, Jr., and V. W. Goldschmidt, "Virtual origins of a free turbulent jet," AIAA J. 7, 12, (December 1969).

[17] S. Corrsin and A. L. Kistler, "Free stream boundaries of turbulent flows," NACA Report 1244, (1955).

[18] J. O. Hinze, Turbulence (McGraw-Hill, 1959).

[19] H. Reichardt, "On a new theory of free turbulence," ZAMM 21, 5, (October 1941).

[20] T. Baron and L. G. Alexander, "Momentum, mass and heat transfer in jets," Chem. Eng. Progress 47, 4, 181-185 (April 1951).

[21] R. F. Mons and P. M. Sforza, "Turbulent heat and mass transfer in in axisymmetric jets," PIBAL Report No. 71-14, (May 1971).

[22] N. Trentacoste and P. M. Sforza, "Further experimental results for three-dimensional free jets," AIAA J. 5, 5, (May 1967).

[23] F. H. Champagne, "Turbulence measurements with inclined hotwires," BSRL Document D1-82-0491, (December 1965).

[24] J. Crank, The Mathematics of Diffusion (Oxford University Press, 1956).

[25] H. S. Carslaw and J. C. Jaeger, Conduction of Heat in Solids (Oxford Press, 1959), 2nd ed.

[26] F. A. MacMillan, Experiments on Pitot Tubes in Shear Flow, A. R. C., R. and M. 3028, (1956).

[27] A. A. Townsend, The Structure of turbulent shear flow (Cambridge University Press, 1956).

[28] F. P. Ricou and D. B. Spalding, "Measurements of entrainment by axisymmetric turbulent jets," J. Fluid Mech. 11, 1, 21-32 (August 1961).

[29] S. Corrsin, "Some current problems in turbulent shear flow," Naval Hydrodynamics Publication 575, (1957).

Z-COMPONENT MOMENTUM/SIN(ALPHA)

	15.000			- 0.99999		- 0.99999
	12.000				- 1.00000	
ALPHA	9.000				- 0.99999	
	6.000					
	3.000					
x/d = 1	0.000					
		0.50000	0.75000	1.00000	1.50000	2.00000
					H/D	

Z-COMPONENT MOMENTUM/SIN(ALPHA)

	15.000			- 0.80419		- 1.00529
	12.000				- 1.00951	
ALPHA	9.000			- 0.99999	- 1.00192	
	6.000				- 0.99999	
	3.000					
x/d = 2	0.000					
		0.50000	0.75000	1.00000	1.50000	2.00000
					H/D	

Z-COMPONENT MOMENTUM/SIN(ALPHA)

	15.000			- 0.39684		- 1.01222
	12.000				- 1.00922	
ALPHA	9.000			- 0.86540	- 1.00471	
	6.000		- 0.99999	- 0.99999	- 0.99938	
	3.000		- 1.00000	- 1.00000		
x/d = 3	0.000		0.00000	0.00000		
		0.50000	0.75000	1.00000	1.50000	2.00000
					H/D	

Z-COMPONENT MOMENTUM/SIN(ALPHA)

	15.000			- 0.10517		
	12.000				- 0.92929	
ALPHA	9.000			- 0.61194	- 1.00707	
	6.000		- 0.60765	- 0. 9245	- 0.99814	
	3.000		- 0.74821	- 0.96427		
x/d = 4	0.000		0.00000	0.00000		
		0.50000	0.75000	1.00000	1.50000	2.00000
					H/D	

Z-COMPONENT MOMENTUM/SIN(ALPHA)

	15.000					
	12.000				- 0.68396	
ALPHA	9.000				- 0.94577	
	6.000		- 0.38323	- 1.23213	- 1.00061	
	3.000		- 0.50039	- 0.87497		
x/d = 5	0.000		0.00000	0.00000		
		0.50000	0.75000	1.00000	1.50000	2.00000
					H/D	

Z-COMPONENT MOMENTUM/SIN(ALPHA)

	15.000					
	12.000					
ALPHA	9.000					
	6.000			- 1.41309	- 0.97193	
	3.000			- 0.73271		
x/d = 6	0.000		0.00000			
		0.50000	0.75000	1.00000	1.50000	2.00000
					H/D	

Table 1.a. Normalized J_z values to show the effective development length for the uniform nozzle exit condition ($J_z/J(0) \sin \alpha$).

Z-COMPONENT MOMENTUM/SIN(ALPHA)

	15.000					
	12.000					
ALPHA	9.000					
	6.000		- 0.99999	- 0.99999		
	3.000	- 1.00000	- 1.00000			
x/d = 1	0.000		0.00000			
		0.50000	0.75000	1.00000	1.50000	2.00000
					H/D	

Z-COMPONENT MOMENTUM/SIN(ALPHA)

	15.000					- 0.99999
	12.000				- 0.99999	- 1.00000
ALPHA	9.000			- 0.99999	- 0.99999	- 1.00000
	6.000		- 0.94906	- 1.14371	- 0.99999	
	3.000	- 0.78155	- 1.06855	- 0.99999		
x/d = 2	0.000		0.00000			
		0.50000	0.75000	1.00000	1.50000	2.00000
					H/D	

Z-COMPONENT MOMENTUM/SIN(ALPHA)

	15.000					- 1.00657
	12.000				- 1.01113	- 1.00790
ALPHA	9.000			- 0.87519	- 1.01432	- 1.01000
	6.000		- 0.75791	- 1.13051	- 1.02154	
	3.000	- 0.59022	- 0.99070	- 1.07225		
x/d = 3	0.000		0.00000	0.00000		
		0.50000	0.75000	1.00000	1.50000	2.00000
					H/D	

Z-COMPONENT MOMENTUM/SIN(ALPHA)

	15.000					- 1.00085
	12.000				- 0.94033	- 1.01273
ALPHA	9.000			- 0.62151	- 1.00971	- 1.01775
	6.000		- 0.55041	- 0.99402	- 1.03662	
	3.000	- 0.39153	- 0.84778	- 1.06332		
x/d = 4	0.000		0.00000	0.00000		
		0.50000	0.75000	1.00000	1.50000	2.00000
					H/D	

Z-COMPONENT MOMENTUM/SIN(ALPHA)

	15.000					- 0.87263
	12.000				- 0.72149	- 0.99729
ALPHA	9.000			- 0.37006	- 0.92051	- 1.02847
	6.000		- 0.34967	- 0.78143	- 1.03995	
	3.000	- 0.18936	- 0.67969	- 0.97979		
x/d = 5	0.000		0.00000	0.00000		
		0.50000	0.75000	1.00000	1.50000	2.00000
					H/D	

Z-COMPONENT MOMENTUM/SIN(ALPHA)

	15.000					- 0.59647
	12.000				- 0.46072	- 0.88841
ALPHA	9.000			- 0.15981	- 0.73887	- 1.01775
	6.000		- 0.17319	- 0.55339	- 0.99001	
	3.000	0.00816	- 0.50772	- 0.83373		
x/d = 6	0.000		0.00000	0.00000		
		0.50000	0.75000	1.00000	1.50000	2.00000
					H/D	

Table 1. b. Normalized J_z values to show the effective development length for the fully developed nozzle exit condition ($J_z/J(0)$ sin α).

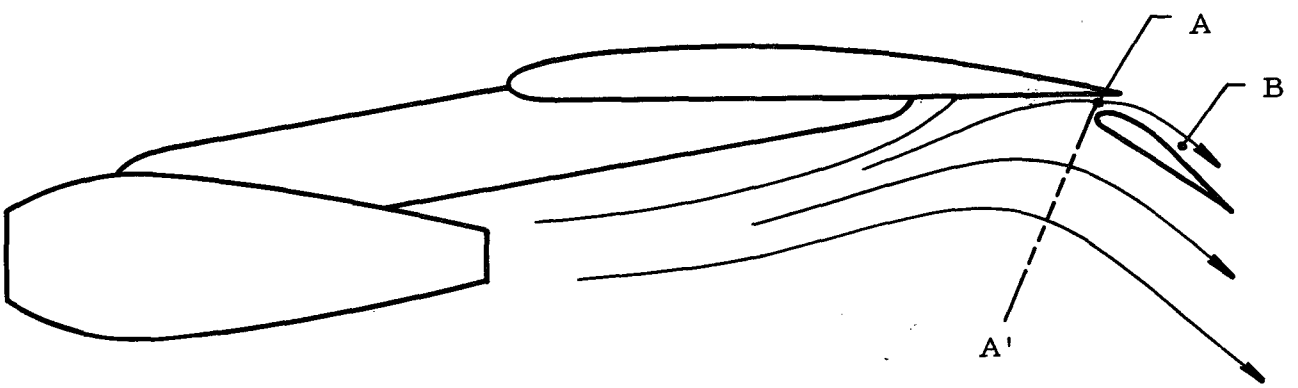

Figure 1. Externally blown flap STOL aircraft configuration.

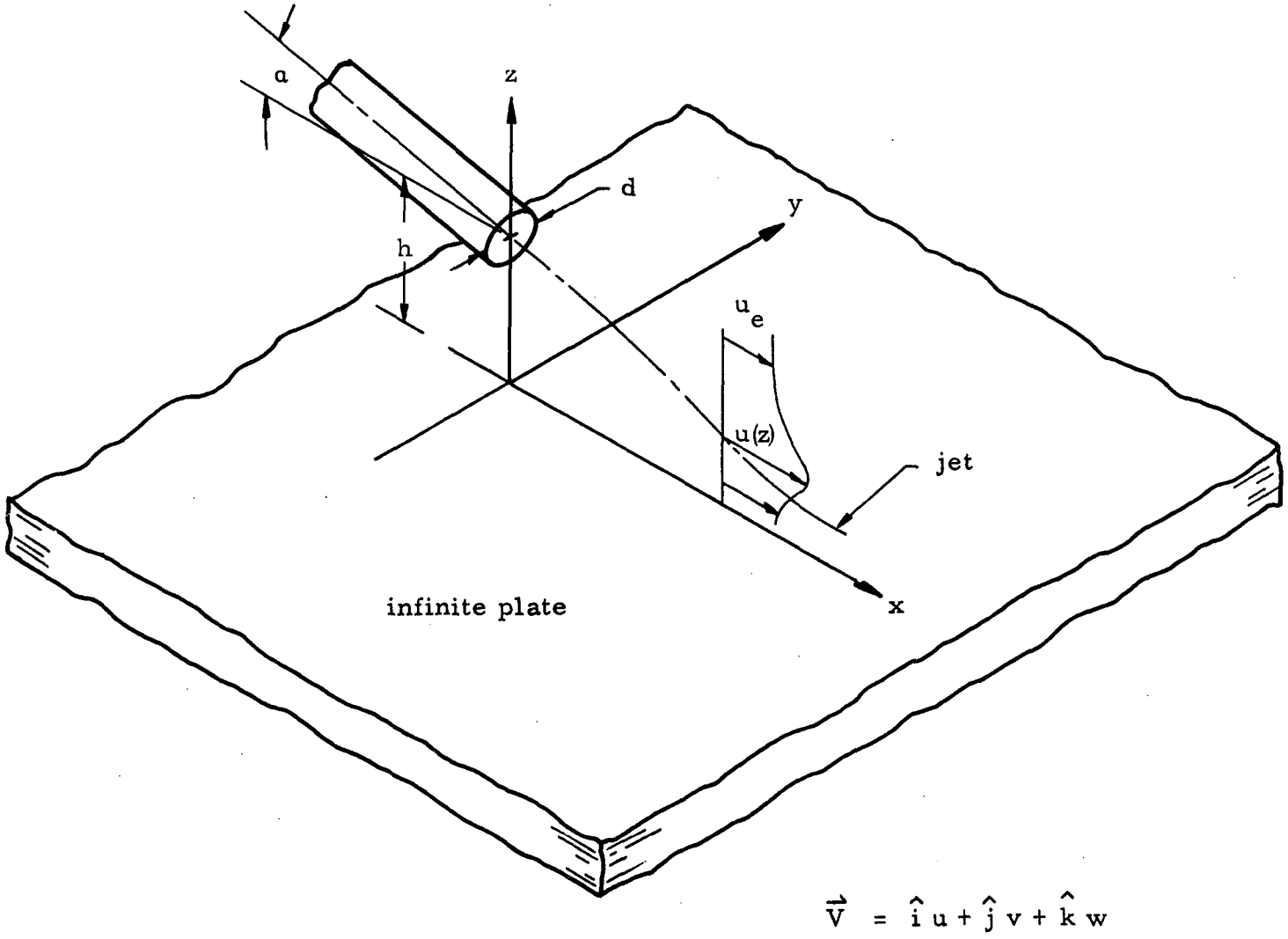

Figure 2. The round-jet/plane-wall flow field, coordinate system and nomenclature.

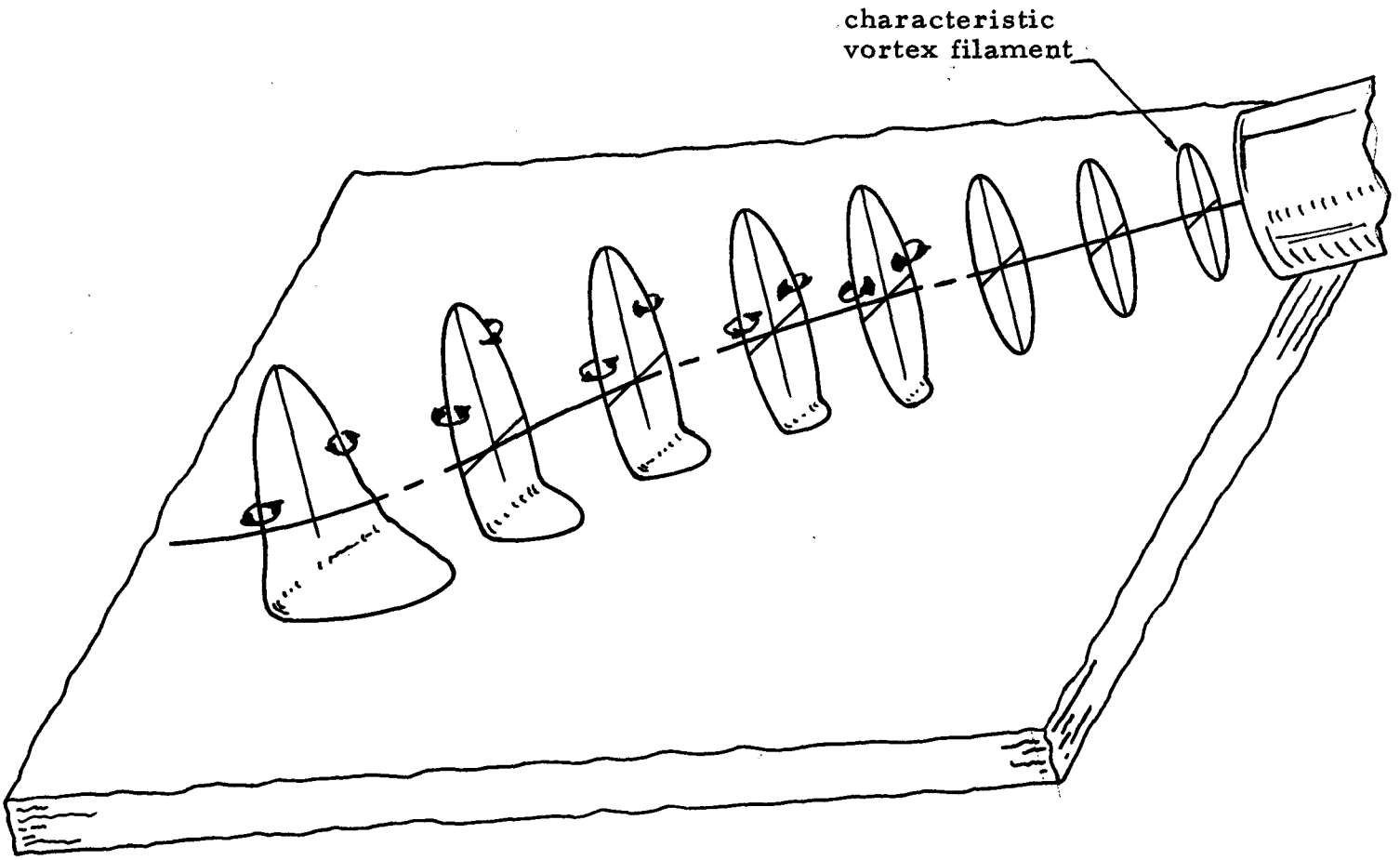

Figure 3a. Hypothesized development of a characteristic vortex filament.

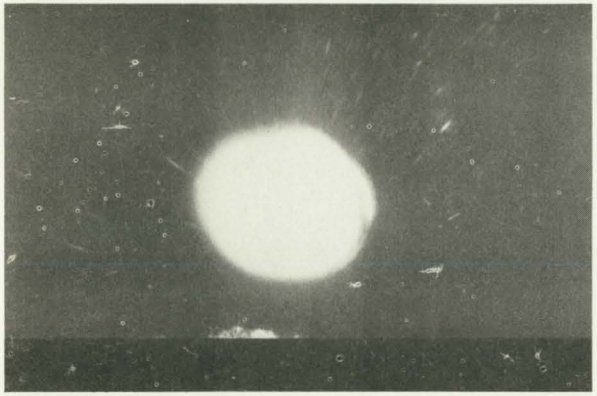

a) x/d ≈ o

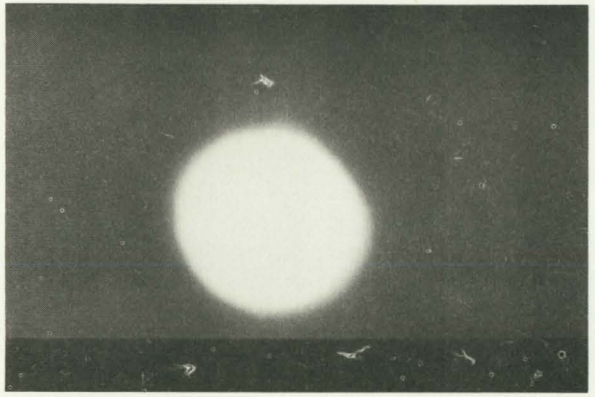

b) x/d = 1

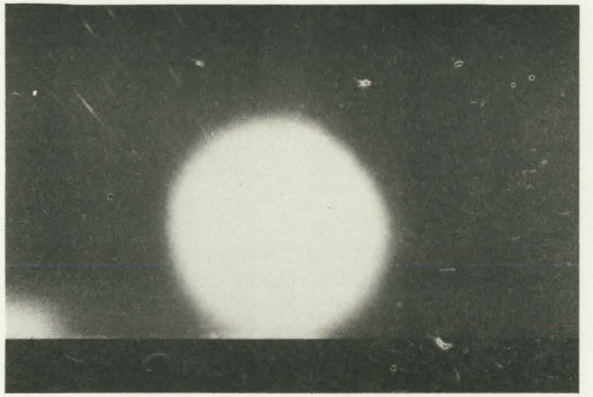

c) x/d = 2

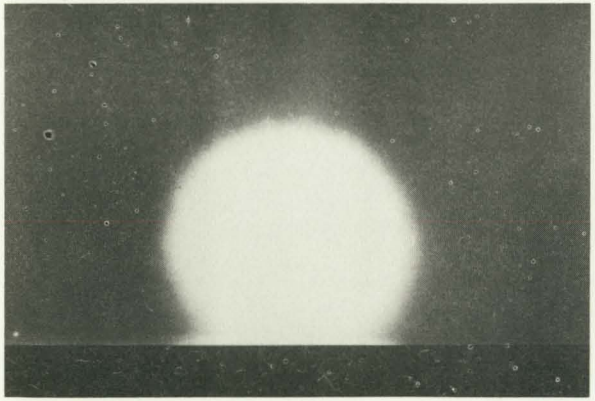

d) x/d = 3

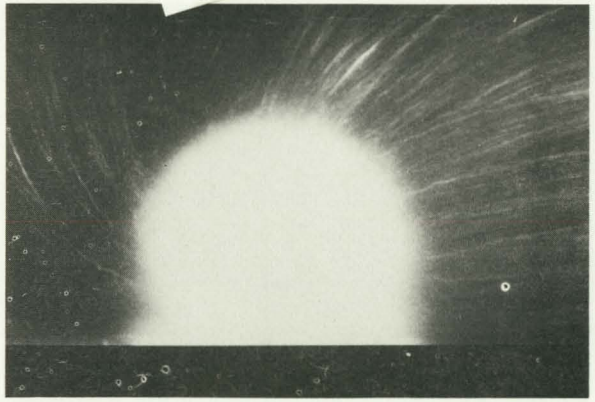

e) x/d = 4

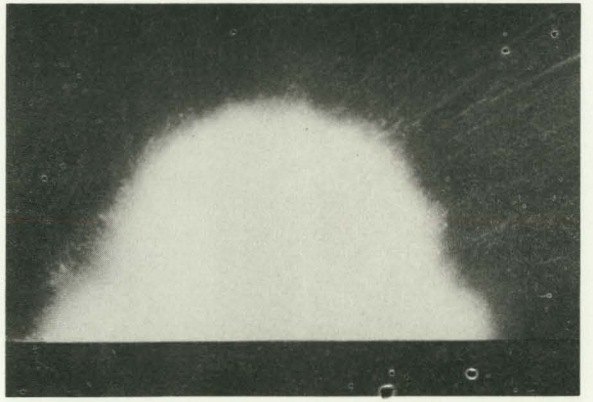

f) x/d = 5

Figure 3b. The cross section of a powder seeded jet (as shown by a plane sheet of light) to demonstrate the existence of streamwise vorticity. $a = 6$, $h/d = 0.75$.

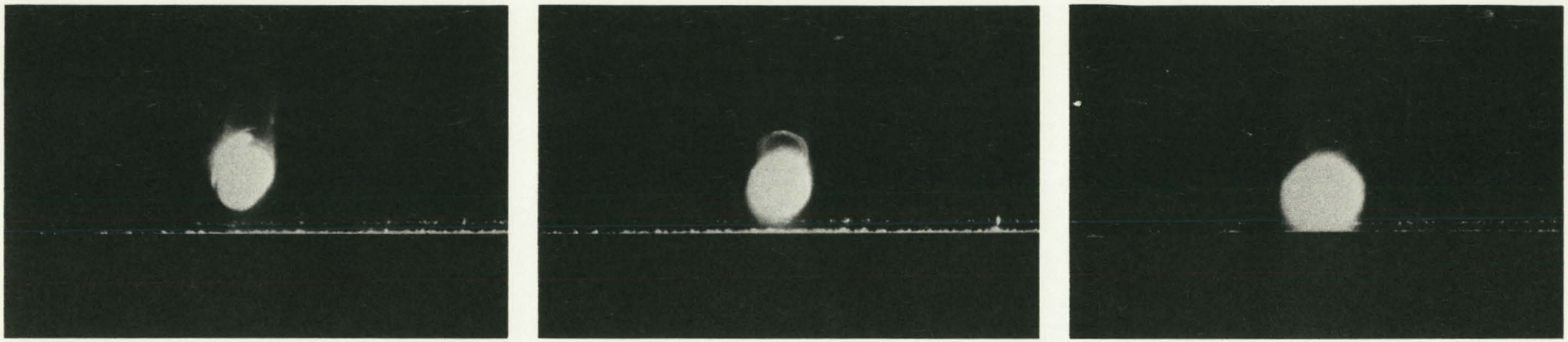

a) x/d ≈ 0 b) x/d = 1 c) x/d = 2

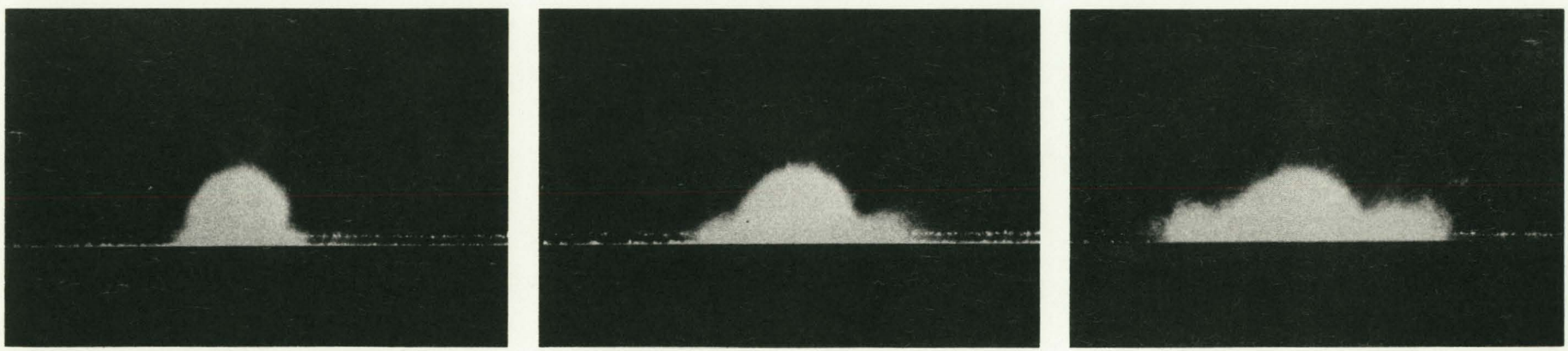

d) x/d = 3 e) x/d = 4 f) x/d = 5

Figure 3c. The cross section of a powder seeded jet (as shown by a plane sheet of light) to demonstrate the existence of streamwise vorticity. $\alpha = 12$, $h/d = 1.5$.

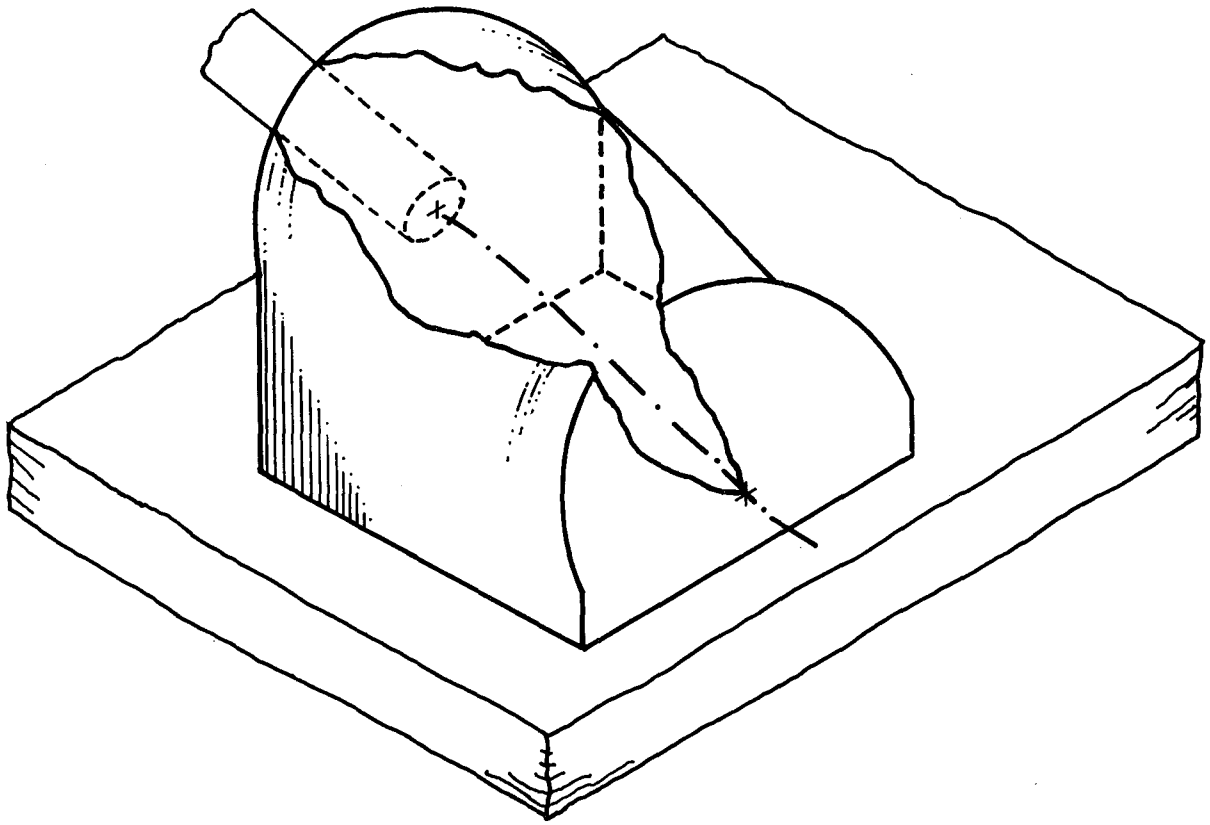

TOP

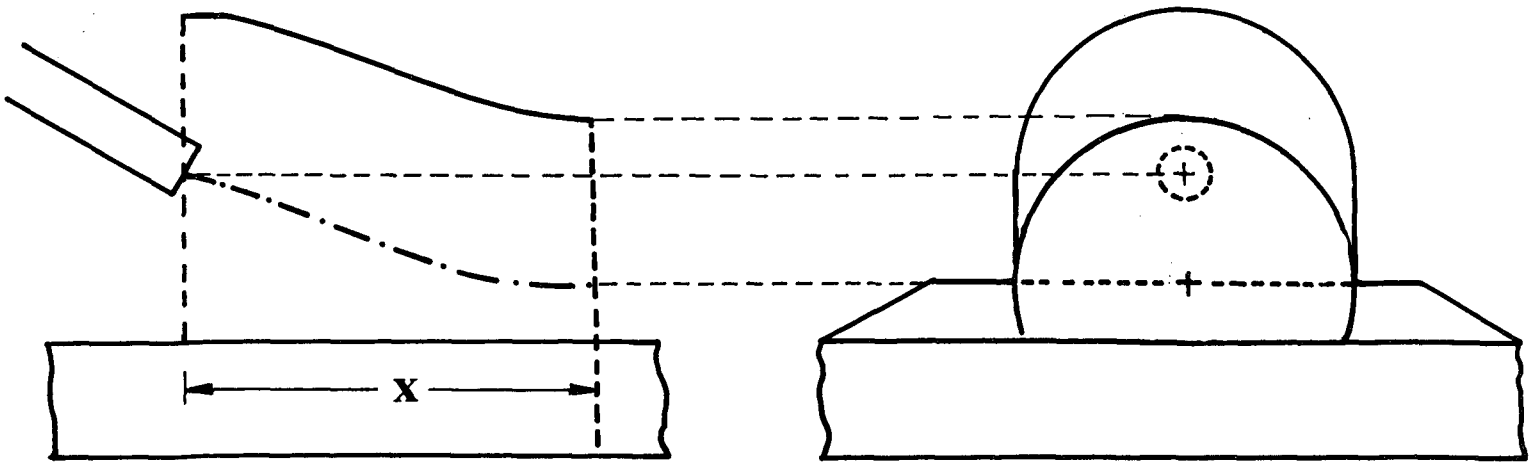

SIDE FRONT

Figure 4. Control volume for the analysis of the round-jet/plane-wall flow field.

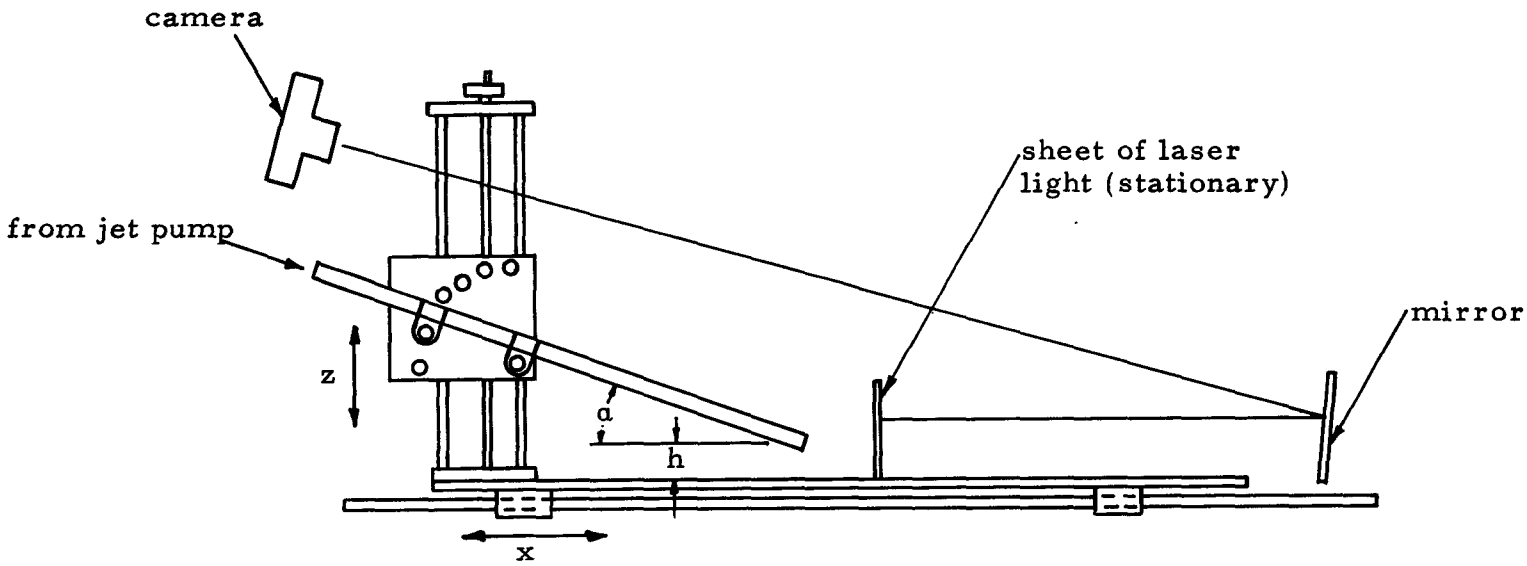

Figure 5. Flow visualization facility.

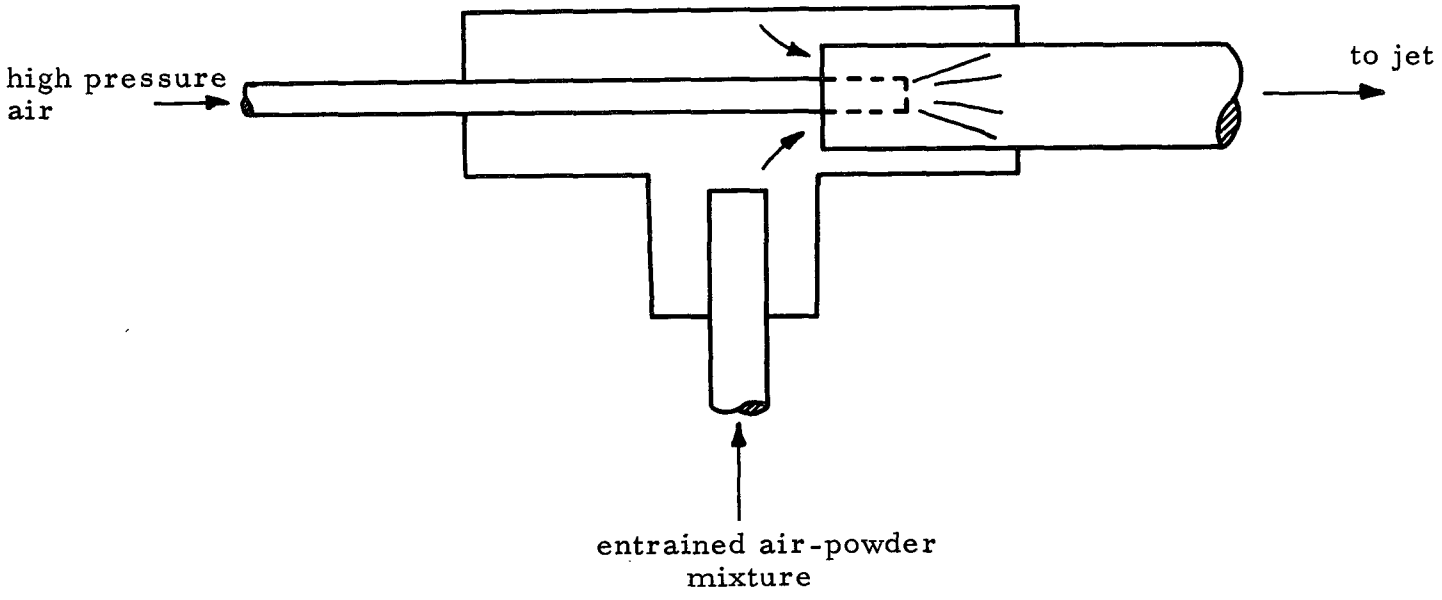

Figure 6. Jet pump for the powder seeded jet.

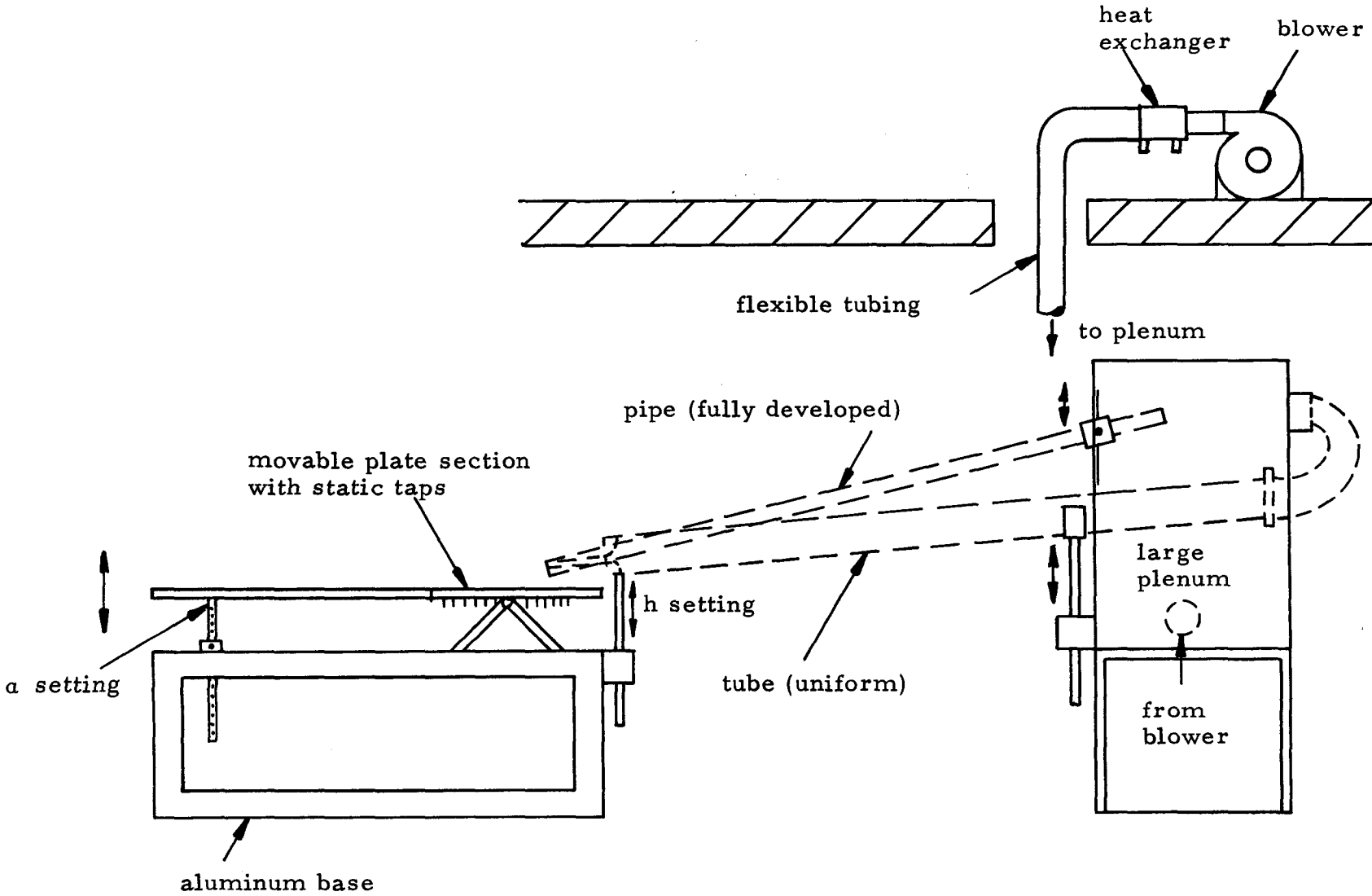

Figure 7. Quantitative data acquisition flow system.

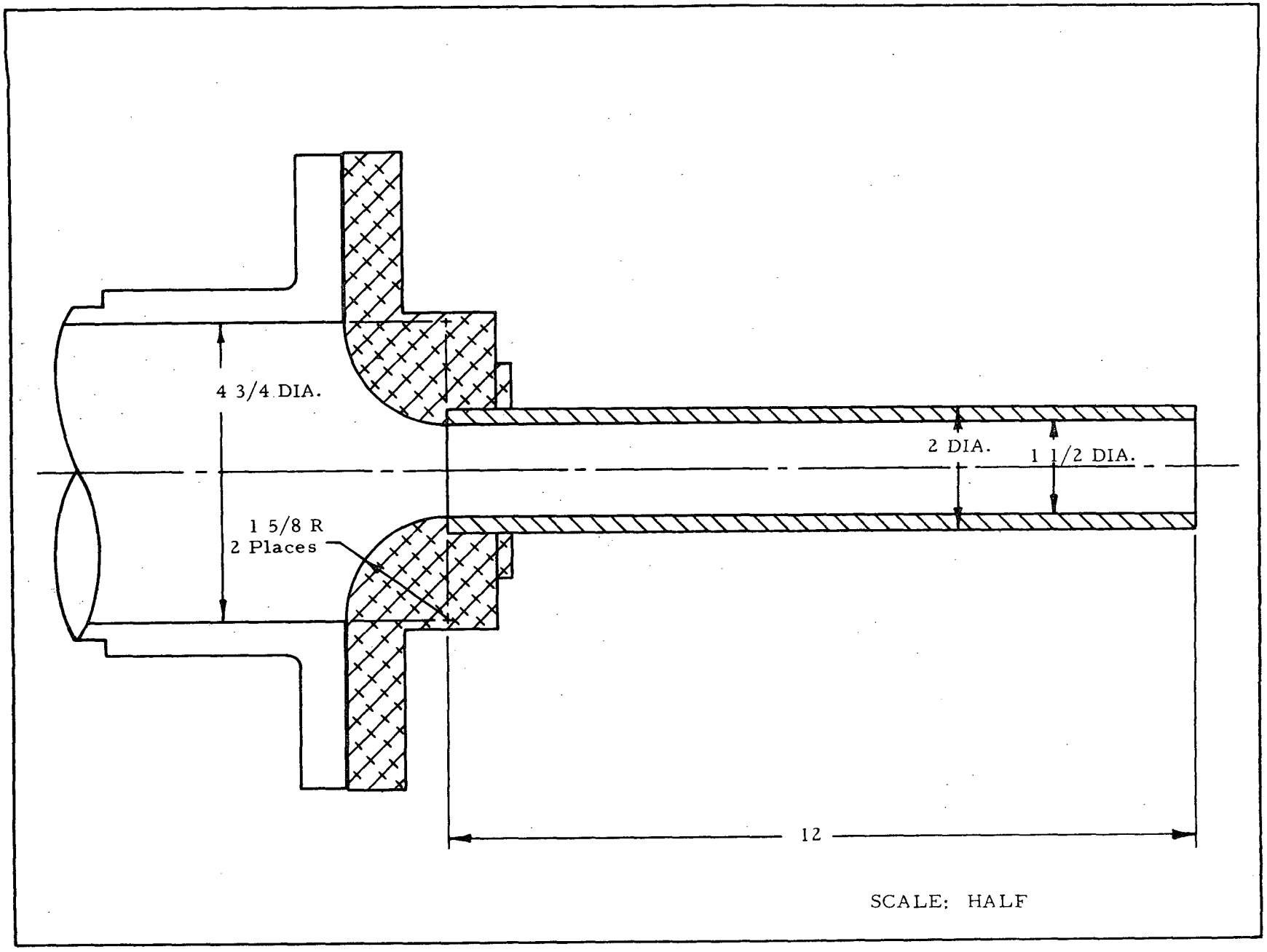

Figure 8. Detail of uniform flow nozzle.

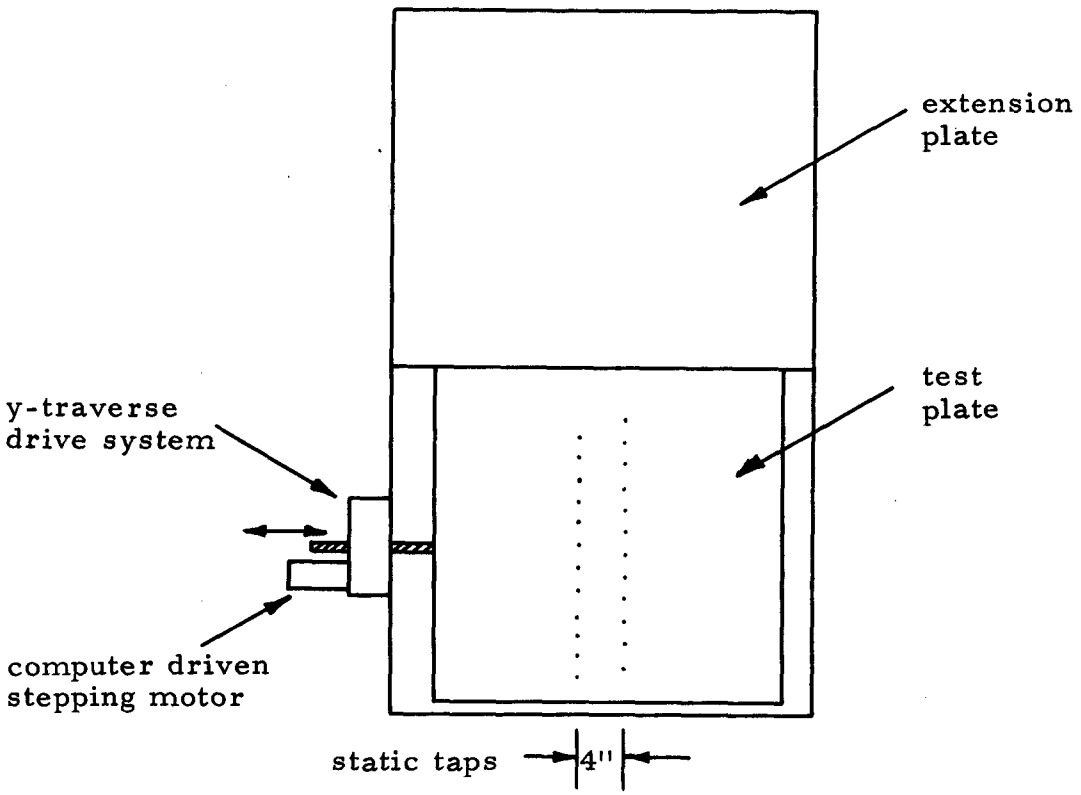

Figure 9. Facility detail for surface state pressure measurements.

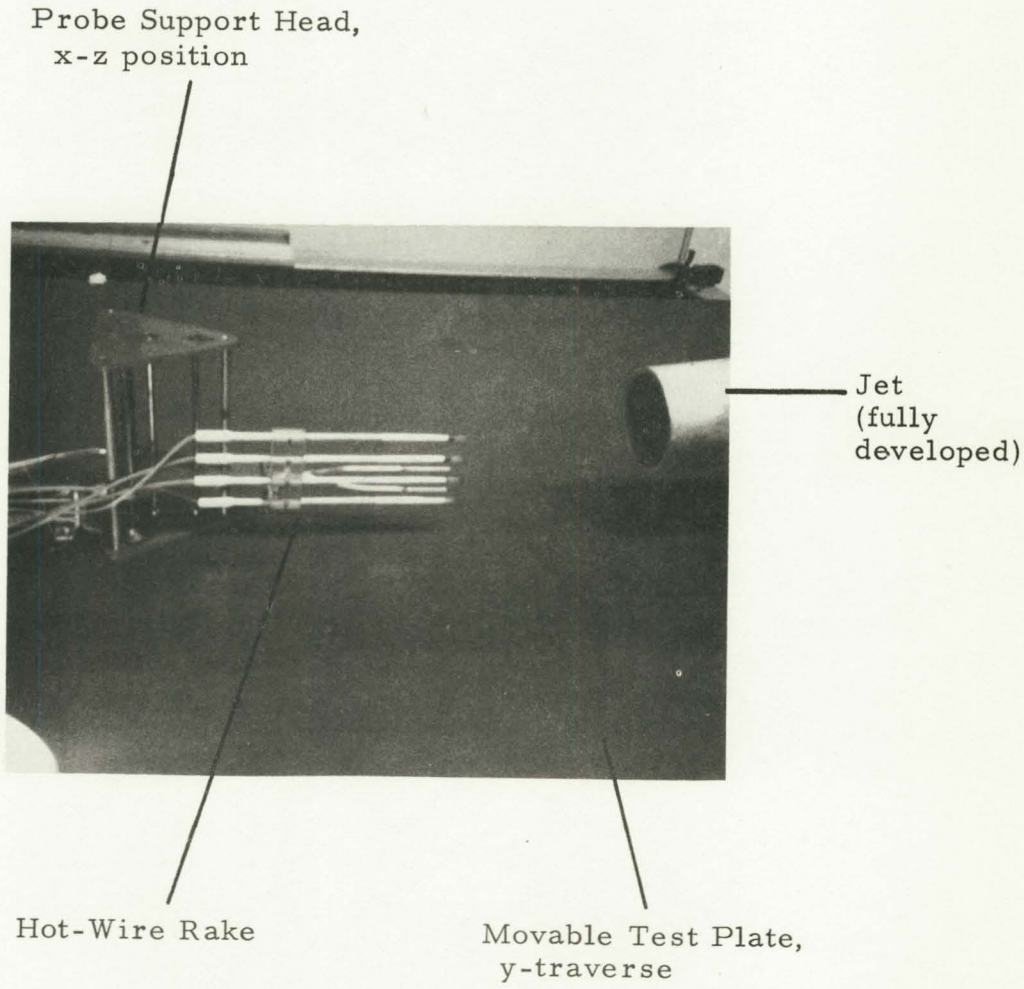

Figure 10. Hot-wire rake and z-position traverse head.

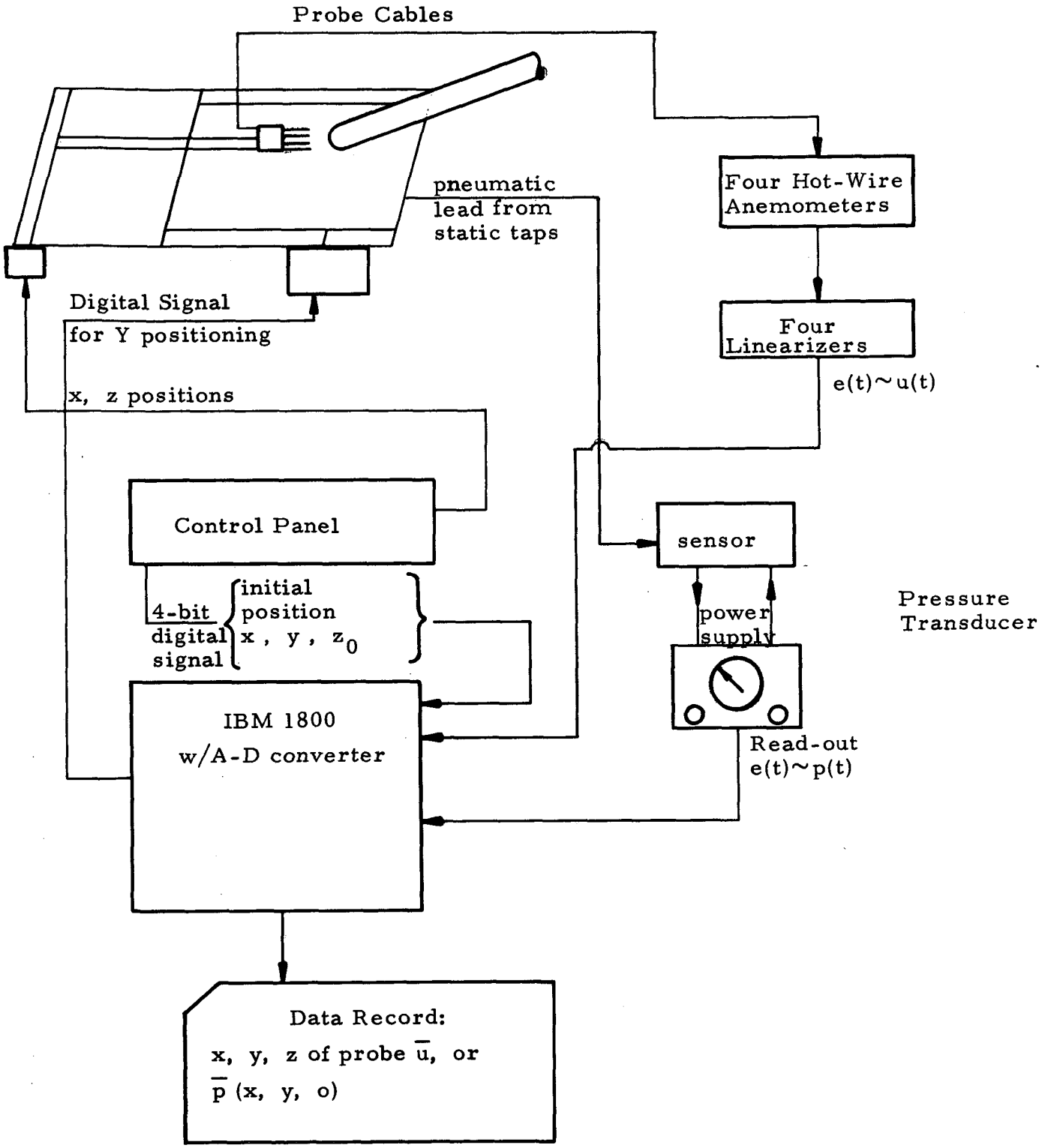

Figure 11. Data acquisition and recording system.

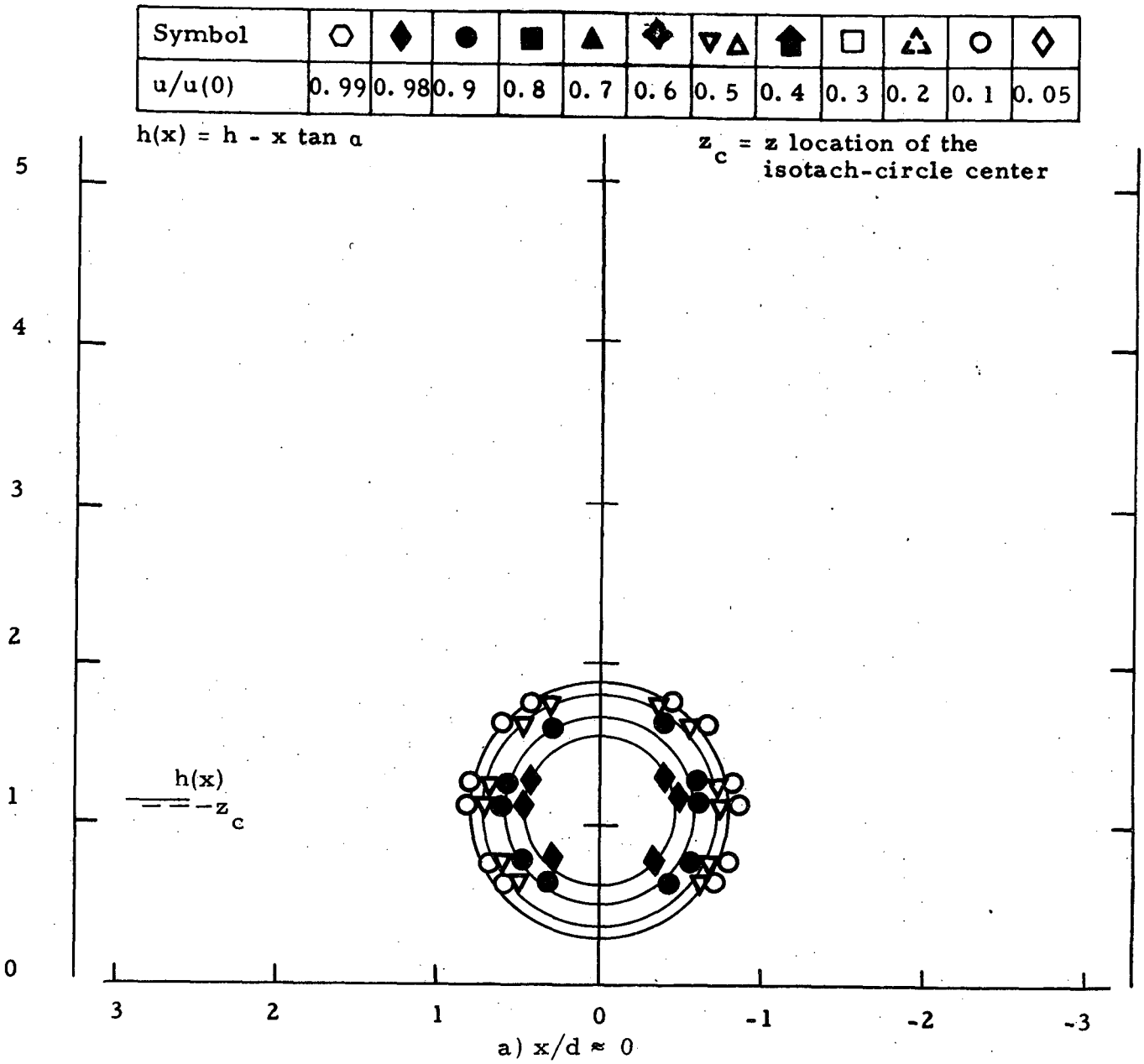

Figure 12. Isotach contours, $\alpha = 0$, $h/d = 0.75$, uniform.

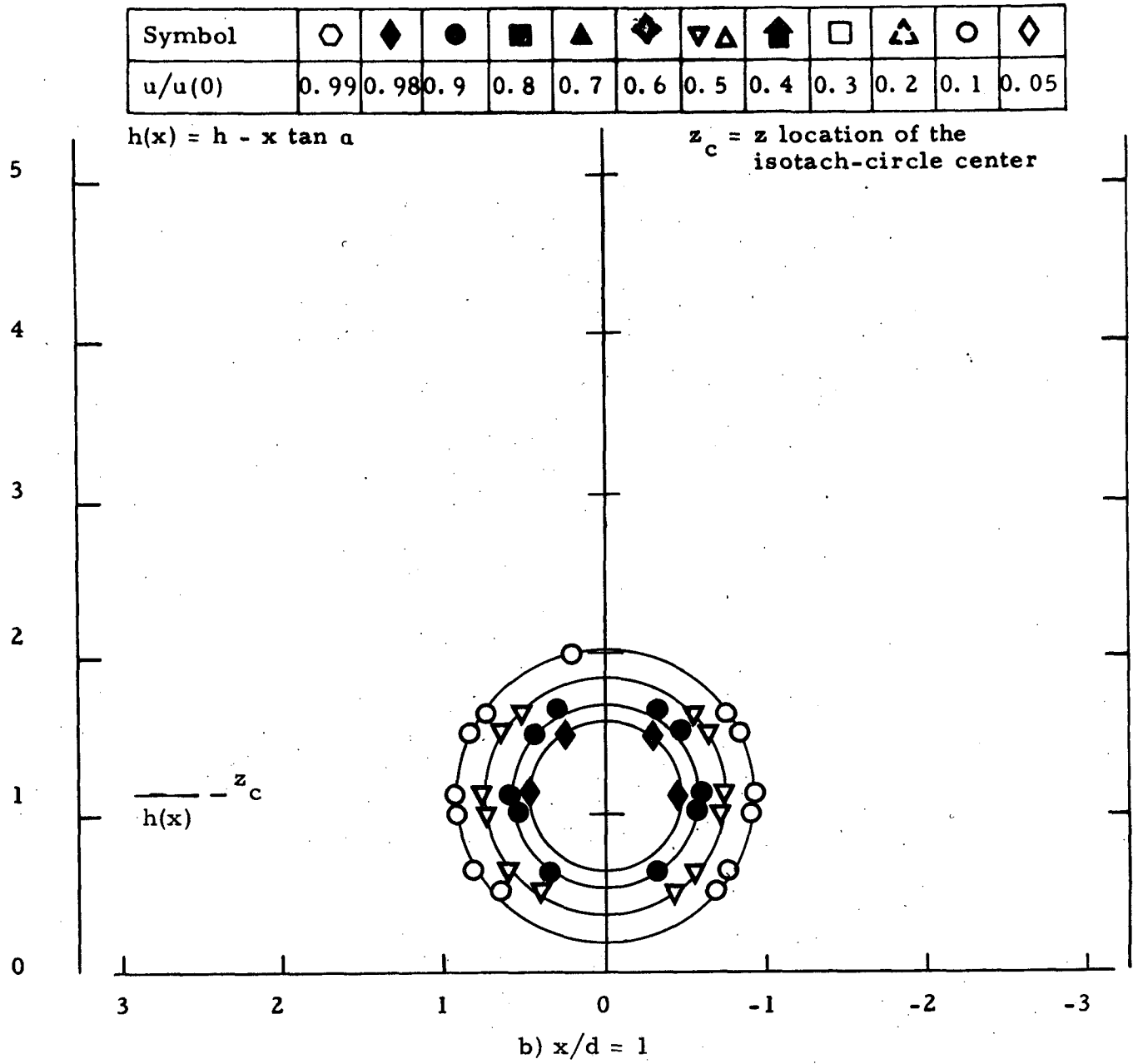
Symbol
u/u(0)
0.99
0.98
0.9
0.8
0.7
0.6
0.5
0.4
0.3
0.2
0.1
0.05
h(x) = h - x tan α
z_c = z location of the isotach-circle center
$\frac{z}{h(x)} - z_c$
5
4
3
2
1
0
3
2
1
0
-1
-2
-3

b) x/d = 1

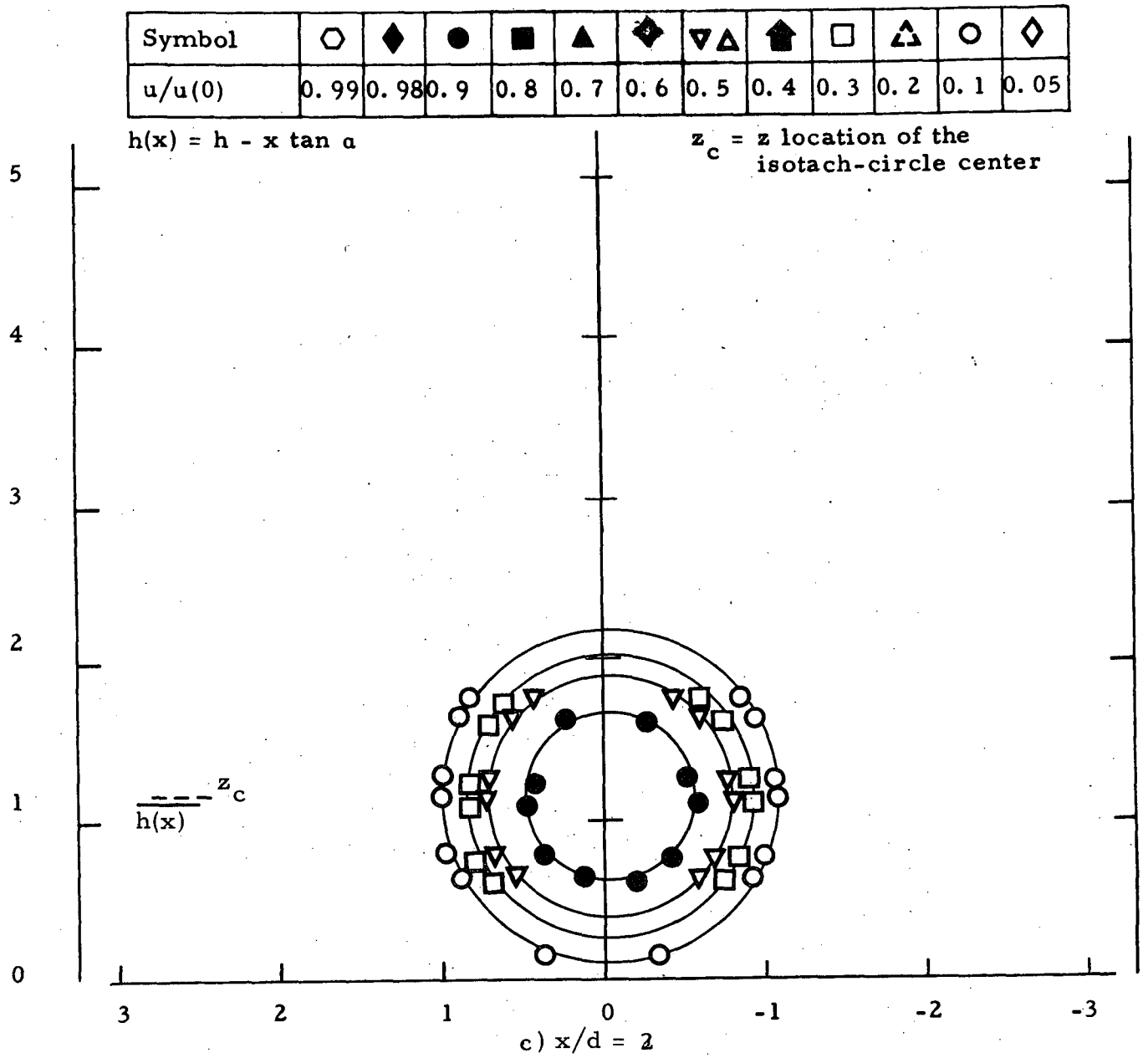
Symbol
u/u(0)
0.99
0.98
0.9
0.8
0.7
0.6
0.5
0.4
0.3
0.2
0.1
0.05
h(x) = h - x tan α
z_c = z location of the isotach-circle center
$\frac{z_c}{h(x)}$
5
4
3
2
1
0
3
2
1
0
-1
-2
-3
c) x/d = 2

Symbol	⬡	◆	●	■	▲	◆	▽△	⬟	□	△	○	◇
u/u(0)	0.99	0.98	0.9	0.8	0.7	0.6	0.5	0.4	0.3	0.2	0.1	0.05

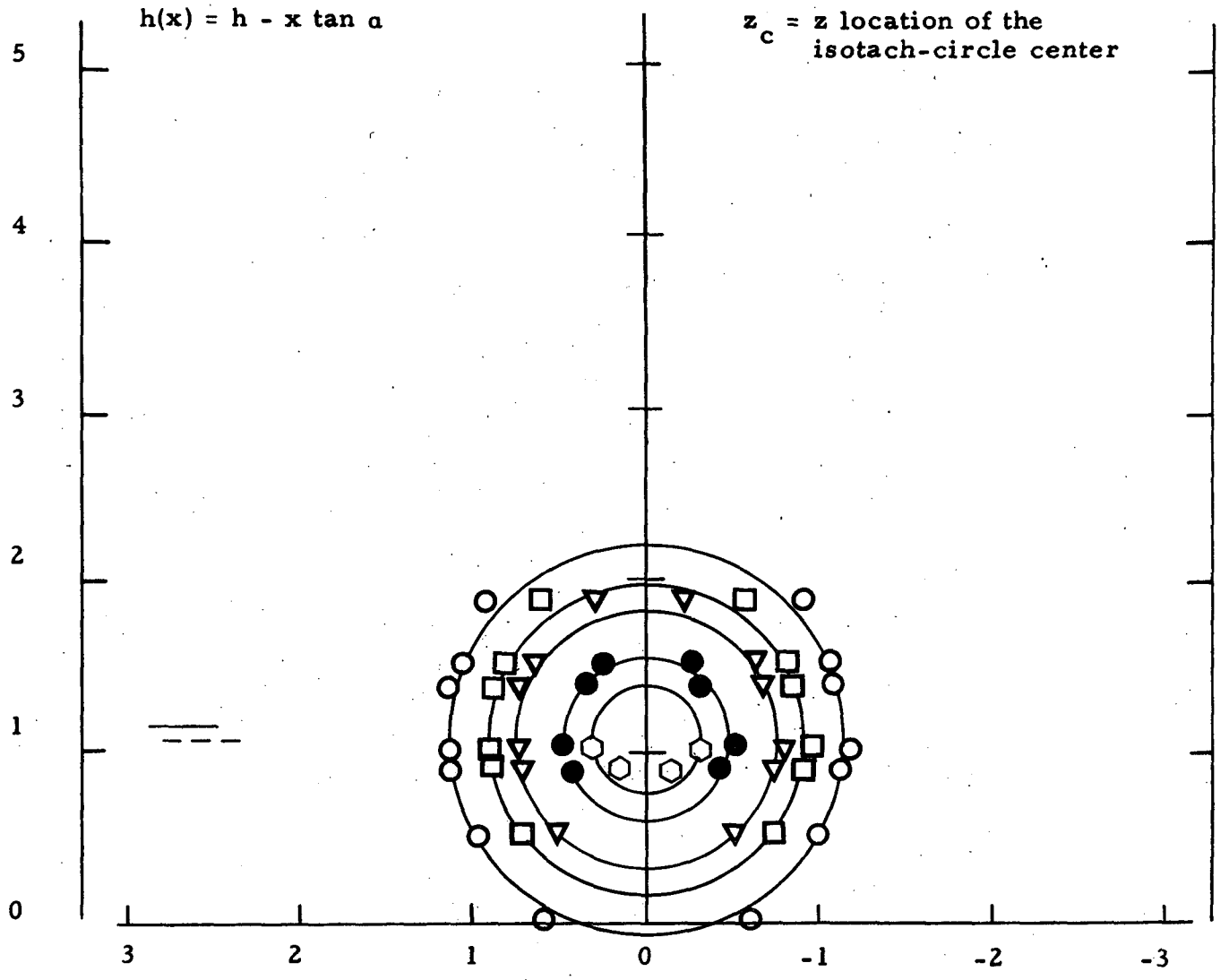

d) x/d = 3

Symbol	⬡	♦	●	■	▲	◆	▽△	⬟	□	△	○	◇
u/u(0)	0.99	0.98	0.9	0.8	0.7	0.6	0.5	0.4	0.3	0.2	0.1	0.05

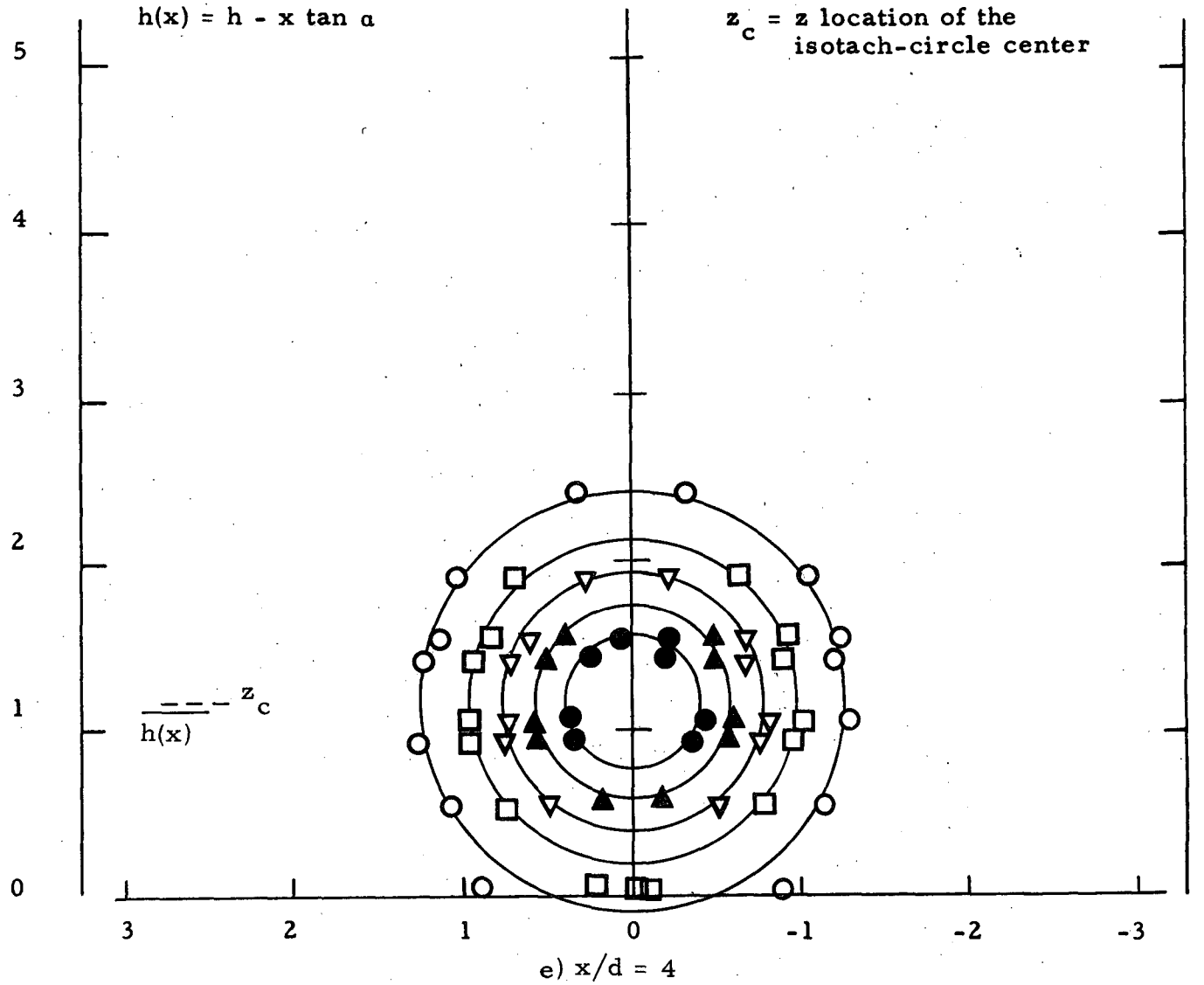

e) x/d = 4

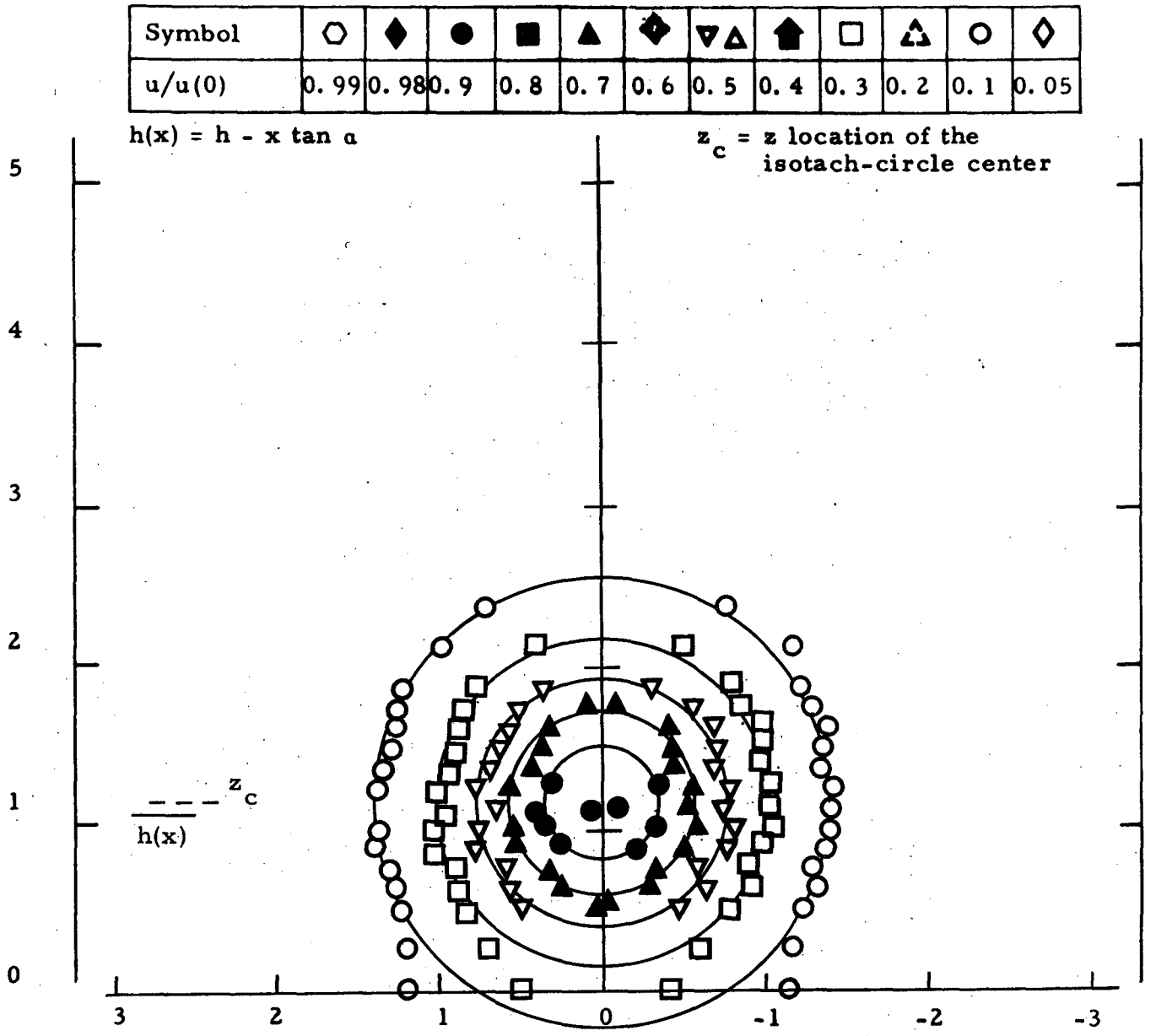
Symbol
u/u(0)
0.99
0.98
0.9
0.8
0.7
0.6
0.5
0.4
0.3
0.2
0.1
0.05
h(x) = h - x tan α
z_c = z location of the isotach-circle center
z_c / h(x)
5
4
3
2
1
0
3
2
1
0
-1
-2
-3

f) x/d = 5

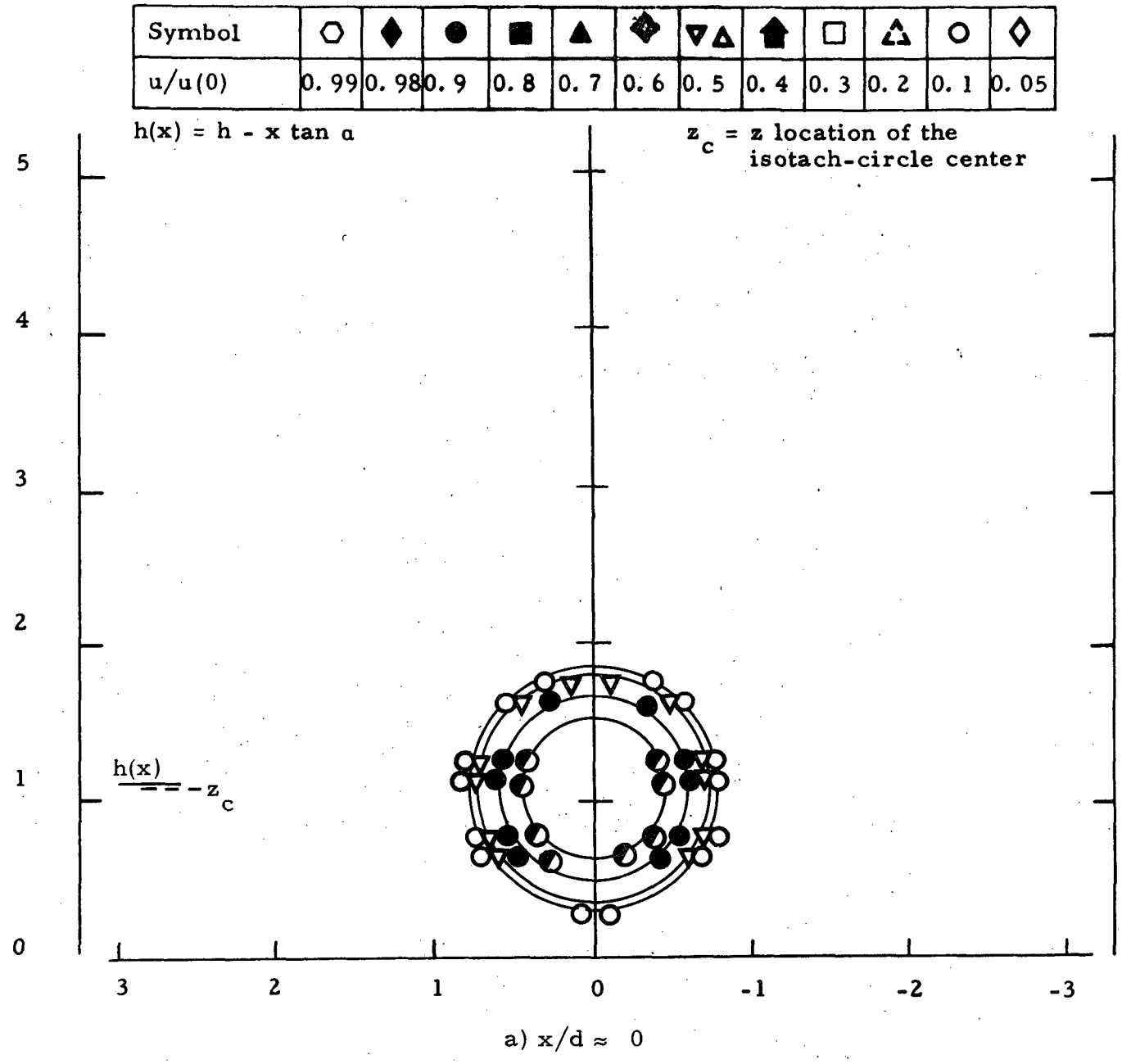

a) x/d ≈ 0

Figure 13. Isotach contours $\alpha = 3$, $h/d = 0.75$, uniform.

Symbol	⬡	◆	●	■	▲	◈	▽△	⬟	□	⧋	○	◇
u/u(0)	0.99	0.98	0.9	0.8	0.7	0.6	0.5	0.4	0.3	0.2	0.1	0.05

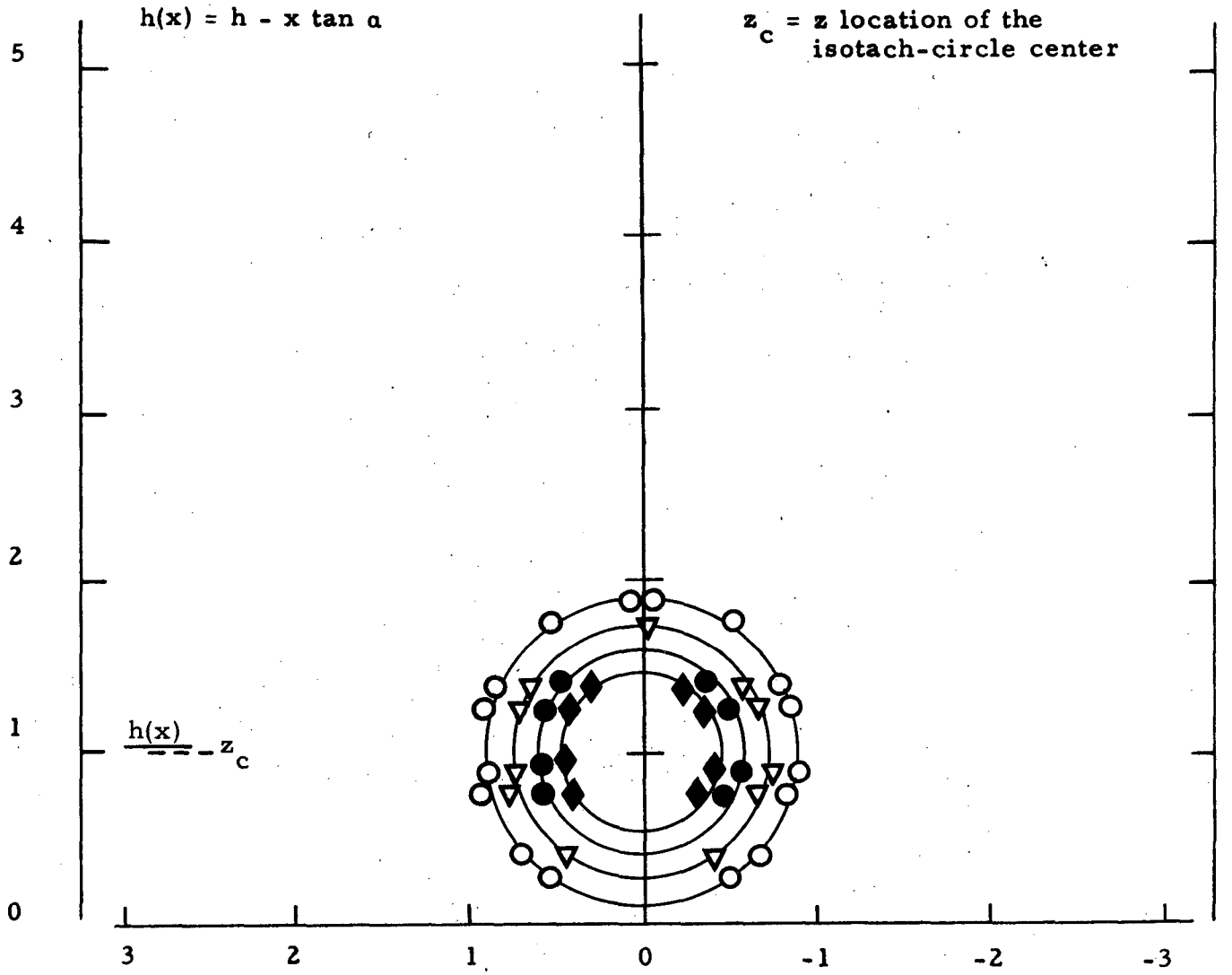

b) x/d = 1

Symbol	⬡	◆	●	■	▲	◆	▽△	⬟	□	△	○	◇
u/u(0)	0.99	0.98	0.9	0.8	0.7	0.6	0.5	0.4	0.3	0.2	0.1	0.05

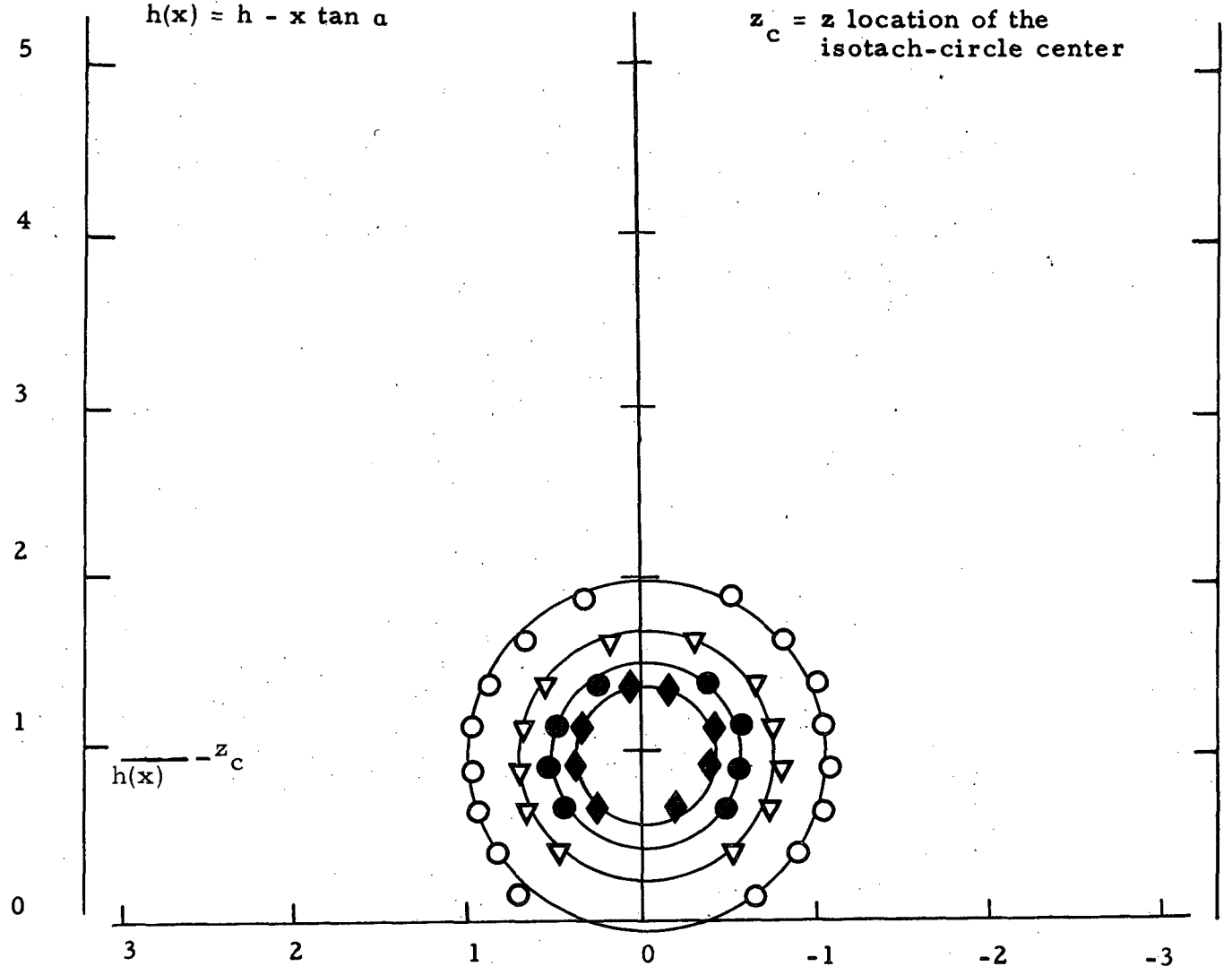

c) x/d = 2

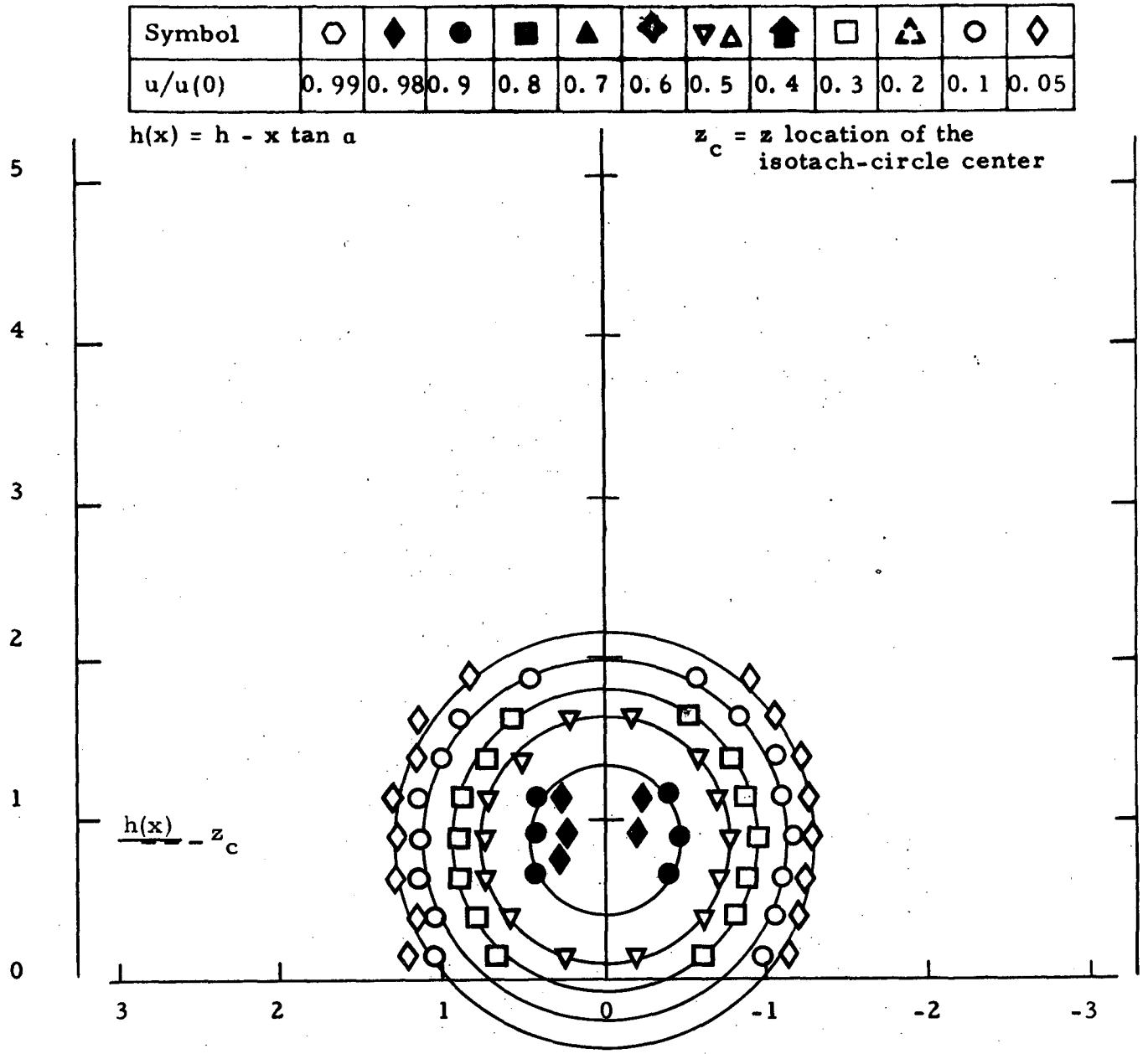
Symbol
u/u(0)
0.99
0.98
0.9
0.8
0.7
0.6
0.5
0.4
0.3
0.2
0.1
0.05
h(x) = h - x tan α
z_c = z location of the isotach-circle center
5
4
3
2
1
0
$\frac{h(x)}{} - z_c$
3
2
1
0
-1
-2
-3

d) x/d = 3

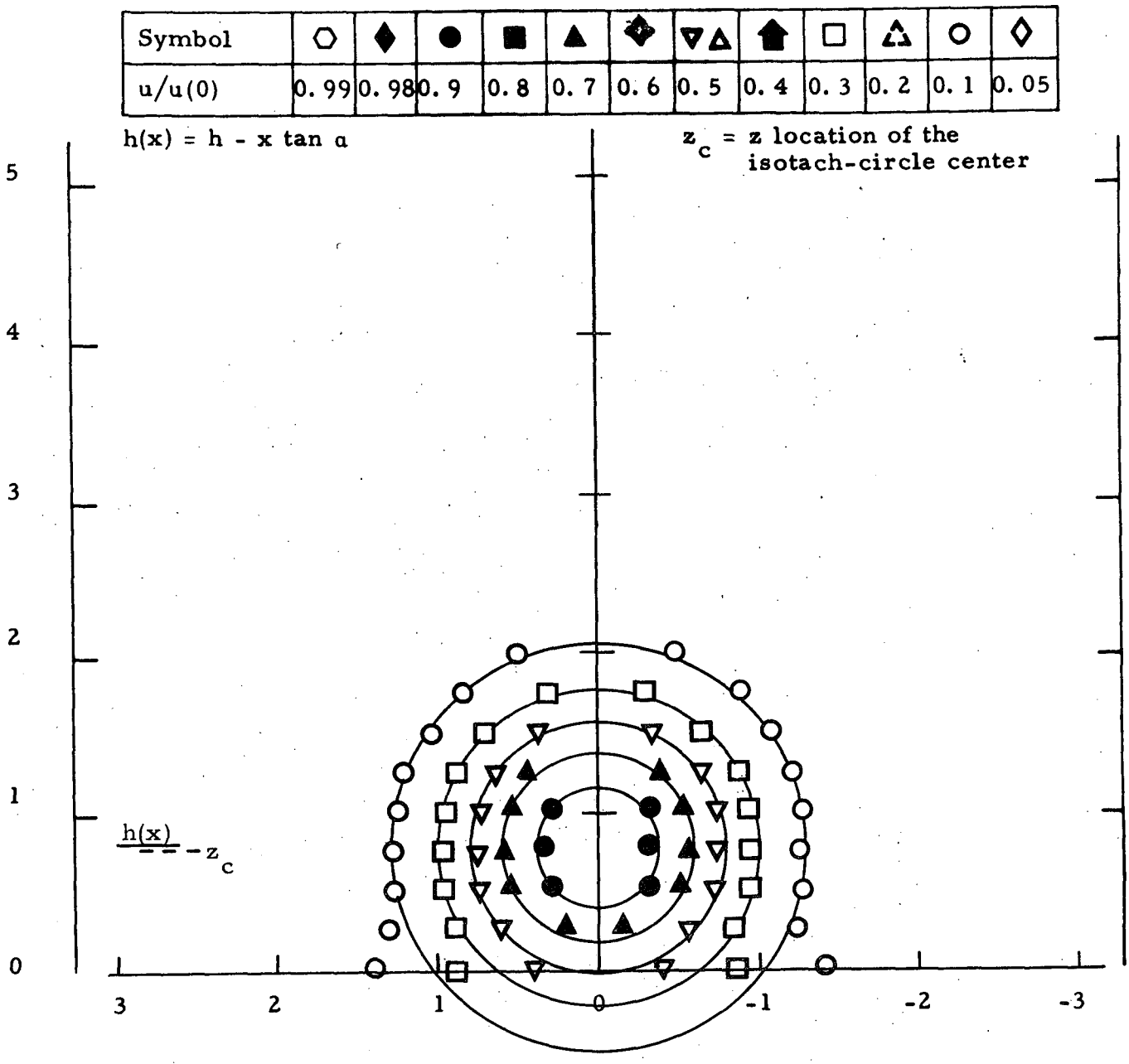
Symbol
u/u(0)
0.99
0.98
0.9
0.8
0.7
0.6
0.5
0.4
0.3
0.2
0.1
0.05
h(x) = h - x tan α
z_c = z location of the isotach-circle center
5
4
3
2
1
0
$\frac{h(x)}{d} - z_c$
3
2
1
0
-1
-2
-3

e) x/d = 4

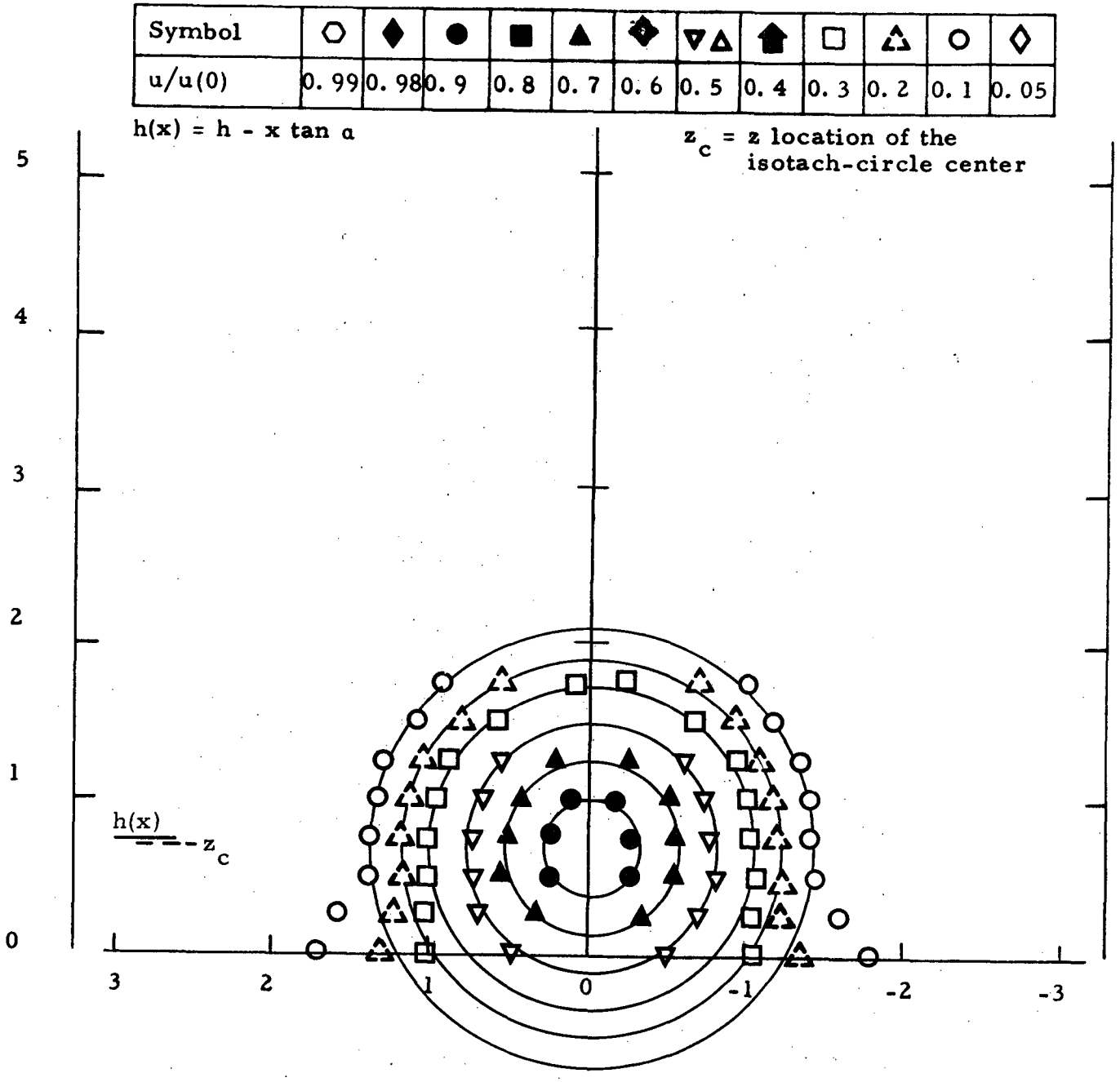
Symbol
u/u(0)
0.99
0.98
0.9
0.8
0.7
0.6
0.5
0.4
0.3
0.2
0.1
0.05
h(x) = h - x tan α
z_c = z location of the isotach-circle center
5
4
3
2
1
0
h(x)
z_c
3
2
1
0
-1
-2
-3

f) x/d = 5

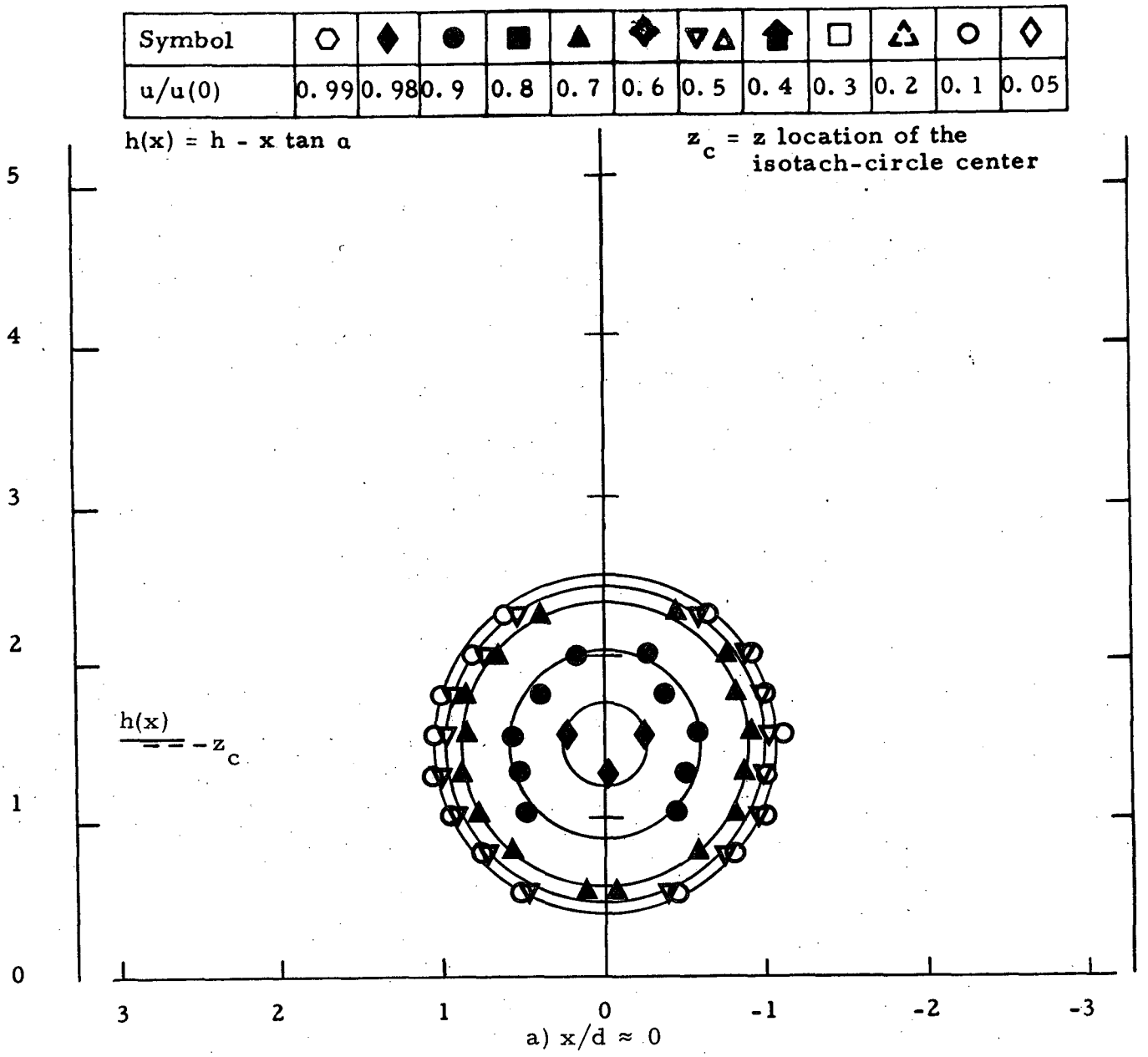

Figure 14. Isotach contours α = 3, h/d = 0.75, fully developed.

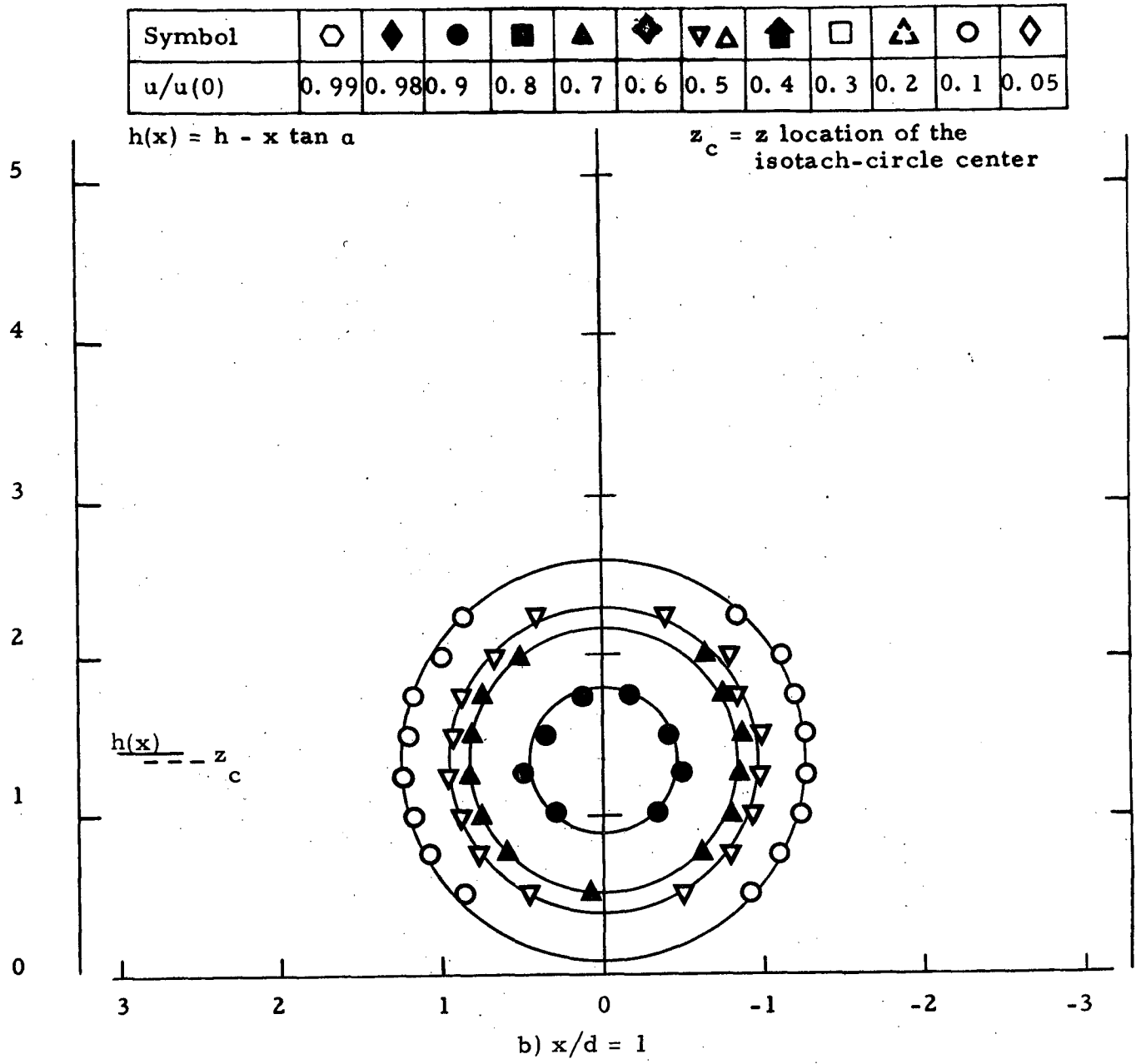
Symbol
u/u(0)
0.99
0.98
0.9
0.8
0.7
0.6
0.5
0.4
0.3
0.2
0.1
0.05
h(x) = h - x tan α
z_c = z location of the isotach-circle center
h(x)/d
z_c/d
5
4
3
2
1
0
3
2
1
0
-1
-2
-3

b) x/d = 1

Symbol	⬡	♦	●	■	▲	◆	▽△	⬟	□	△	○	◇
u/u(0)	0.99	0.98	0.9	0.8	0.7	0.6	0.5	0.4	0.3	0.2	0.1	0.05

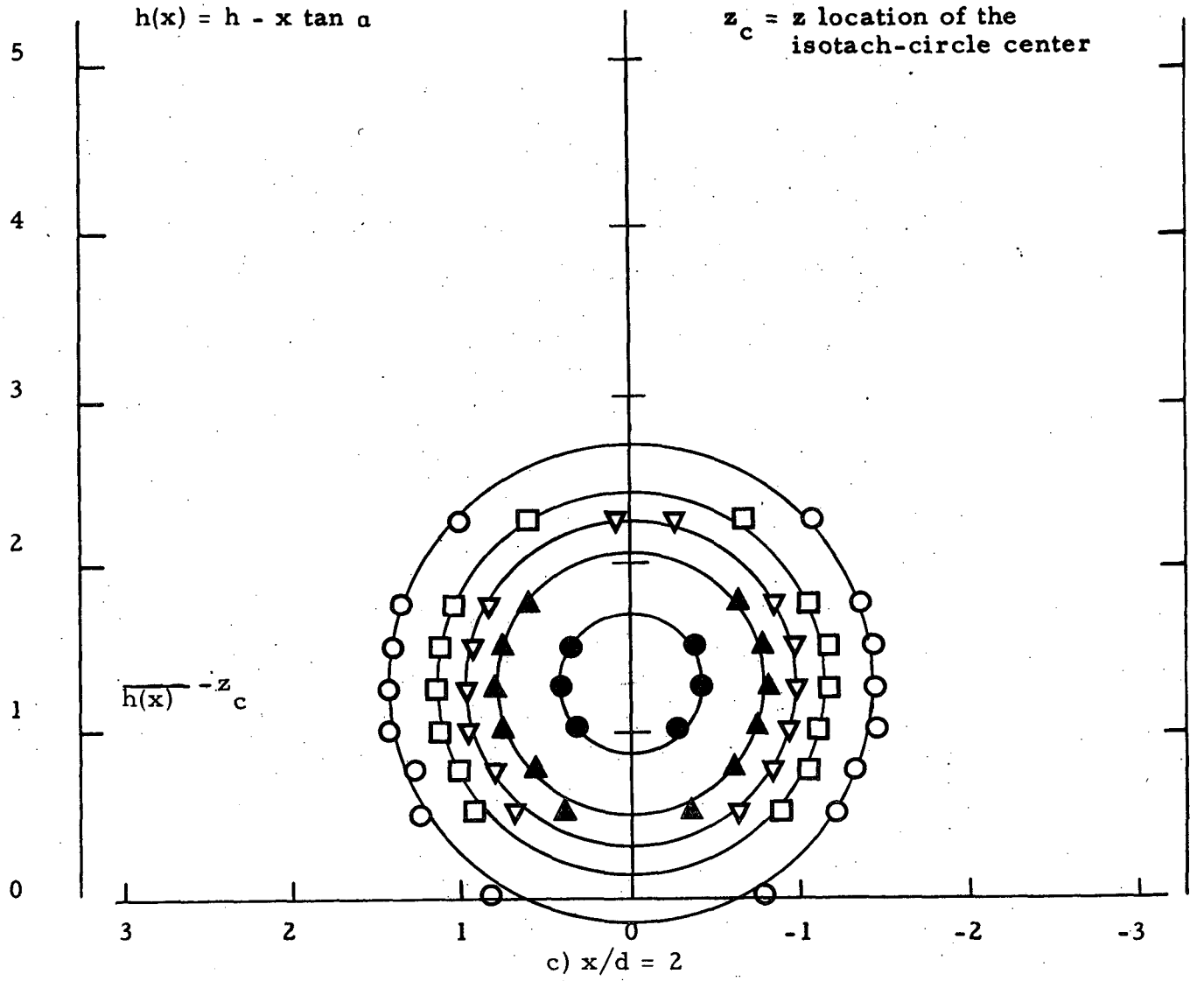

c) x/d = 2

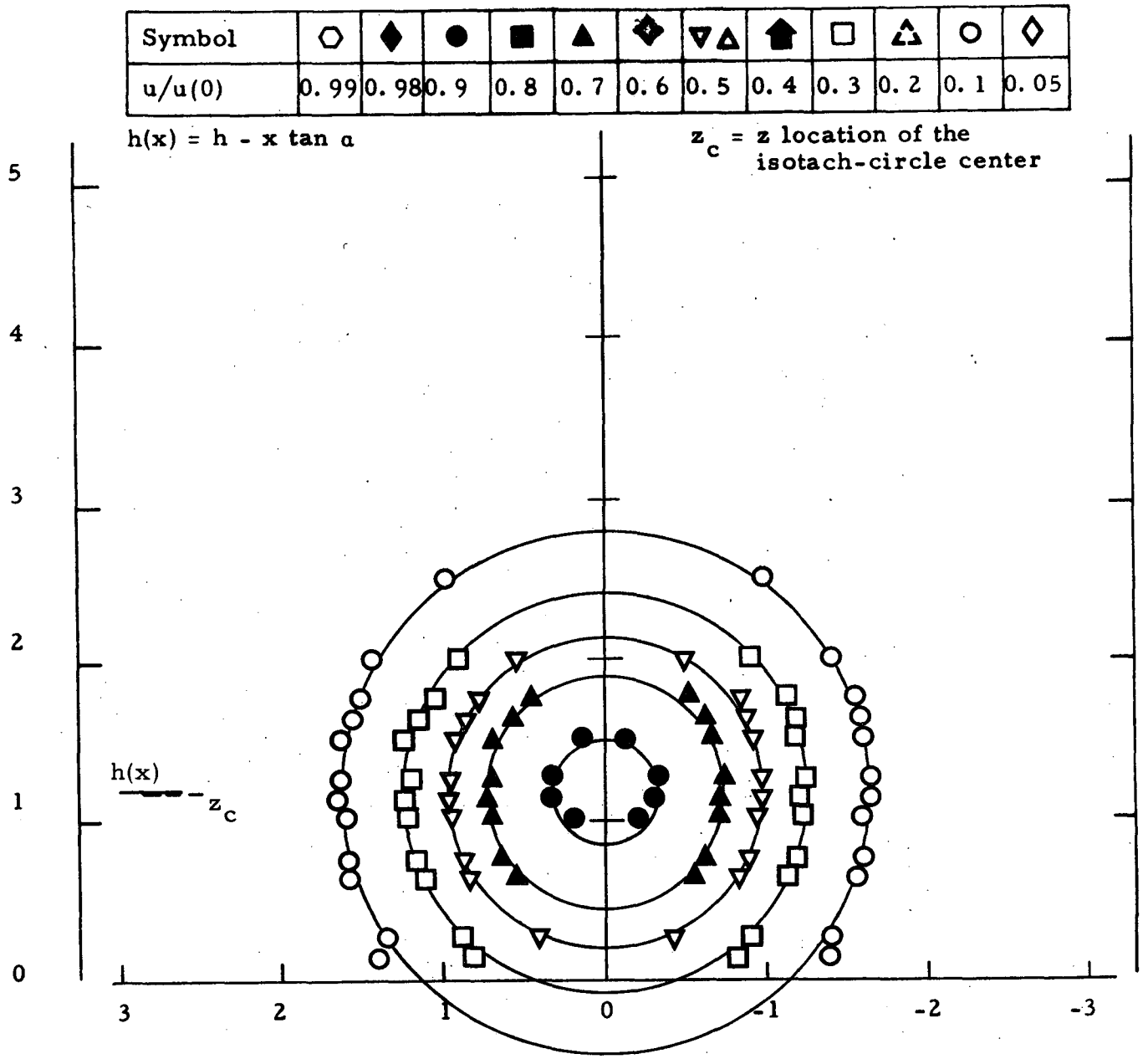
Symbol
u/u(0)
0.99
0.98
0.9
0.8
0.7
0.6
0.5
0.4
0.3
0.2
0.1
0.05
h(x) = h - x tan α
z_c = z location of the isotach-circle center
h(x)
z_c
5
4
3
2
1
0
3
2
1
0
-1
-2
-3

d) x/d = 3

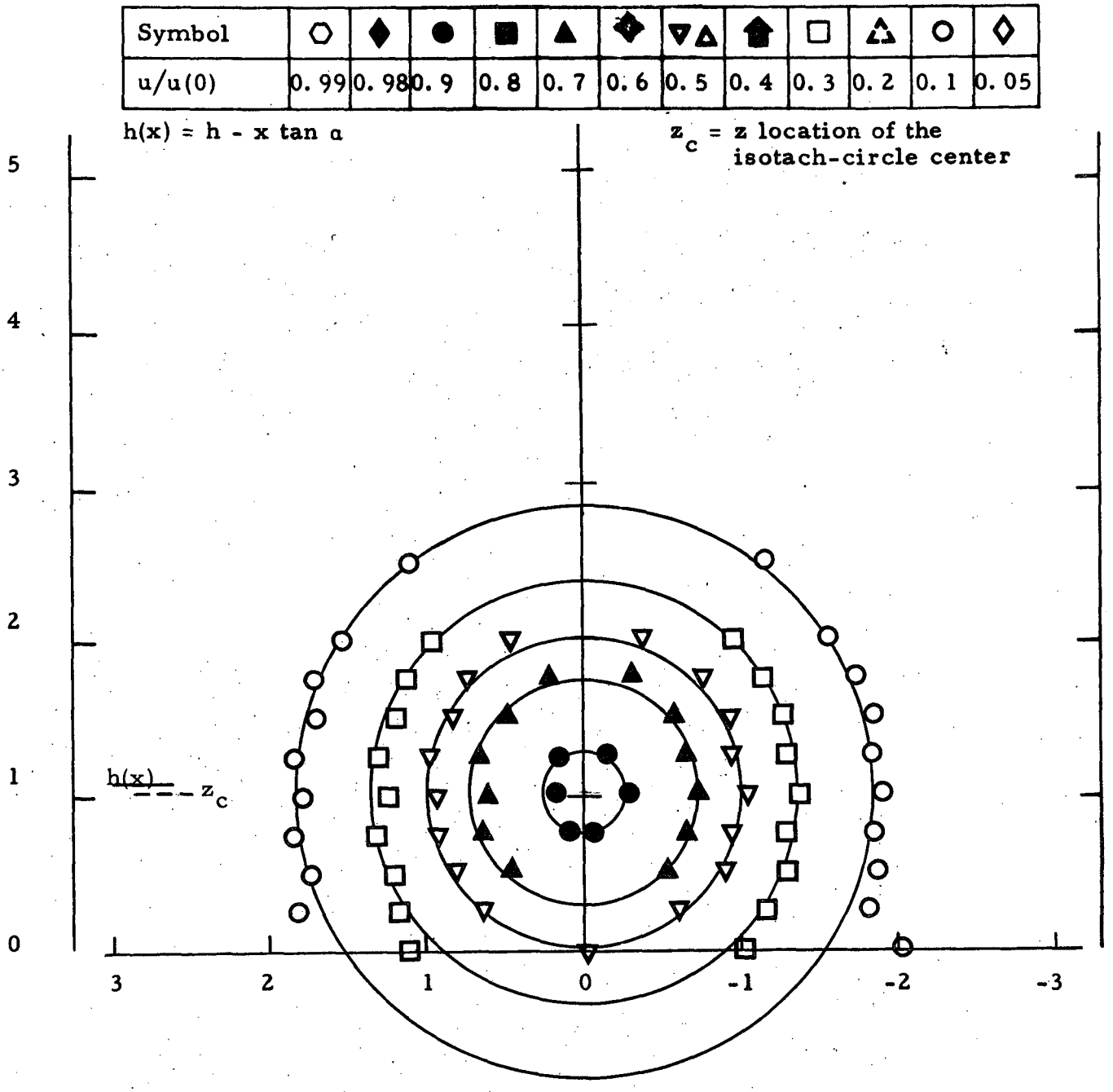
Symbol
u/u(0)
0.99
0.98
0.9
0.8
0.7
0.6
0.5
0.4
0.3
0.2
0.1
0.05
h(x) = h - x tan α
z_c = z location of the isotach-circle center
h(x)
z_c
5
4
3
2
1
0
3
2
1
0
-1
-2
-3

e) x/d = 4

Symbol	⬡	◆	●	■	▲	◈	▽△	⬟	□	△	○	◇
u/u(0)	0.99	0.98	0.9	0.8	0.7	0.6	0.5	0.4	0.3	0.2	0.1	0.05

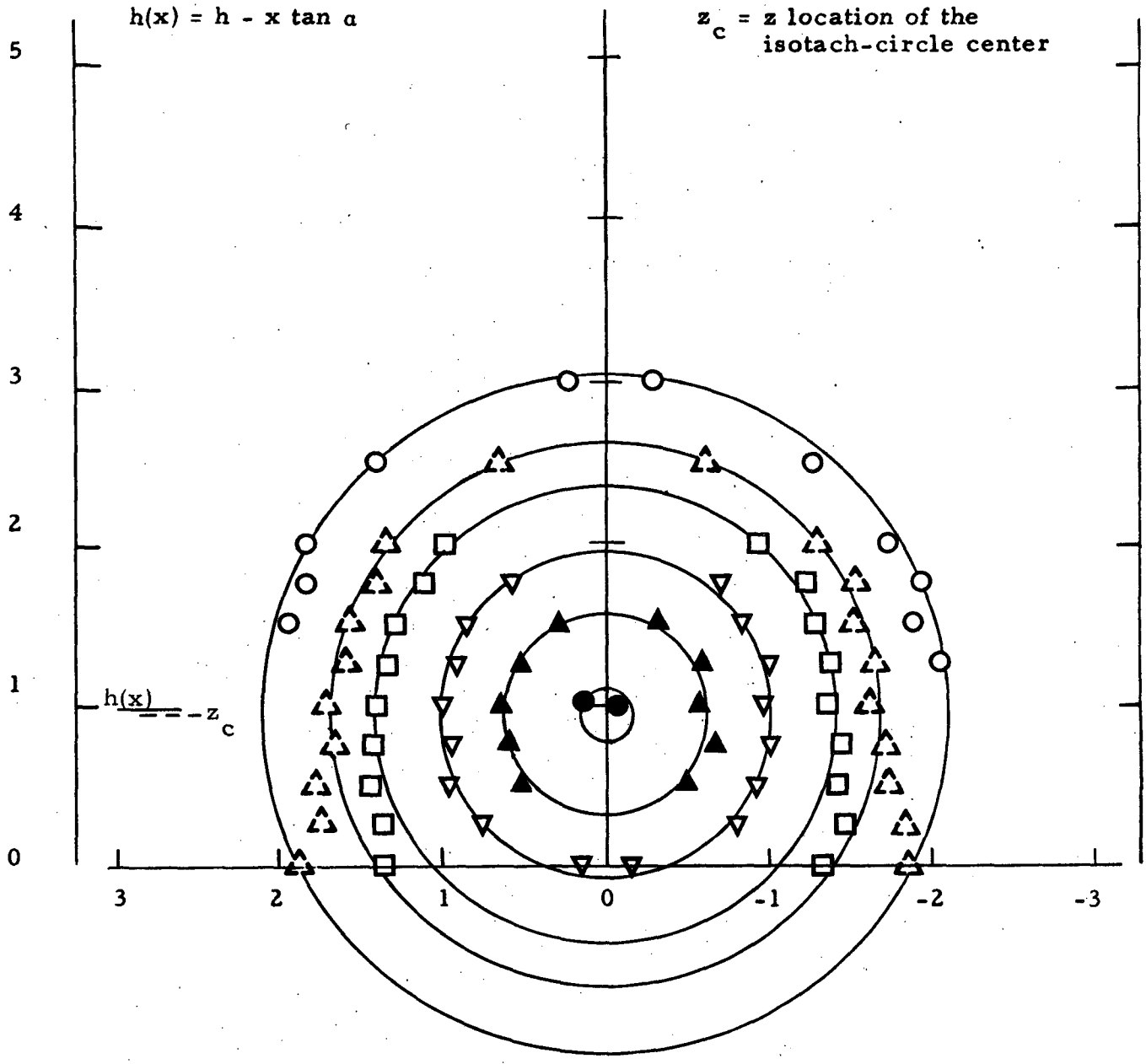

f) x/d = 5

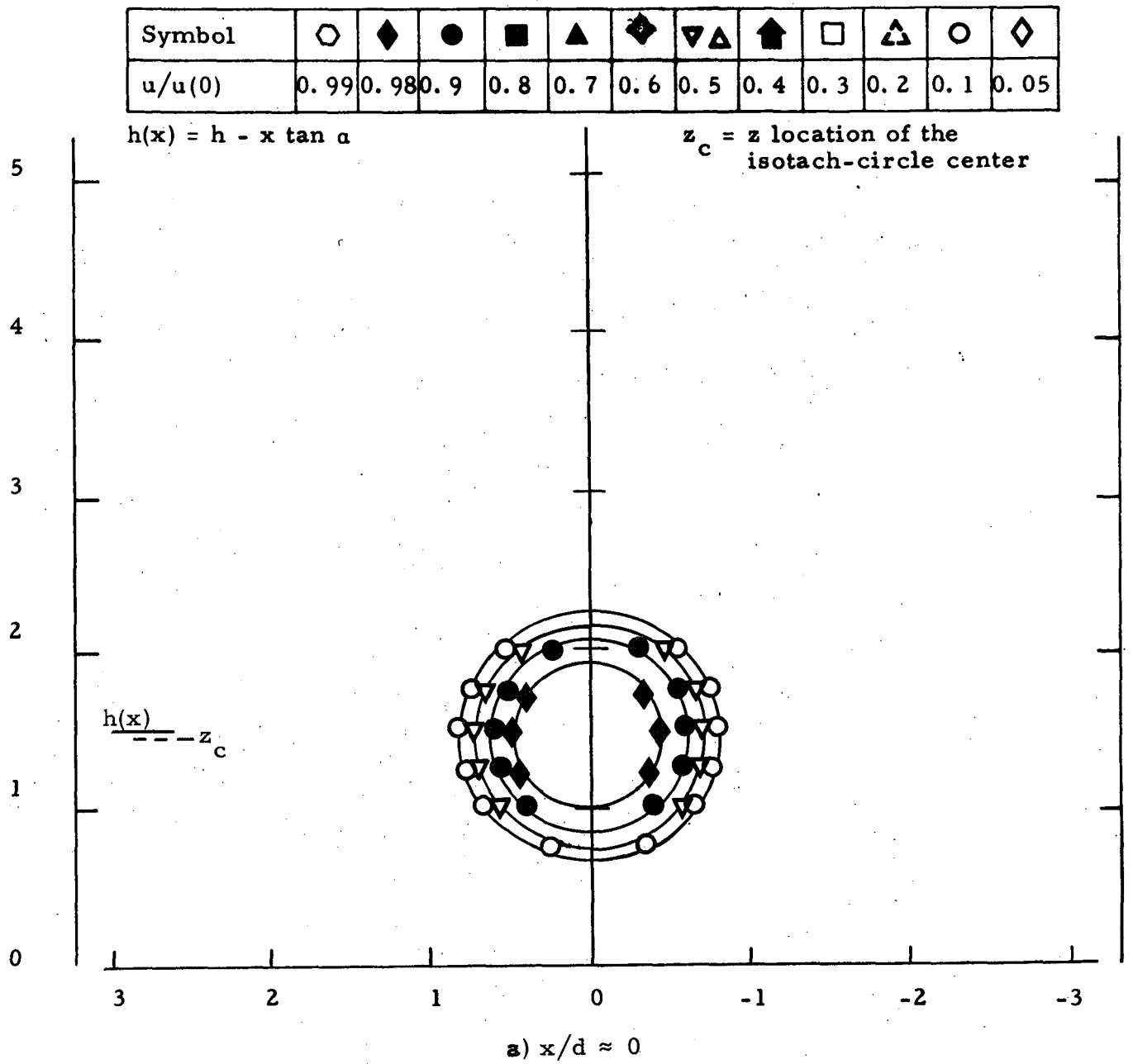

Figure 15. Isotach contours α = 3, h/d = 1, uniform.

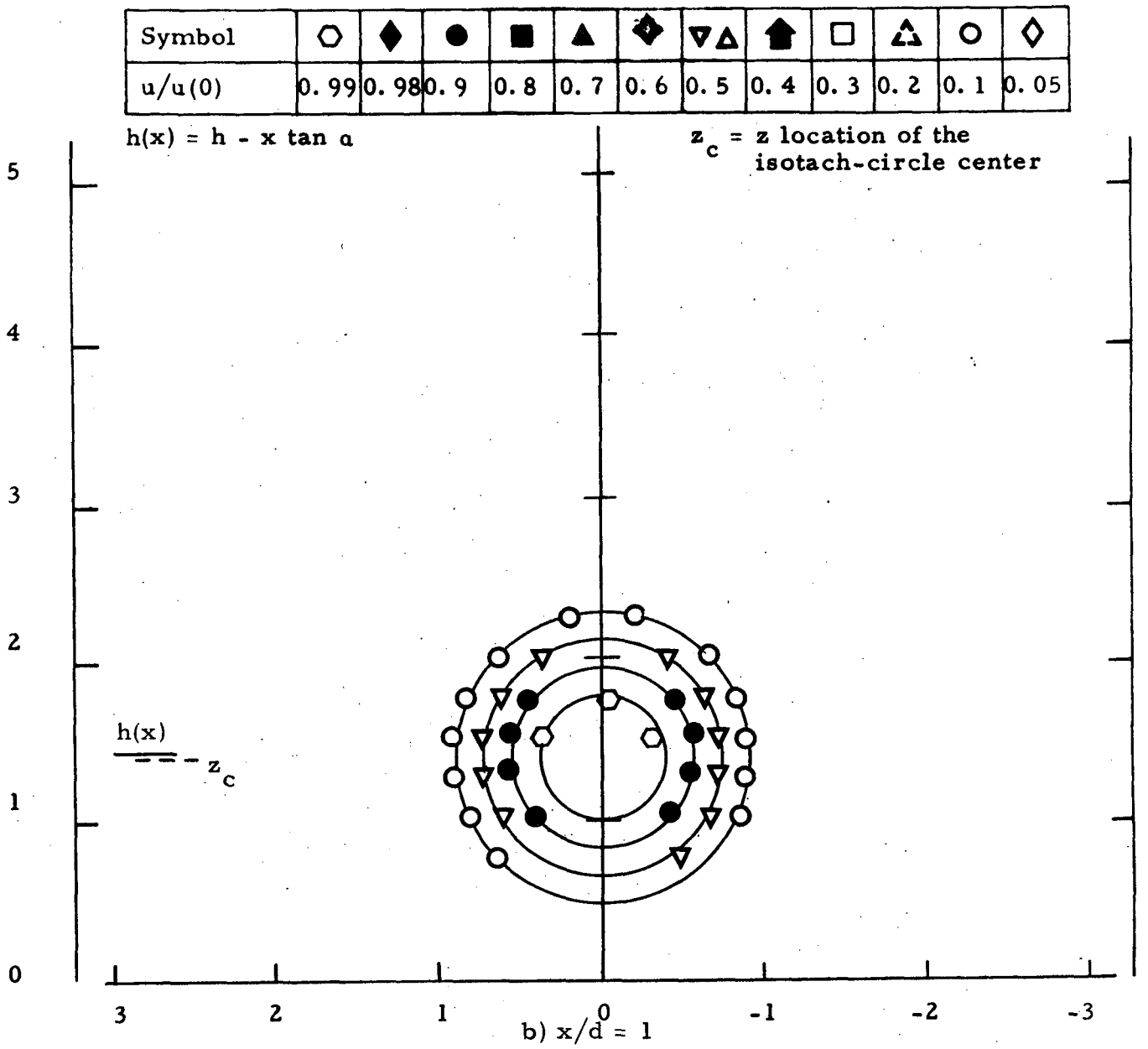
Symbol
u/u(0)
0.99
0.98
0.9
0.8
0.7
0.6
0.5
0.4
0.3
0.2
0.1
0.05
h(x) = h - x tan α
z_c = z location of the isotach-circle center
h(x)
z_c
5
4
3
2
1
0
3
2
1
0
-1
-2
-3
b) x/d = 1

Symbol	⬡	◆	●	■	▲	✦	▽△	⬟	□	△△△	○	◇
u/u(0)	0.99	0.98	0.9	0.8	0.7	0.6	0.5	0.4	0.3	0.2	0.1	0.05

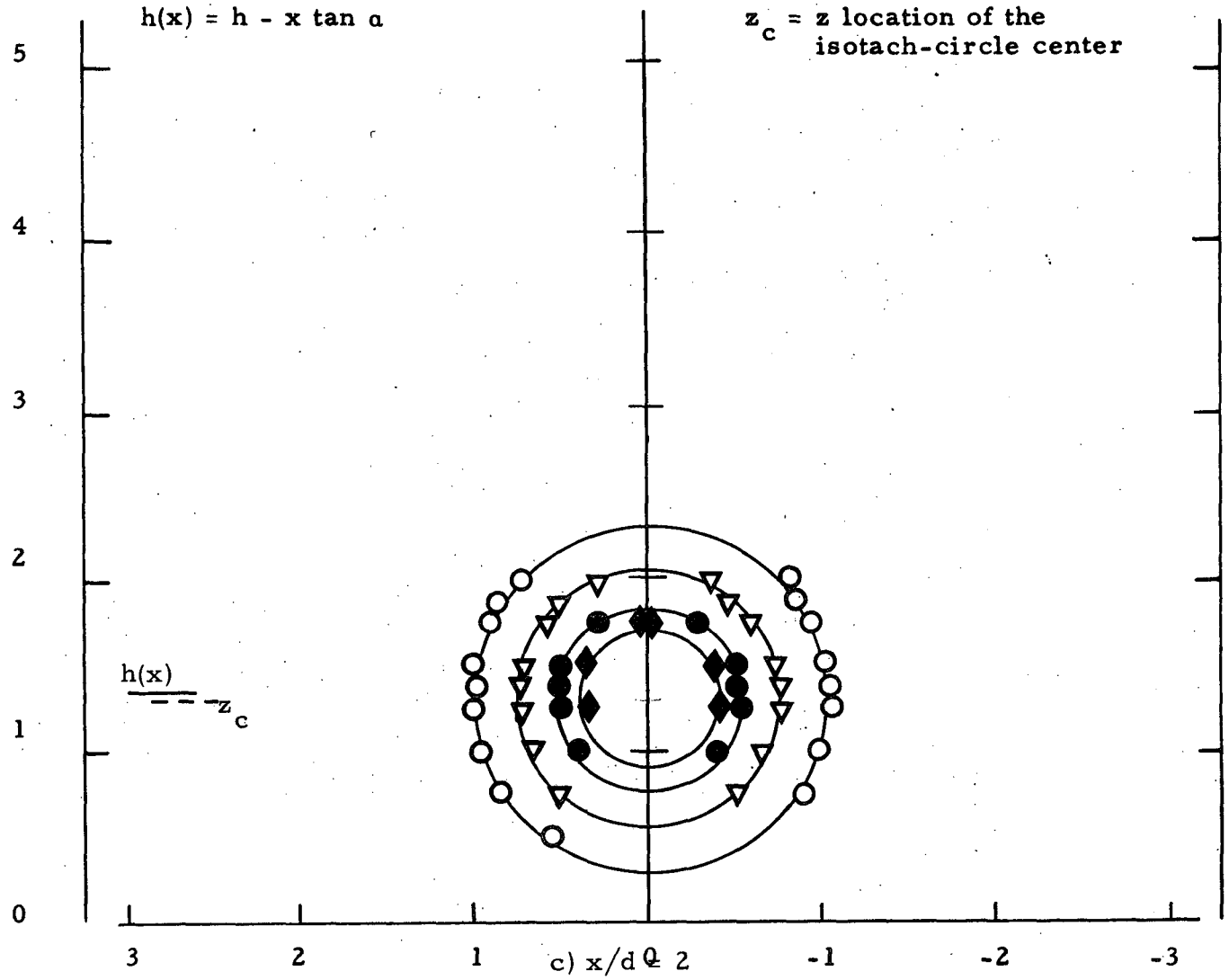

Symbol	⬡	◆	●	■	▲	◈	▽△	⬟	□	△	○	◇
u/u(0)	0.99	0.98	0.9	0.8	0.7	0.6	0.5	0.4	0.3	0.2	0.1	0.05

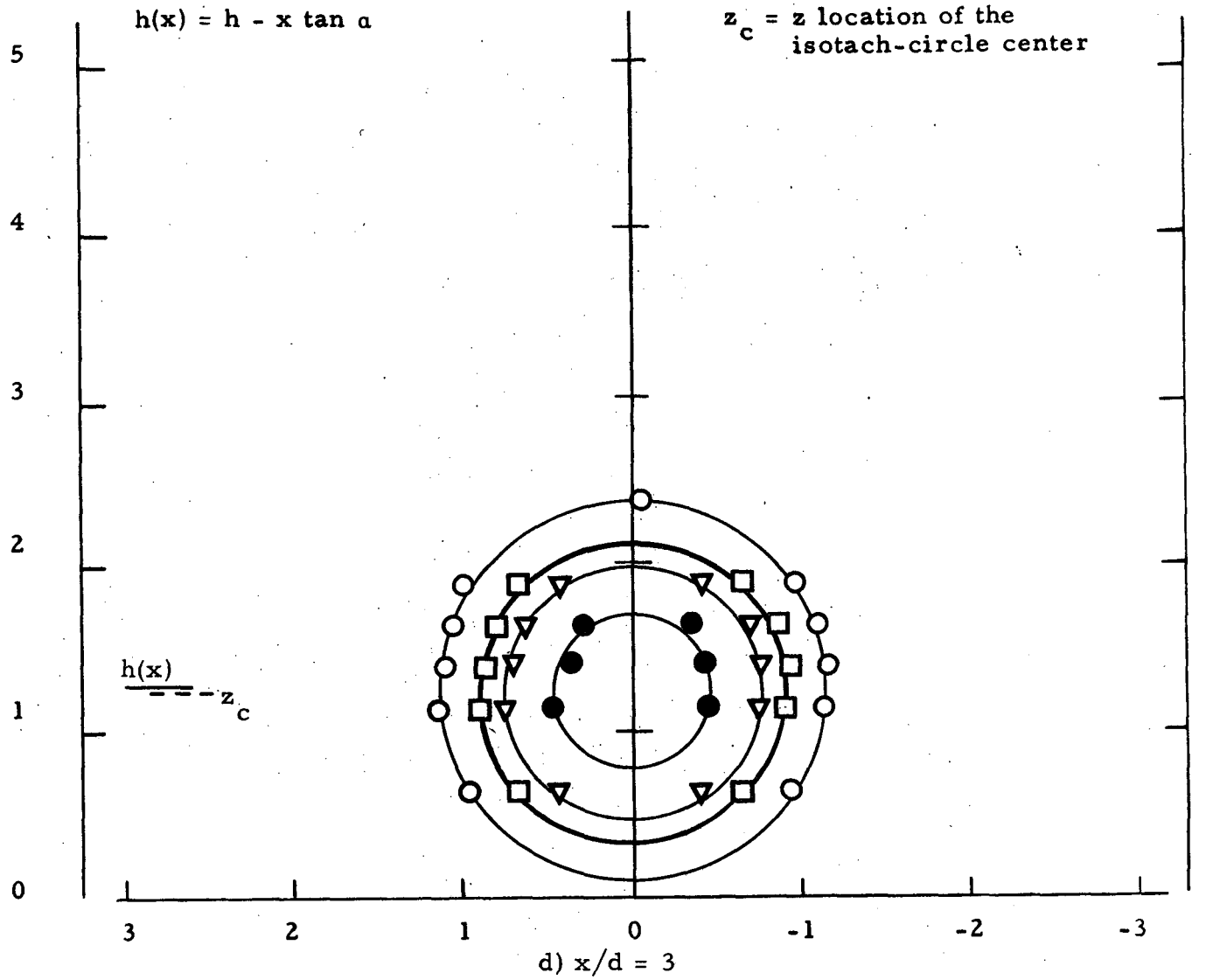

d) x/d = 3

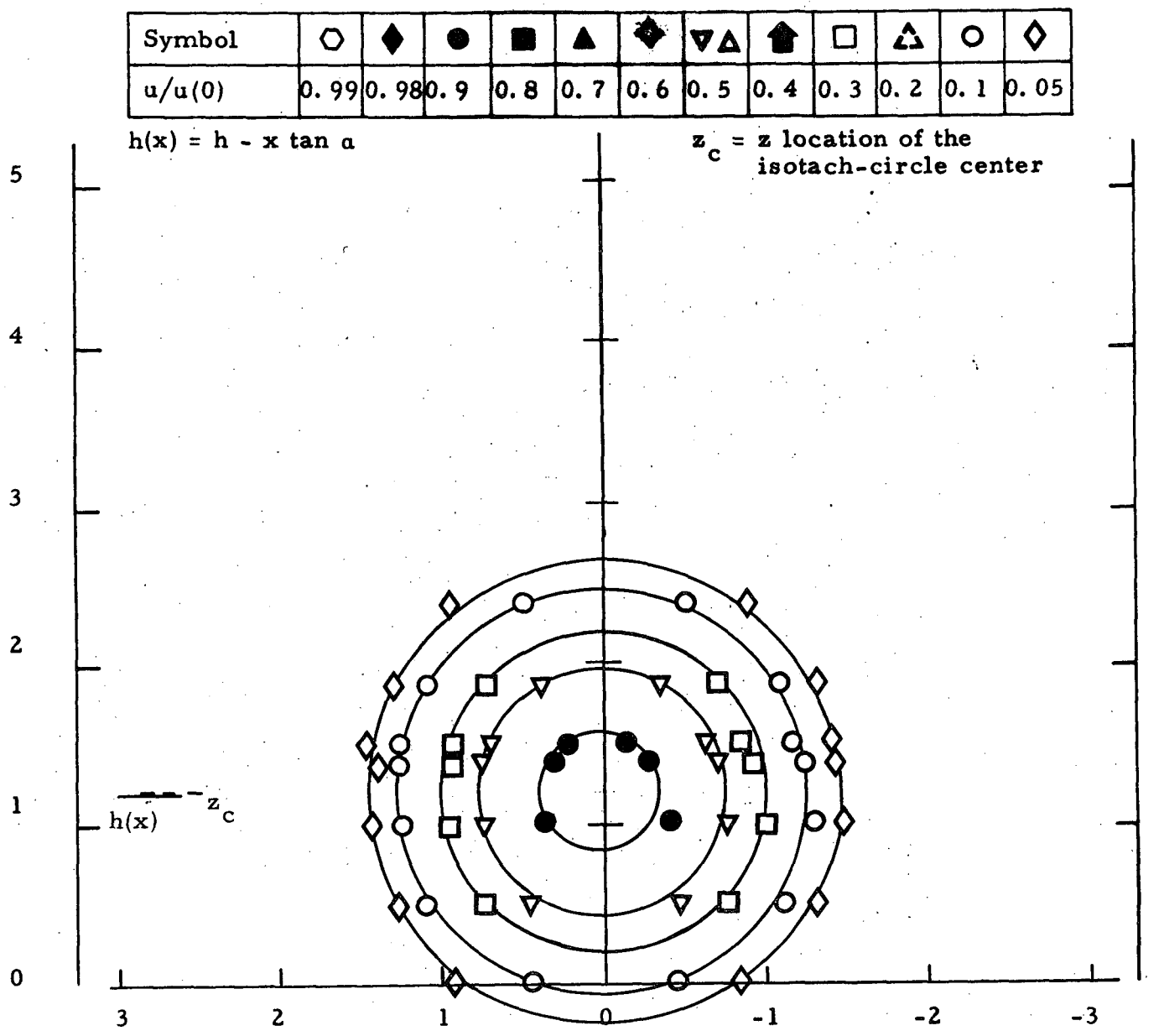
Symbol
u/u(0)
0.99
0.98
0.9
0.8
0.7
0.6
0.5
0.4
0.3
0.2
0.1
0.05
h(x) = h - x tan α
z_c = z location of the isotach-circle center
h(x)
z_c
5
4
3
2
1
0
3
2
1
0
-1
-2
-3

e) x/d = 4

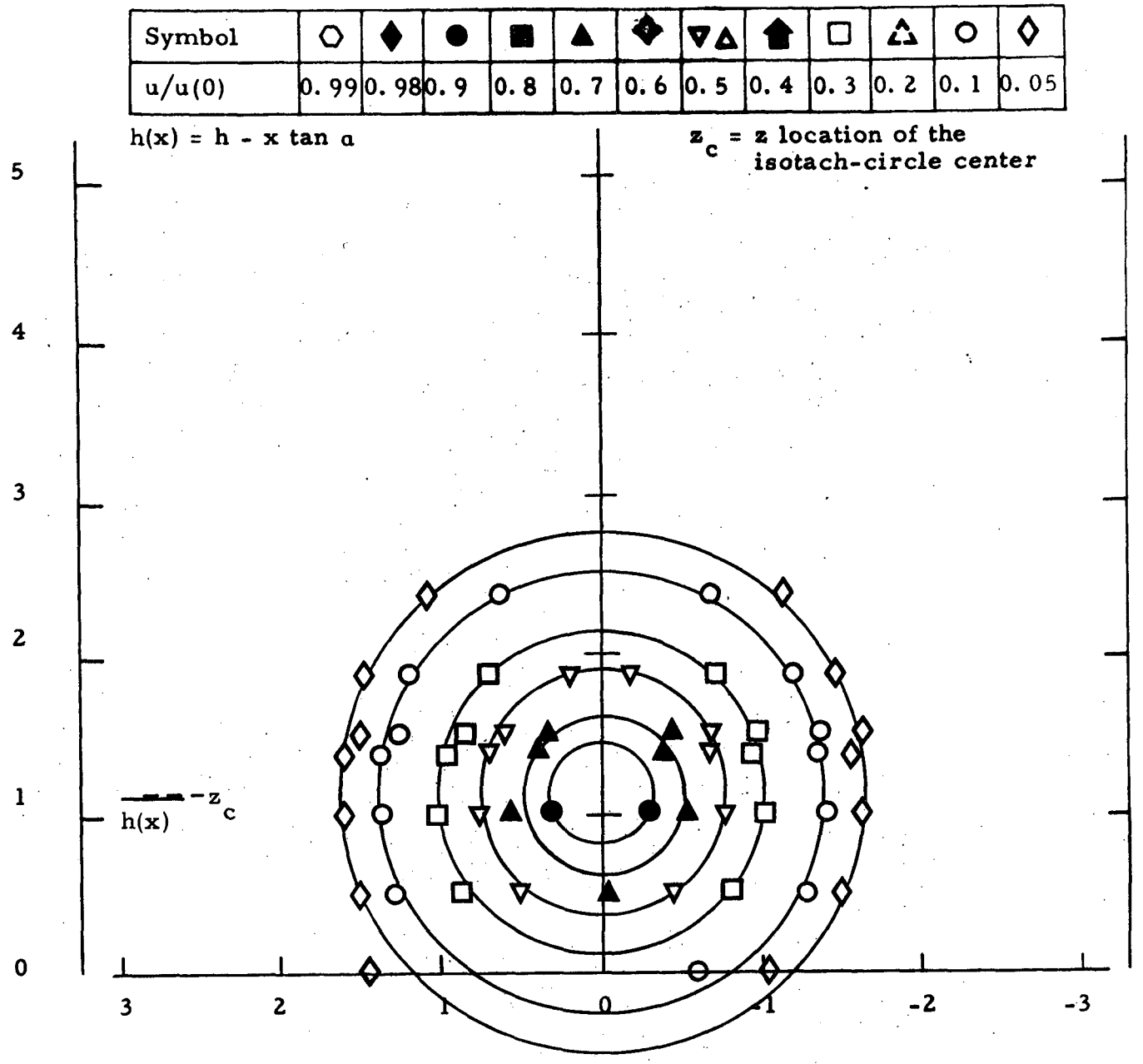
Symbol
u/u(0)
0.99
0.98
0.9
0.8
0.7
0.6
0.5
0.4
0.3
0.2
0.1
0.05
h(x) = h - x tan α
z_c = z location of the isotach-circle center
5
4
3
2
1
0
h(x)
z_c
3
2
1
0
-1
-2
-3

f) x/d = 5

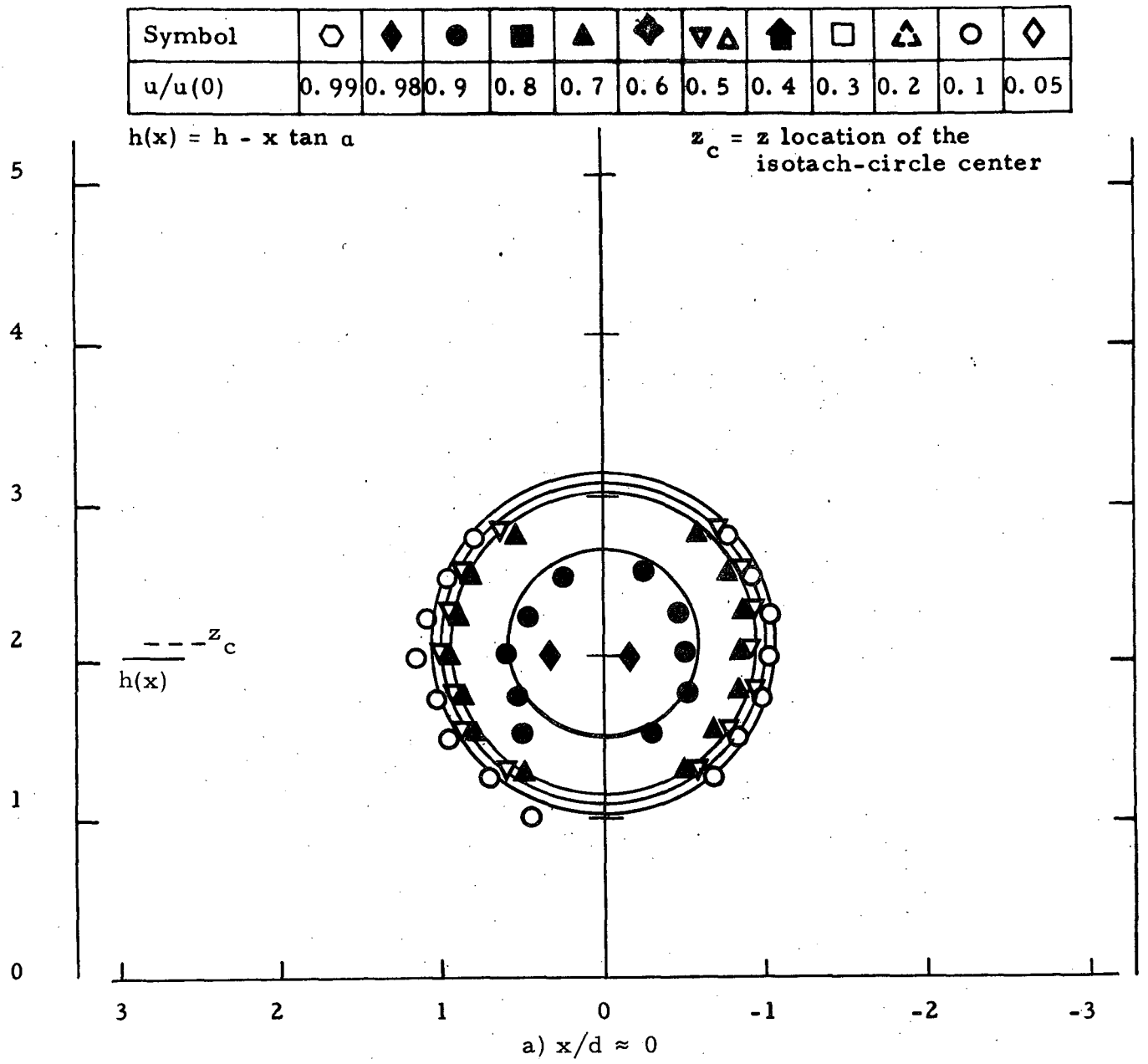

Figure 16. Isotach contours α = 3, h/d = 1, fully developed.

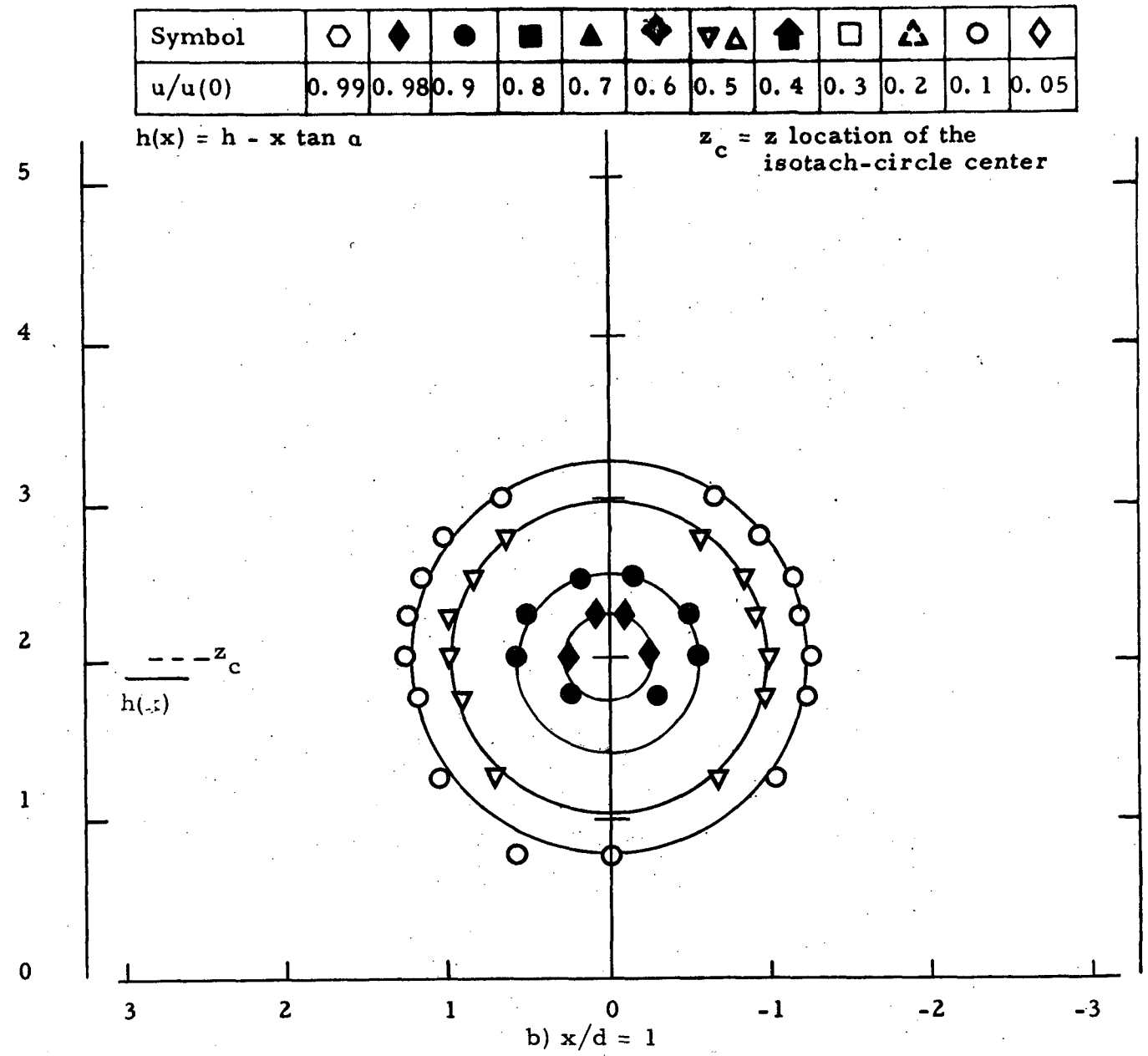
Symbol
u/u(0)
0.99
0.98
0.9
0.8
0.7
0.6
0.5
0.4
0.3
0.2
0.1
0.05
h(x) = h - x tan α
z_c = z location of the isotach-circle center
z_c
h(x)
5
4
3
2
1
0
3
2
1
0
-1
-2
-3
b) x/d = 1

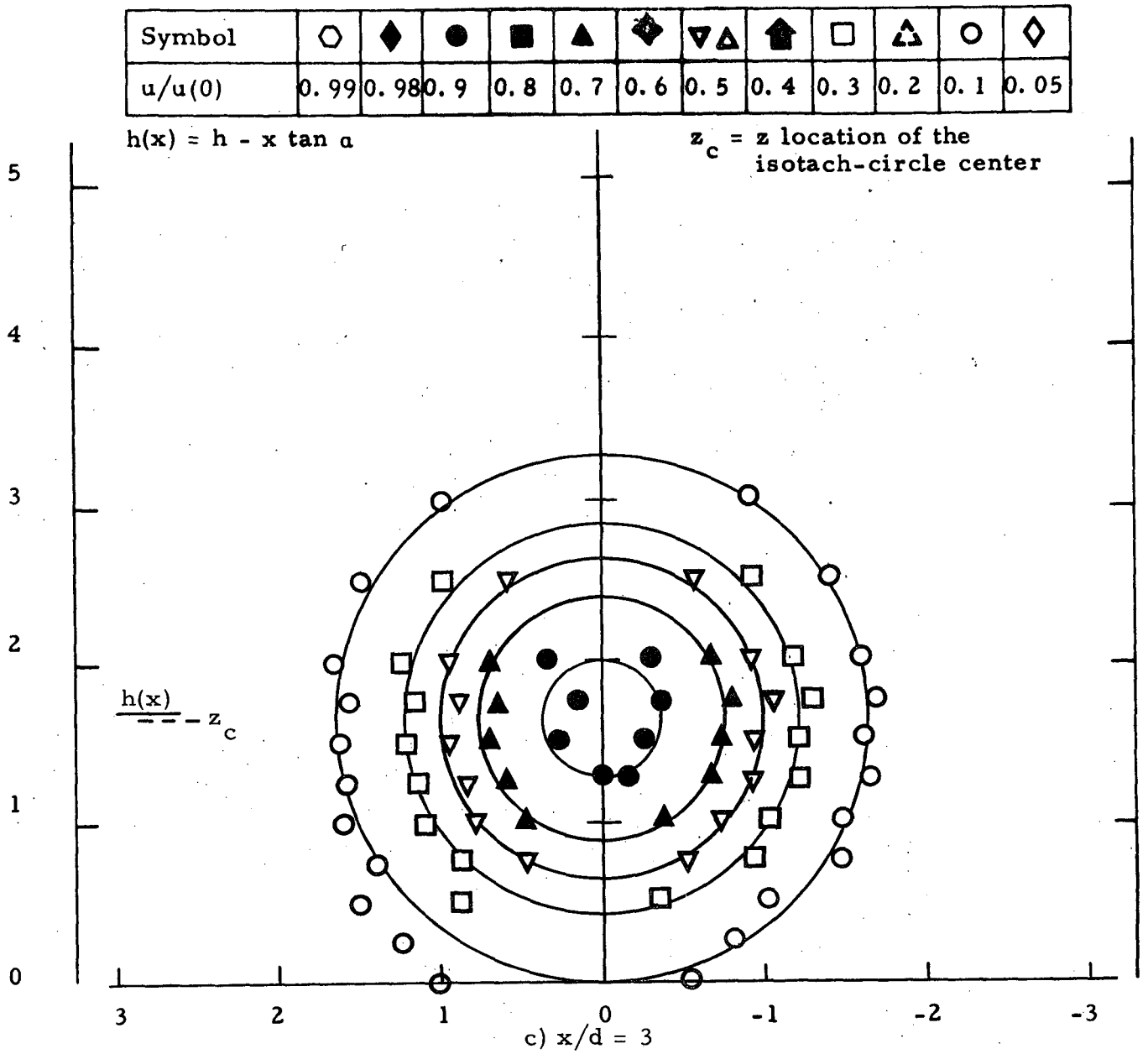
Symbol
u/u(0)
0.99
0.98
0.9
0.8
0.7
0.6
0.5
0.4
0.3
0.2
0.1
0.05
h(x) = h - x tan α
z_c = z location of the isotach-circle center
h(x)/d - z_c
5
4
3
2
1
0
3
2
1
0
-1
-2
-3
c) x/d = 3

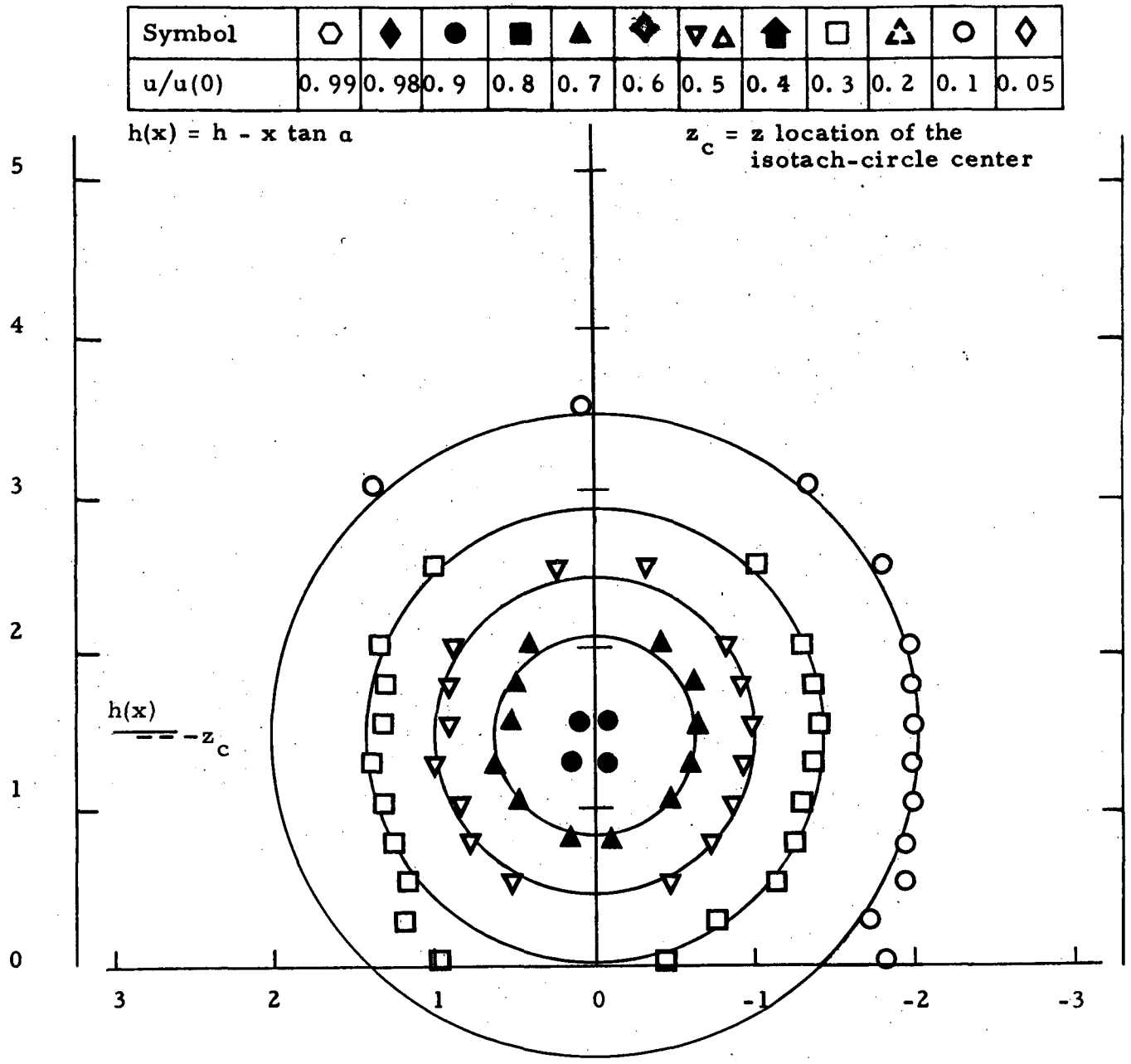
Symbol
u/u(0)
0.99
0.98
0.9
0.8
0.7
0.6
0.5
0.4
0.3
0.2
0.1
0.05
h(x) = h - x tan α
z_c = z location of the isotach-circle center
h(x)
---- - z_c
5
4
3
2
1
0
3
2
1
0
-1
-2
-3

d) x/d = 5

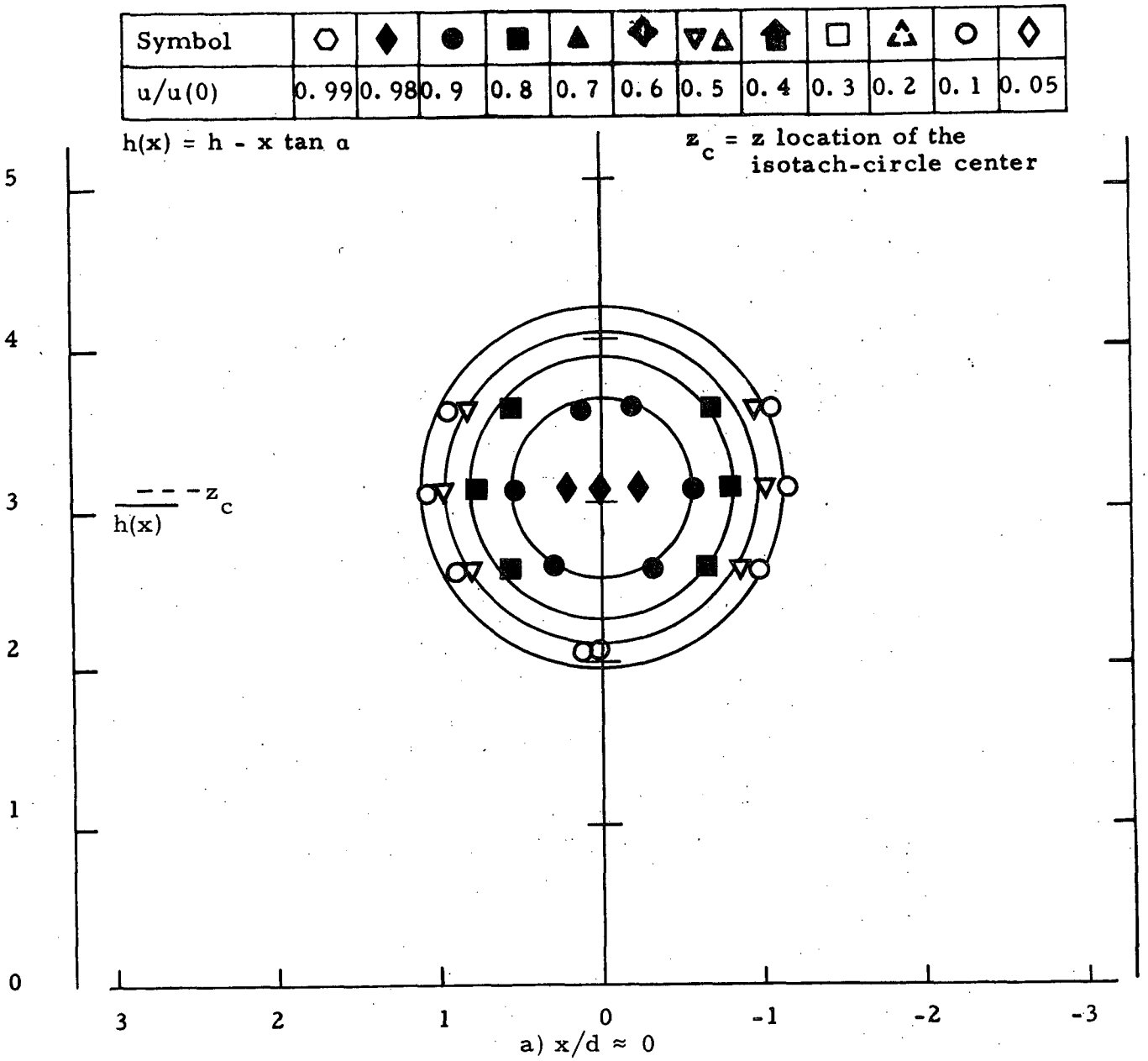

Figure 17. Isotach contours $\alpha = 3$, $h/d = 1.5$, fully developed.

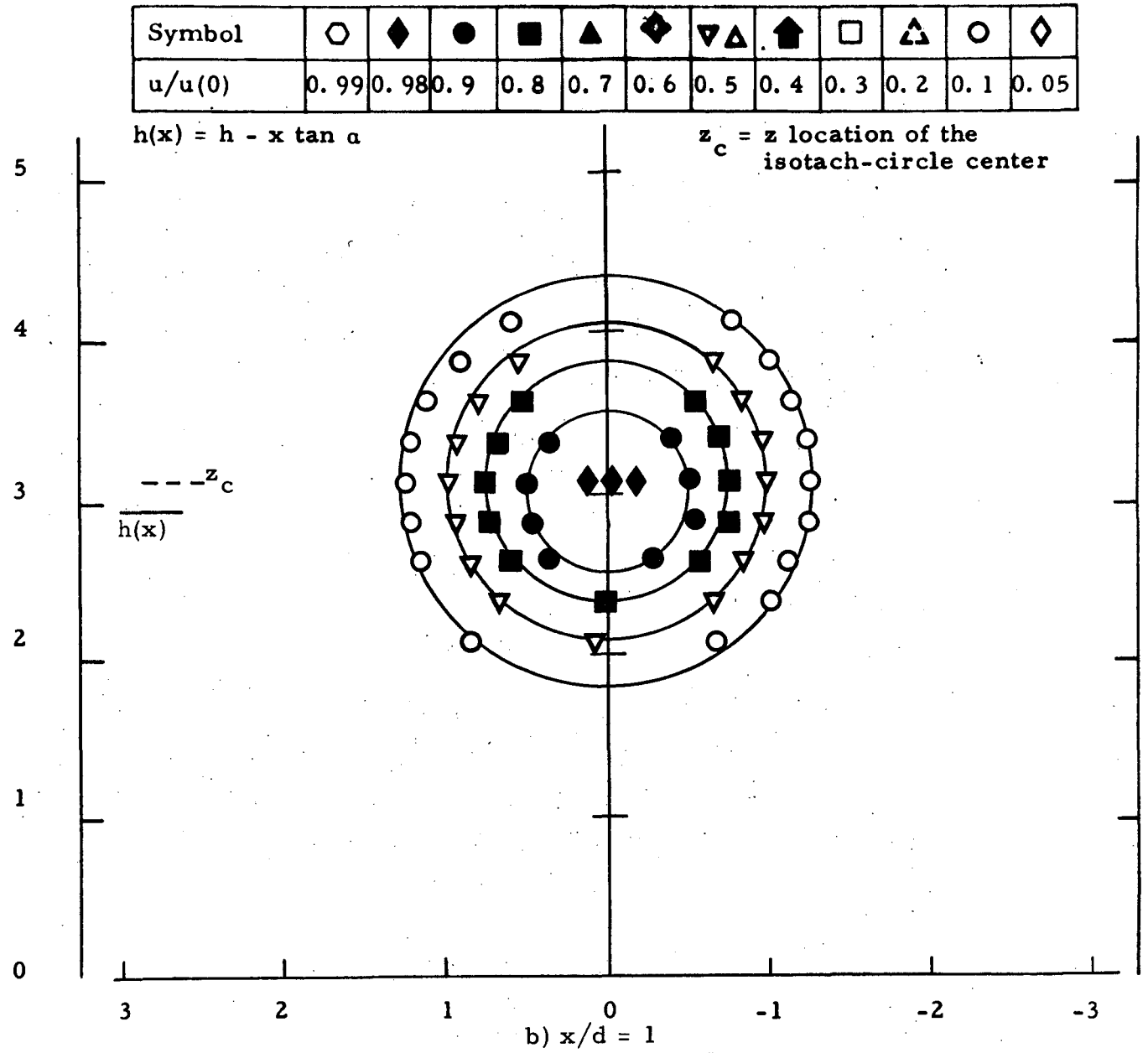
Symbol
u/u(0)
0.99
0.98
0.9
0.8
0.7
0.6
0.5
0.4
0.3
0.2
0.1
0.05
h(x) = h - x tan α
z_c = z location of the isotach-circle center
z_c / h(x)
5
4
3
2
1
0
3
2
1
0
-1
-2
-3
b) x/d = 1

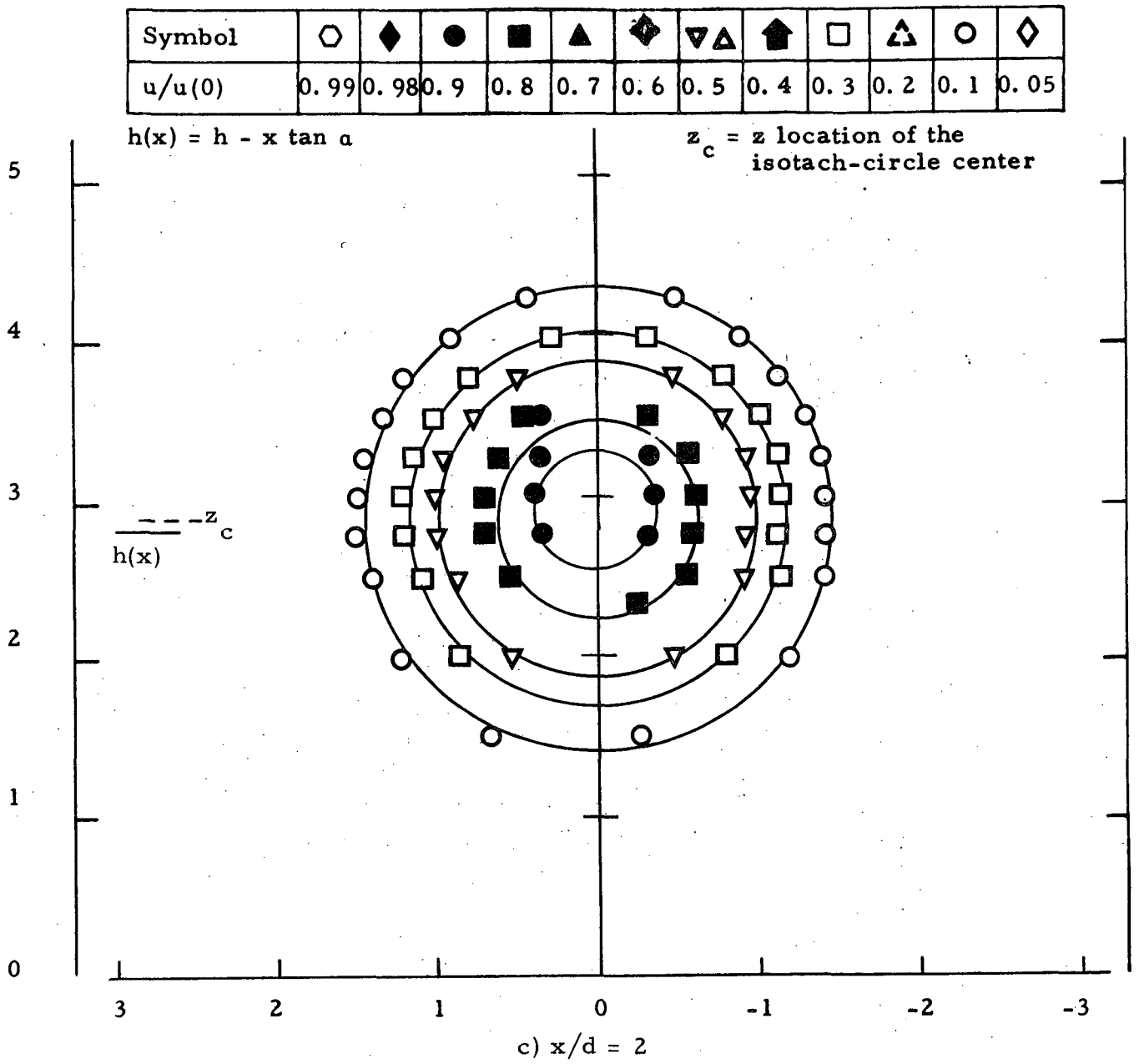
Symbol
u/u(0)
0.99
0.98
0.9
0.8
0.7
0.6
0.5
0.4
0.3
0.2
0.1
0.05
h(x) = h - x tan α
z_c = z location of the isotach-circle center
$\frac{z - z_c}{h(x)}$
5
4
3
2
1
0
3
2
1
0
-1
-2
-3

c) x/d = 2

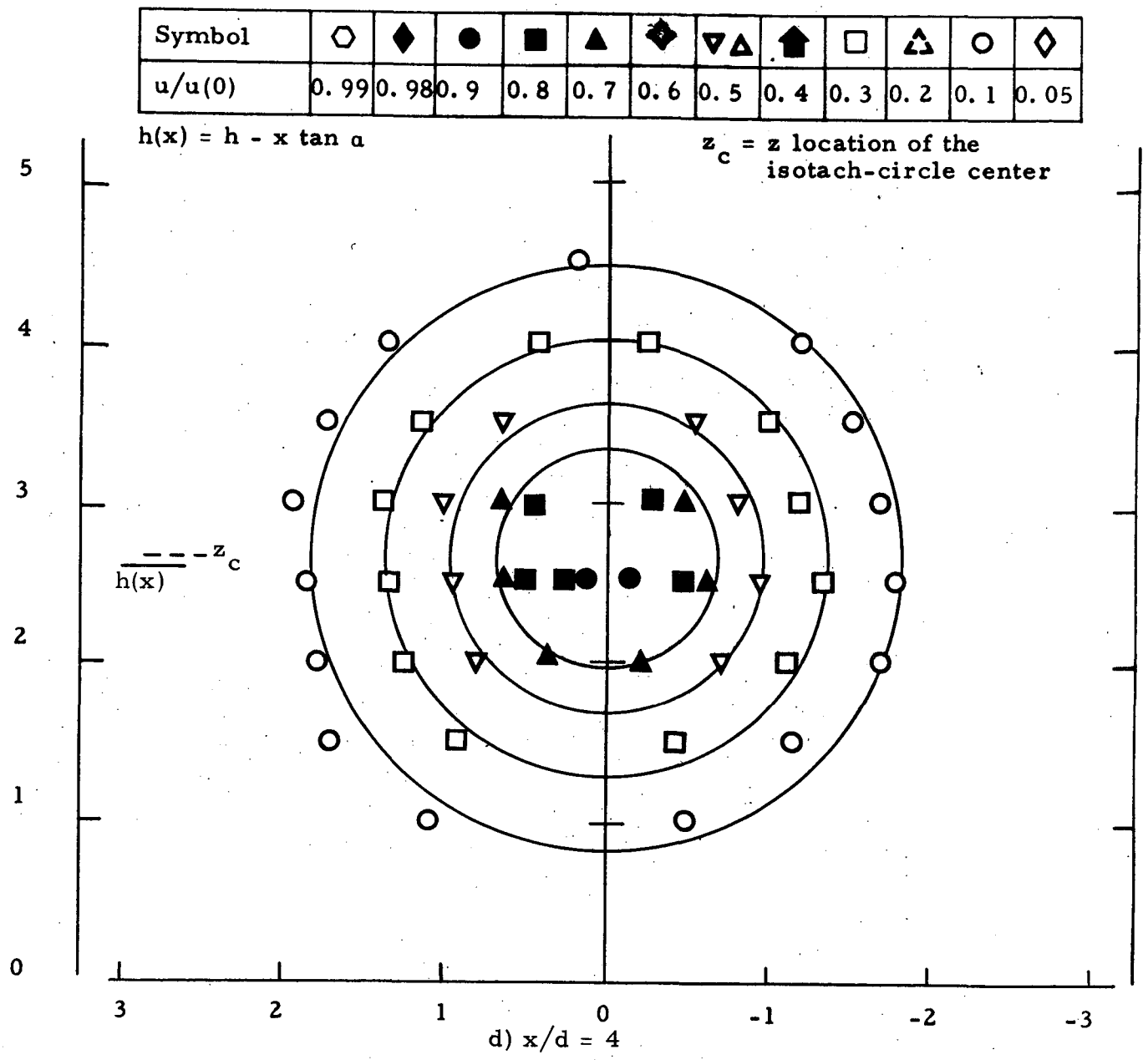
Symbol
u/u(0)
0.99
0.98
0.9
0.8
0.7
0.6
0.5
0.4
0.3
0.2
0.1
0.05
h(x) = h - x tan α
z_c = z location of the isotach-circle center
$\frac{z_c}{h(x)}$
5
4
3
2
1
0
3
2
1
0
-1
-2
-3
d) x/d = 4

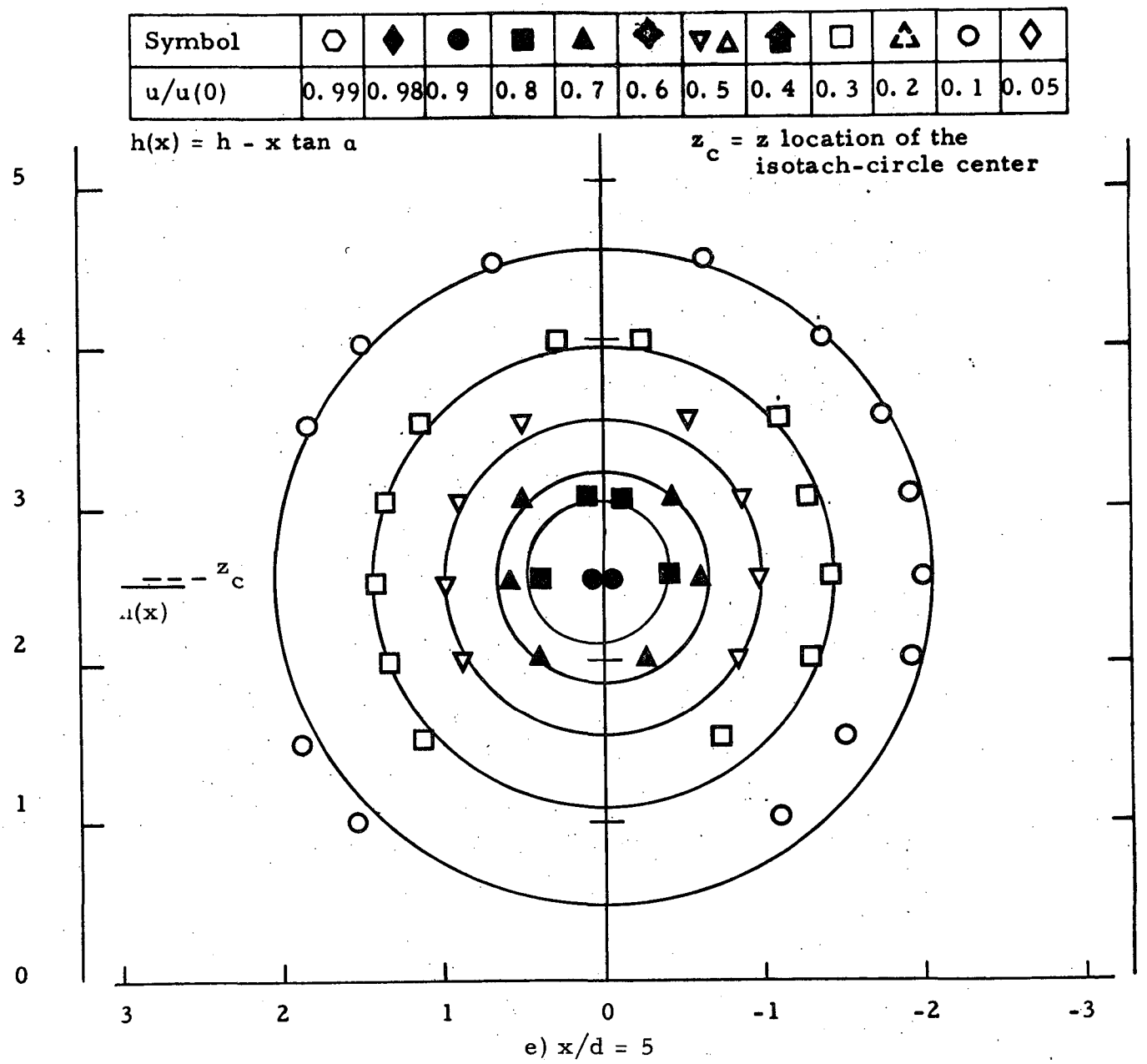
Symbol
u/u(0)
0.99
0.98
0.9
0.8
0.7
0.6
0.5
0.4
0.3
0.2
0.1
0.05
h(x) = h - x tan α
z_c = z location of the isotach-circle center
z_c
u(x)
5
4
3
2
1
0
3
2
1
0
-1
-2
-3

e) x/d = 5

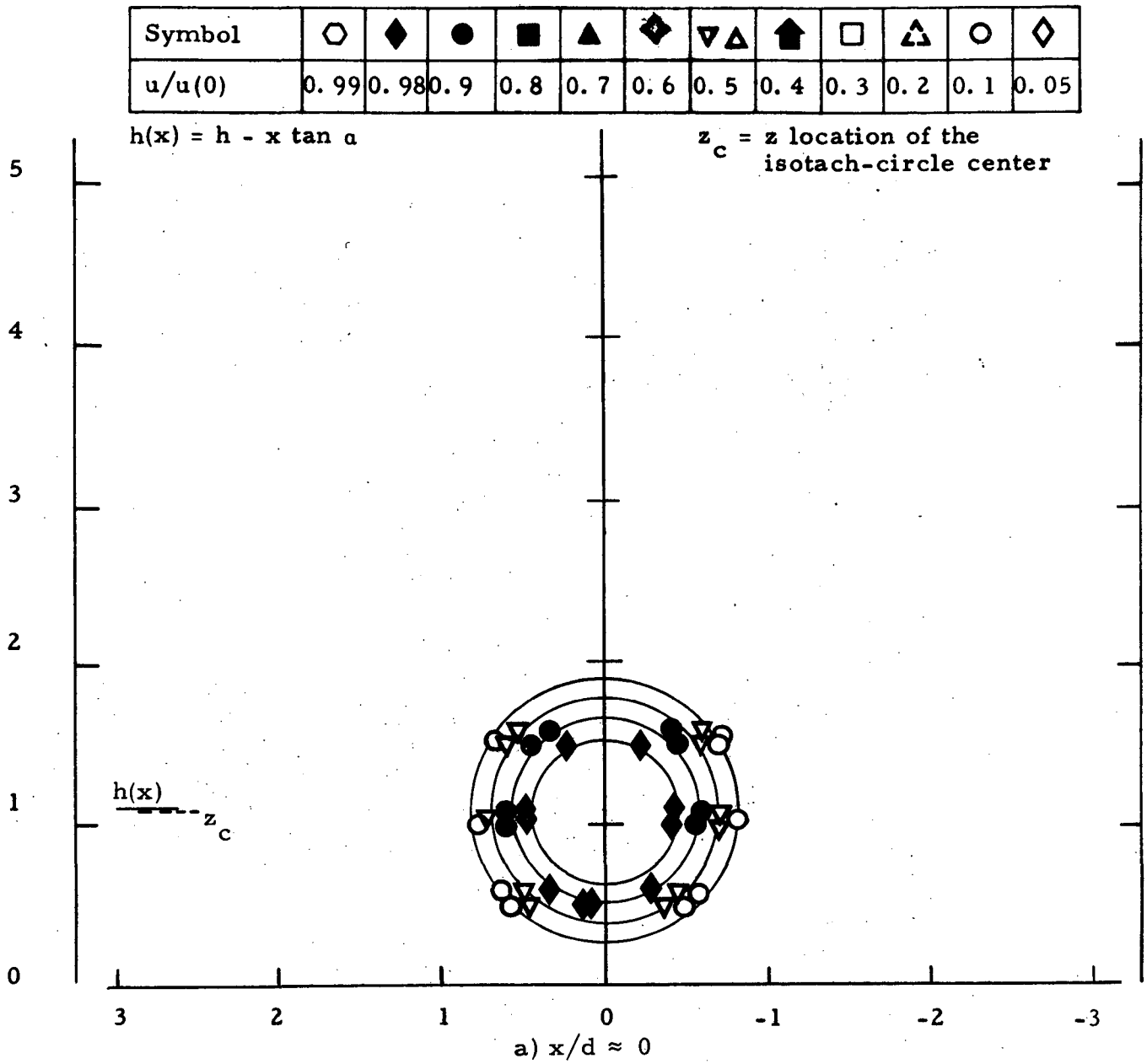

Figure 18. Isotach contours $\alpha = 6$, $h/d = 0.75$, uniform.

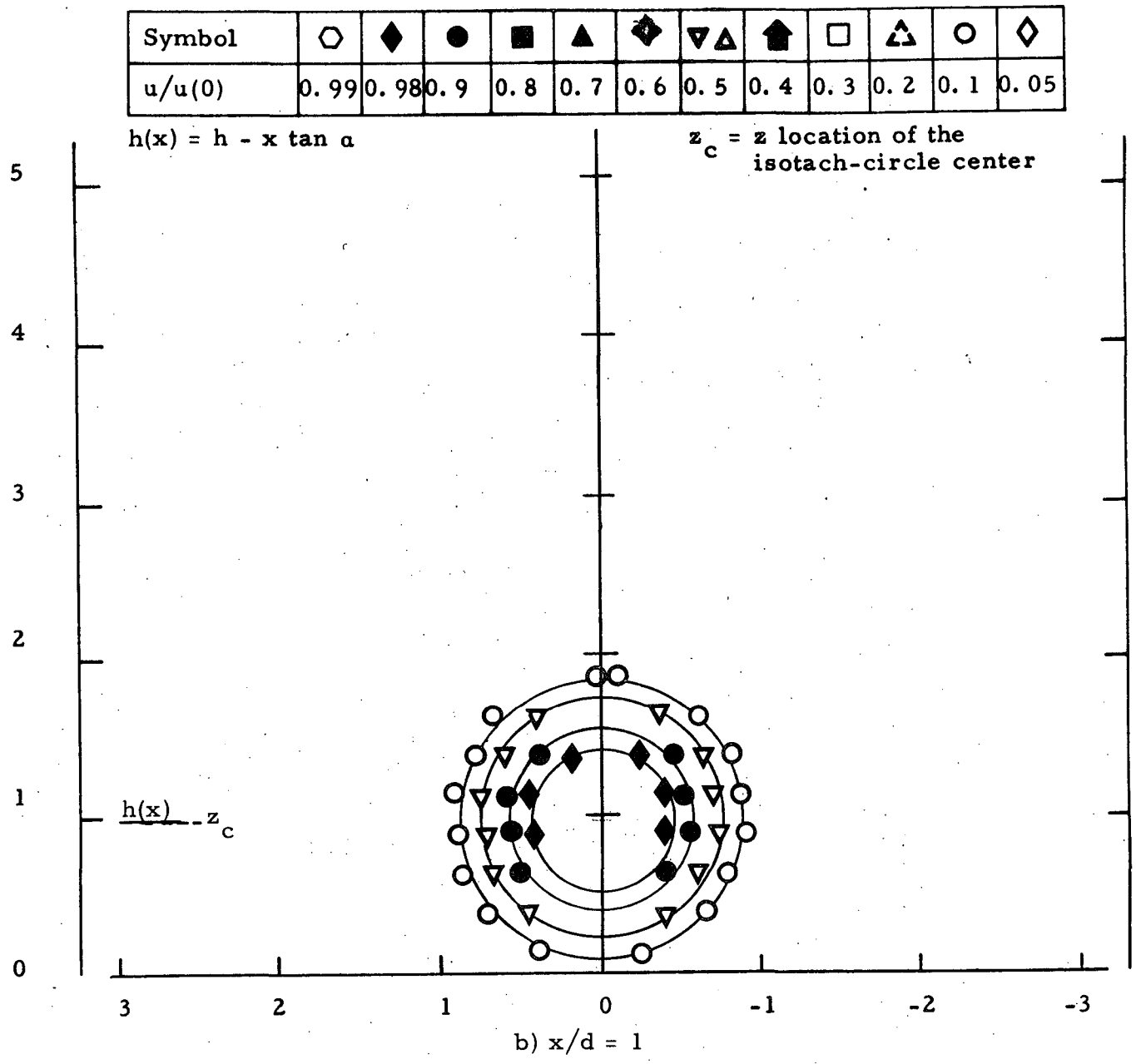
Symbol
u/u(0)
0.99
0.98
0.9
0.8
0.7
0.6
0.5
0.4
0.3
0.2
0.1
0.05
h(x) = h - x tan α
z_c = z location of the isotach-circle center
h(x)
z_c
5
4
3
2
1
0
3
2
1
0
-1
-2
-3

b) x/d = 1

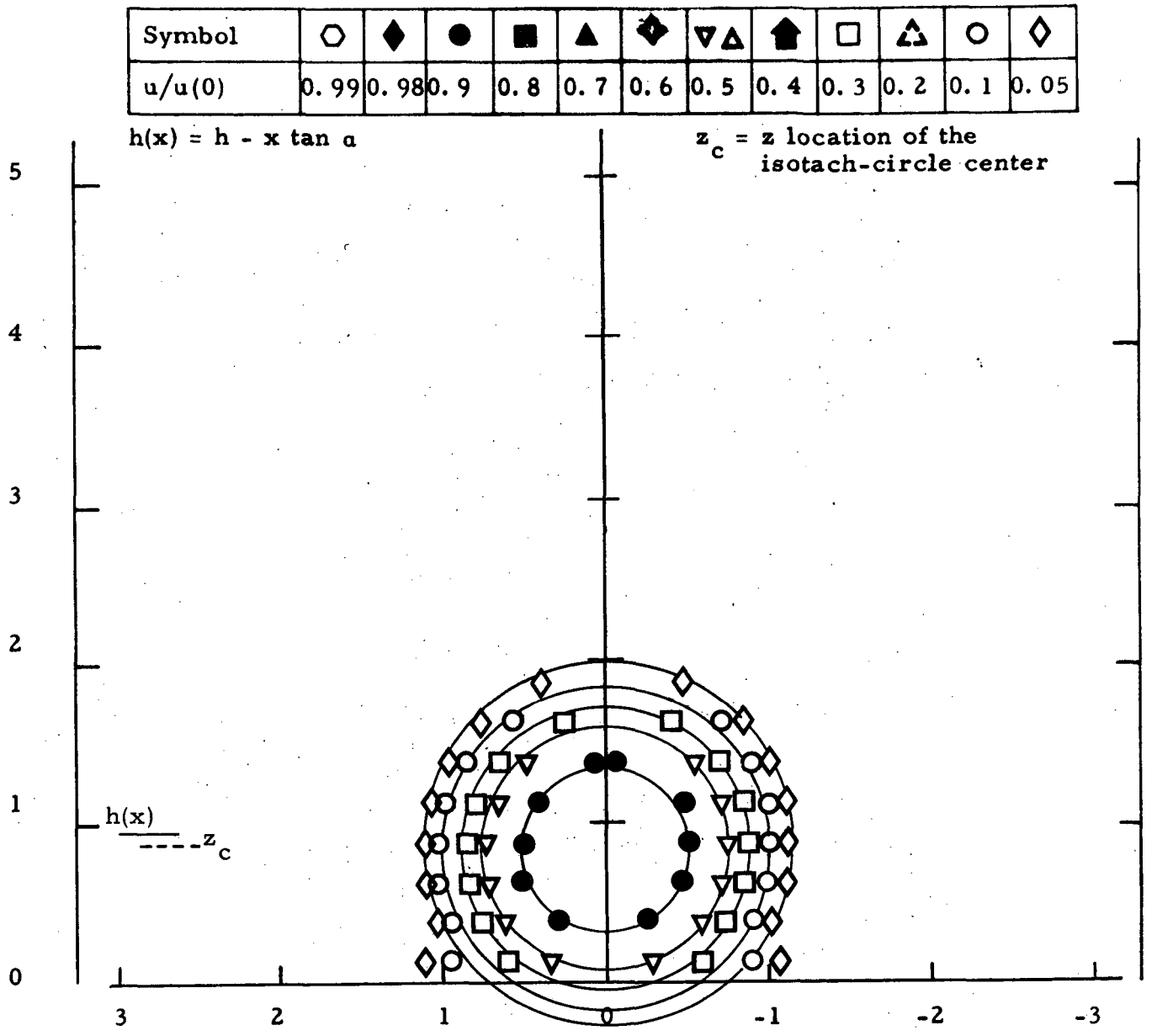
Symbol
u/u(0)
0.99
0.98
0.9
0.8
0.7
0.6
0.5
0.4
0.3
0.2
0.1
0.05
h(x) = h - x tan α
z_c = z location of the isotach-circle center
5
4
3
2
1
0
h(x)
z_c
3
2
1
0
-1
-2
-3

c) x/d = 2

Symbol	⬡	◆	●	■	▲	◈	▽△	⬟	□	△	○	◇
u/u(0)	0.99	0.98	0.9	0.8	0.7	0.6	0.5	0.4	0.3	0.2	0.1	0.05

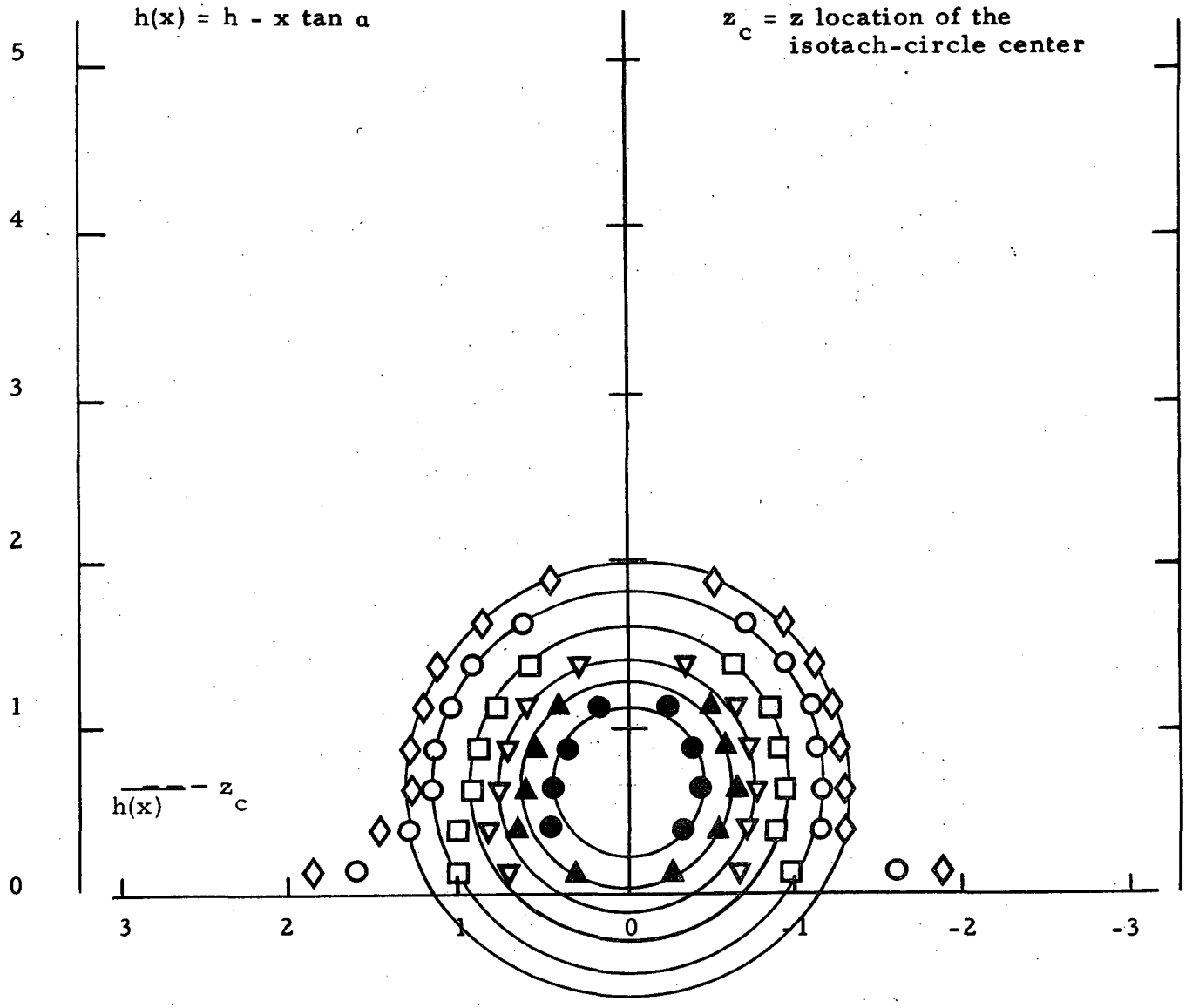

d) x/d = 3

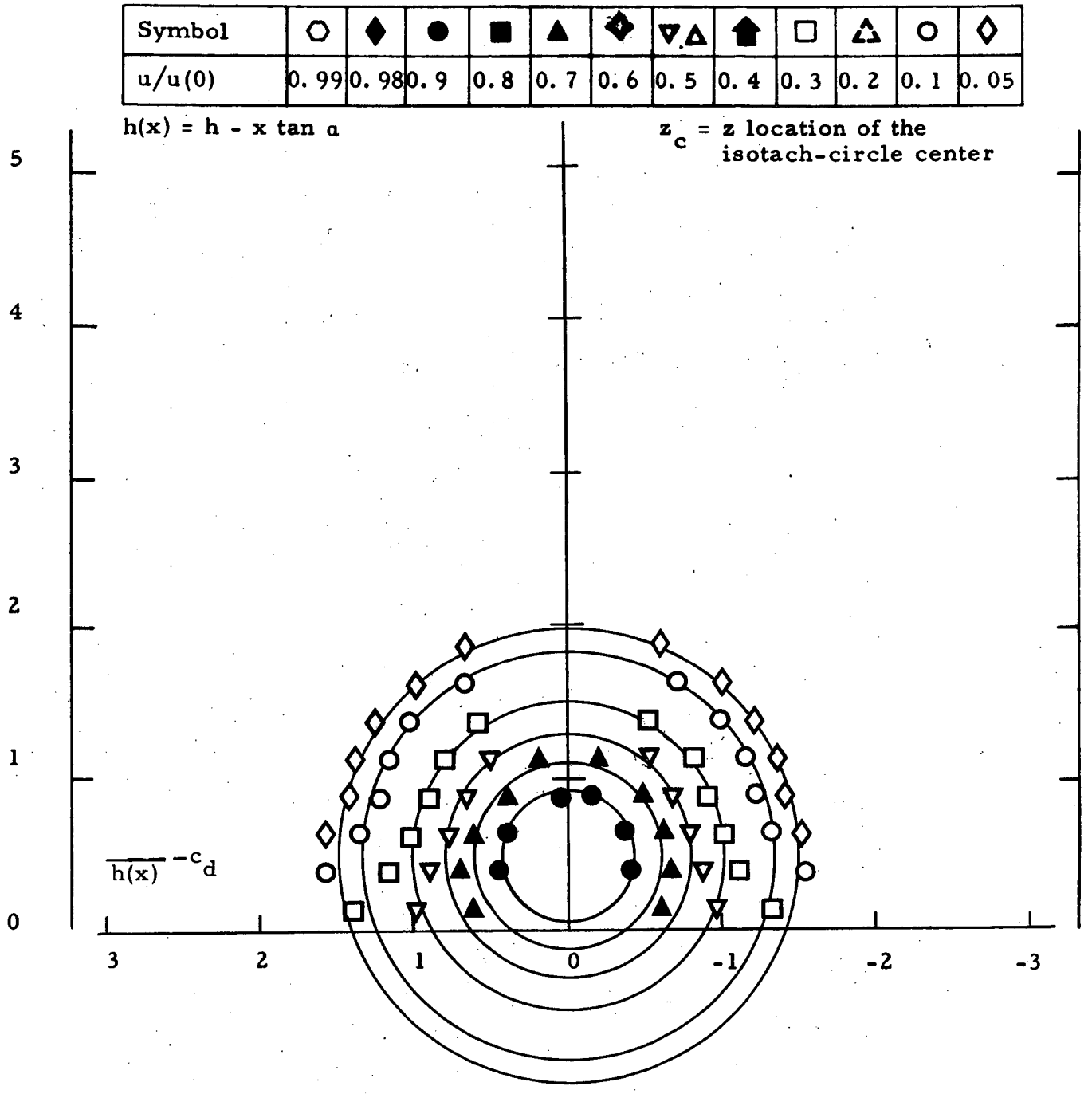
Symbol
u/u(0)
0.99
0.98
0.9
0.8
0.7
0.6
0.5
0.4
0.3
0.2
0.1
0.05
h(x) = h - x tan α
z_c = z location of the isotach-circle center
5
4
3
2
1
0
3
2
1
0
-1
-2
-3
$\frac{}{h(x)}^{-c_d}$

e) x/d = 4

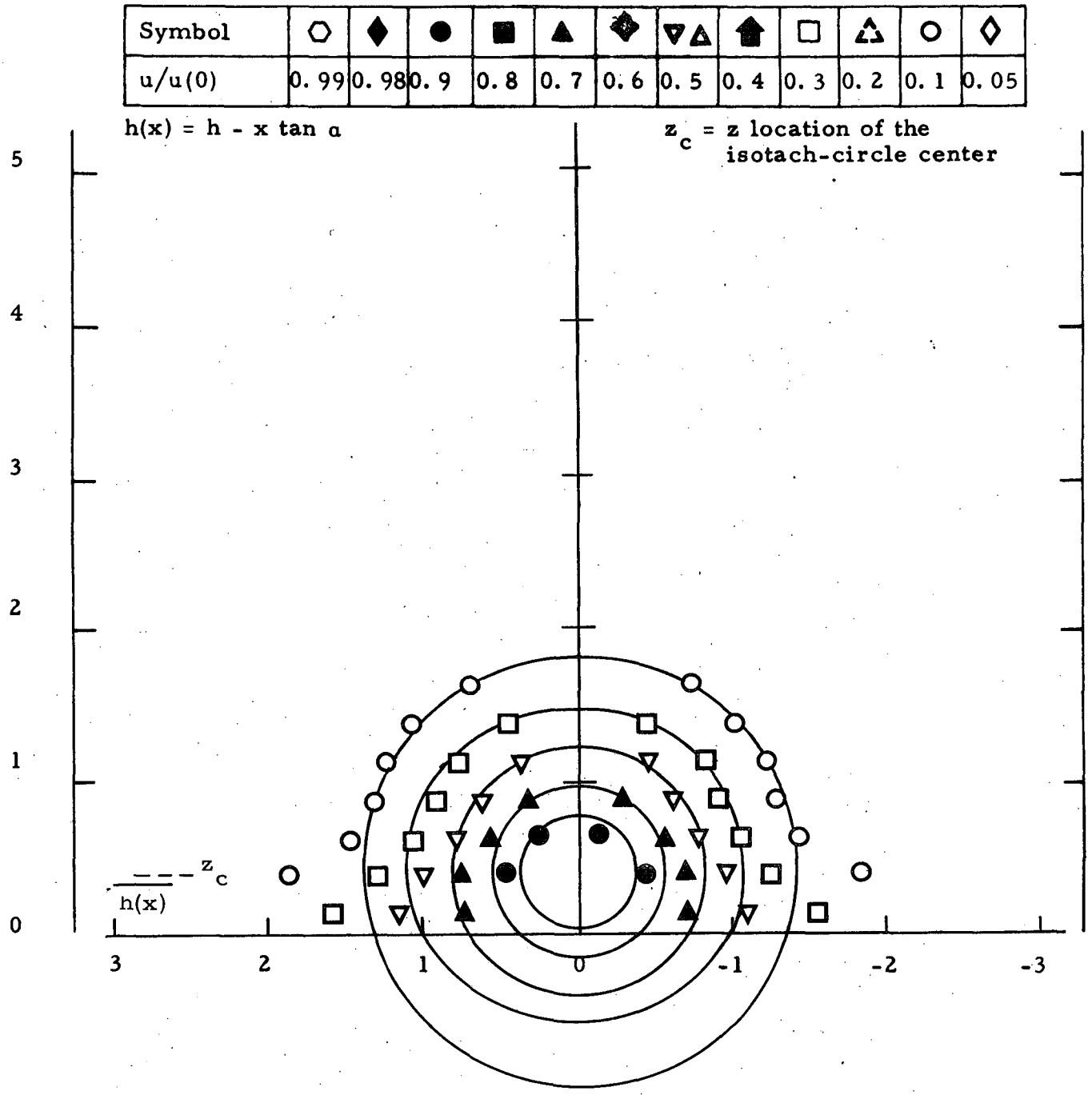
Symbol
u/u(0)
0.99
0.98
0.9
0.8
0.7
0.6
0.5
0.4
0.3
0.2
0.1
0.05
h(x) = h - x tan α
z_c = z location of the isotach-circle center
5
4
3
2
1
0
3
2
1
0
-1
-2
-3
z_c
h(x)

f) x/d = 5

3

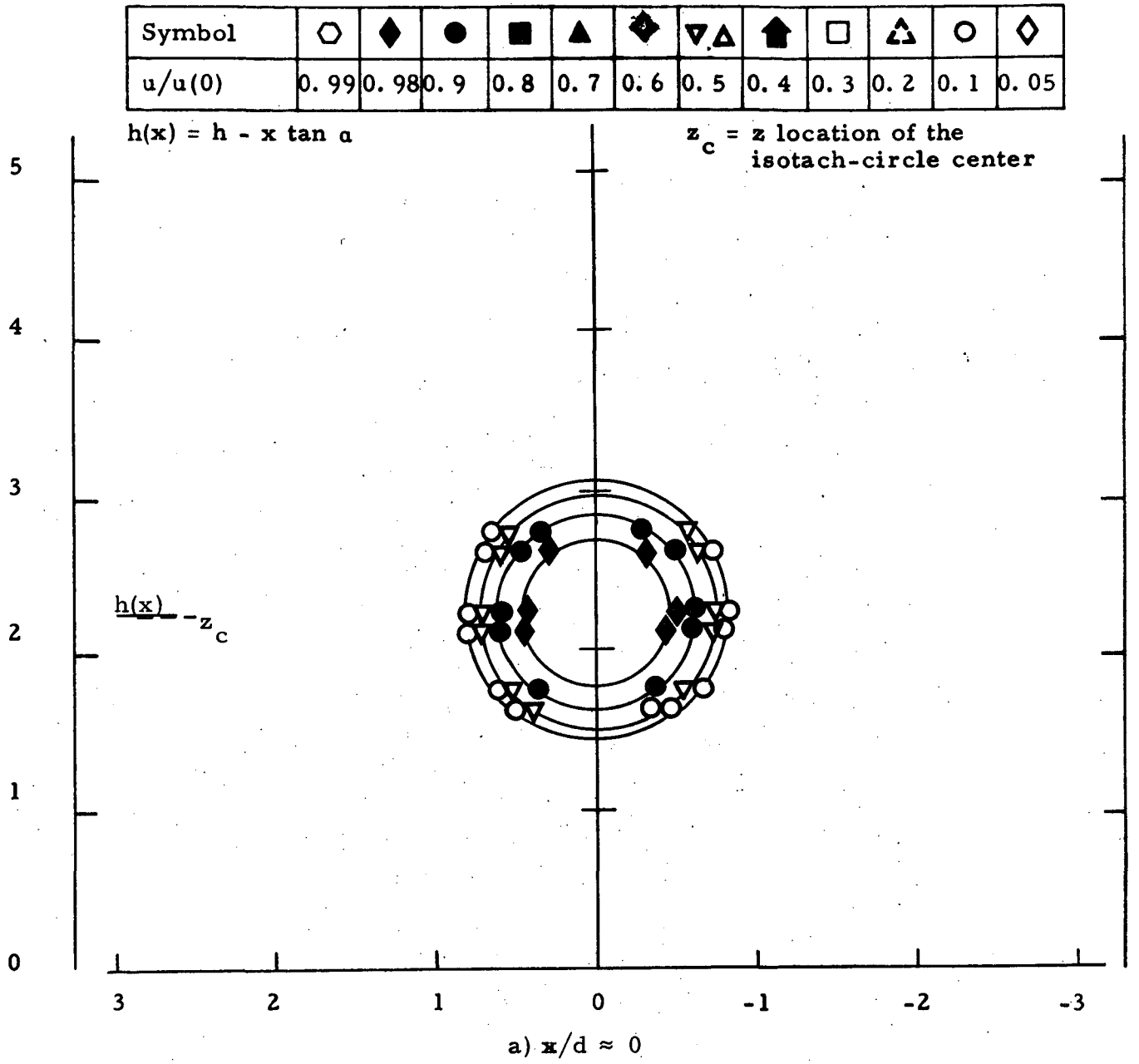

Figure 19. Isotach contours α = 6, h/d = 1.5, uniform.

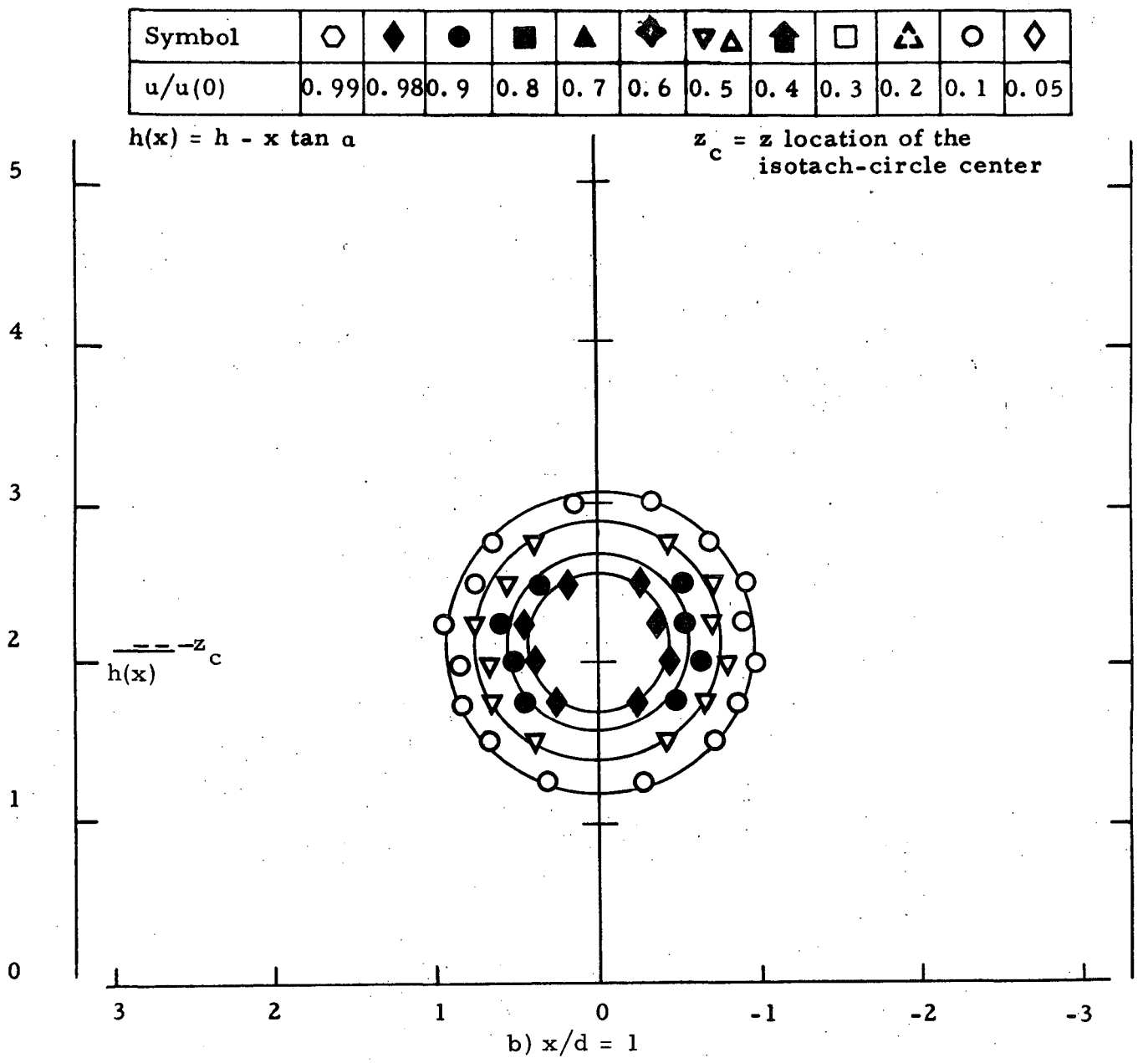
Symbol
u/u(0)
0.99
0.98
0.9
0.8
0.7
0.6
0.5
0.4
0.3
0.2
0.1
0.05
h(x) = h - x tan α
z_c = z location of the isotach-circle center
z_c
h(x)
5
4
3
2
1
0
3
2
1
0
-1
-2
-3
b) x/d = 1

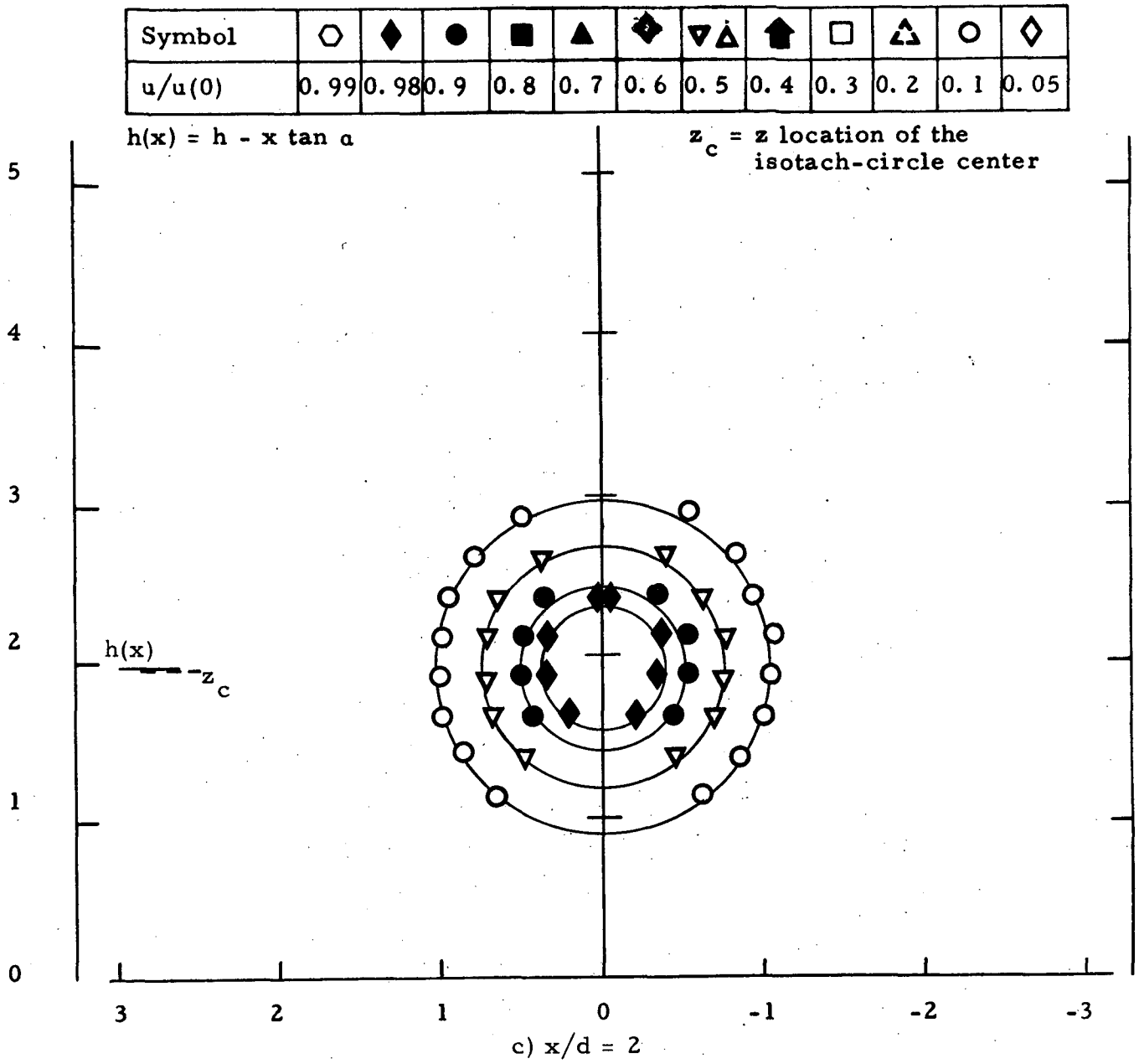
Symbol
u/u(0)
0.99
0.98
0.9
0.8
0.7
0.6
0.5
0.4
0.3
0.2
0.1
0.05
h(x) = h - x tan α
z_c = z location of the isotach-circle center
h(x)
z_c
5
4
3
2
1
0
3
2
1
0
-1
-2
-3

c) x/d = 2

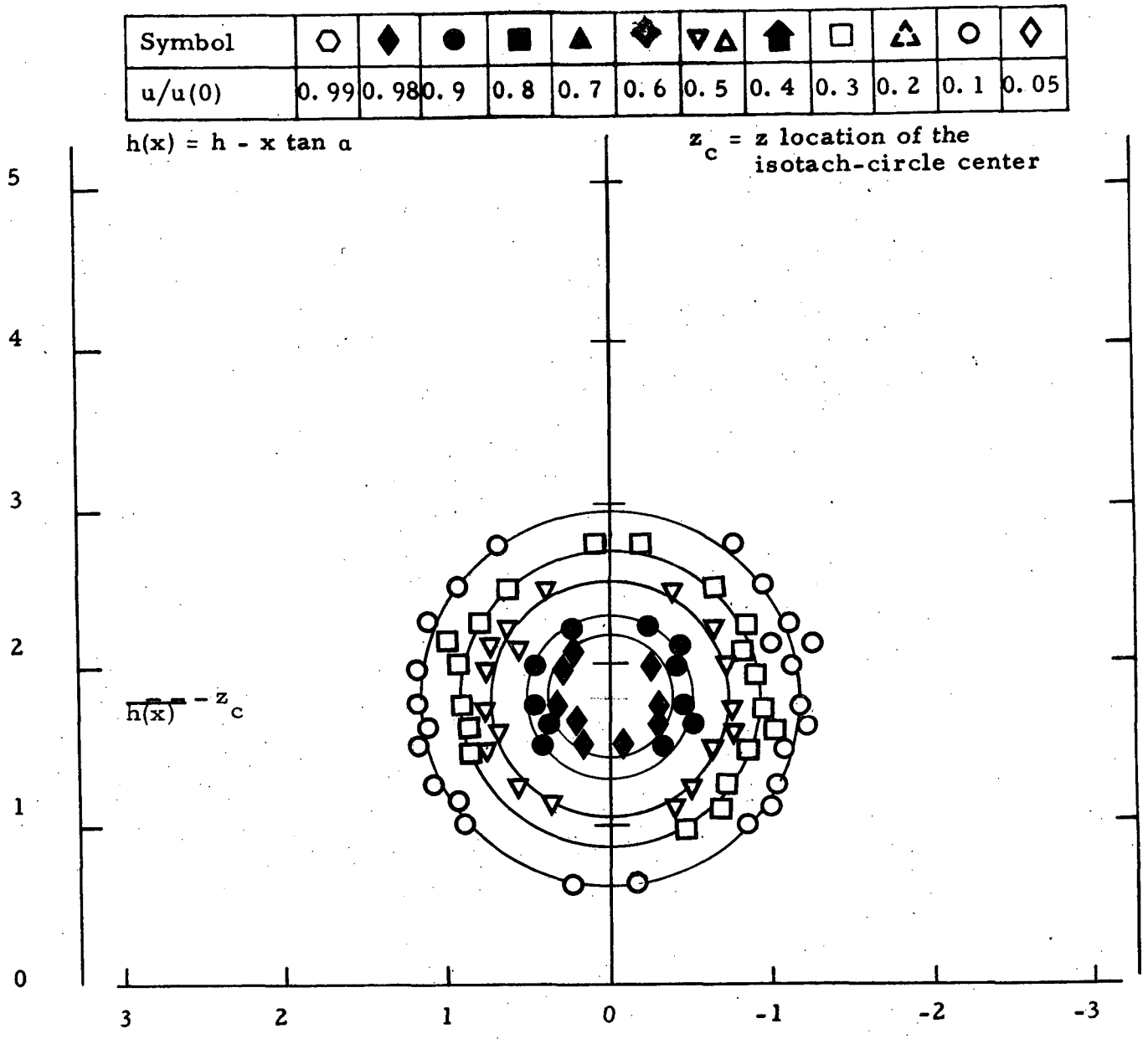
Symbol
u/u(0)
0.99
0.98
0.9
0.8
0.7
0.6
0.5
0.4
0.3
0.2
0.1
0.05
h(x) = h - x tan α
z_c = z location of the isotach-circle center
$\frac{z}{h(x)} - z_c$
5
4
3
2
1
0
3
2
1
0
-1
-2
-3

d) x/d = 3

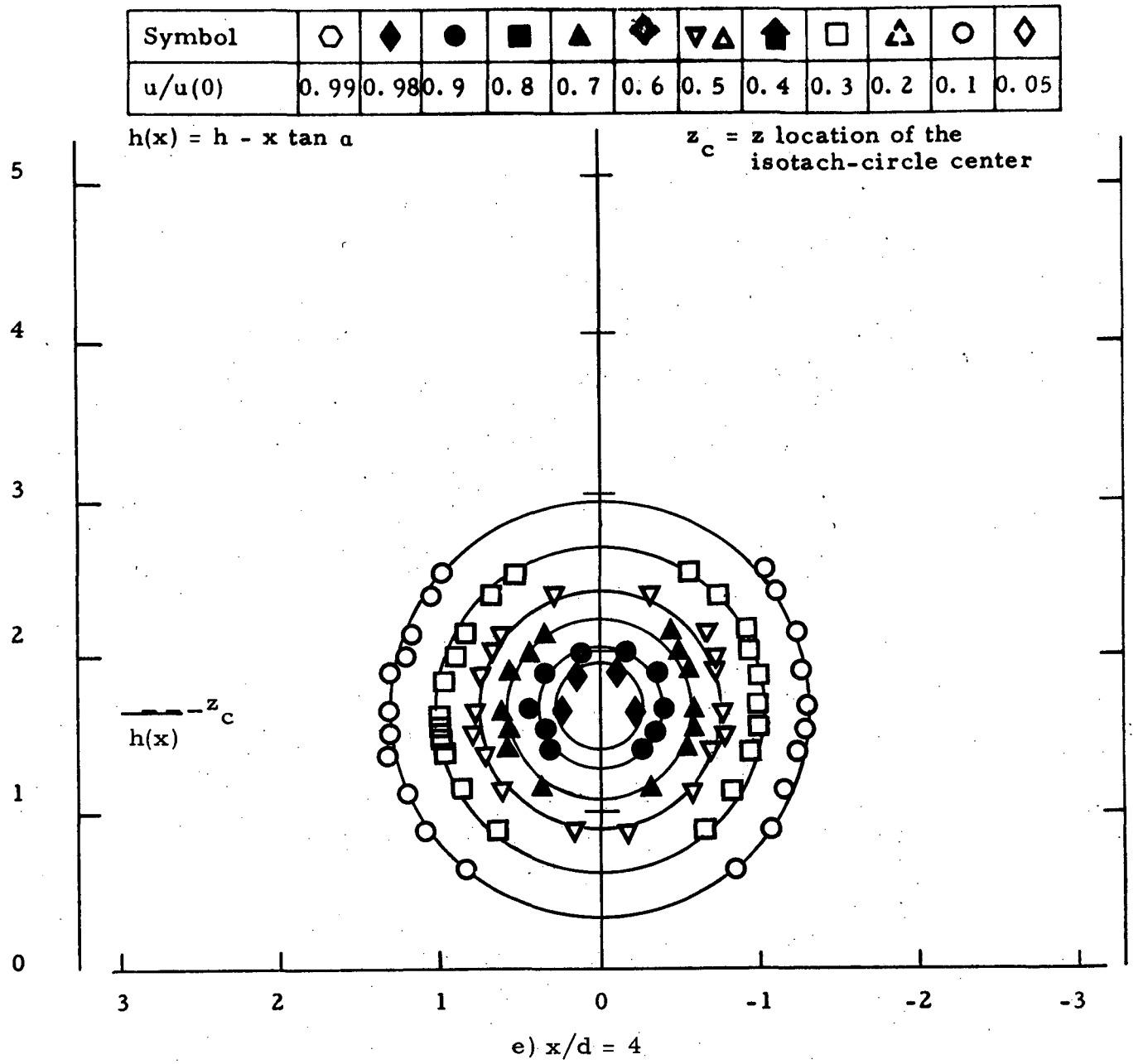
Symbol
u/u(0)
0.99
0.98
0.9
0.8
0.7
0.6
0.5
0.4
0.3
0.2
0.1
0.05
h(x) = h - x tan α
z_c = z location of the isotach-circle center
$\frac{z - z_c}{h(x)}$
5
4
3
2
1
0
3
2
1
0
-1
-2
-3

e) x/d = 4

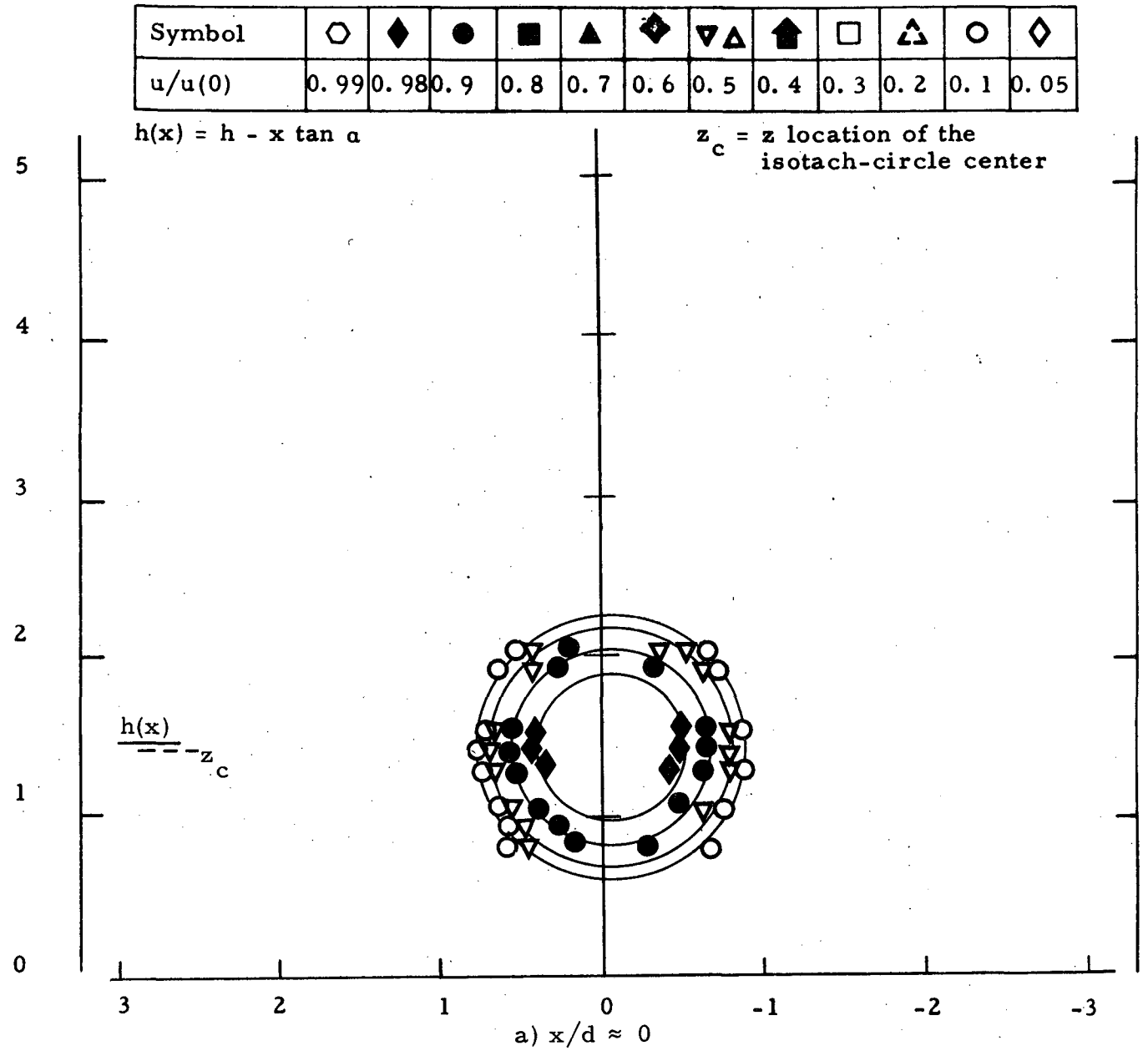

Figure 20. Isotach contours $\alpha = 9$, $h/d = 1$, uniform.

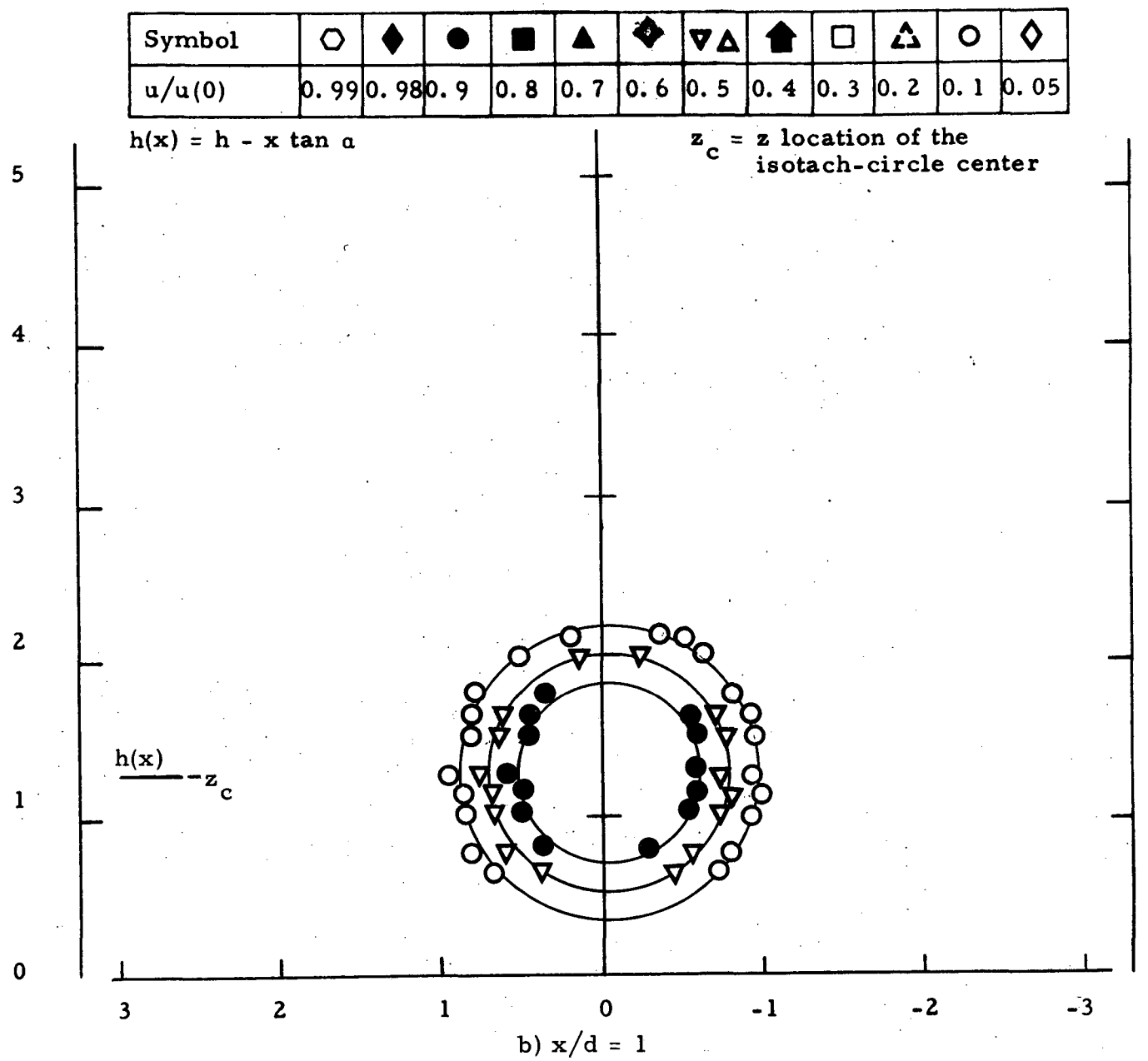
Symbol
u/u(0)
0.99
0.98
0.9
0.8
0.7
0.6
0.5
0.4
0.3
0.2
0.1
0.05
h(x) = h - x tan α
z_c = z location of the isotach-circle center
h(x)
z_c
5
4
3
2
1
0
3
2
1
0
-1
-2
-3

b) x/d = 1

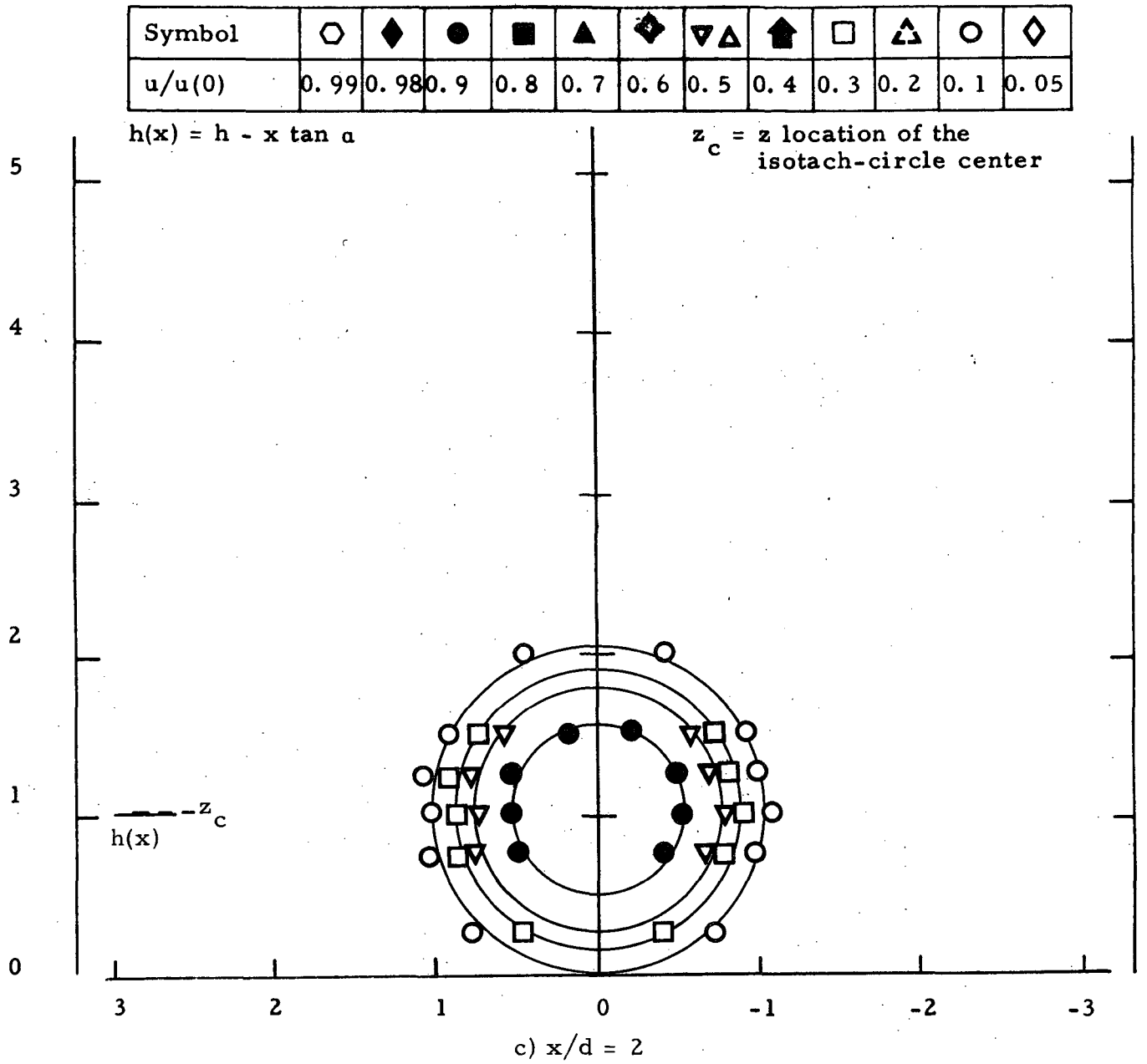
Symbol
u/u(0)
0.99
0.98
0.9
0.8
0.7
0.6
0.5
0.4
0.3
0.2
0.1
0.05
h(x) = h - x tan α
z_c = z location of the isotach-circle center
5
4
3
2
1
0
z_c
h(x)
3
2
1
0
-1
-2
-3

c) x/d = 2

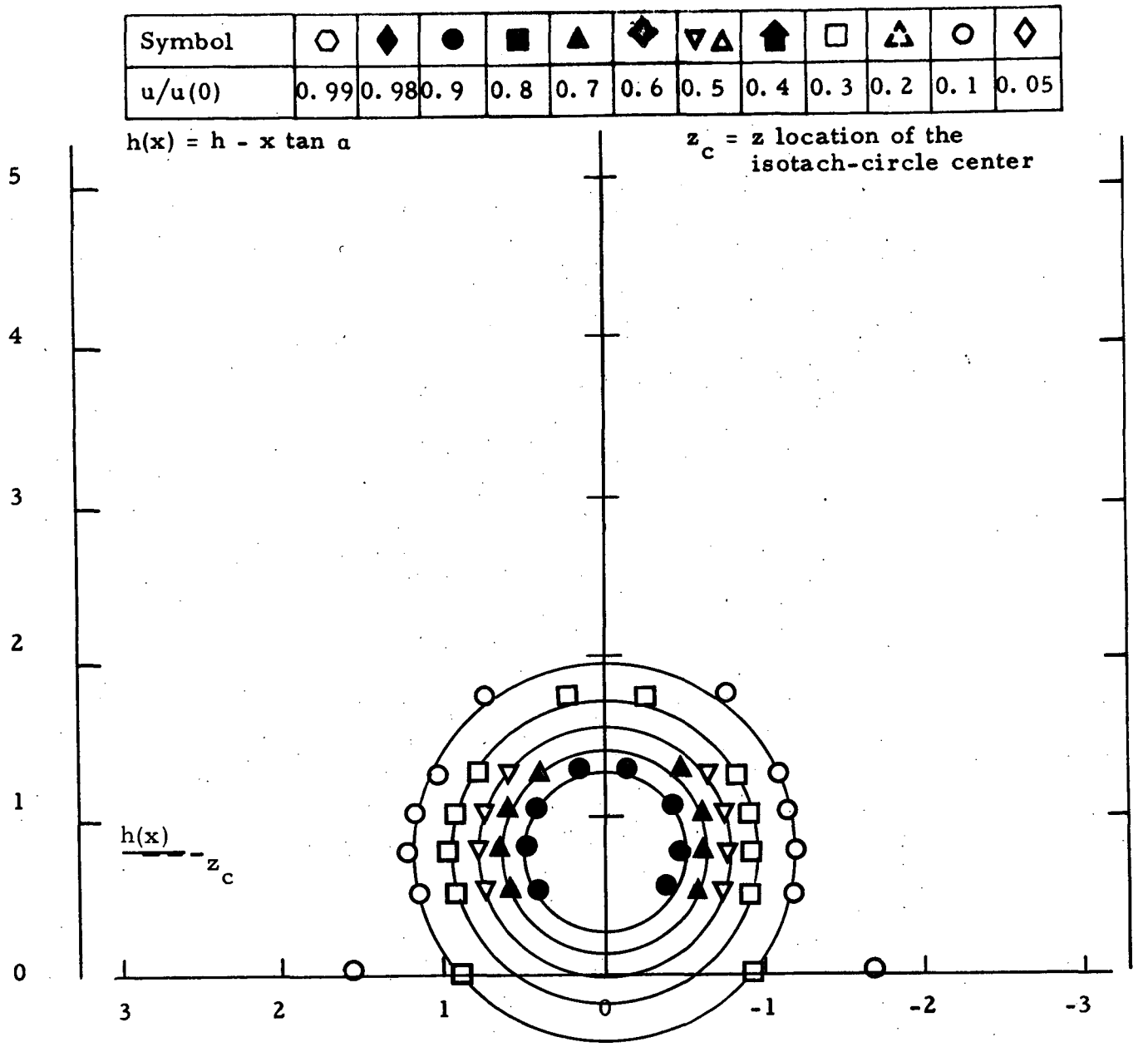
Symbol
u/u(0)
0.99
0.98
0.9
0.8
0.7
0.6
0.5
0.4
0.3
0.2
0.1
0.05
h(x) = h - x tan α
z_c = z location of the isotach-circle center
5
4
3
2
1
0
h(x)
z_c
3
2
1
0
-1
-2
-3

d) x/d = 3

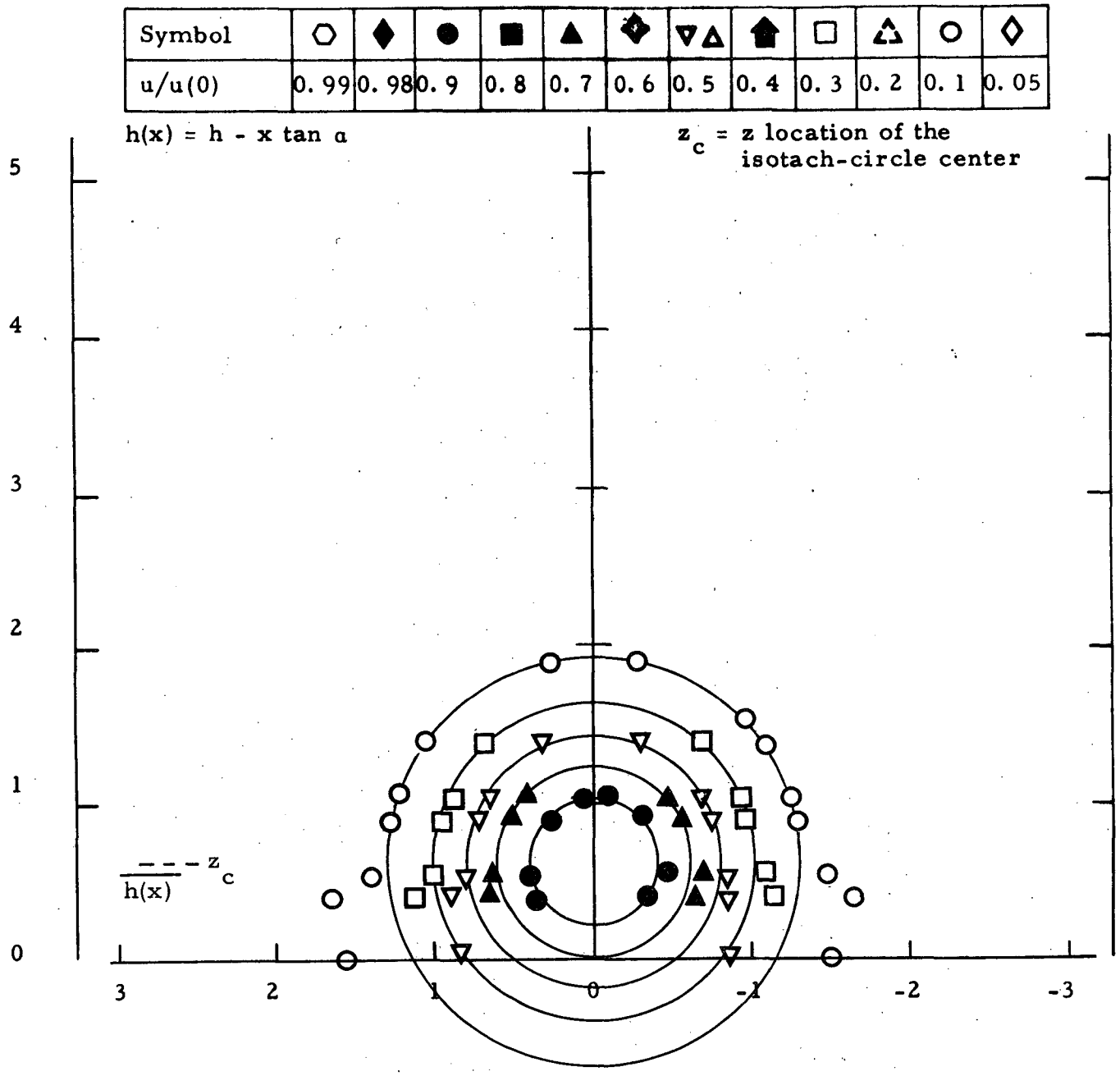
Symbol
u/u(0)
0.99
0.98
0.9
0.8
0.7
0.6
0.5
0.4
0.3
0.2
0.1
0.05
h(x) = h - x tan α
z_c = z location of the isotach-circle center
5
4
3
2
1
0
$\frac{z_c}{h(x)}$
3
2
1
0
-1
-2
-3

e) x/d = 4

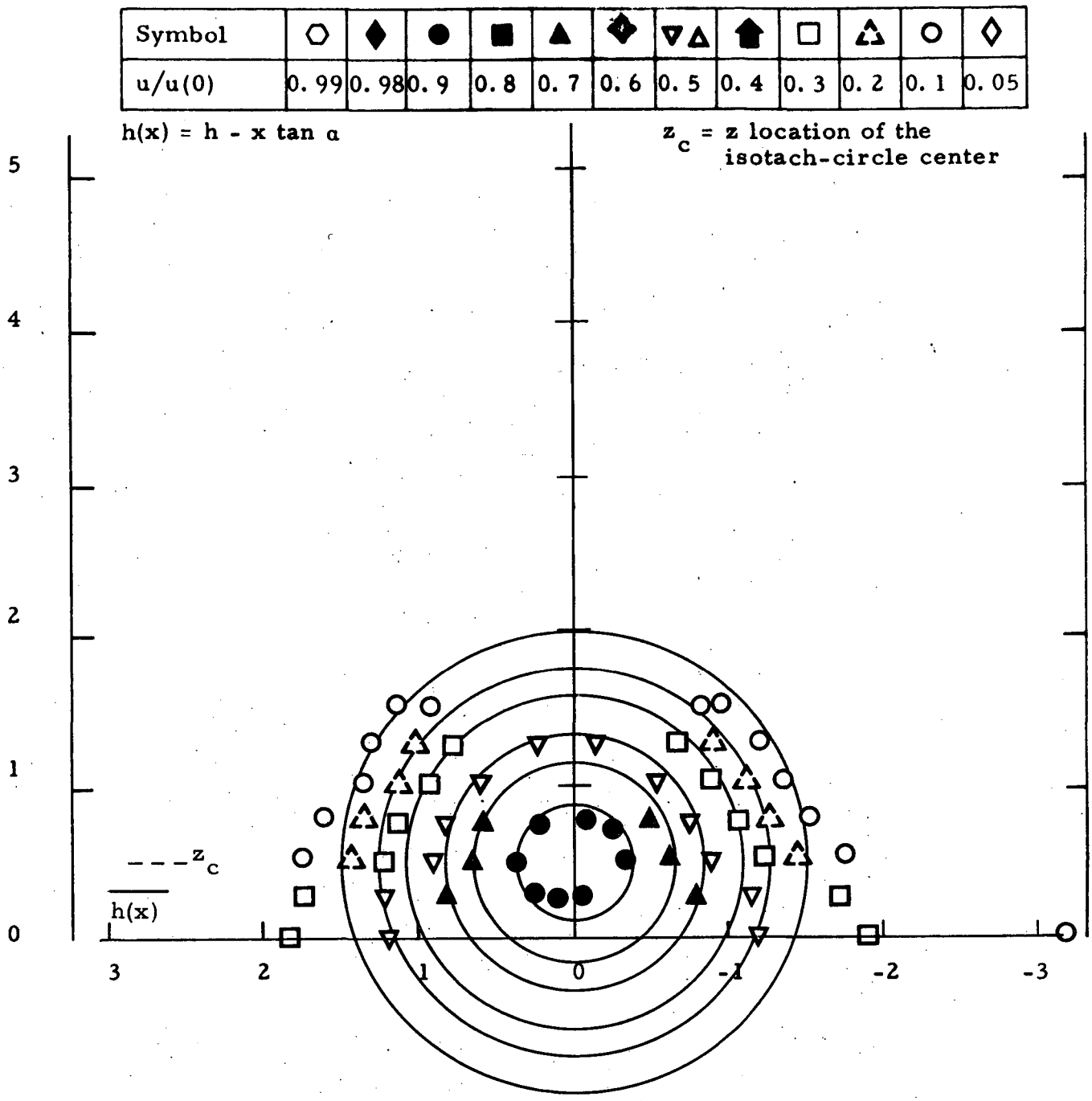
Symbol
u/u(0)
0.99
0.98
0.9
0.8
0.7
0.6
0.5
0.4
0.3
0.2
0.1
0.05
h(x) = h - x tan α
z_c = z location of the isotach-circle center
5
4
3
2
1
0
---z_c
h(x)
3
2
1
0
-1
-2
-3

f) x/d = 5

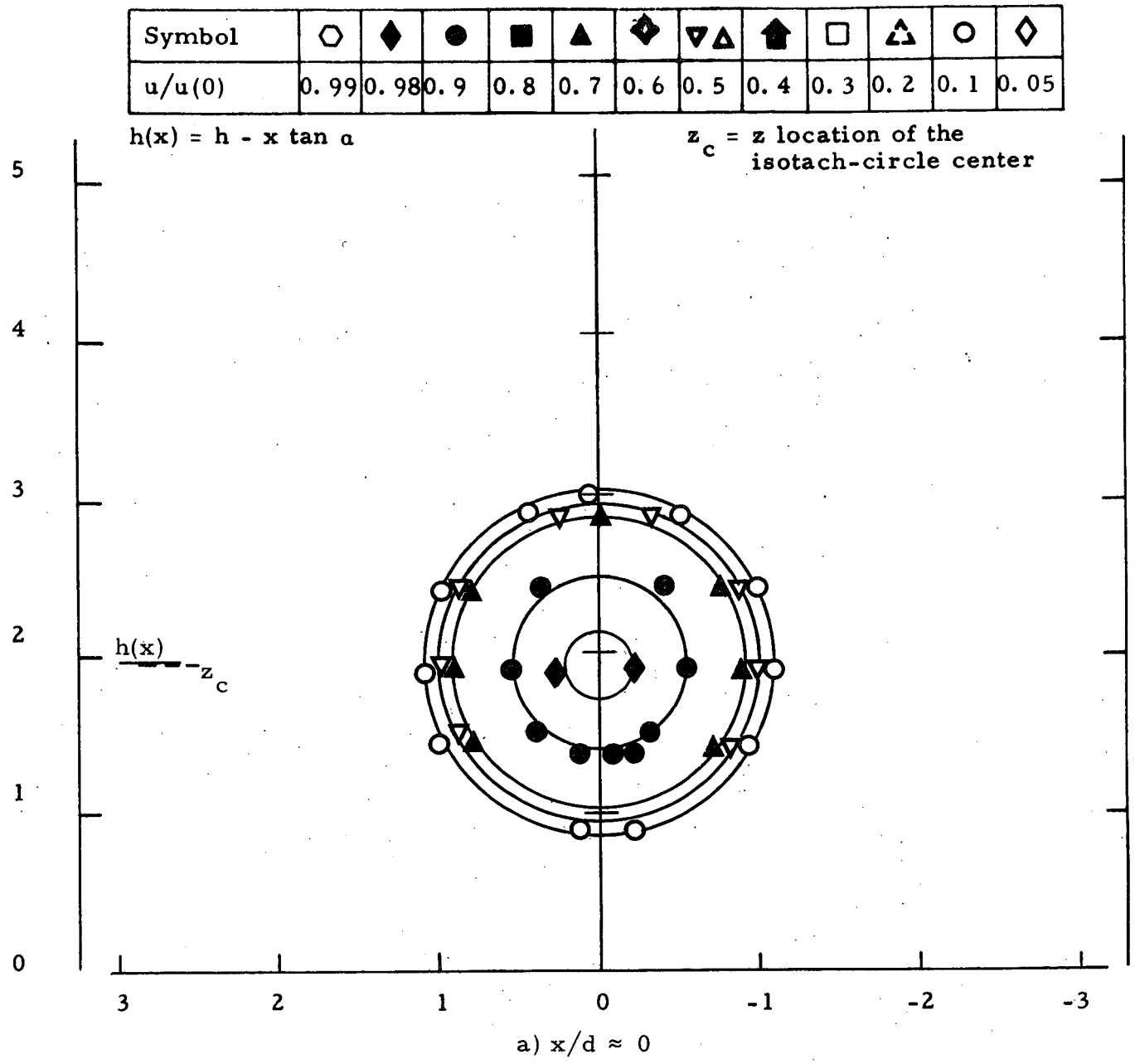

Figure 21. Isotach contours α = 9, h/d = 1, fully developed.

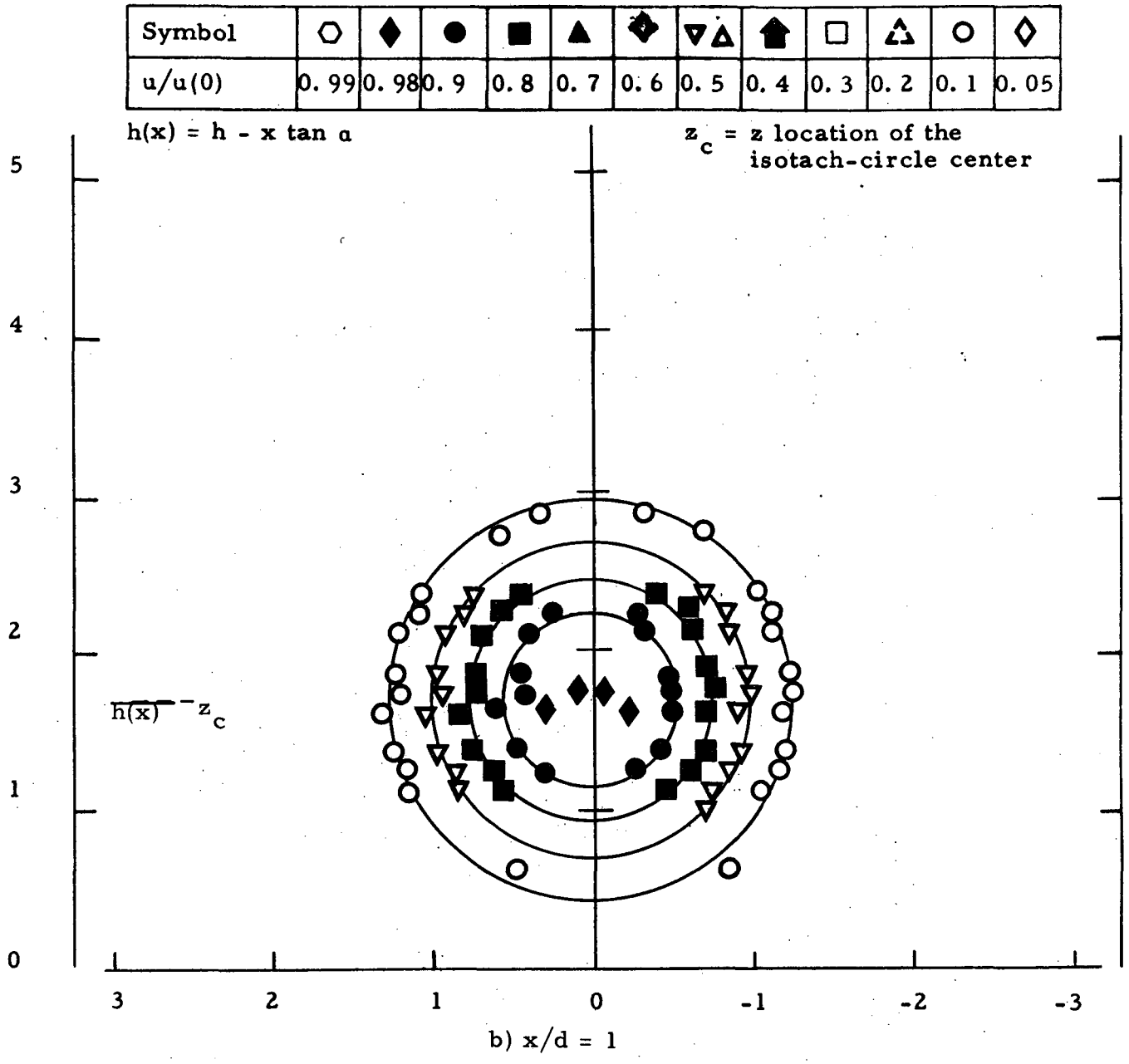
Symbol
u/u(0)
0.99
0.98
0.9
0.8
0.7
0.6
0.5
0.4
0.3
0.2
0.1
0.05
h(x) = h - x tan α
z_c = z location of the isotach-circle center
$\overline{h(x)} - z_c$
5
4
3
2
1
0
3
2
1
0
-1
-2
-3

b) x/d = 1

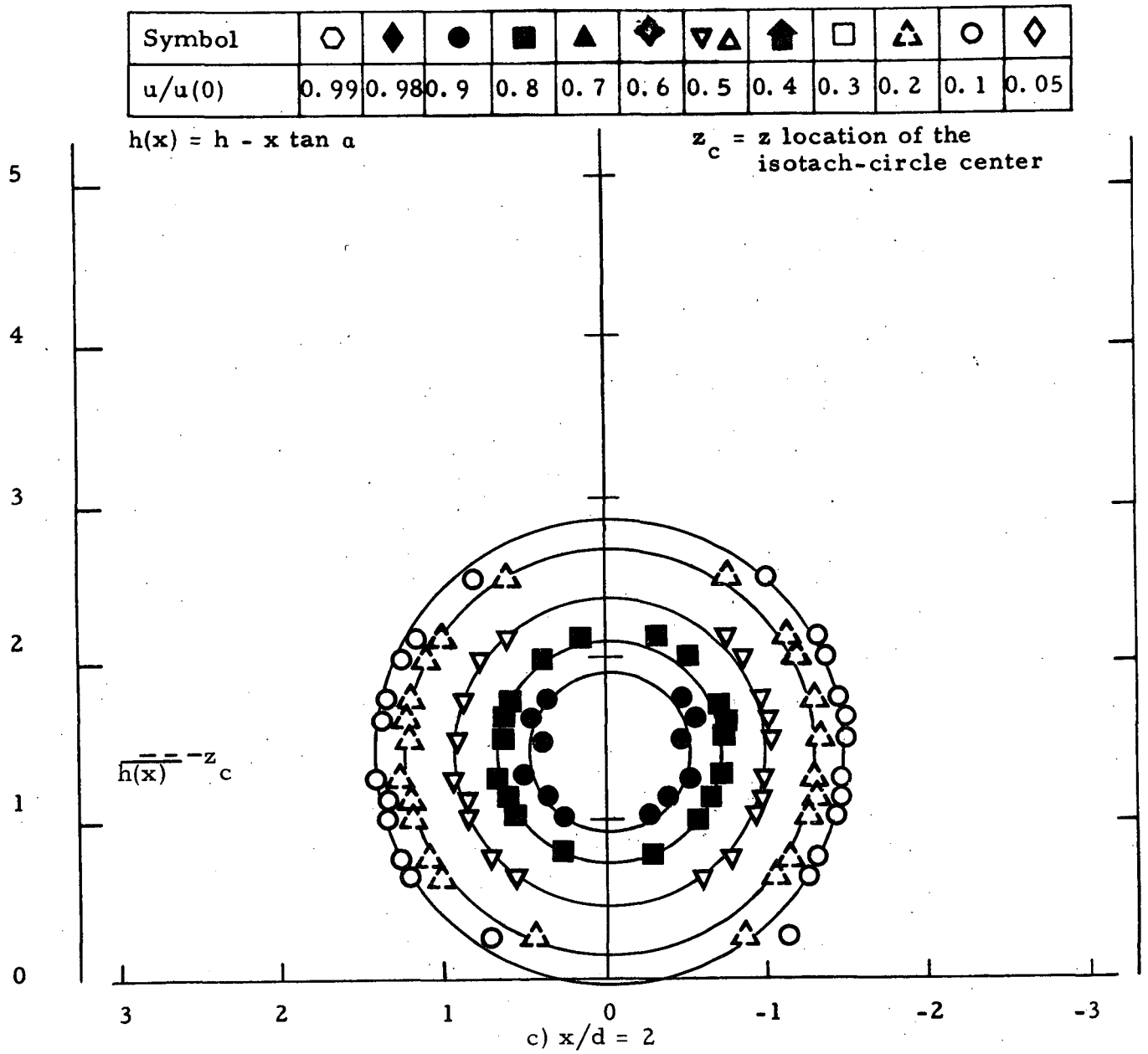
Symbol
u/u(0)
0.99
0.98
0.9
0.8
0.7
0.6
0.5
0.4
0.3
0.2
0.1
0.05
h(x) = h - x tan α
z_c = z location of the isotach-circle center
$\frac{z}{h(x)} - z_c$
5
4
3
2
1
0
3
2
1
0
-1
-2
-3

c) x/d = 2

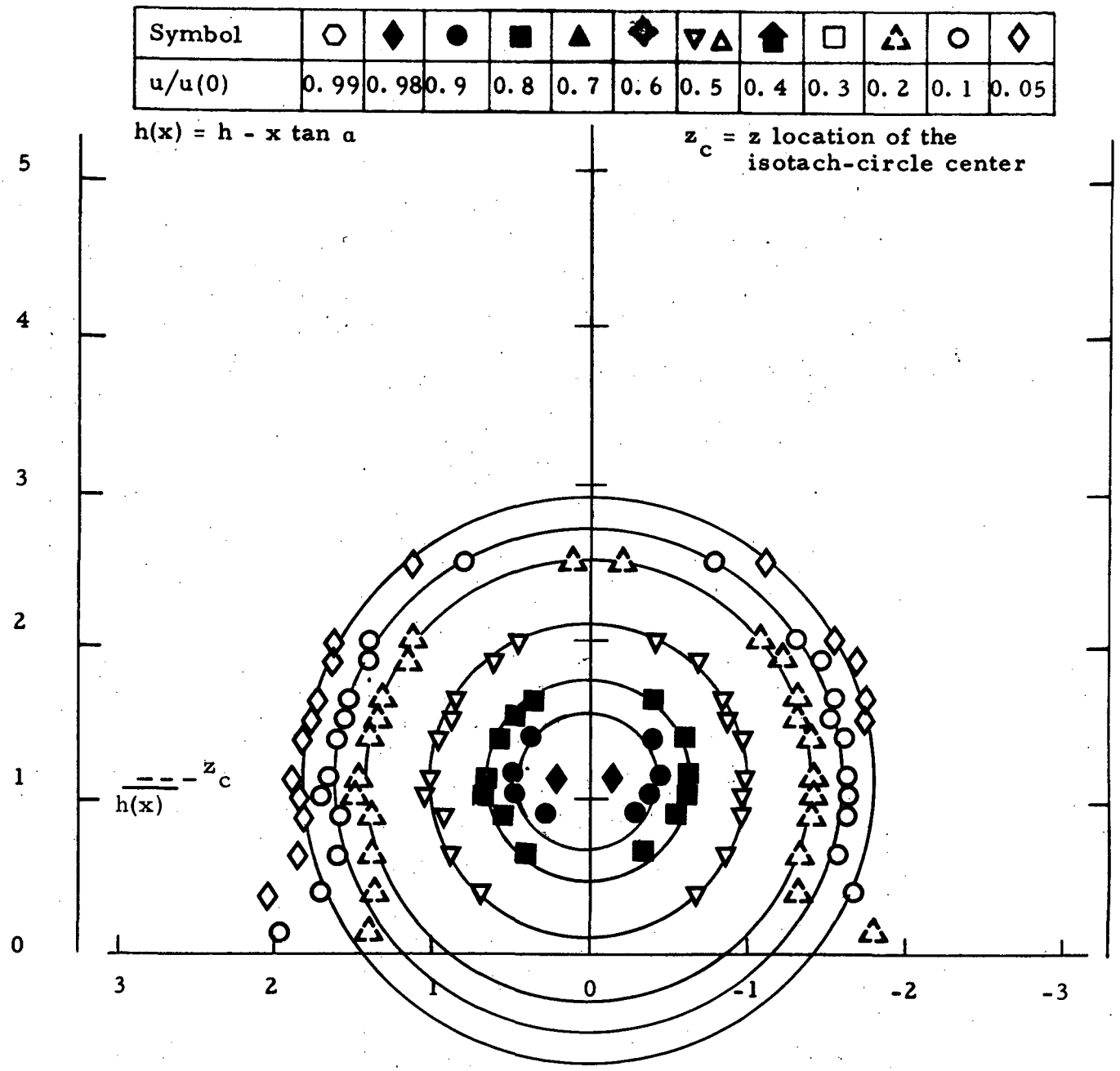
Symbol
u/u(0)
0.99
0.98
0.9
0.8
0.7
0.6
0.5
0.4
0.3
0.2
0.1
0.05
h(x) = h - x tan α
z_c = z location of the isotach-circle center
5
4
3
2
1
0
z_c / h(x)
3
2
1
0
-1
-2
-3

d) x/d = 3

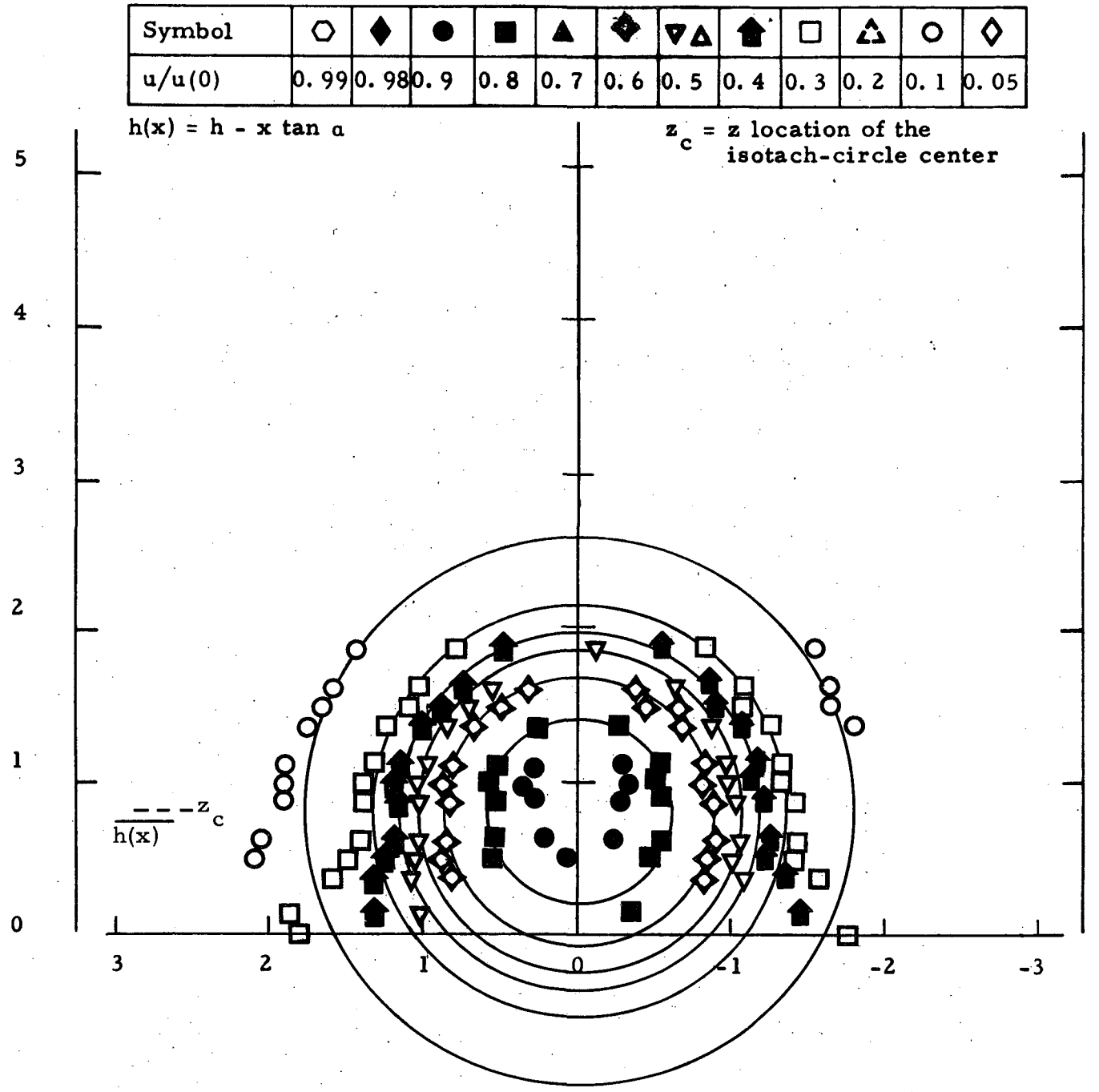
Symbol
u/u(0)
0.99
0.98
0.9
0.8
0.7
0.6
0.5
0.4
0.3
0.2
0.1
0.05
h(x) = h - x tan α
z_c = z location of the isotach-circle center
5
4
3
2
1
0
3
2
1
0
-1
-2
-3
z_c / h(x)

e) x/d = 4

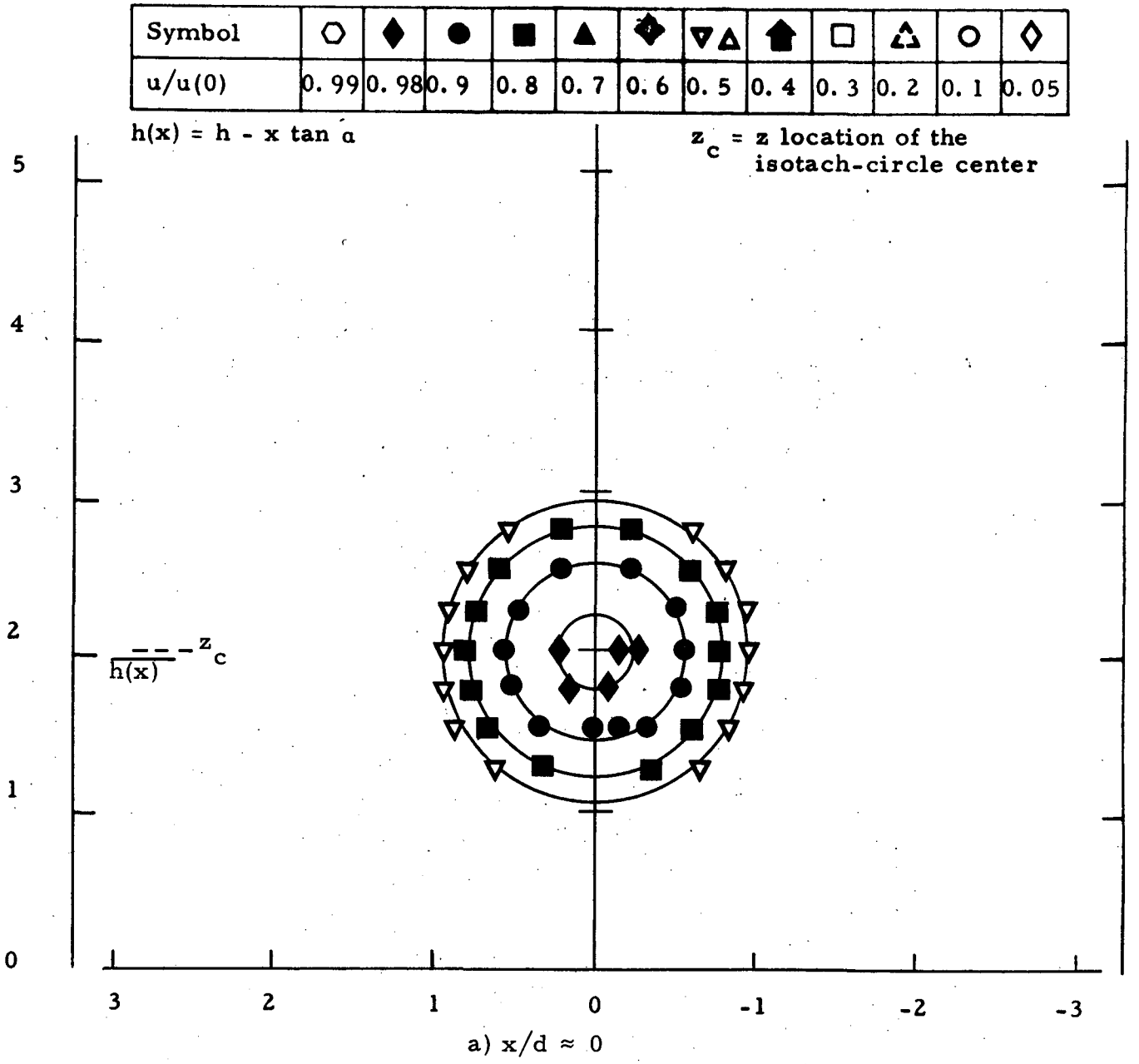

Figure 22. Isotach contours α = 12, h/d = 1, fully developed.

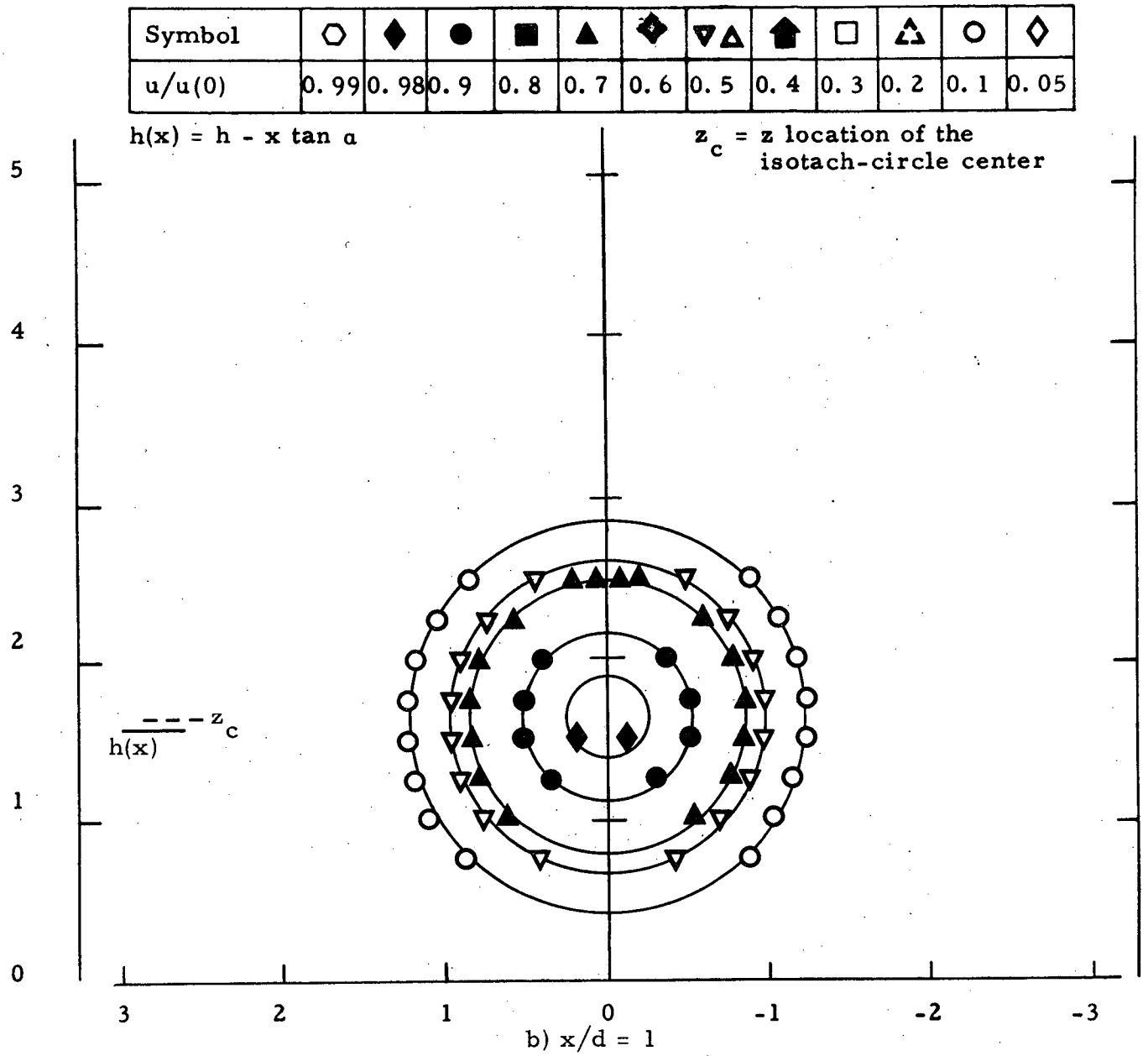
Symbol
u/u(0)
0.99
0.98
0.9
0.8
0.7
0.6
0.5
0.4
0.3
0.2
0.1
0.05
h(x) = h - x tan α
z_c = z location of the isotach-circle center
$\frac{z_c}{h(x)}$
5
4
3
2
1
0
3
2
1
0
-1
-2
-3
b) x/d = 1

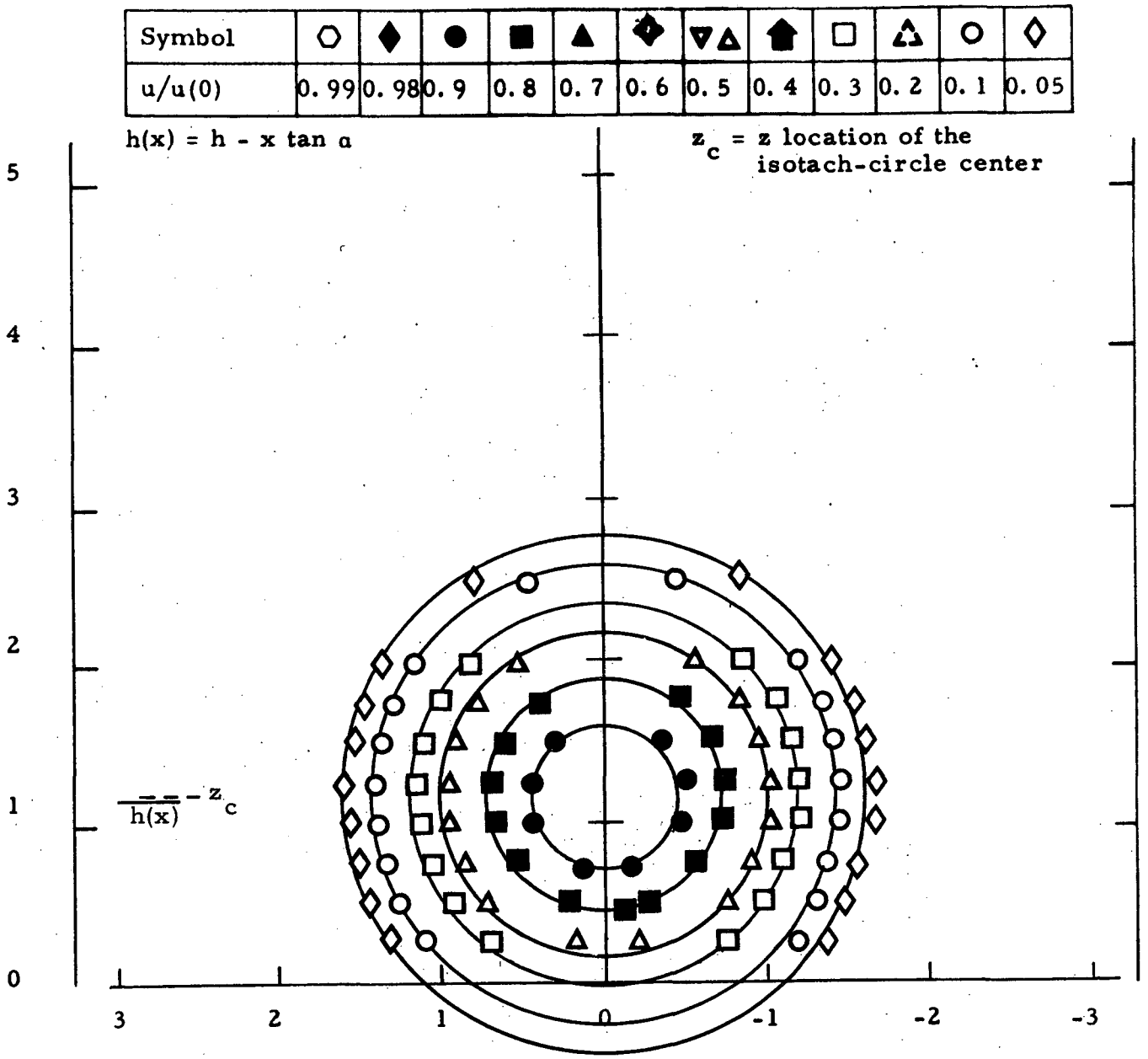
Symbol
u/u(0)
0.99
0.98
0.9
0.8
0.7
0.6
0.5
0.4
0.3
0.2
0.1
0.05
h(x) = h - x tan α
z_c = z location of the isotach-circle center
5
4
3
2
1
0
(z - z_c)/h(x)
3
2
1
0
-1
-2
-3

c) x/d = 2

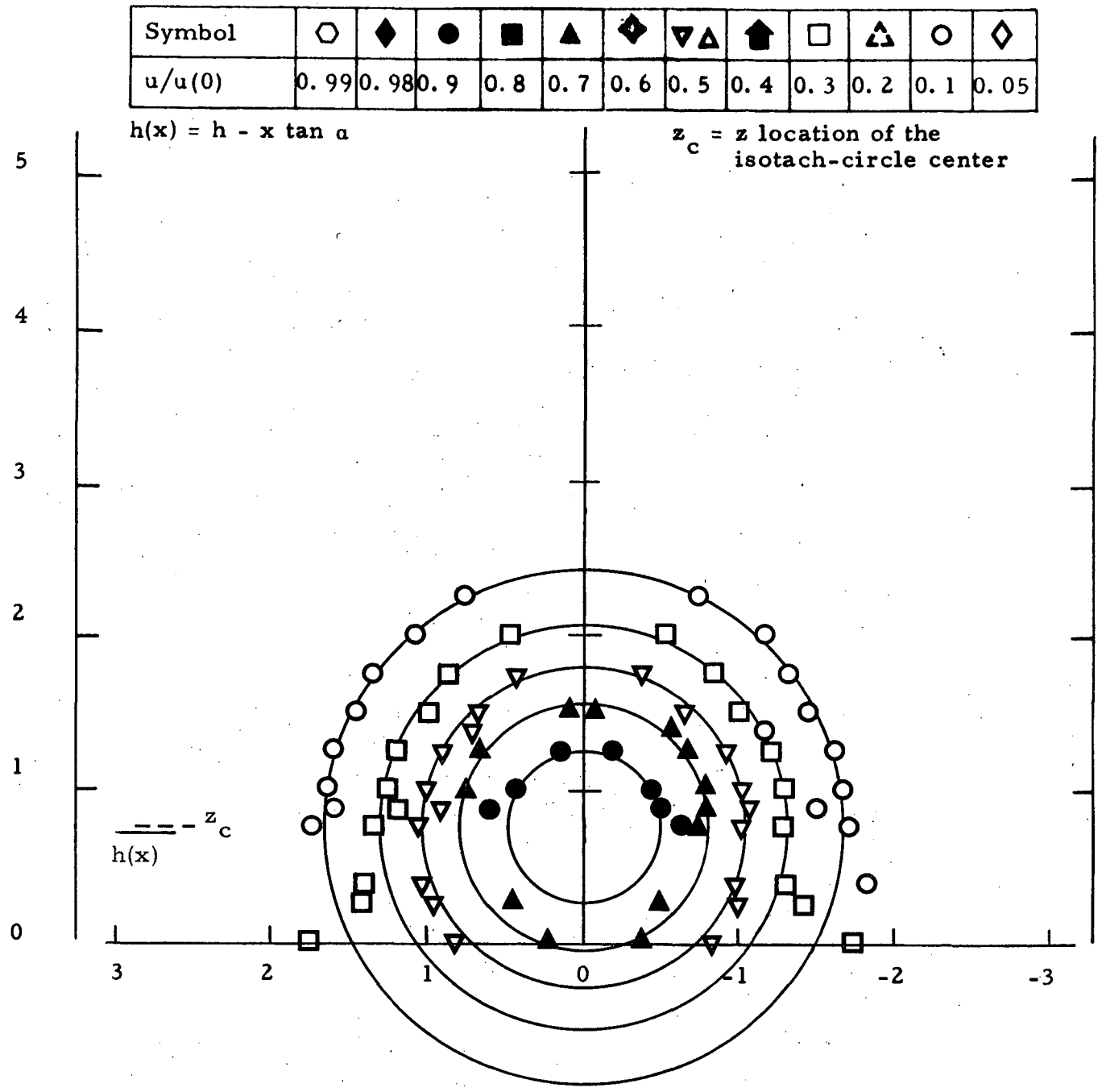
Symbol
u/u(0)
0.99
0.98
0.9
0.8
0.7
0.6
0.5
0.4
0.3
0.2
0.1
0.05
h(x) = h - x tan α
z_c = z location of the isotach-circle center
5
4
3
2
1
0
z_c
h(x)
3
2
1
0
-1
-2
-3

d) x/d = 3

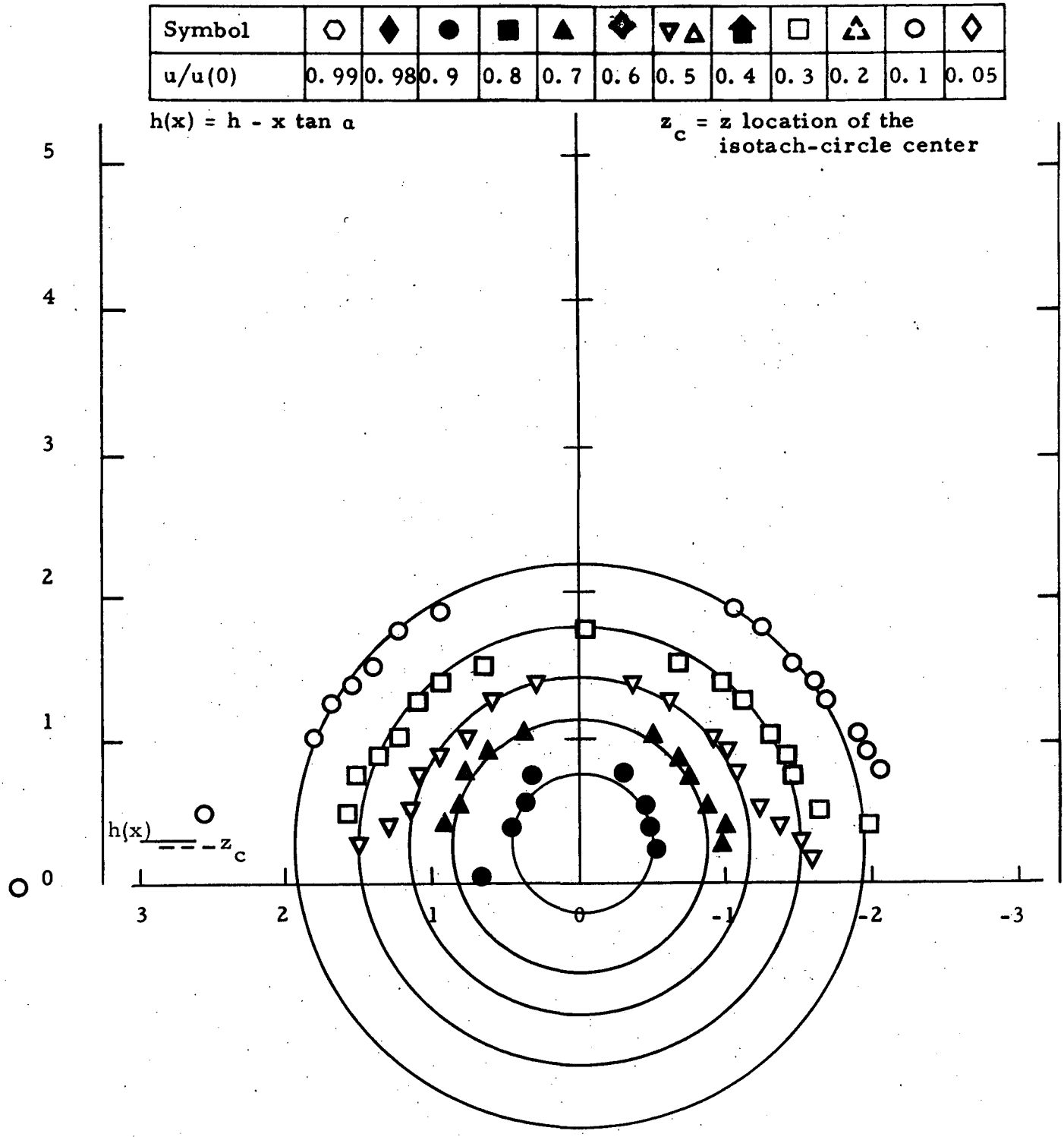
Symbol
u/u(0)
0.99
0.98
0.9
0.8
0.7
0.6
0.5
0.4
0.3
0.2
0.1
0.05
h(x) = h - x tan α
z_c = z location of the isotach-circle center
5
4
3
2
1
0
h(x)
z_c
3
2
1
0
-1
-2
-3

e) x/d = 4

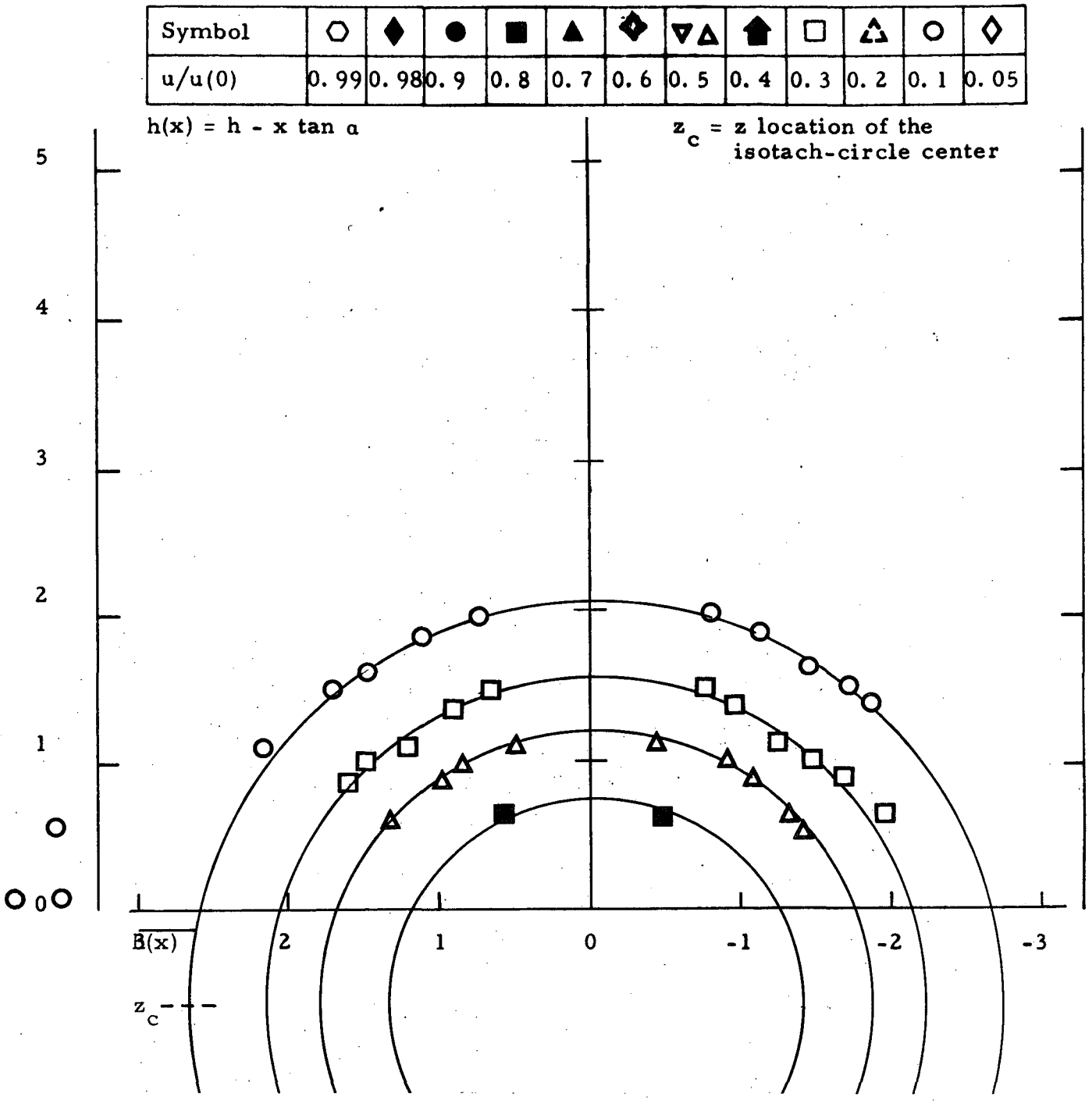
Symbol
u/u(0)
0.99
0.98
0.9
0.8
0.7
0.6
0.5
0.4
0.3
0.2
0.1
0.05
h(x) = h - x tan α
z_c = z location of the isotach-circle center
5
4
3
2
1
0
B(x)
2
1
0
-1
-2
-3
z_c

f) x/d = 5

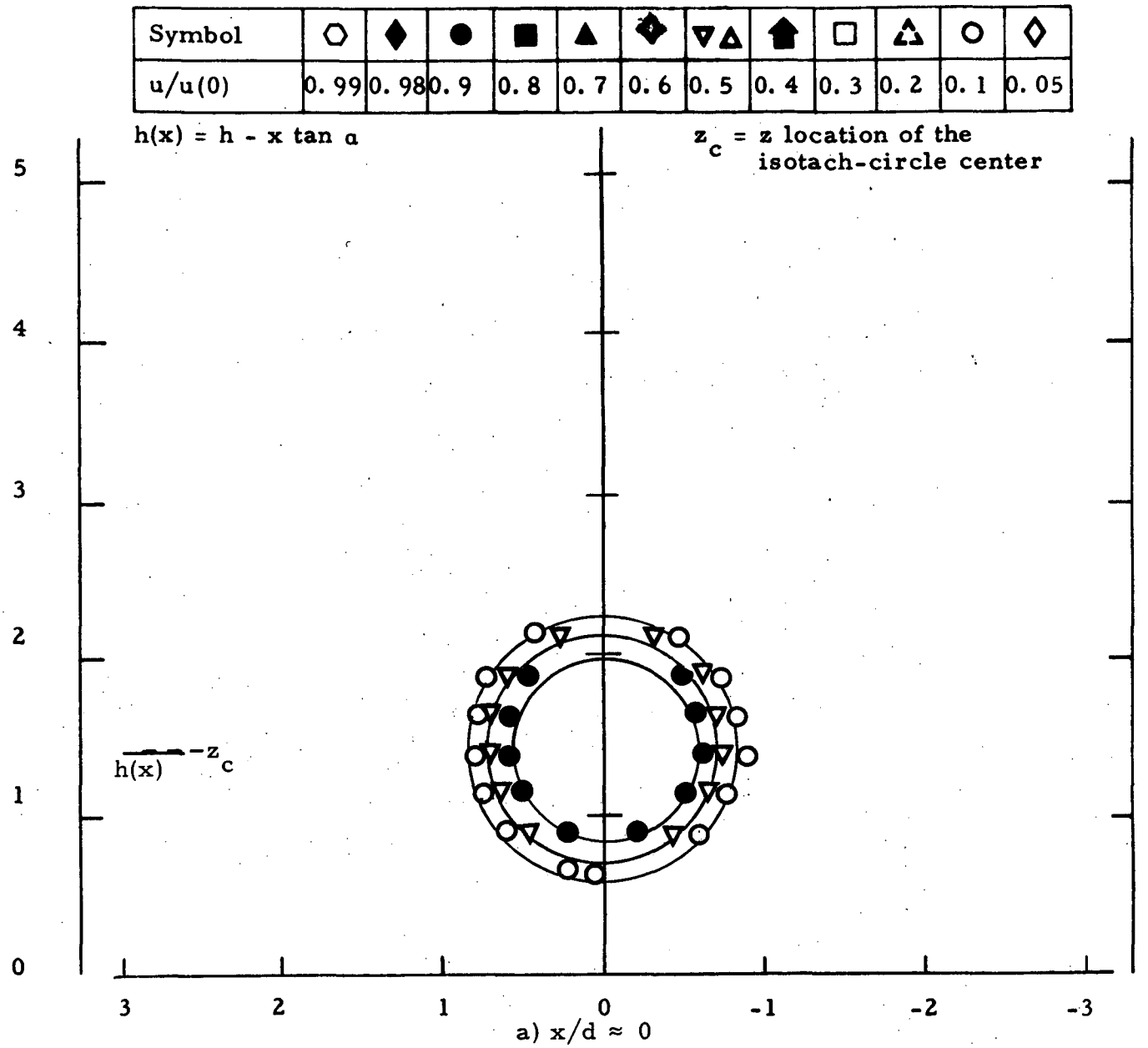

Figure 23. Isotach contours α = 15, h/d = 1, uniform.

Symbol	⬡	♦	●	■	▲	◆	▽△	⬟	□	△	○	◇
u/u(0)	0.99	0.98	0.9	0.8	0.7	0.6	0.5	0.4	0.3	0.2	0.1	0.05

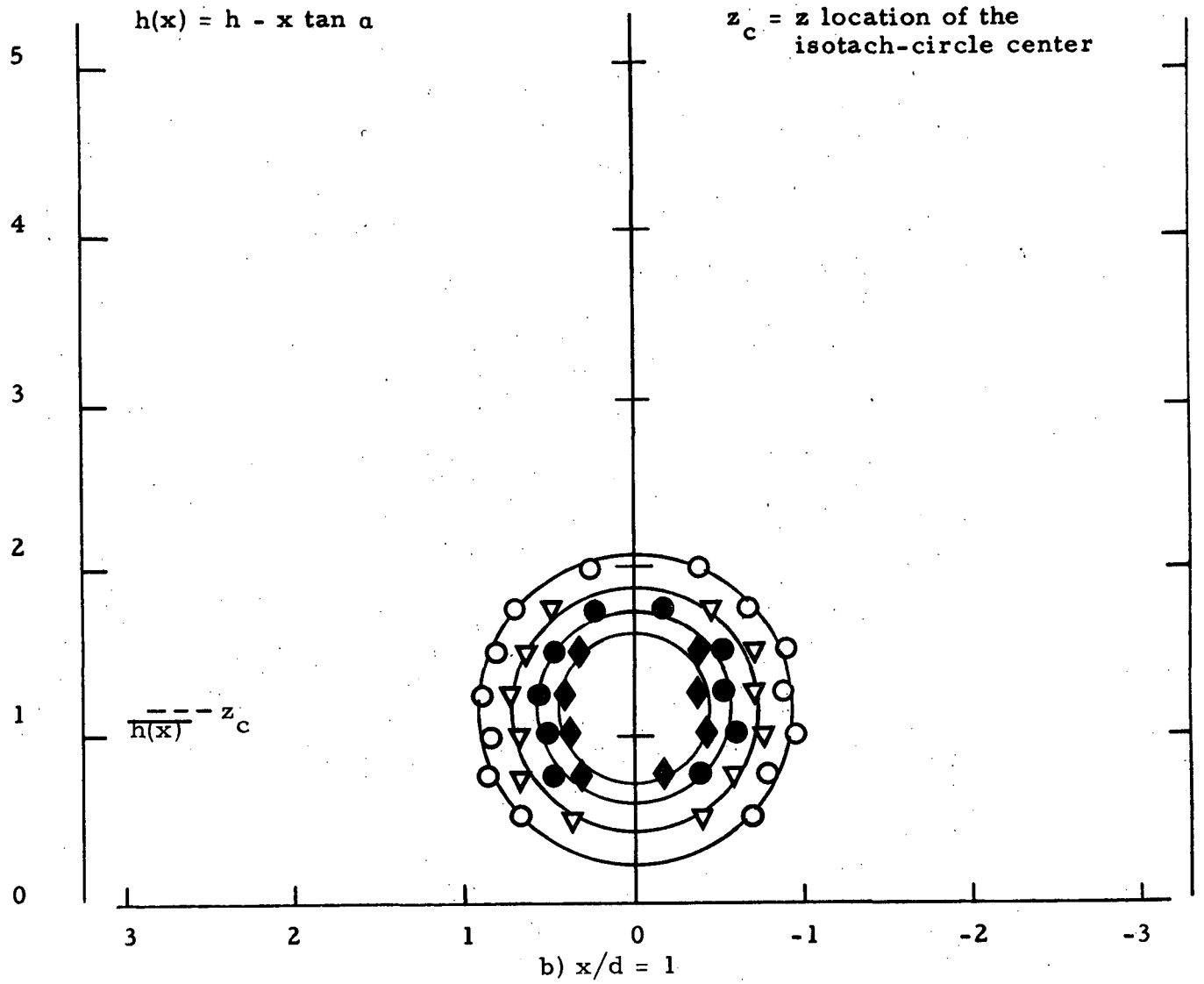

b) x/d = 1

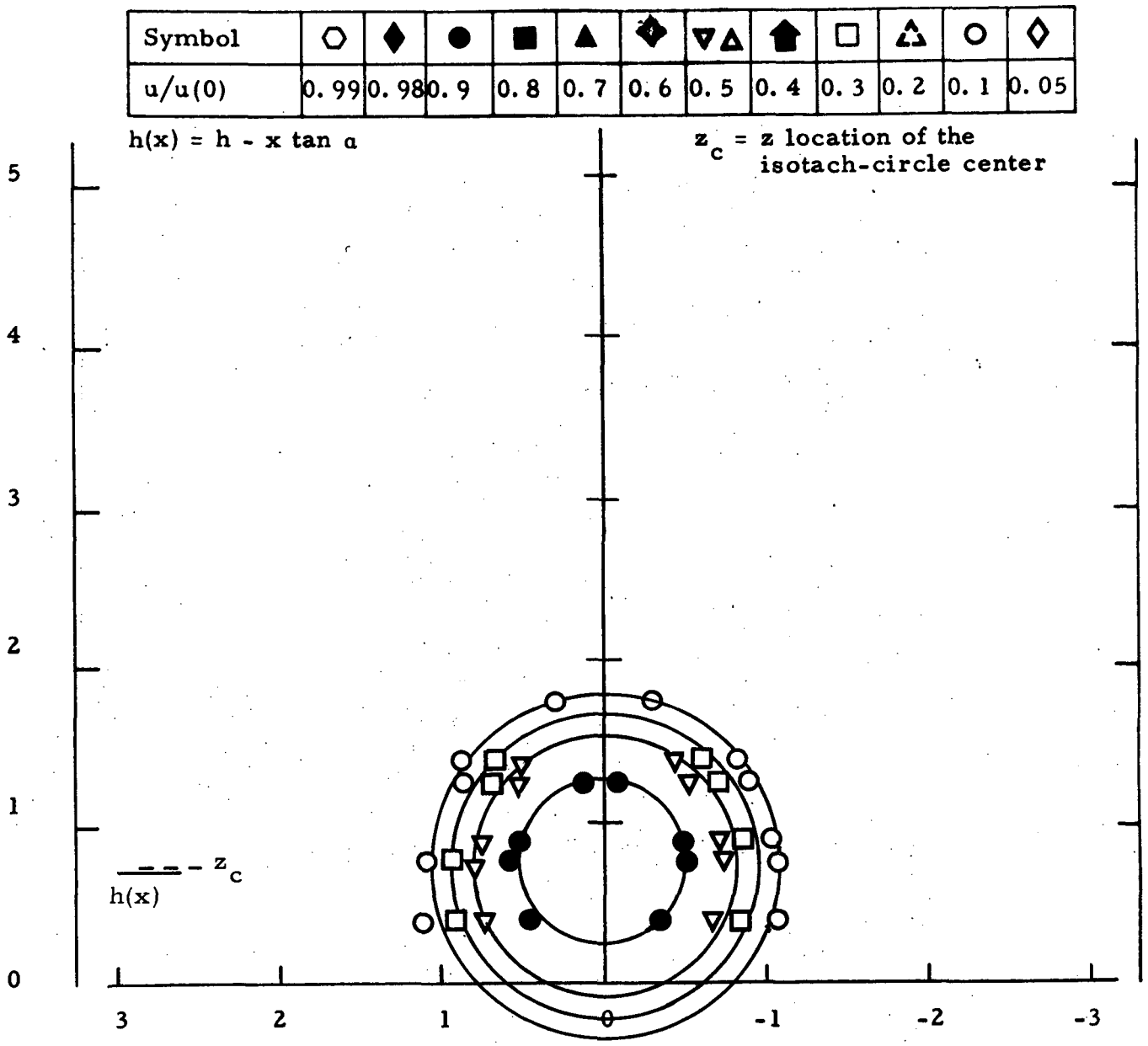
Symbol
u/u(0)
0.99
0.98
0.9
0.8
0.7
0.6
0.5
0.4
0.3
0.2
0.1
0.05
h(x) = h - x tan α
z_c = z location of the isotach-circle center
5
4
3
2
1
0
z_c
h(x)
3
2
1
0
-1
-2
-3

c) x/d = 2

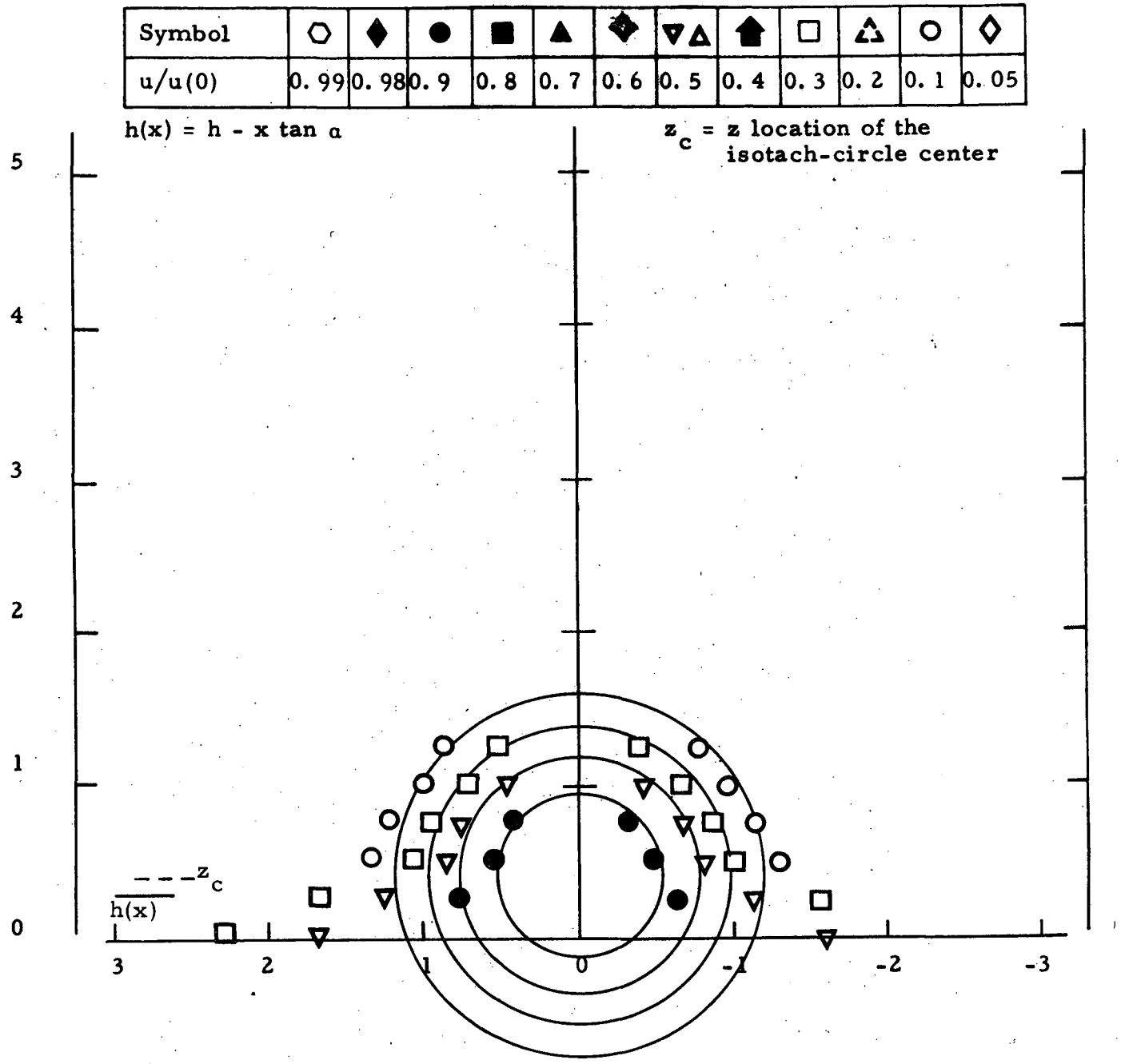
Symbol
u/u(0)
0.99
0.98
0.9
0.8
0.7
0.6
0.5
0.4
0.3
0.2
0.1
0.05
h(x) = h - x tan α
z_c = z location of the isotach-circle center
5
4
3
2
1
0
z_c
h(x)
3
2
1
0
-1
-2
-3

d) x/d = 3

Symbol	⬡	◆	●	■	▲	◆	▽△	⬟	□	♺	○	◇
u/u(0)	0.99	0.98	0.9	0.8	0.7	0.6	0.5	0.4	0.3	0.2	0.1	0.05

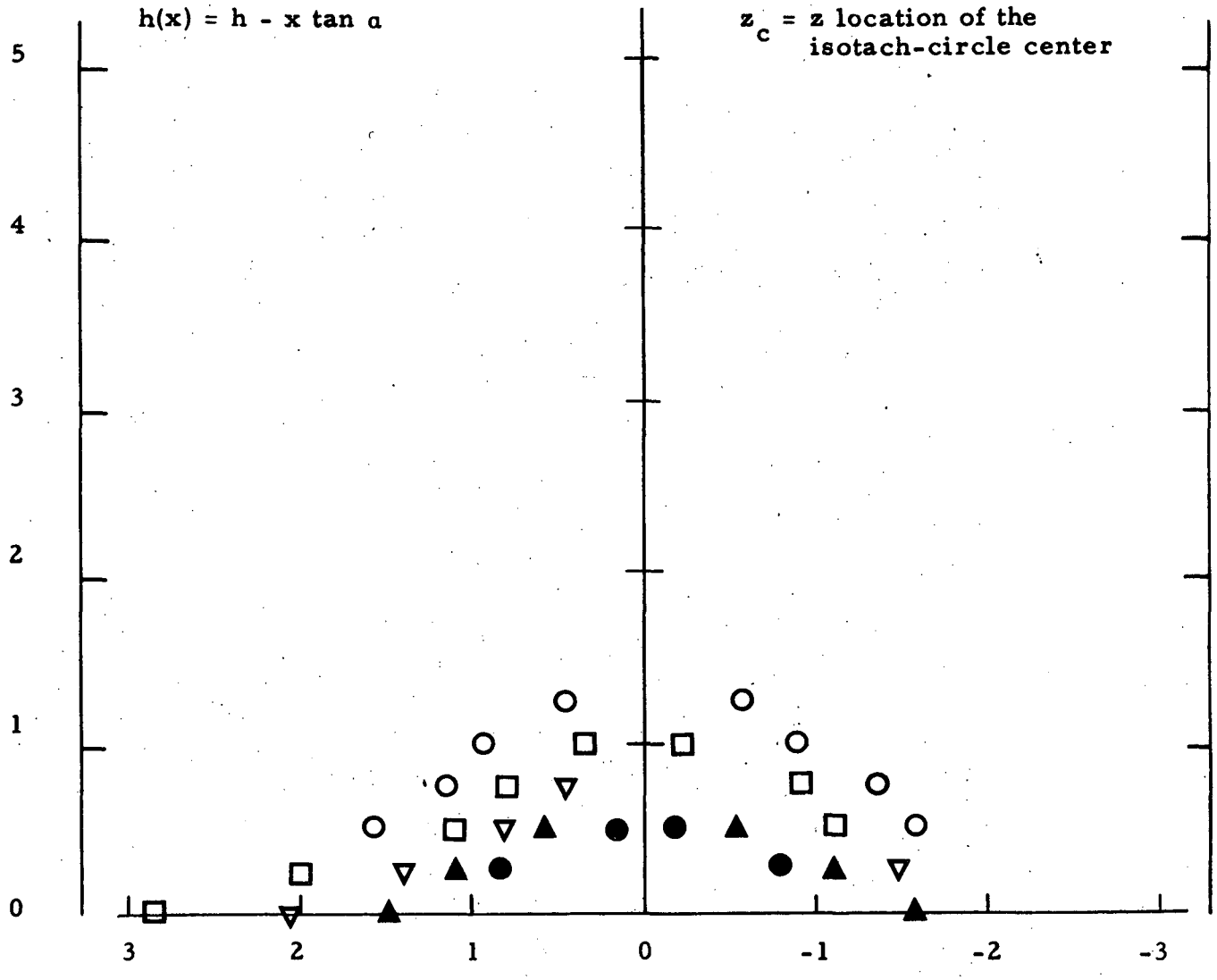

e) x/d = 4

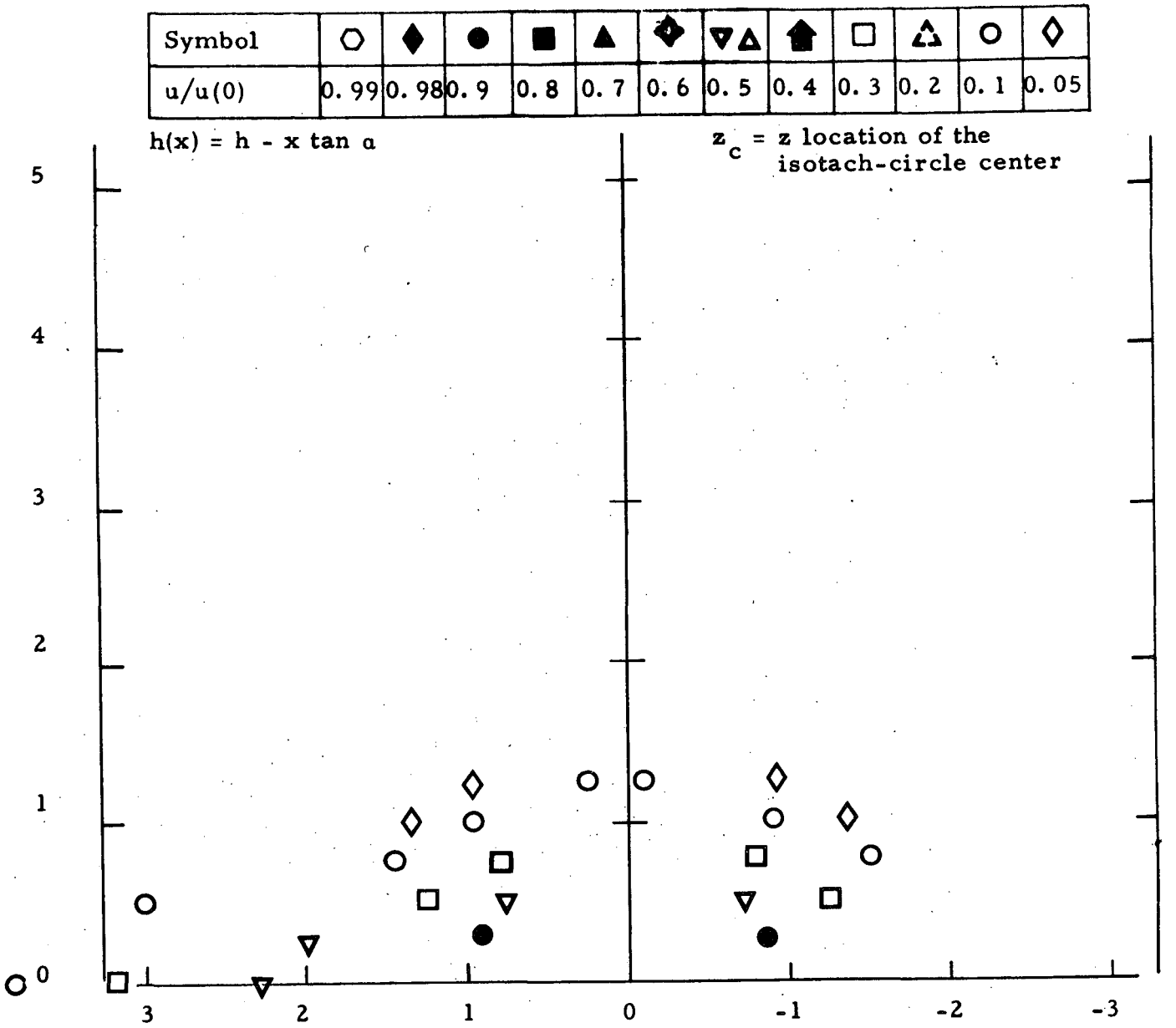
Symbol
u/u(0)
0.99
0.98
0.9
0.8
0.7
0.6
0.5
0.4
0.3
0.2
0.1
0.05
h(x) = h - x tan α
z_c = z location of the isotach-circle center
5
4
3
2
1
0
3
2
1
0
-1
-2
-3

f) x/d = 5

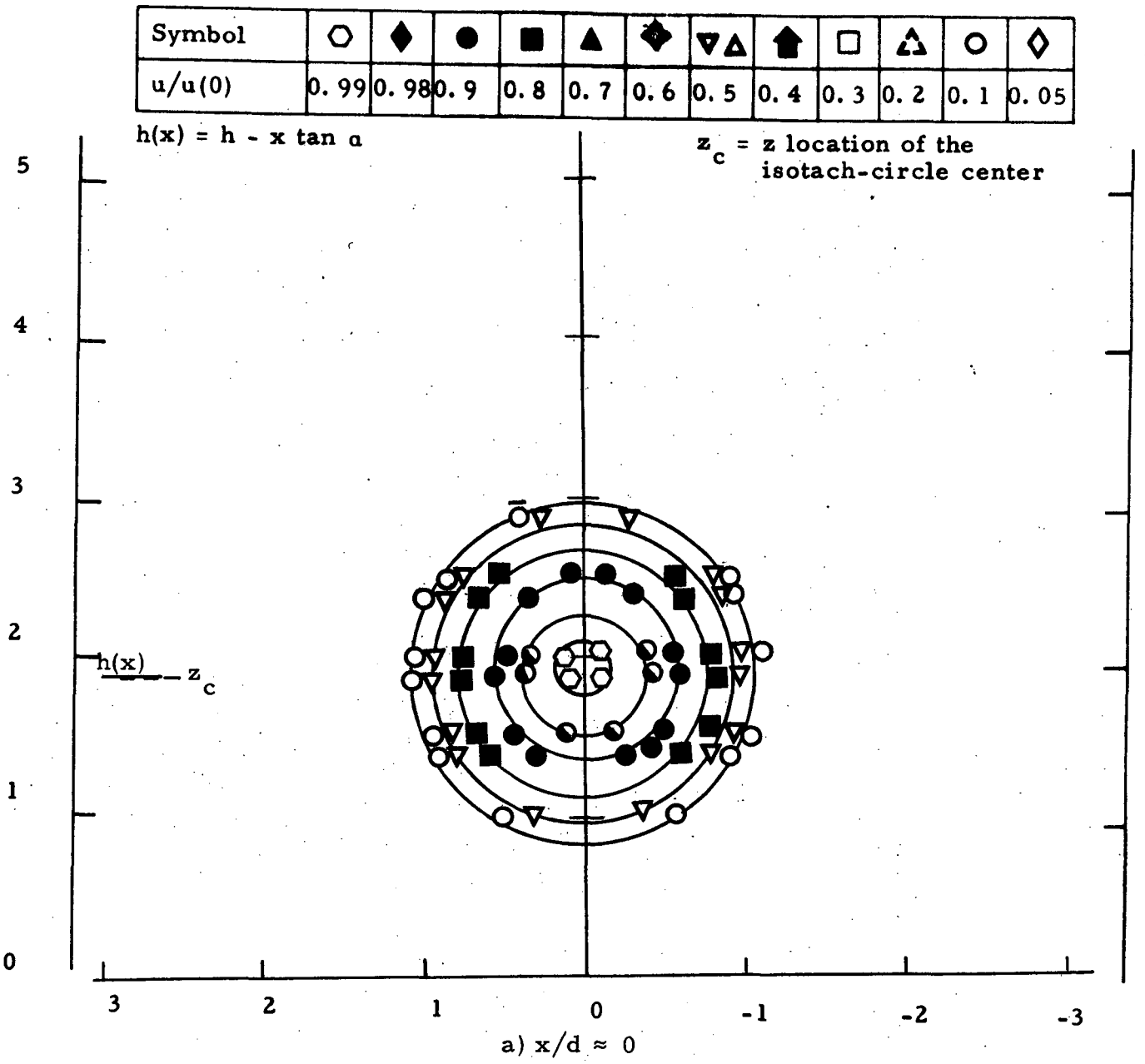

Figure 24. Isotach contours α = 15, h/d = 1, fully developed.

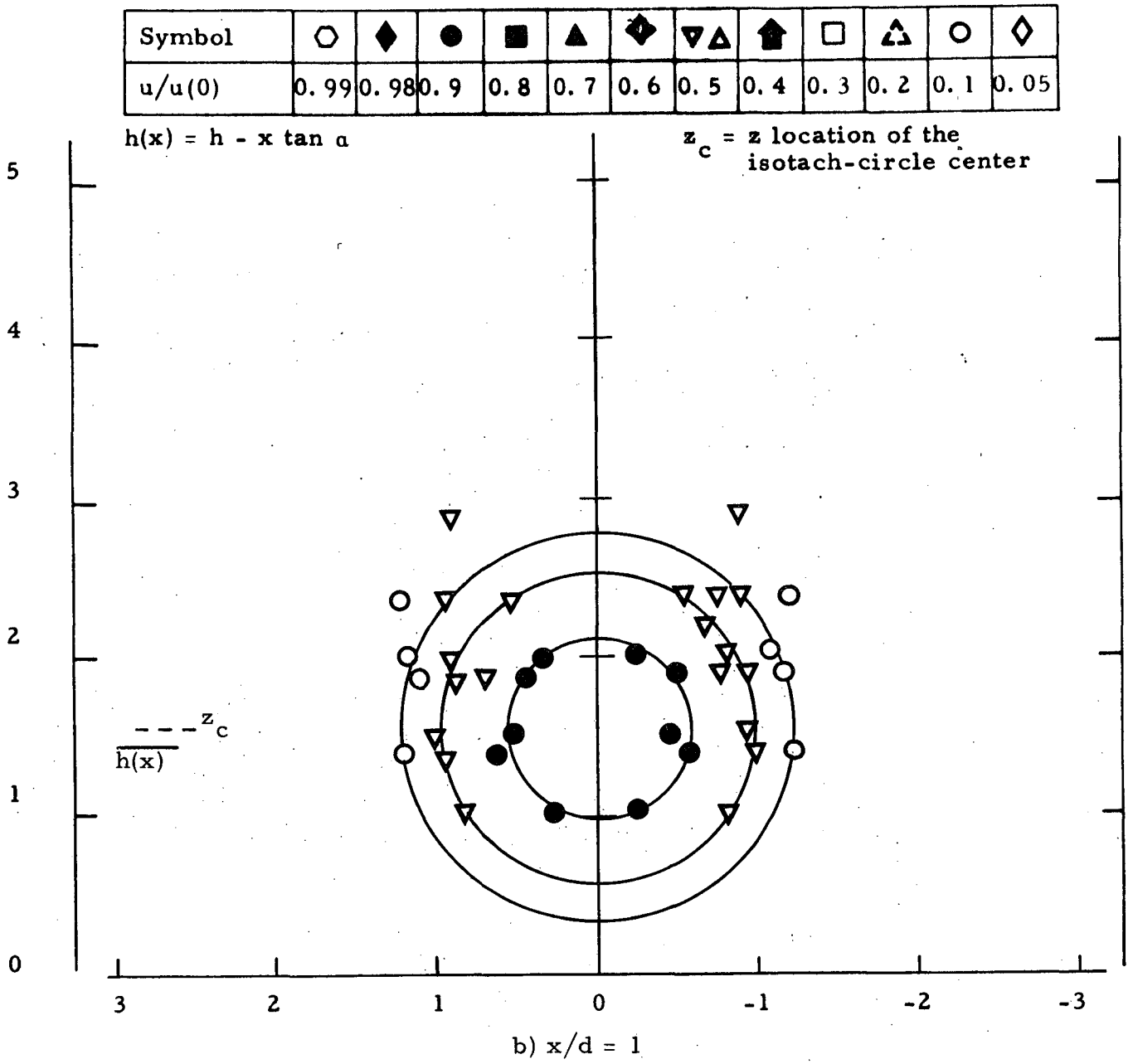
Symbol
u/u(0)
0.99
0.98
0.9
0.8
0.7
0.6
0.5
0.4
0.3
0.2
0.1
0.05
h(x) = h - x tan α
z_c = z location of the isotach-circle center
$\frac{z_c}{h(x)}$
5
4
3
2
1
0
3
2
1
0
-1
-2
-3

b) x/d = 1

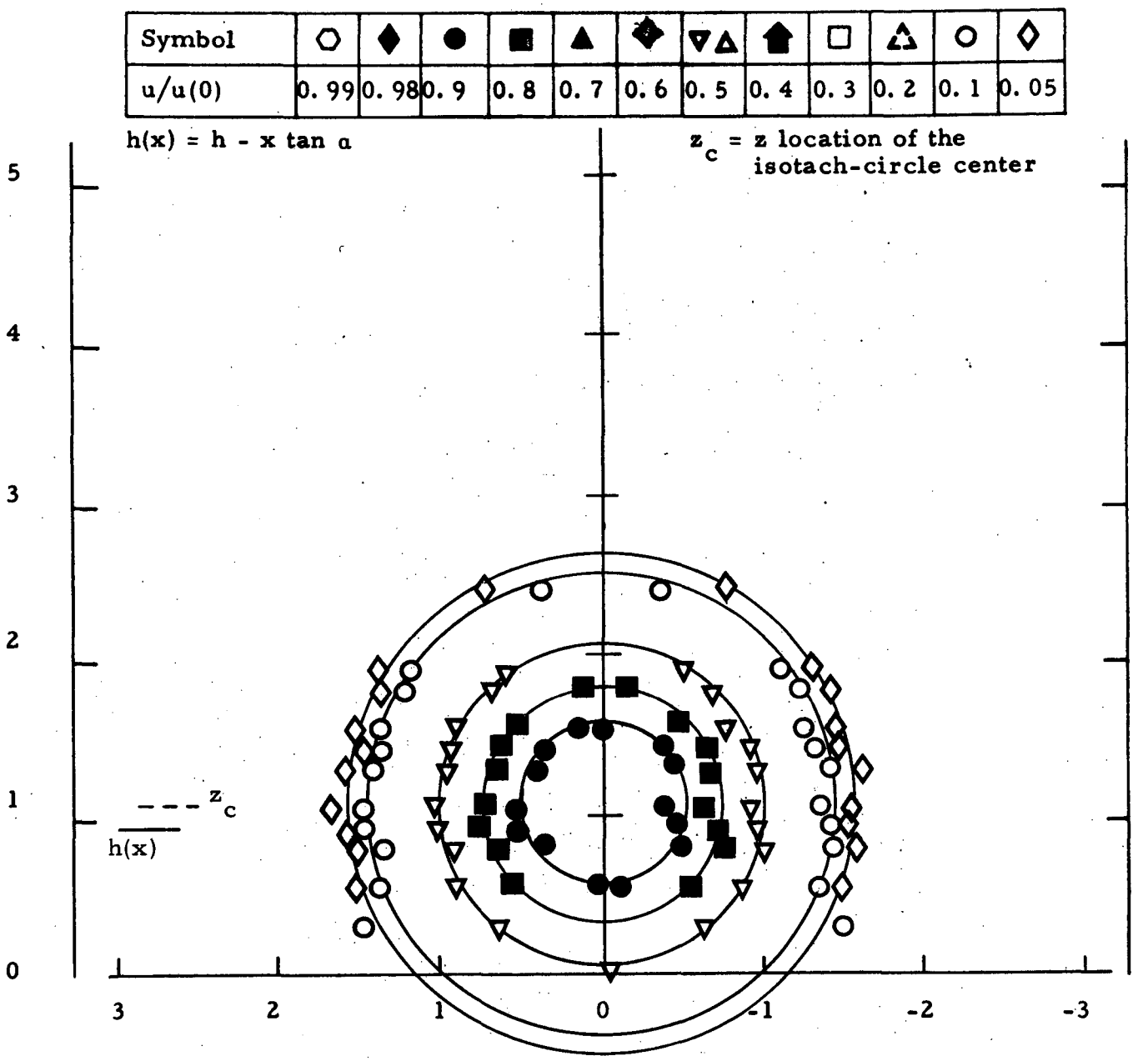
Symbol
u/u(0)
0.99
0.98
0.9
0.8
0.7
0.6
0.5
0.4
0.3
0.2
0.1
0.05
h(x) = h - x tan α
z_c = z location of the isotach-circle center
5
4
3
2
1
0
z_c
h(x)
3
2
1
0
-1
-2
-3

c) x/d = 2

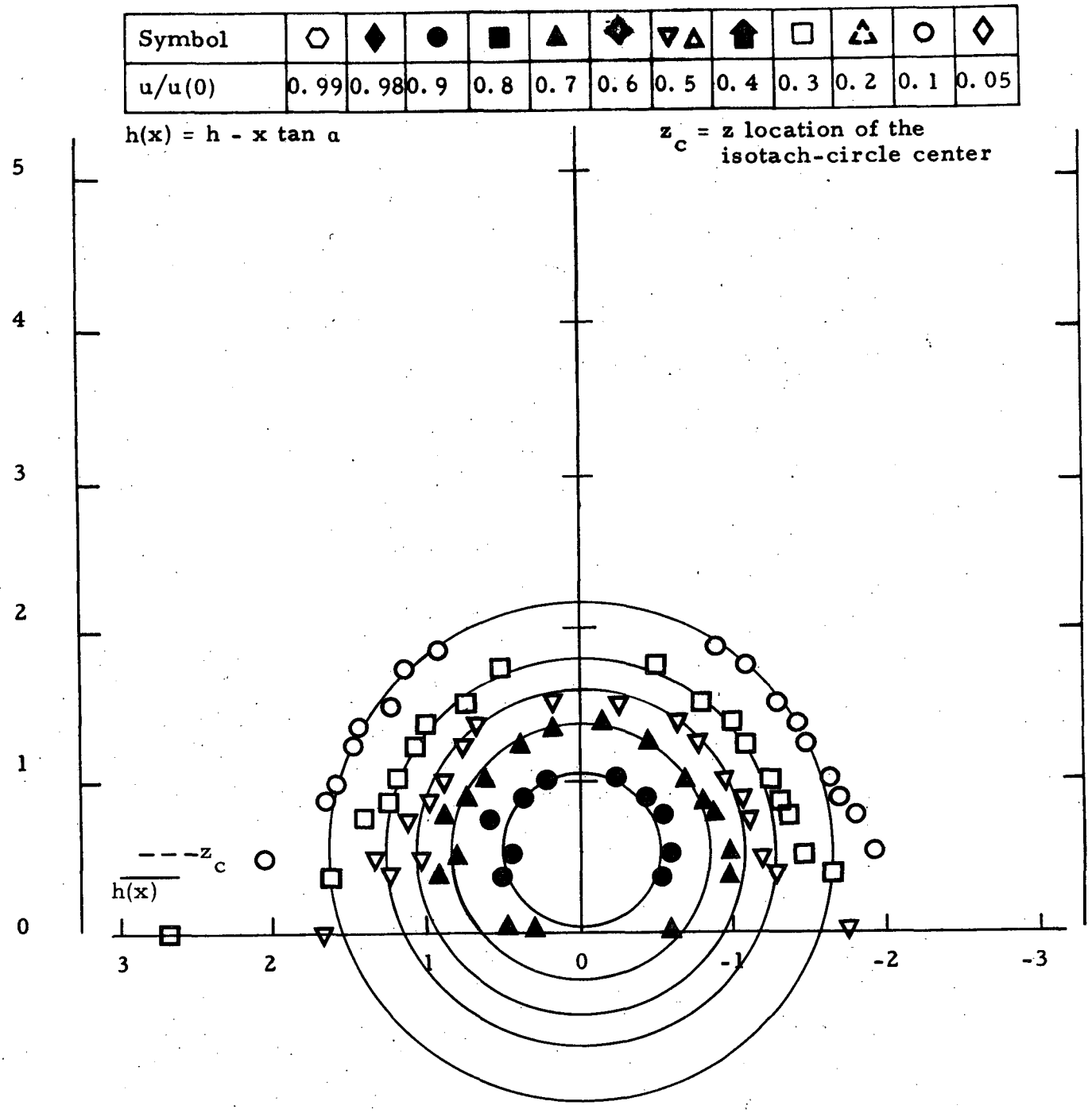
Symbol
u/u(0)
0.99
0.98
0.9
0.8
0.7
0.6
0.5
0.4
0.3
0.2
0.1
0.05
h(x) = h - x tan α
z_c = z location of the isotach-circle center
5
4
3
2
1
0
---z_c
h(x)
3
2
1
0
-1
-2
-3

d) x/d = 3

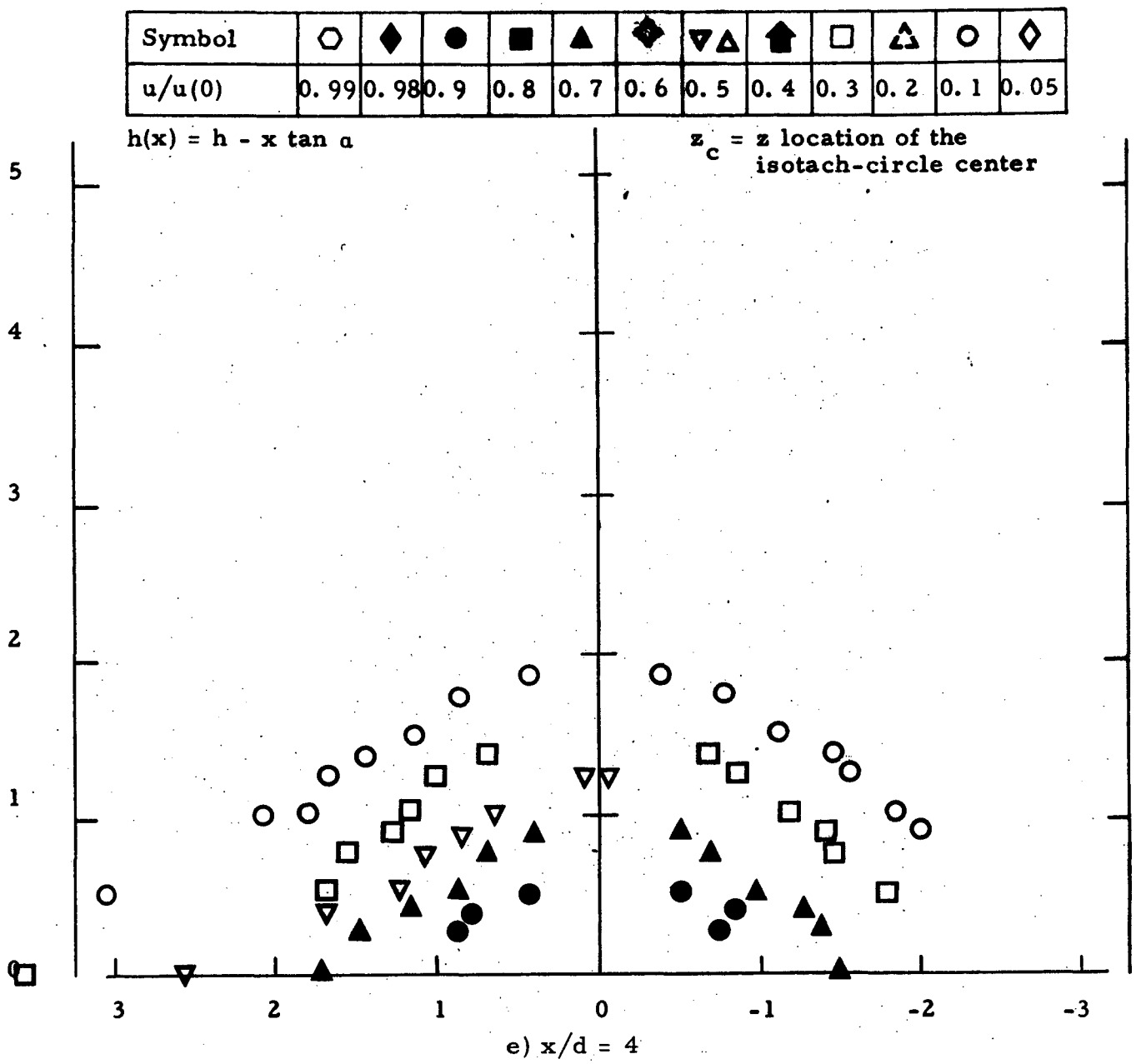
Symbol
u/u(0)
0.99
0.98
0.9
0.8
0.7
0.6
0.5
0.4
0.3
0.2
0.1
0.05
h(x) = h - x tan α
z_c = z location of the isotach-circle center
5
4
3
2
1
0
3
2
1
0
-1
-2
-3

e) x/d = 4

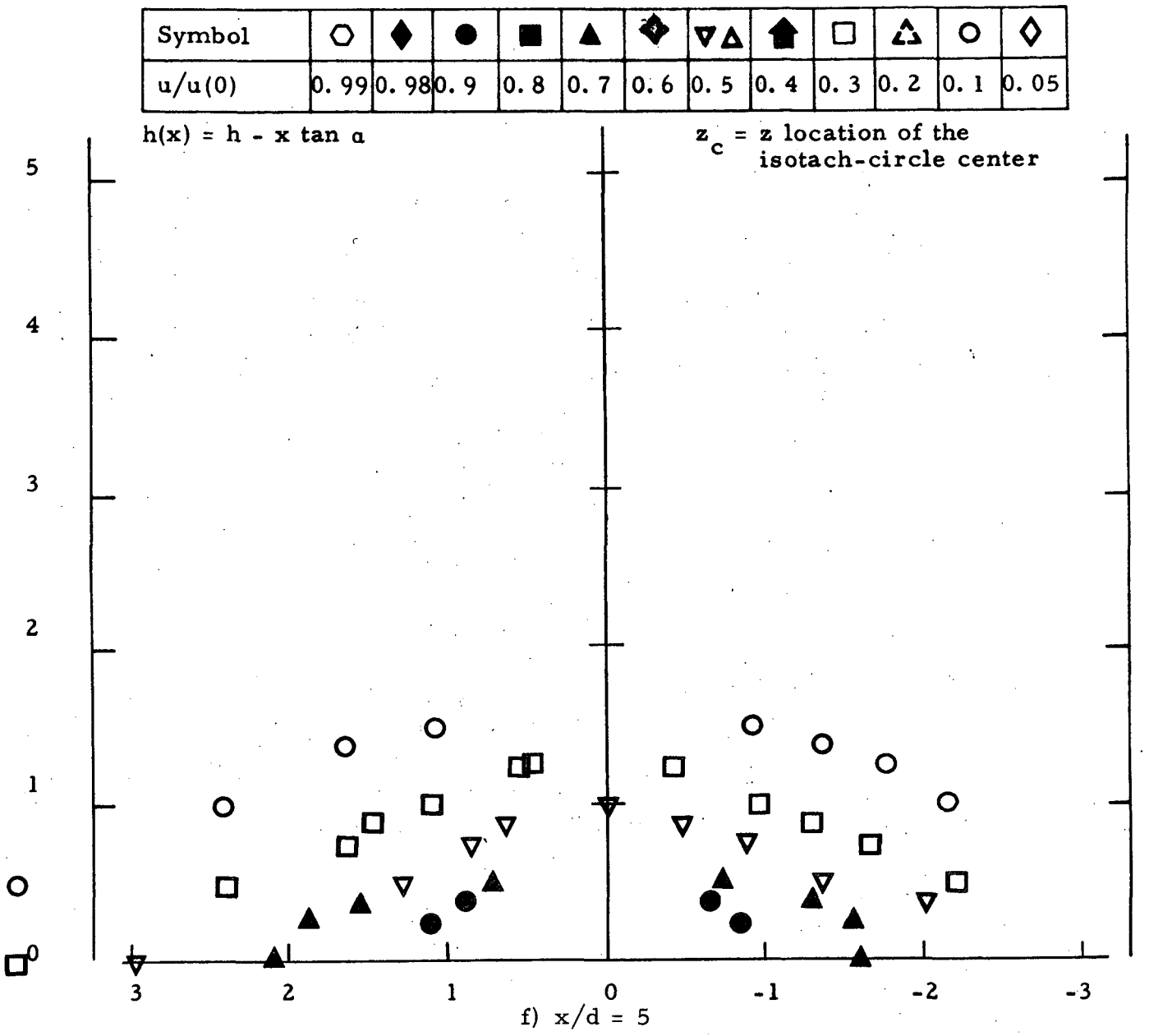
Symbol
u/u(0)
0.99
0.98
0.9
0.8
0.7
0.6
0.5
0.4
0.3
0.2
0.1
0.05
h(x) = h - x tan α
z_c = z location of the isotach-circle center
5
4
3
2
1
0
3
2
1
0
-1
-2
-3

f) x/d = 5

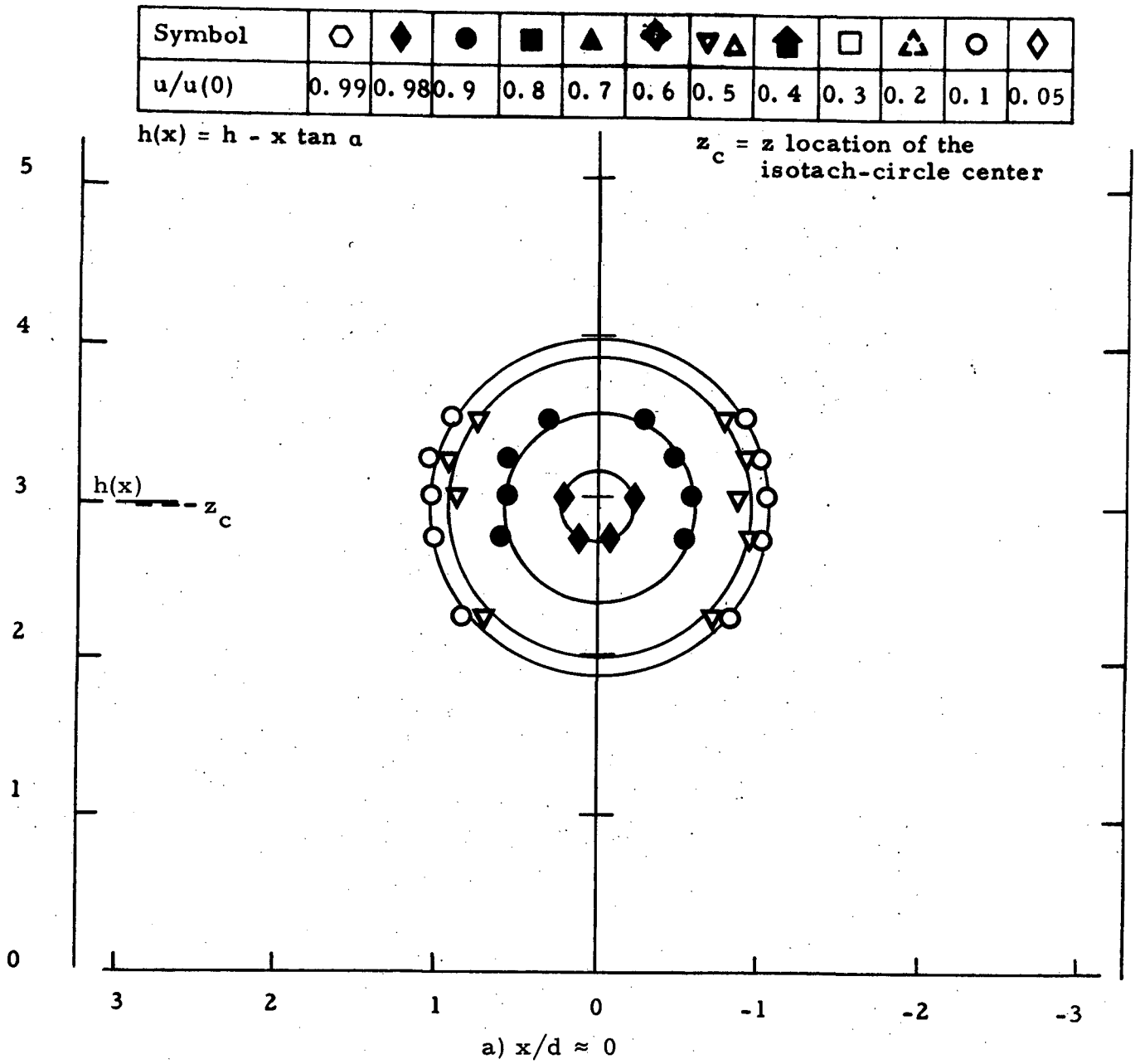

Figure 25. Isotach contours α = 15, h/d = 1.5, fully developed.

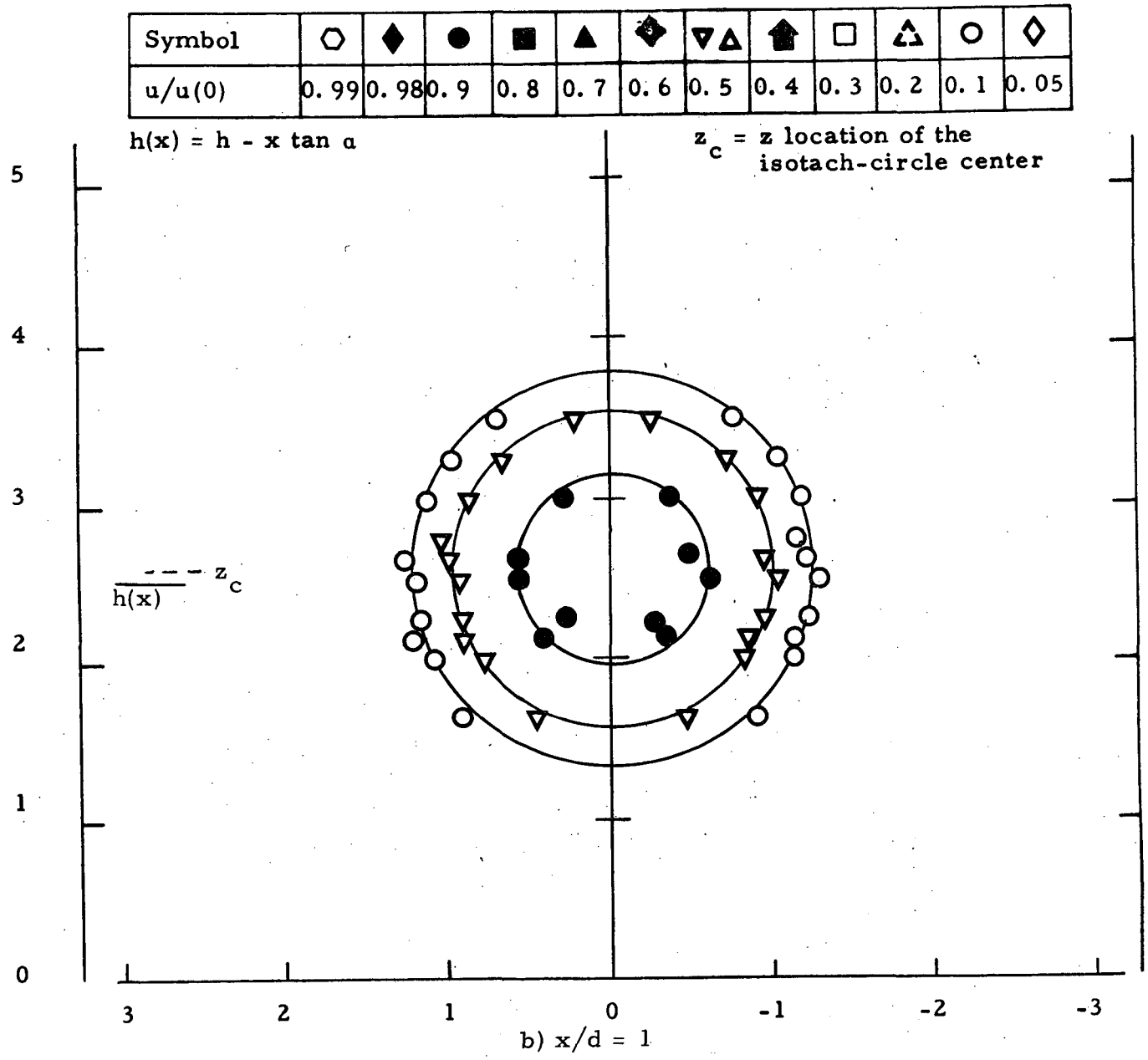
Symbol
u/u(0)
0.99
0.98
0.9
0.8
0.7
0.6
0.5
0.4
0.3
0.2
0.1
0.05
h(x) = h - x tan α
z_c = z location of the isotach-circle center
$\frac{z_c}{h(x)}$
5
4
3
2
1
0
3
2
1
0
-1
-2
-3

b) x/d = 1

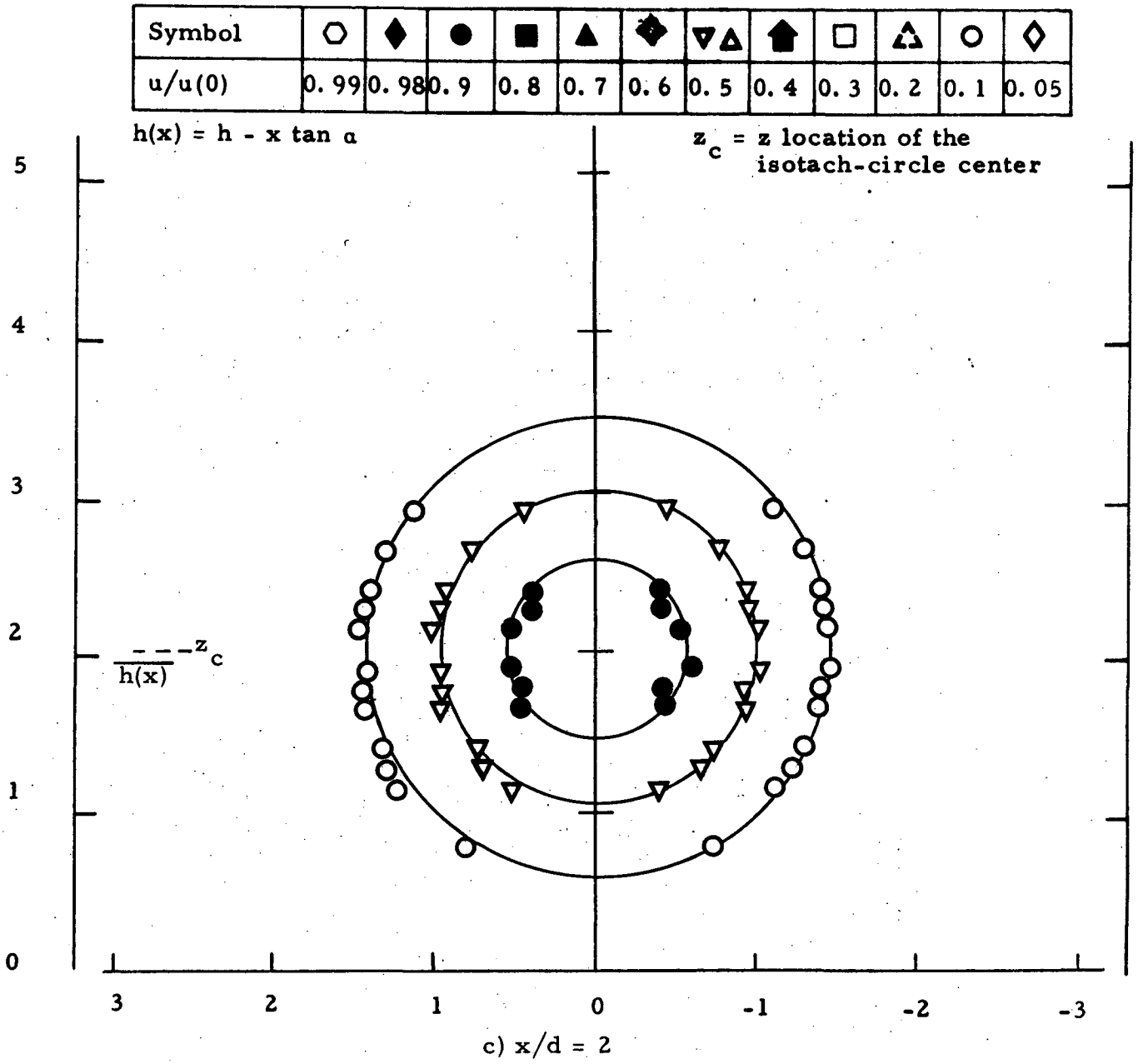
Symbol
u/u(0)
0.99
0.98
0.9
0.8
0.7
0.6
0.5
0.4
0.3
0.2
0.1
0.05
h(x) = h - x tan α
z_c = z location of the isotach-circle center
(z - z_c)/h(x)
5
4
3
2
1
0
3
2
1
0
-1
-2
-3

c) x/d = 2

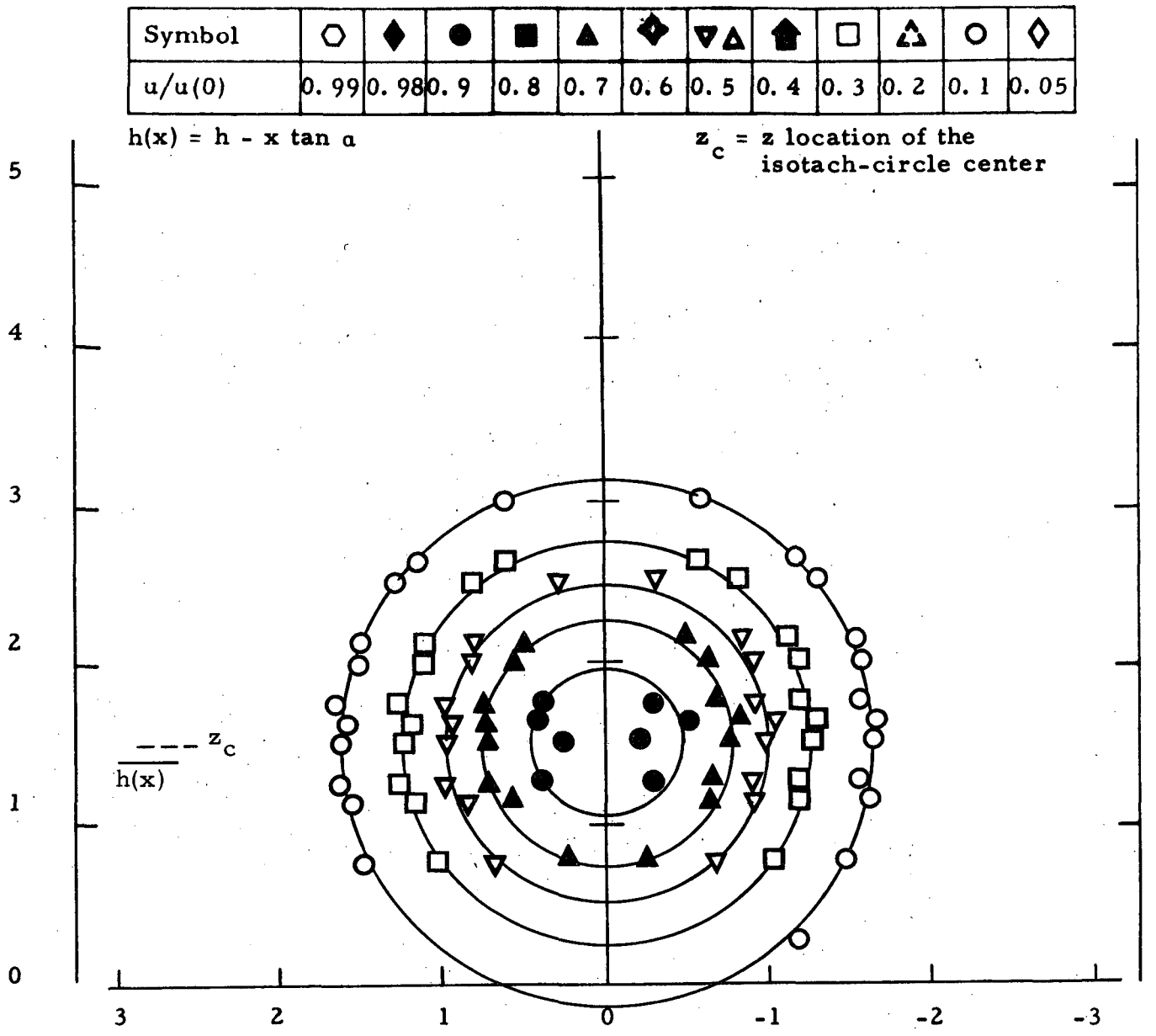
Symbol
u/u(0)
0.99
0.98
0.9
0.8
0.7
0.6
0.5
0.4
0.3
0.2
0.1
0.05
h(x) = h - x tan α
z_c = z location of the isotach-circle center
$\frac{z_c}{h(x)}$
5
4
3
2
1
0
3
2
1
0
-1
-2
-3

d) x/d = 3

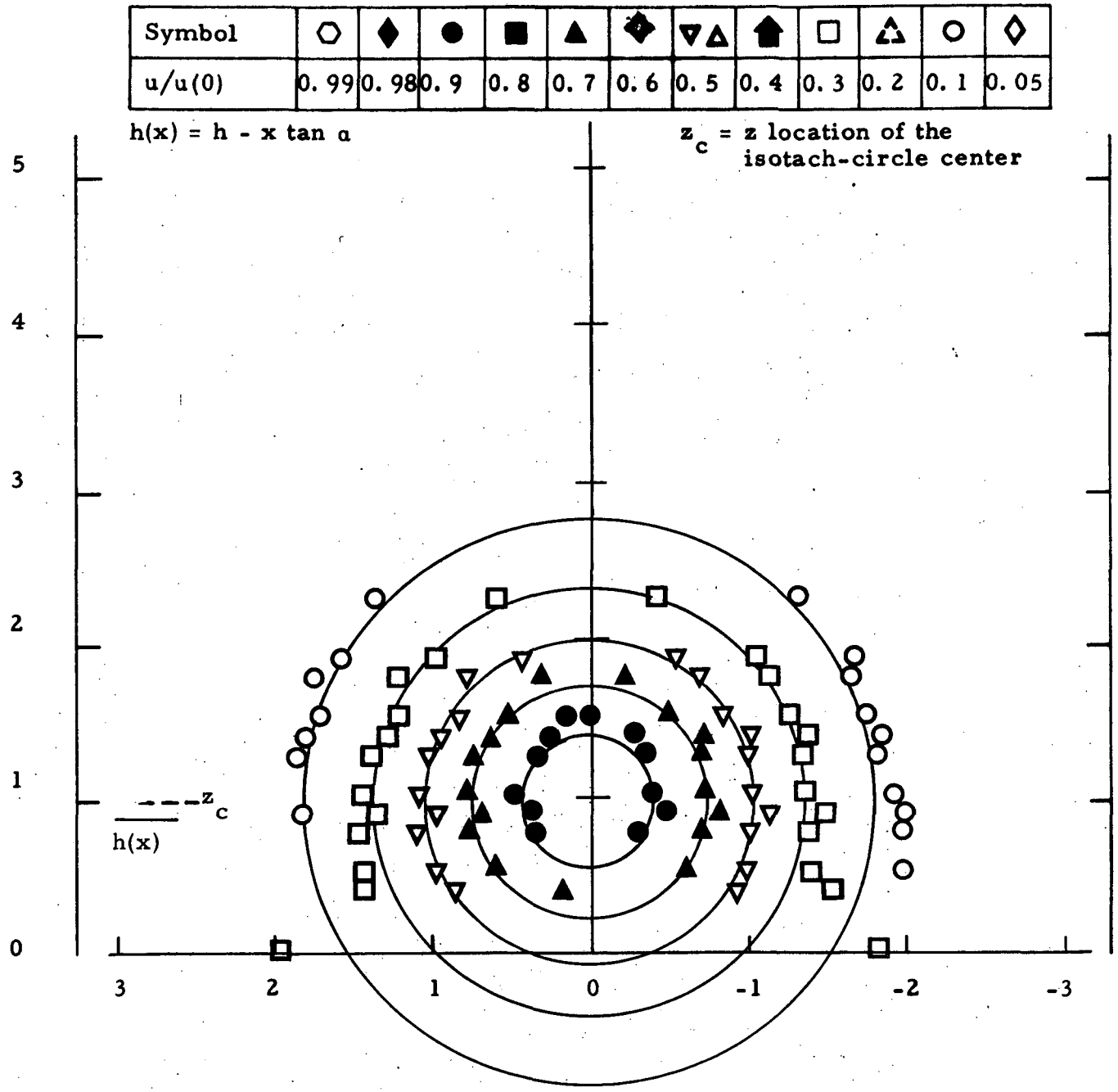
Symbol
u/u(0)
0.99
0.98
0.9
0.8
0.7
0.6
0.5
0.4
0.3
0.2
0.1
0.05
h(x) = h - x tan α
z_c = z location of the isotach-circle center
5
4
3
2
1
0
z_c
h(x)
3
2
1
0
-1
-2
-3

e) x/d = 4

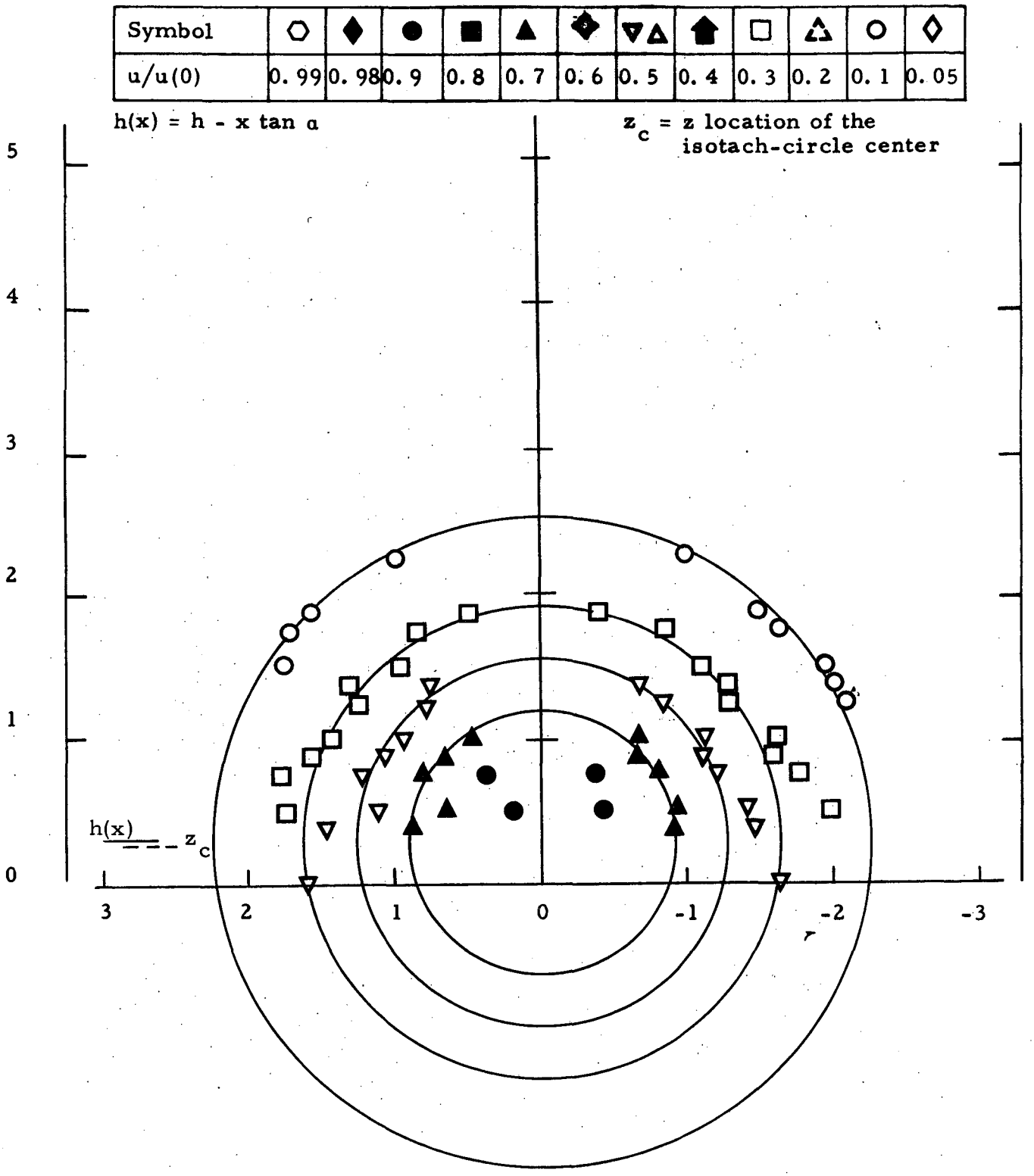
Symbol
u/u(0)
0.99
0.98
0.9
0.8
0.7
0.6
0.5
0.4
0.3
0.2
0.1
0.05
h(x) = h - x tan α
z_c = z location of the isotach-circle center
5
4
3
2
1
0
h(x)
z_c
3
2
1
0
-1
-2
-3
r

f) x/d = 5

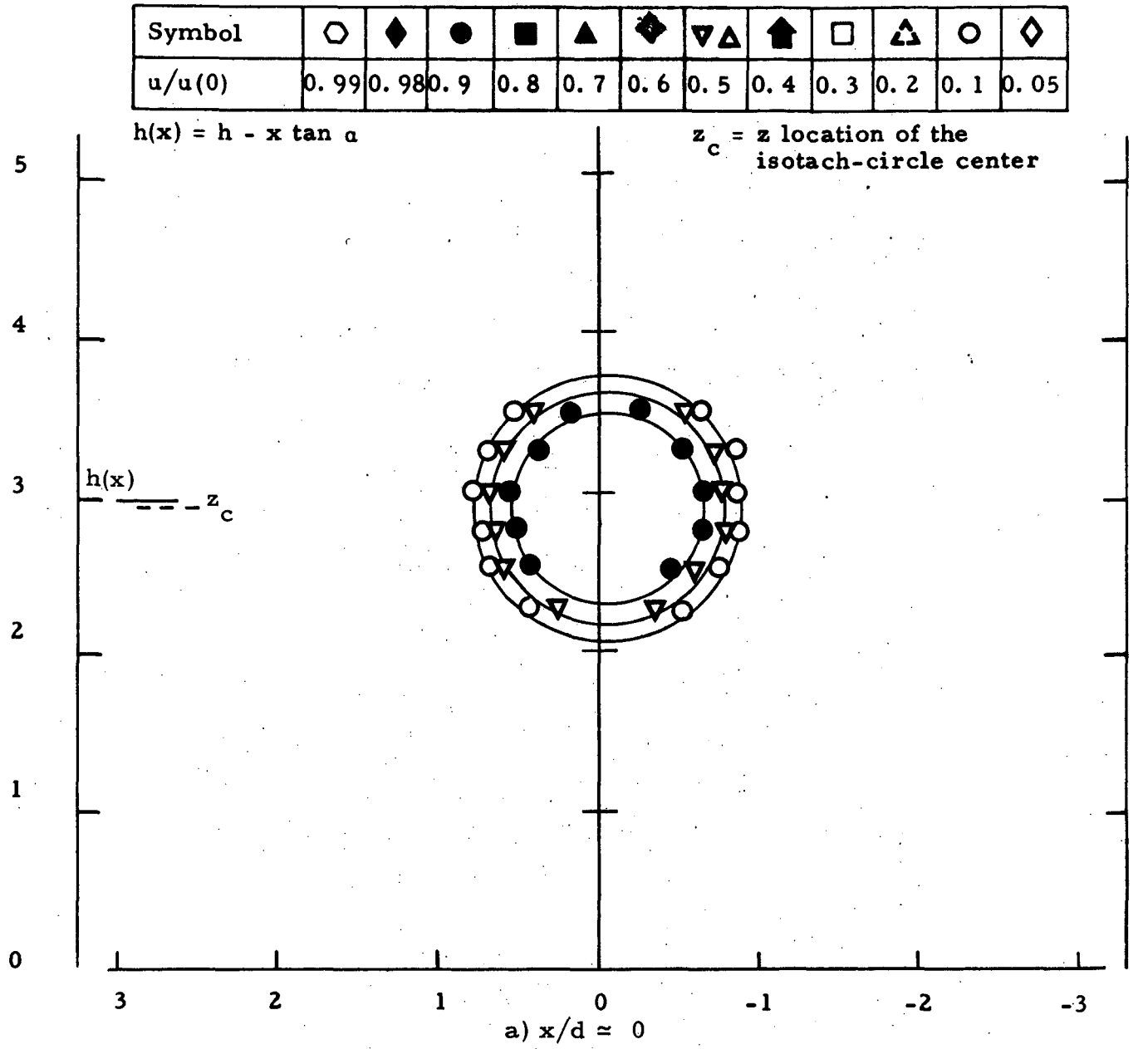

Figure 26. Isotach contours $\alpha = 15$, $h/d = 2$, uniform.

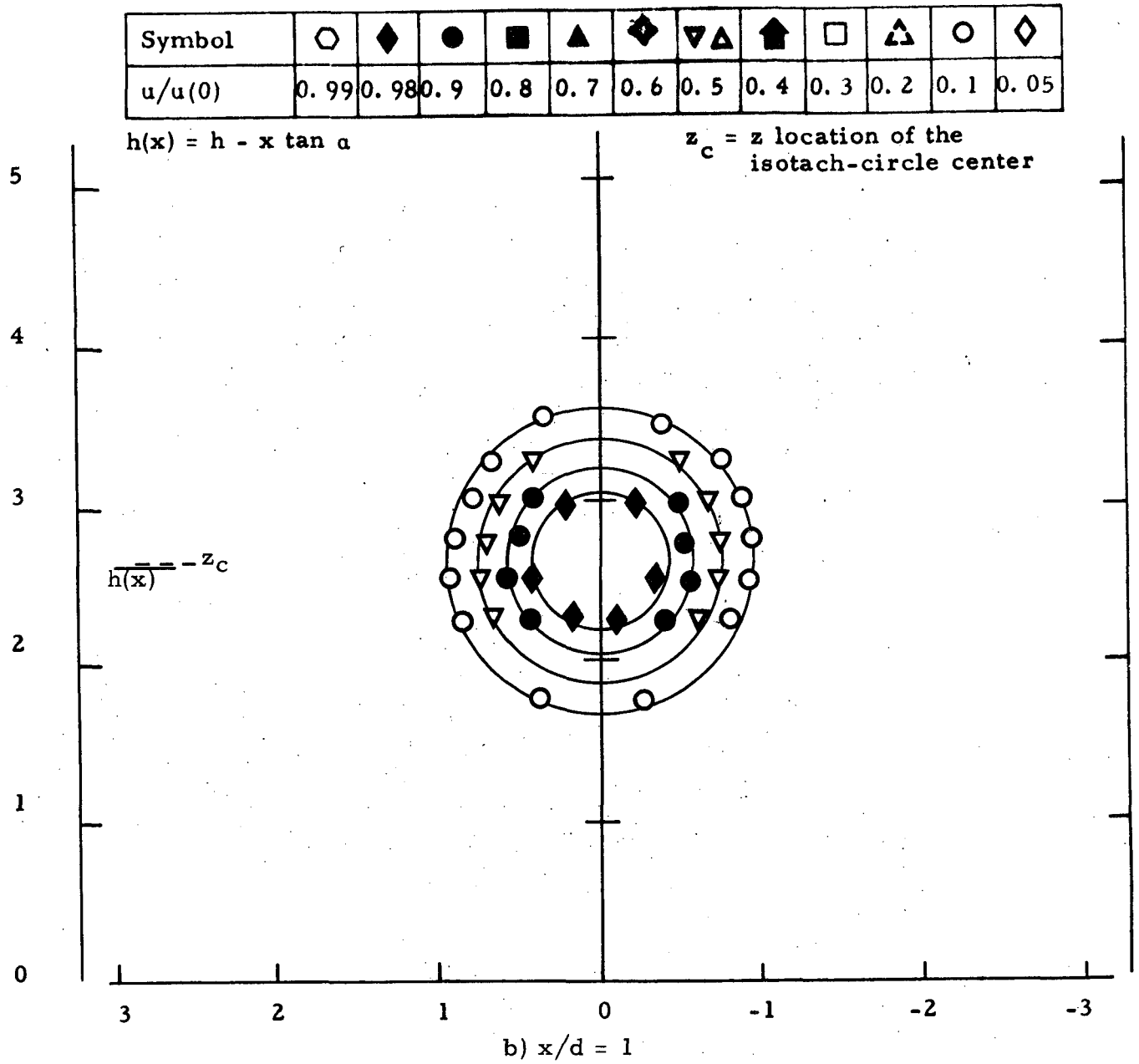
Symbol
u/u(0)
0.99
0.98
0.9
0.8
0.7
0.6
0.5
0.4
0.3
0.2
0.1
0.05
h(x) = h - x tan α
z_c = z location of the isotach-circle center
$\frac{z}{h(x)} - z_c$
5
4
3
2
1
0
3
2
1
0
-1
-2
-3

b) x/d = 1

Symbol	⬡	♦	●	■	▲	◆	▽△	⬟	□	△	○	◇
u/u(0)	0.99	0.98	0.9	0.8	0.7	0.6	0.5	0.4	0.3	0.2	0.1	0.05

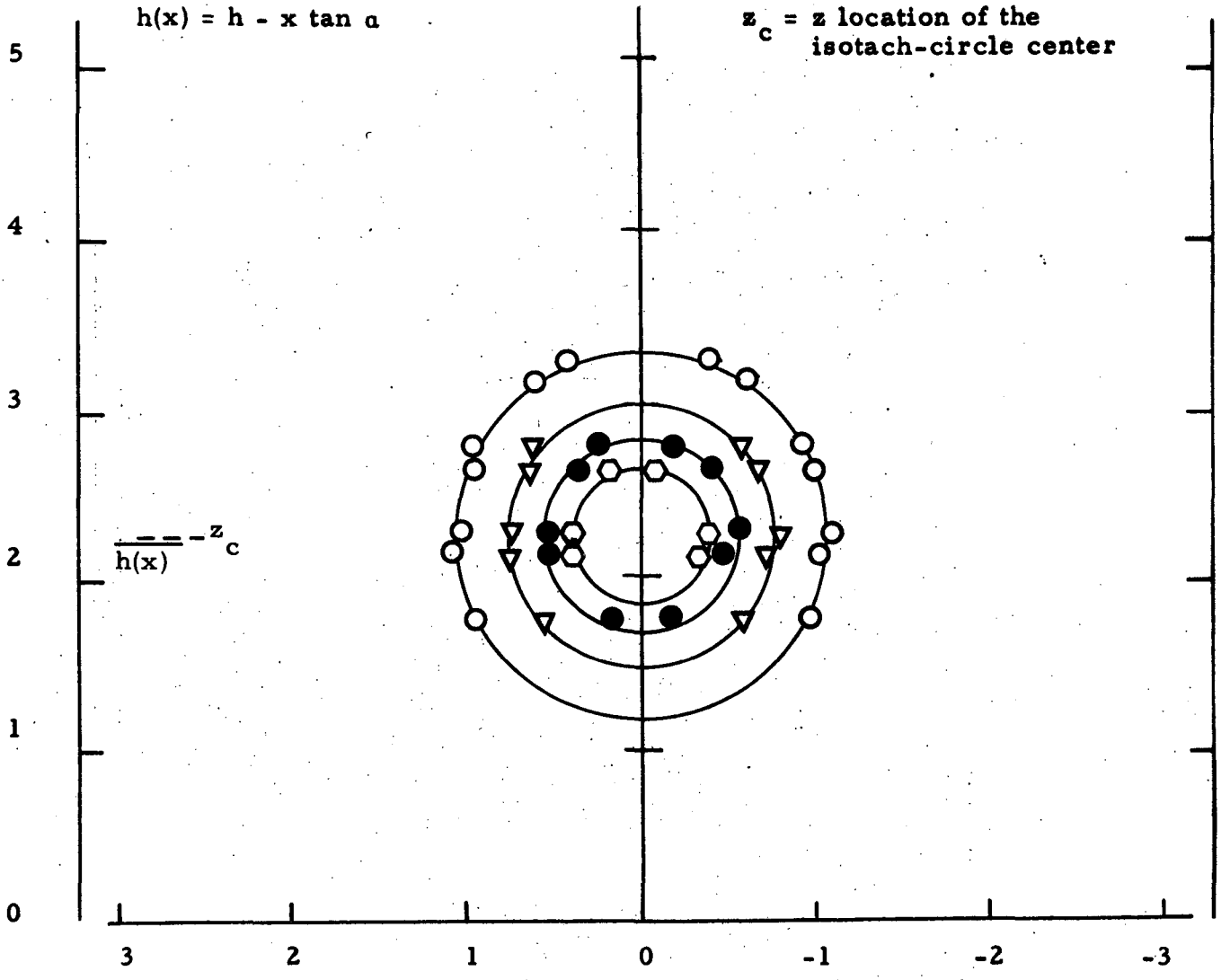

c) x/d = 2

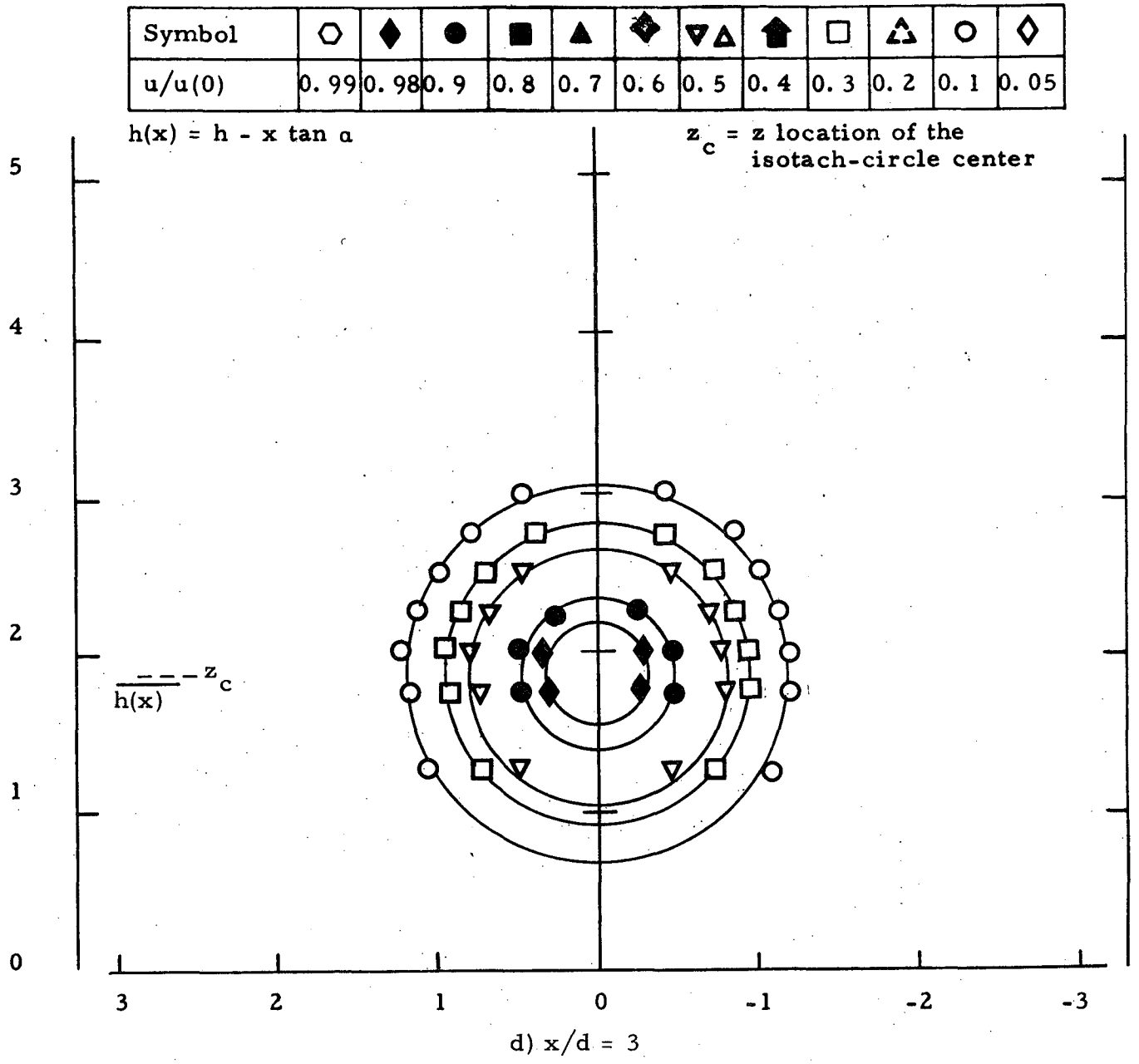
Symbol
u/u(0)
0.99
0.98
0.9
0.8
0.7
0.6
0.5
0.4
0.3
0.2
0.1
0.05
h(x) = h - x tan α
z_c = z location of the isotach-circle center
z_c / h(x)
5
4
3
2
1
0
3
2
1
0
-1
-2
-3

d) x/d = 3

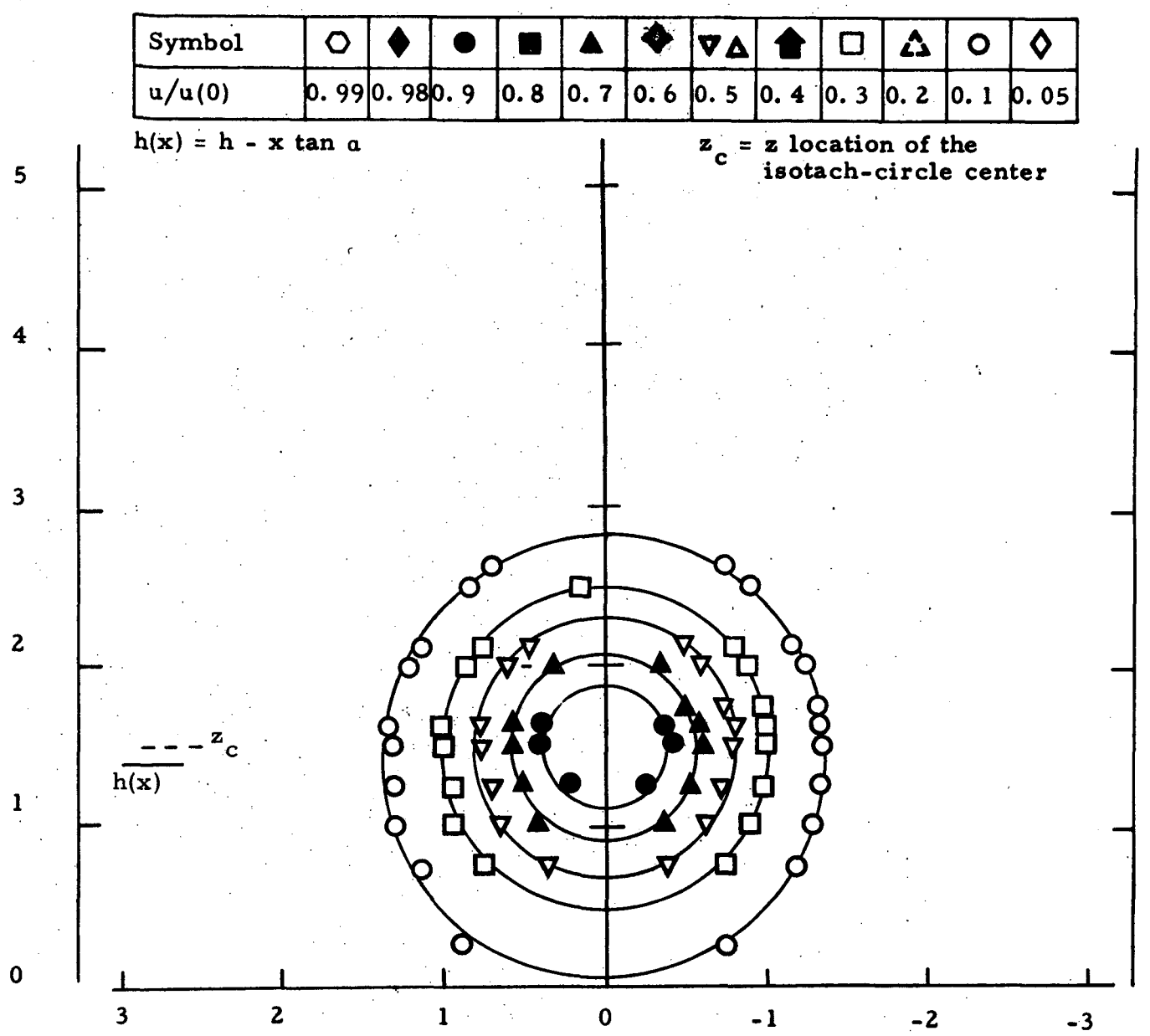
Symbol
u/u(0)
0.99
0.98
0.9
0.8
0.7
0.6
0.5
0.4
0.3
0.2
0.1
0.05
h(x) = h - x tan α
z_c = z location of the isotach-circle center
$\frac{z_c}{h(x)}$
5
4
3
2
1
0
3
2
1
0
-1
-2
-3

e) x/d = 4

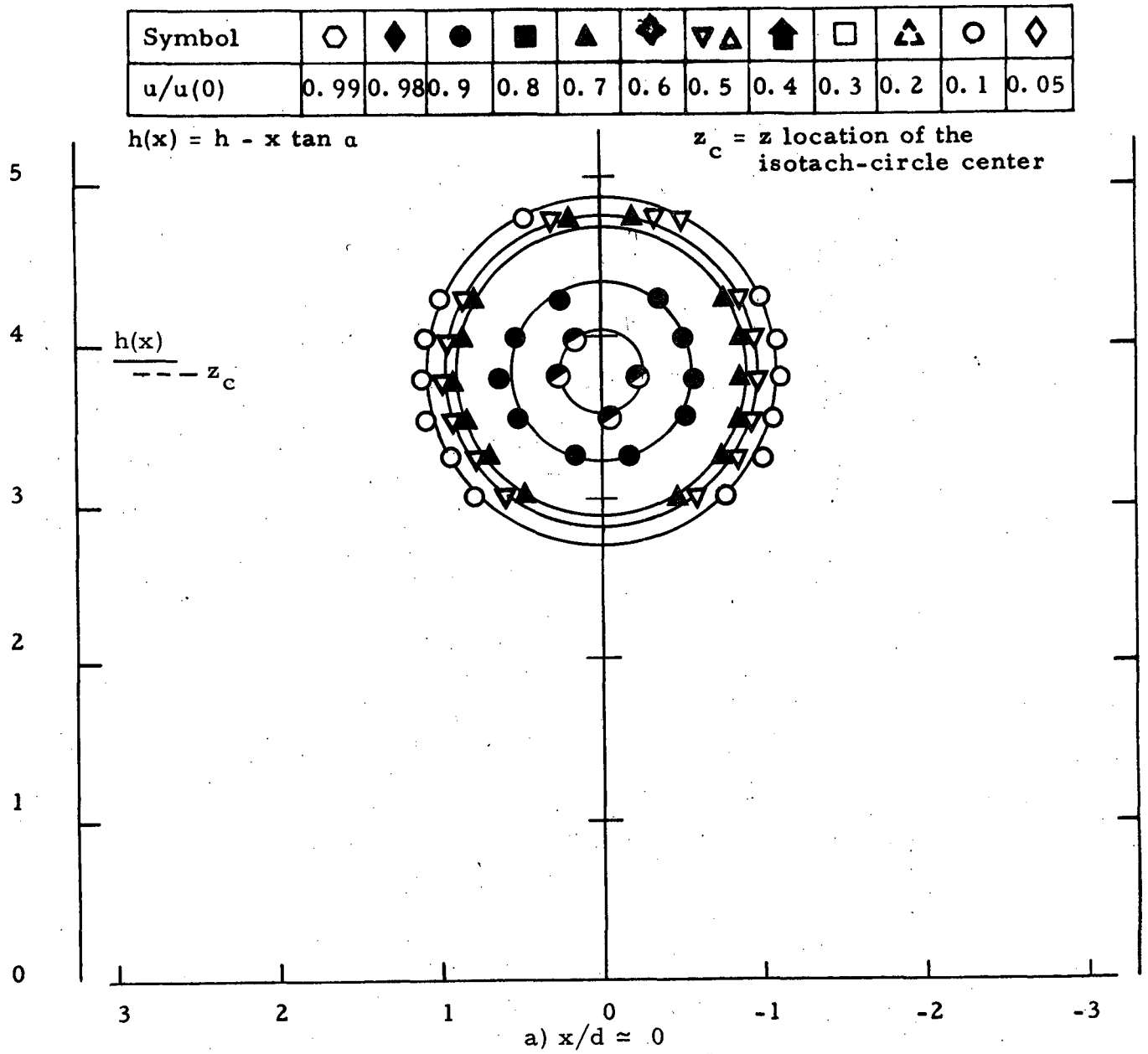

Figure 27. Isotach contours, $\alpha = 15$, $h/d = 2$, fully developed.

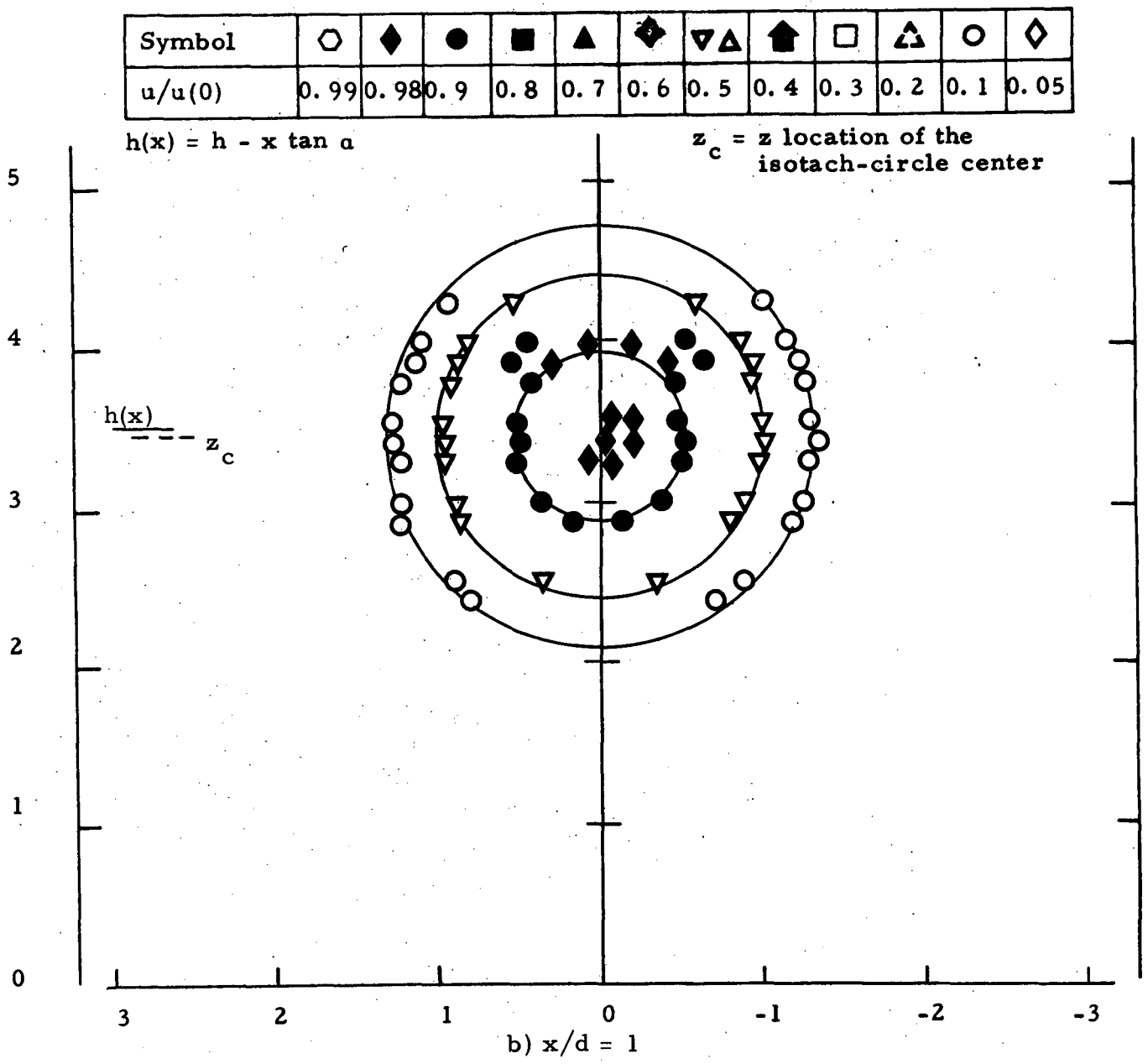
Symbol
u/u(0)
0.99
0.98
0.9
0.8
0.7
0.6
0.5
0.4
0.3
0.2
0.1
0.05
h(x) = h - x tan α
z_c = z location of the isotach-circle center
h(x)
z_c
5
4
3
2
1
0
3
2
1
0
-1
-2
-3
b) x/d = 1

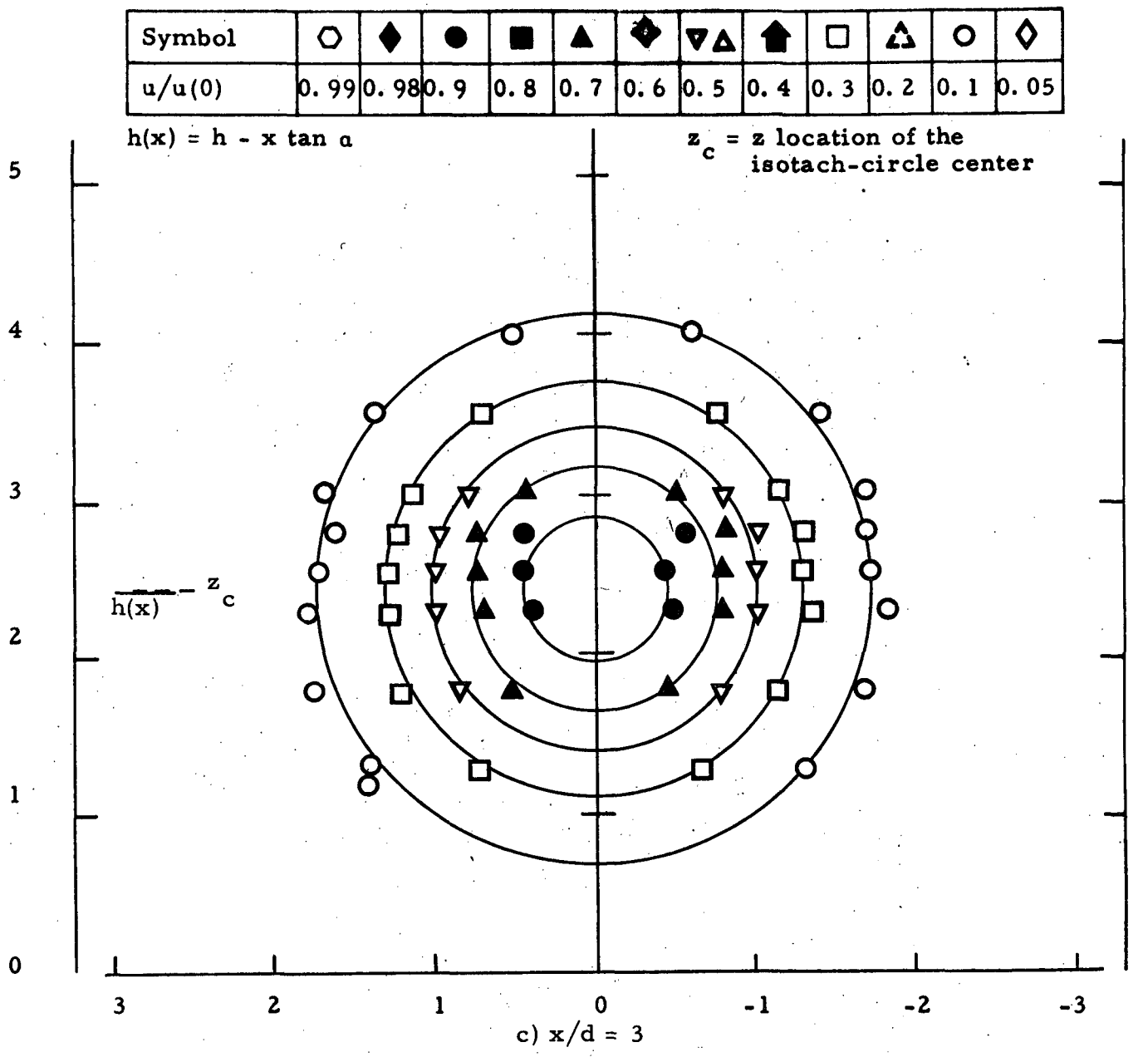
Symbol
u/u(0)
0.99
0.98
0.9
0.8
0.7
0.6
0.5
0.4
0.3
0.2
0.1
0.05
h(x) = h - x tan α
z_c = z location of the isotach-circle center
z_c / h(x)
5
4
3
2
1
0
3
2
1
0
-1
-2
-3
c) x/d = 3

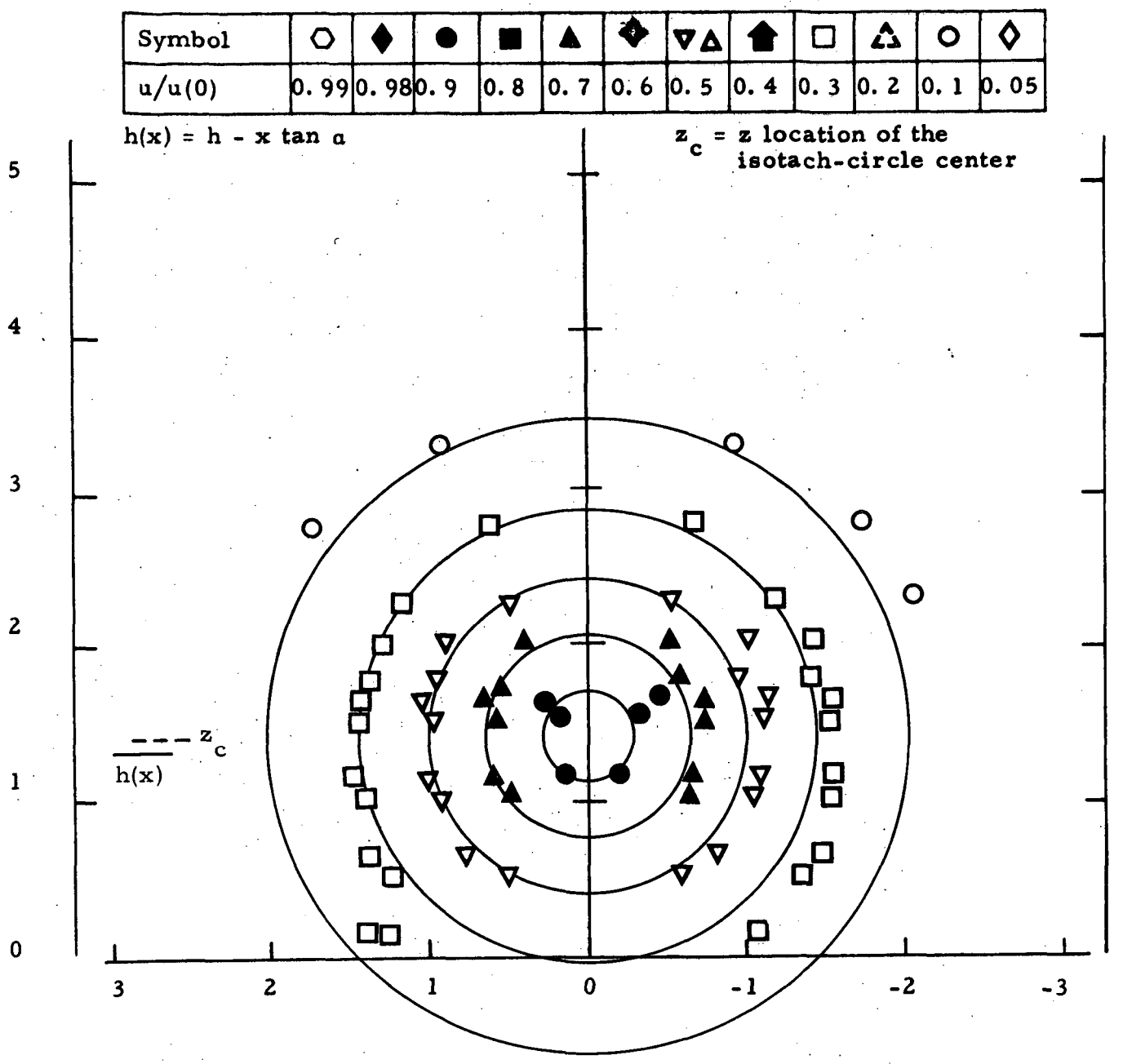
Symbol
u/u(0)
0.99
0.98
0.9
0.8
0.7
0.6
0.5
0.4
0.3
0.2
0.1
0.05
h(x) = h - x tan α
z_c = z location of the isotach-circle center
$\frac{z_c}{h(x)}$
5
4
3
2
1
0
3
2
1
0
-1
-2
-3

d) x/d = 5

$\chi = 0.00032x^2 + 0.0022x$, $u/u(0)$ vs. r/r_o at $x \approx 0$

r/r_o	0	0.05	0.10	0.15	0.20	0.25	0.30	0.35	0.40	0.45
$u/u(0)$	1	1	1	1	1	1	1	1	1	1
r/r_o	0.50	0.55	0.60	0.65	0.70	0.75	0.80	0.85	0.90	0.95
$u/u(0)$	1	1	0.99	0.98	0.96	0.93	0.90	0.83	0.72	0.52

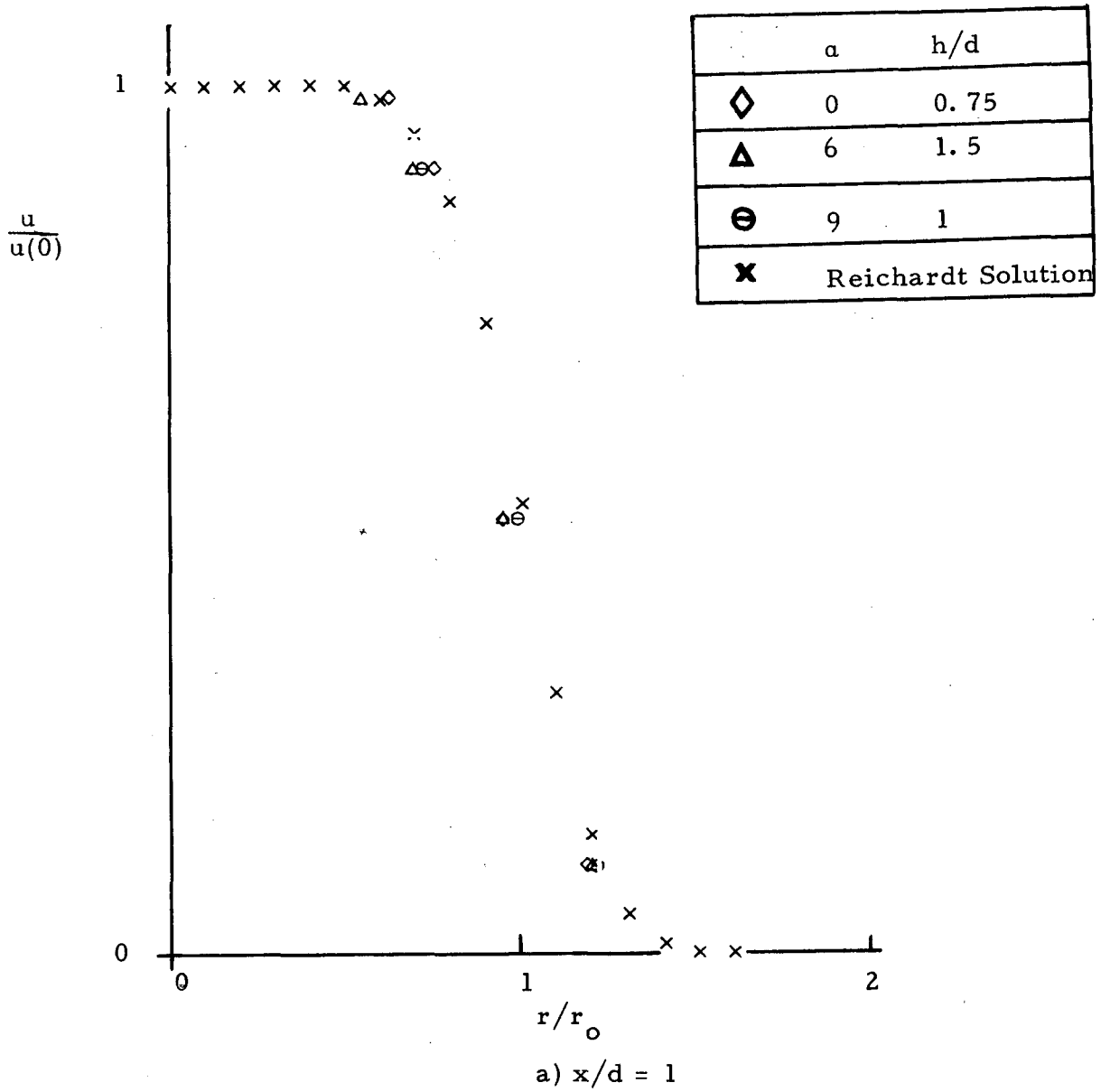

a) x/d = 1

Figure 28. $u/u(0)$ vs. r/r_o, uniform exit condition, for selected experimental data and the Reichardt analysis.

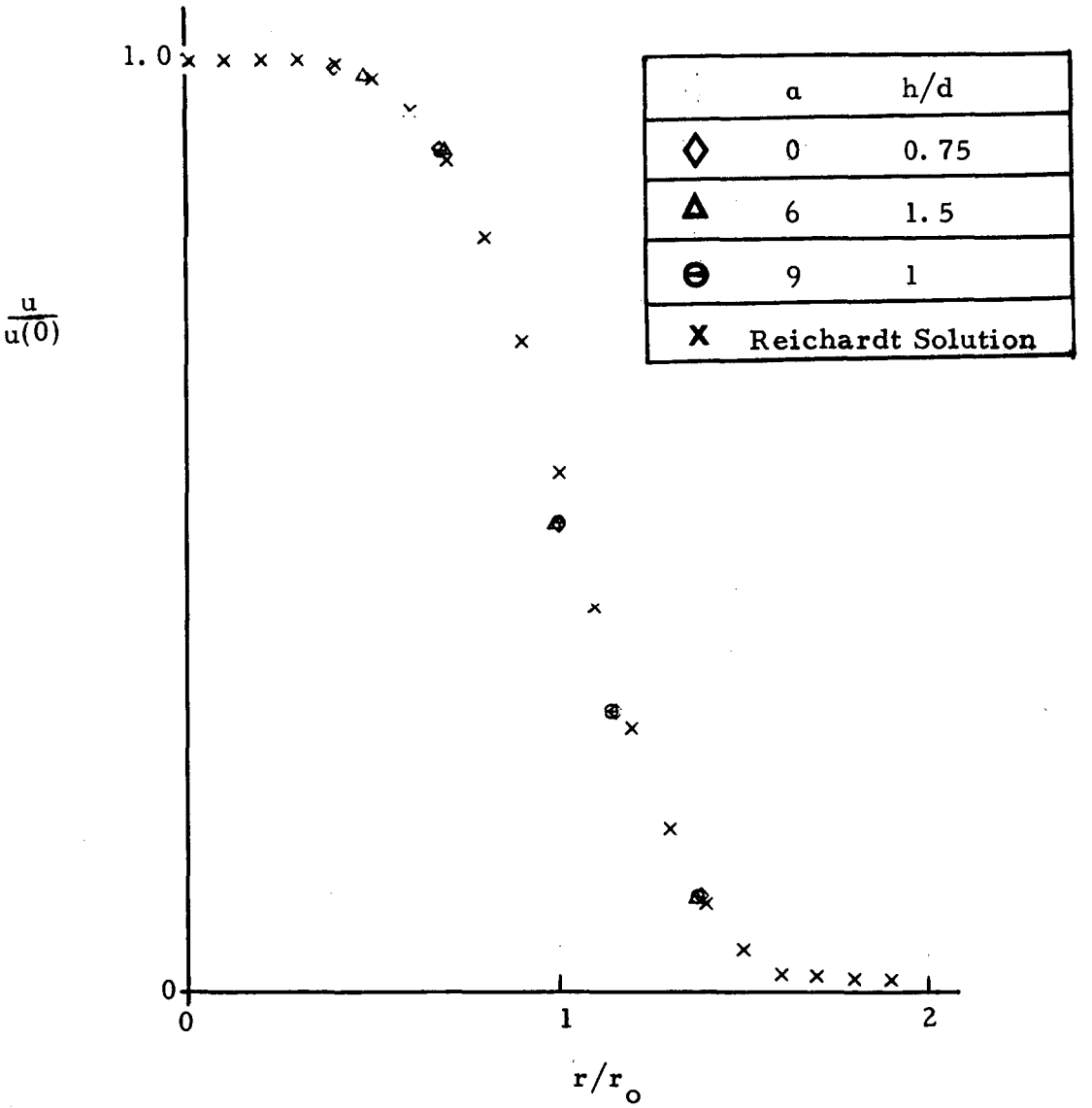

b) x/d = 2

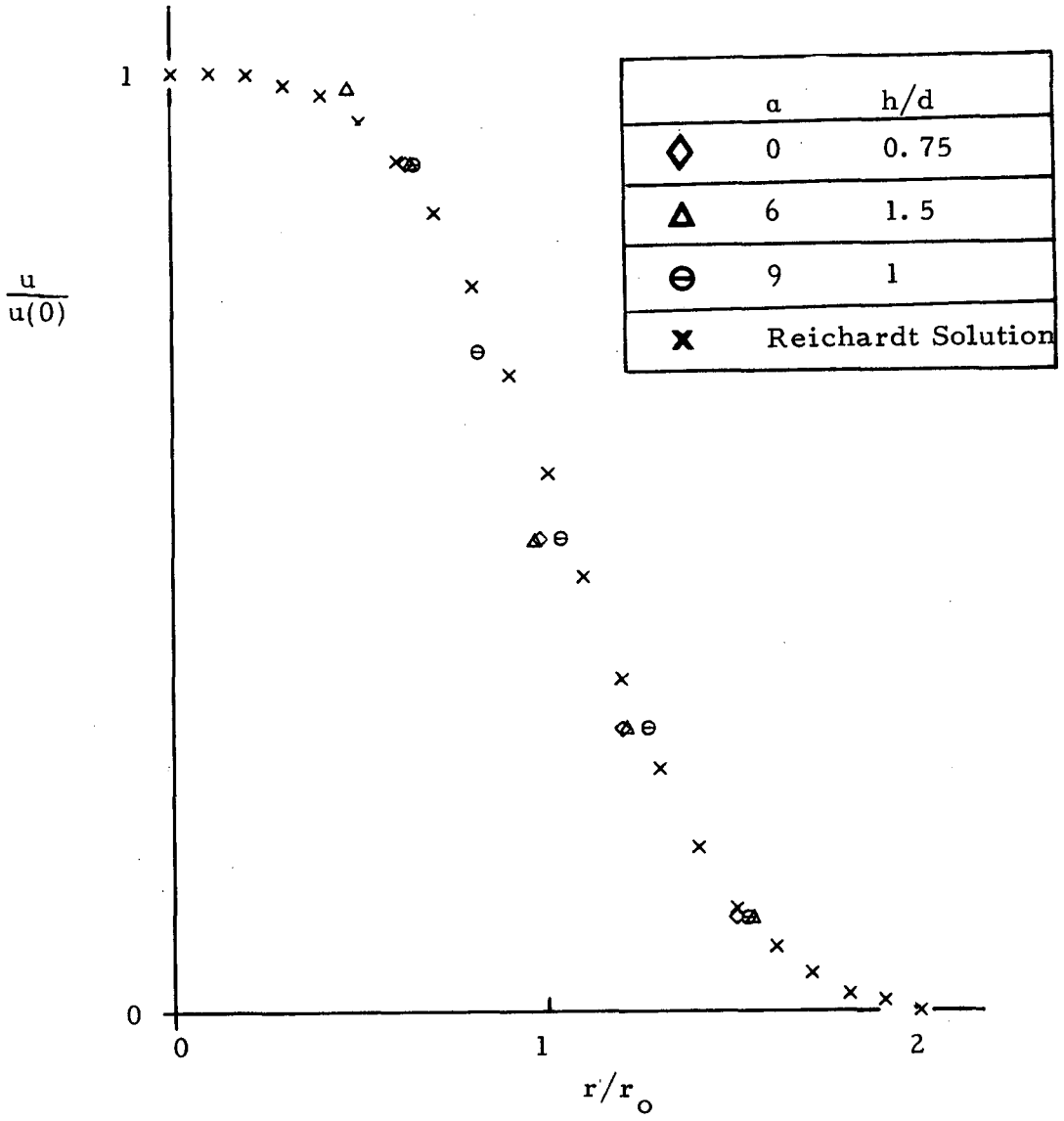

c) x/d = 3

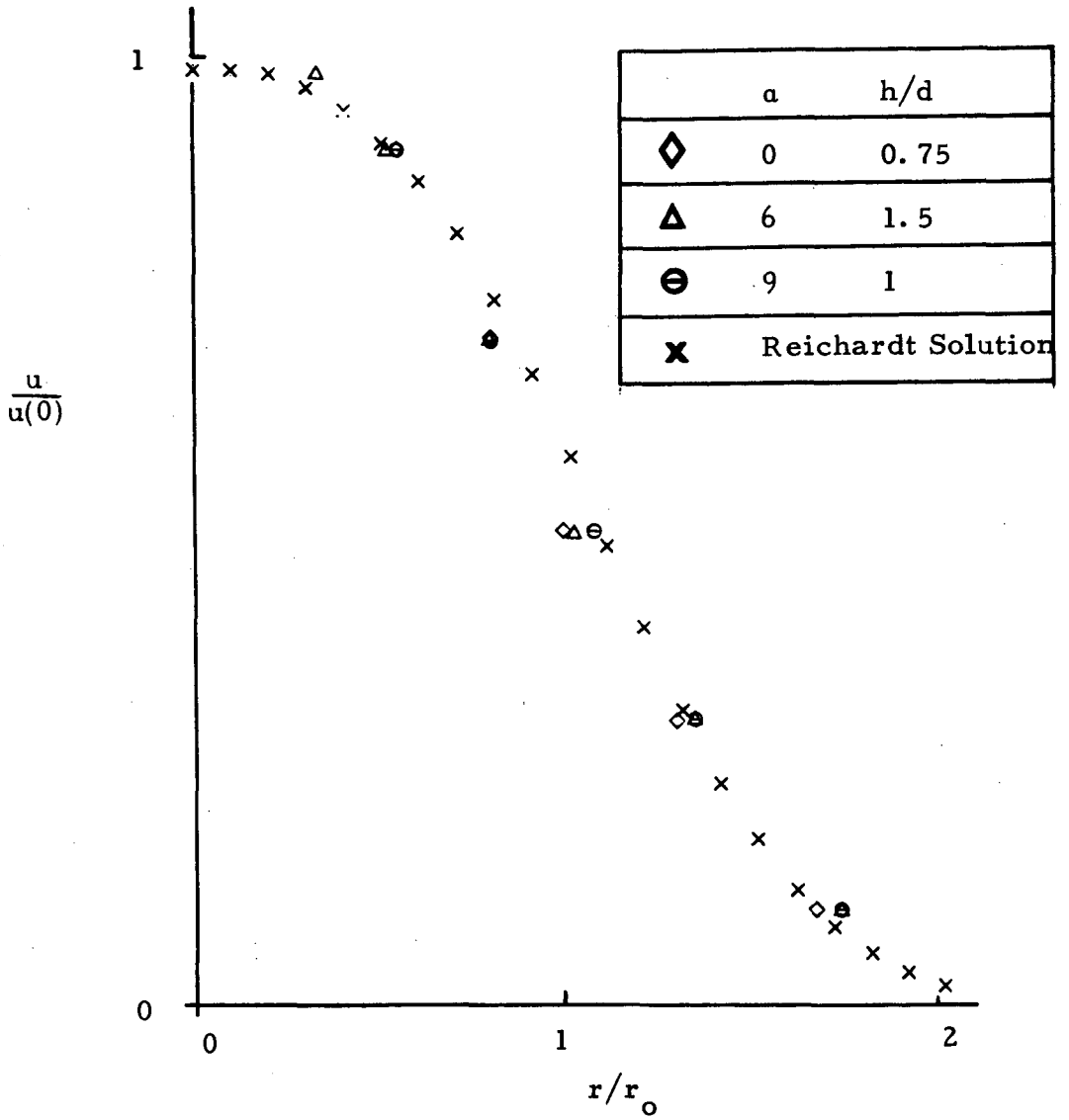

d) x/d = 4

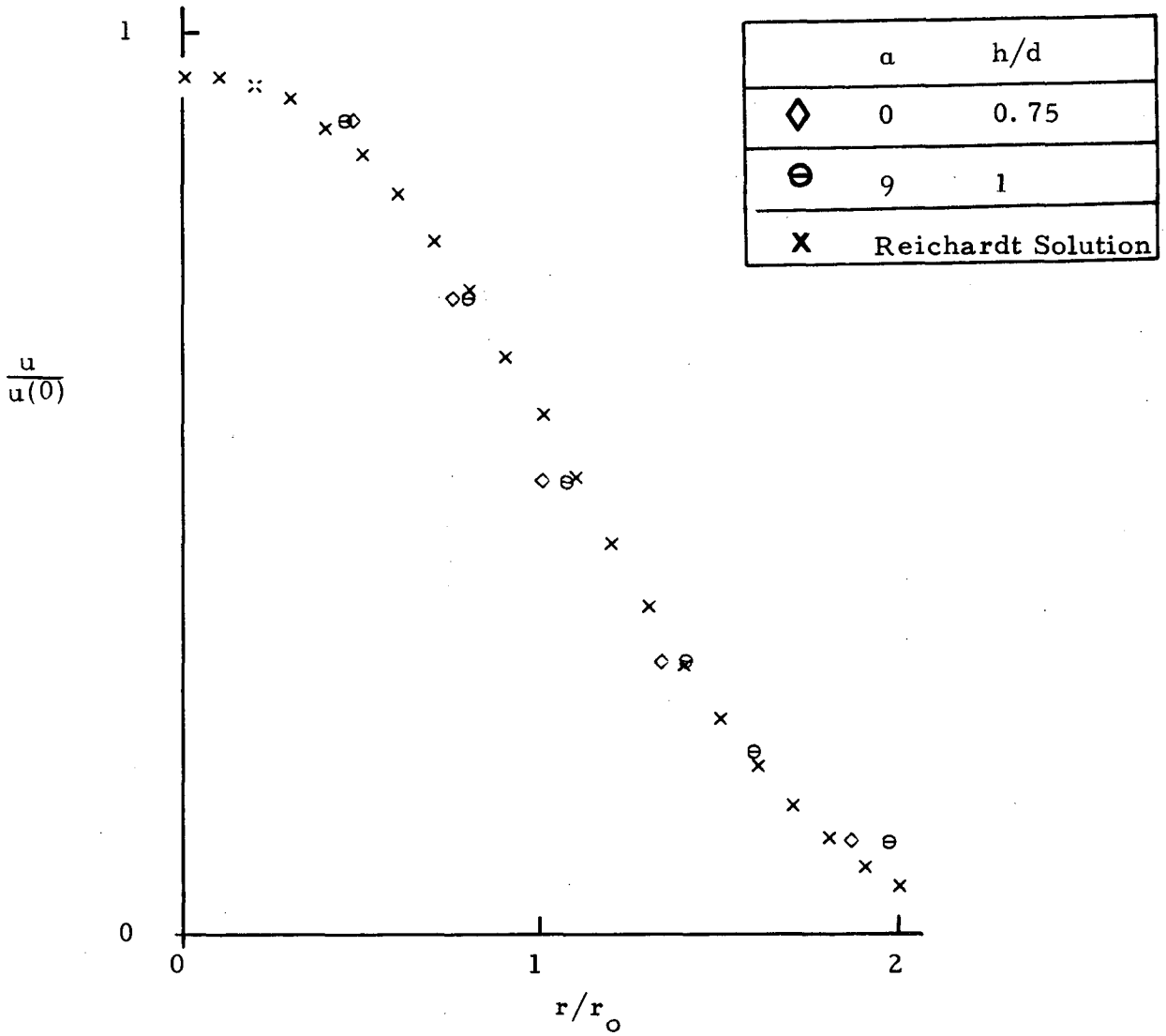

e) x/d = 5

$\chi = 0.00032x^2 + 0.0022x$

u/u(0) vs. r/r_o at $x \approx 0$

r/r_o	0	0.005	0.10	0.15	0.20	0.25	0.30	0.35	0.40	0.45
u/u(0)	1.0	0.999	0.995	0.991	0.986	0.981	0.972	0.963	0.952	0.939
r/r_o	0.50	0.55	0.60	0.65	0.70	0.75	0.80	0.85	0.90	0.95
u/u(0)	0.924	0.907	0.888	0.864	0.836	0.806	0.776	0.721	0.654	0.533

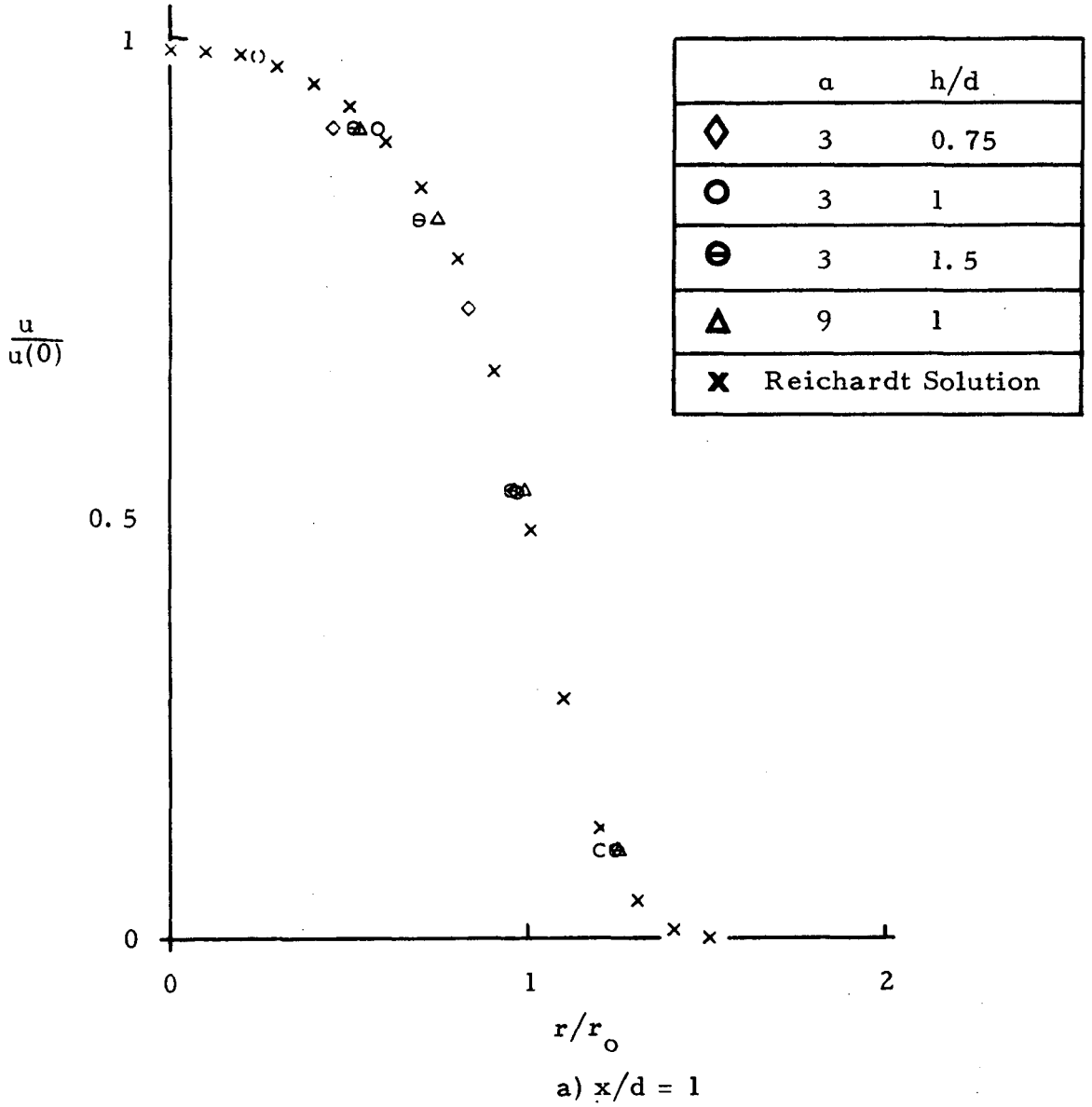

a) x/d = 1

Figure 29. u/u(0) vs. r/r_o, fully developed exit condition, for selected experimental data and the Reichardt analysis.

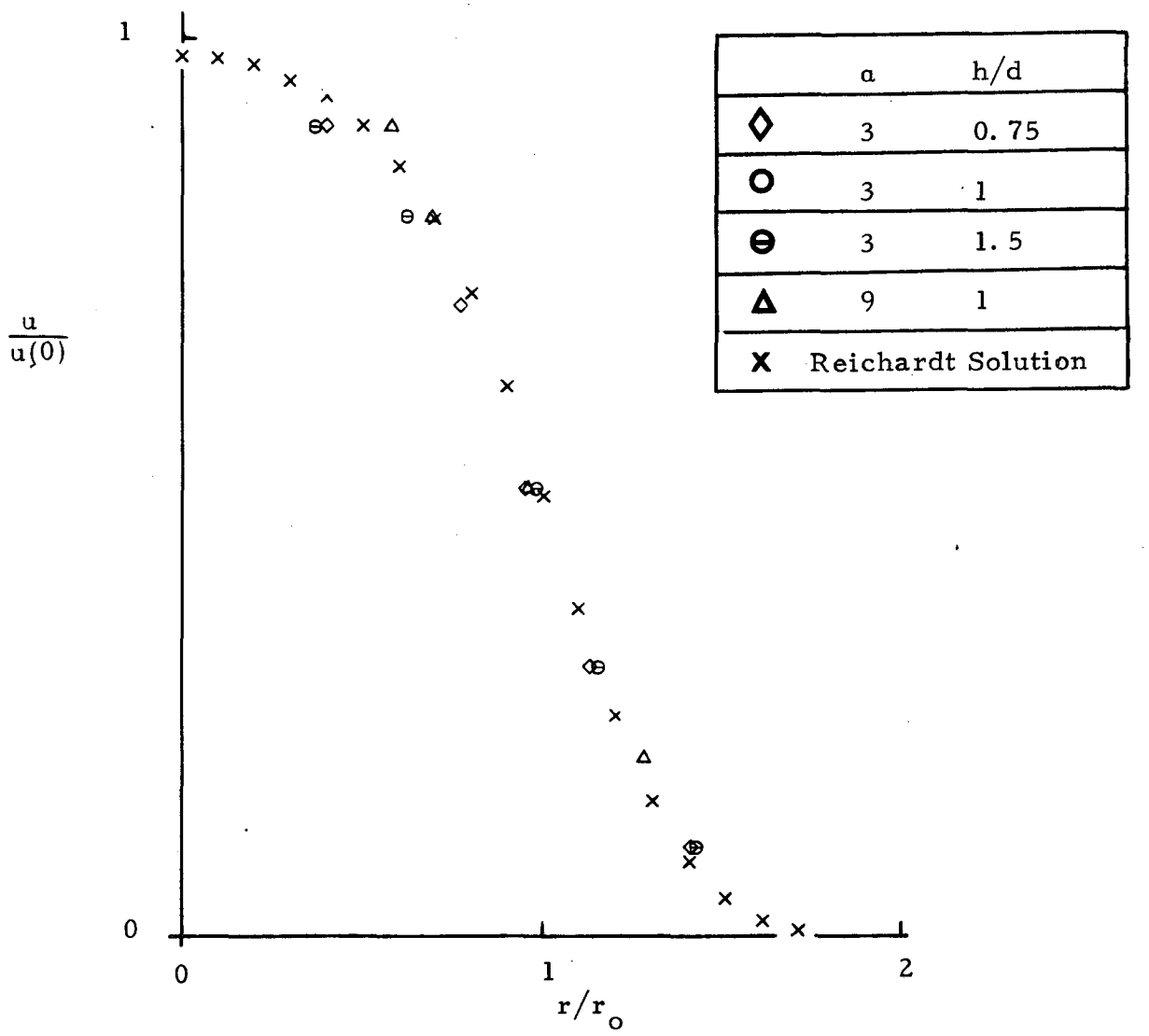

b) x/d = 2

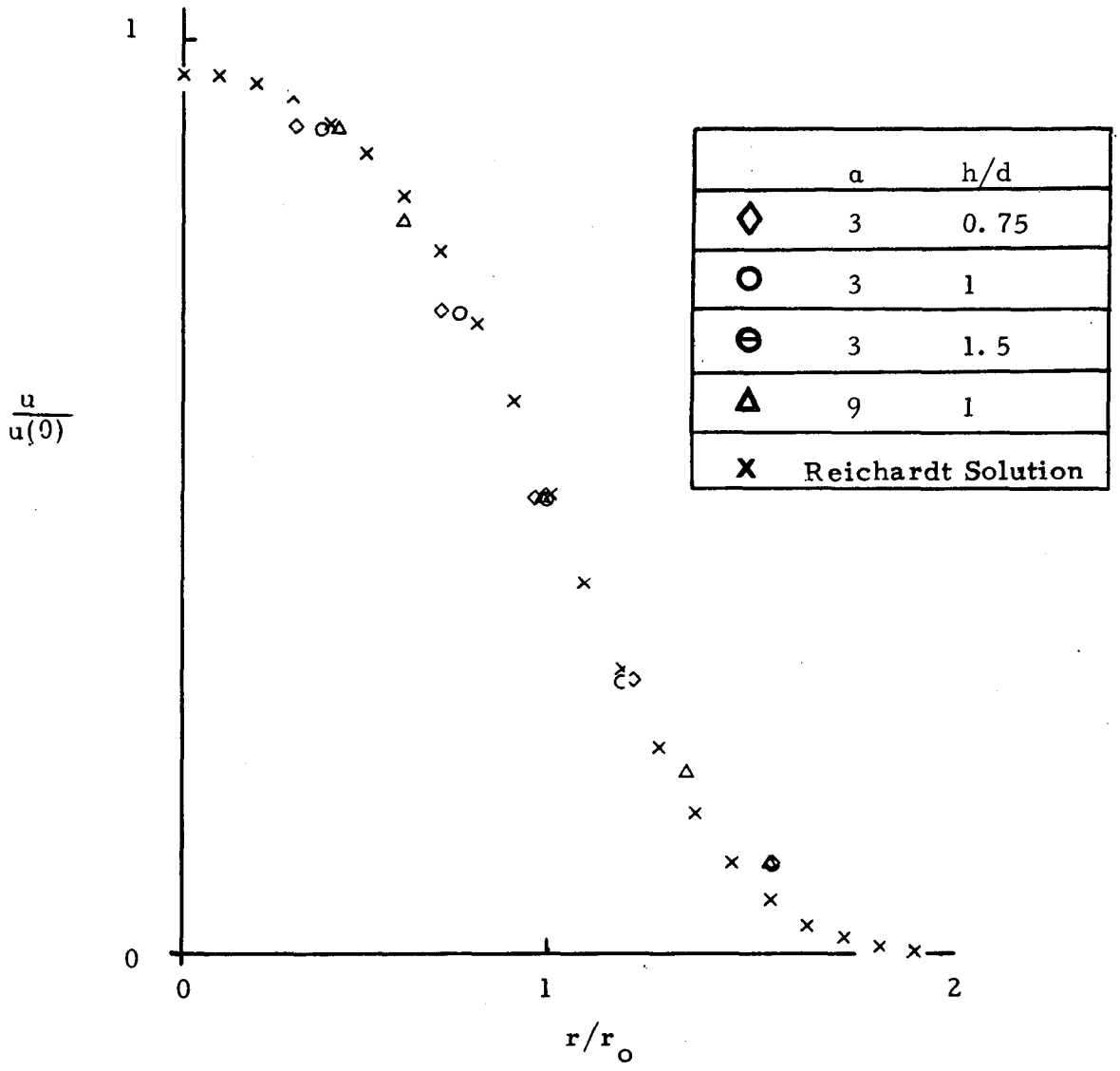

c) x/d = 3

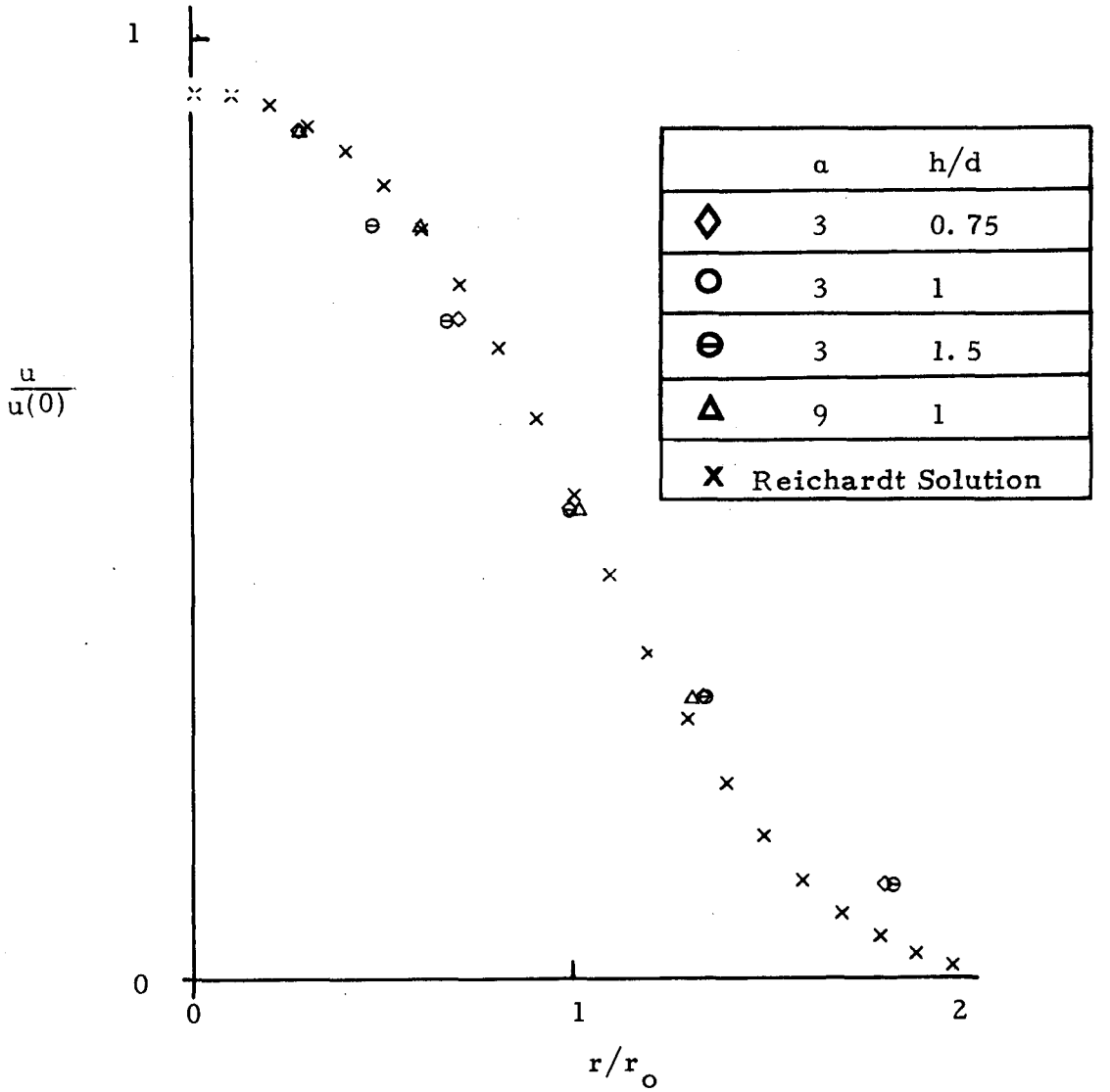

d) $x/d = 4$

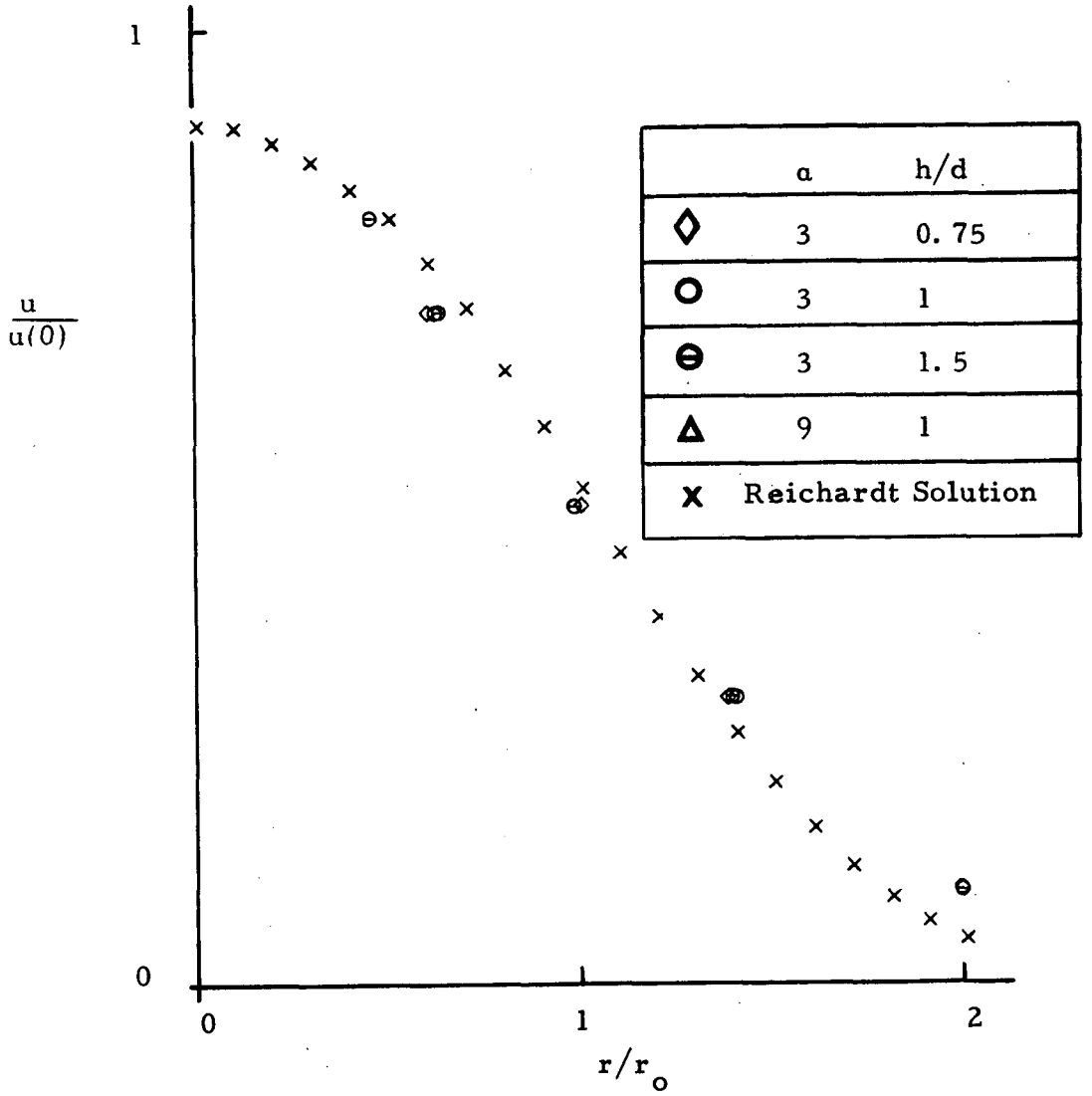

e) x/d = 5

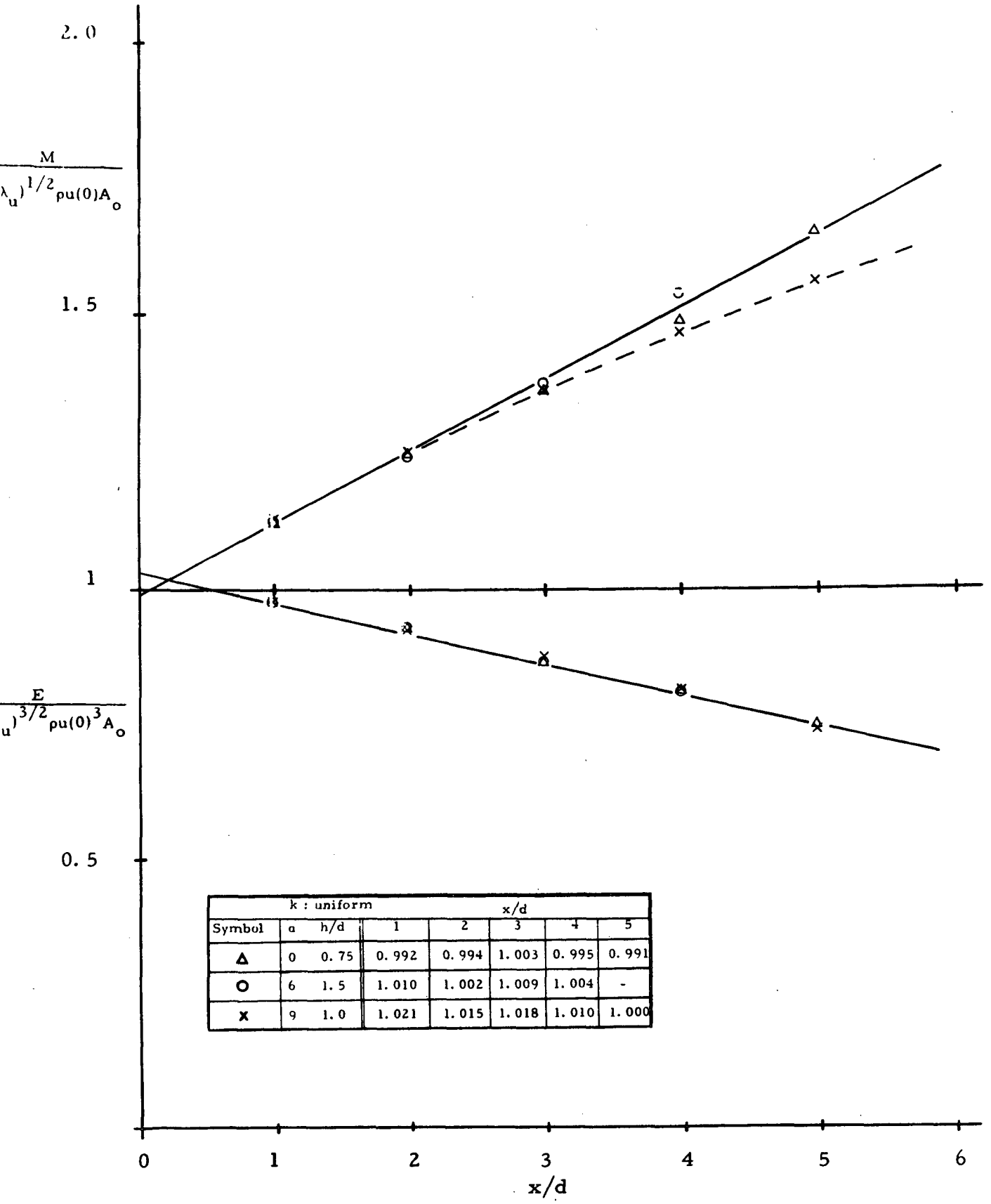

k : uniform			x/d				
Symbol	a	h/d	1	2	3	4	5
△	0	0.75	0.992	0.994	1.003	0.995	0.991
○	6	1.5	1.010	1.002	1.009	1.004	-
×	9	1.0	1.021	1.015	1.018	1.010	1.000

Figure 30. Normalized mass and energy flux values, uniform, $0 \leq |k - 1| \leq 0.03$.

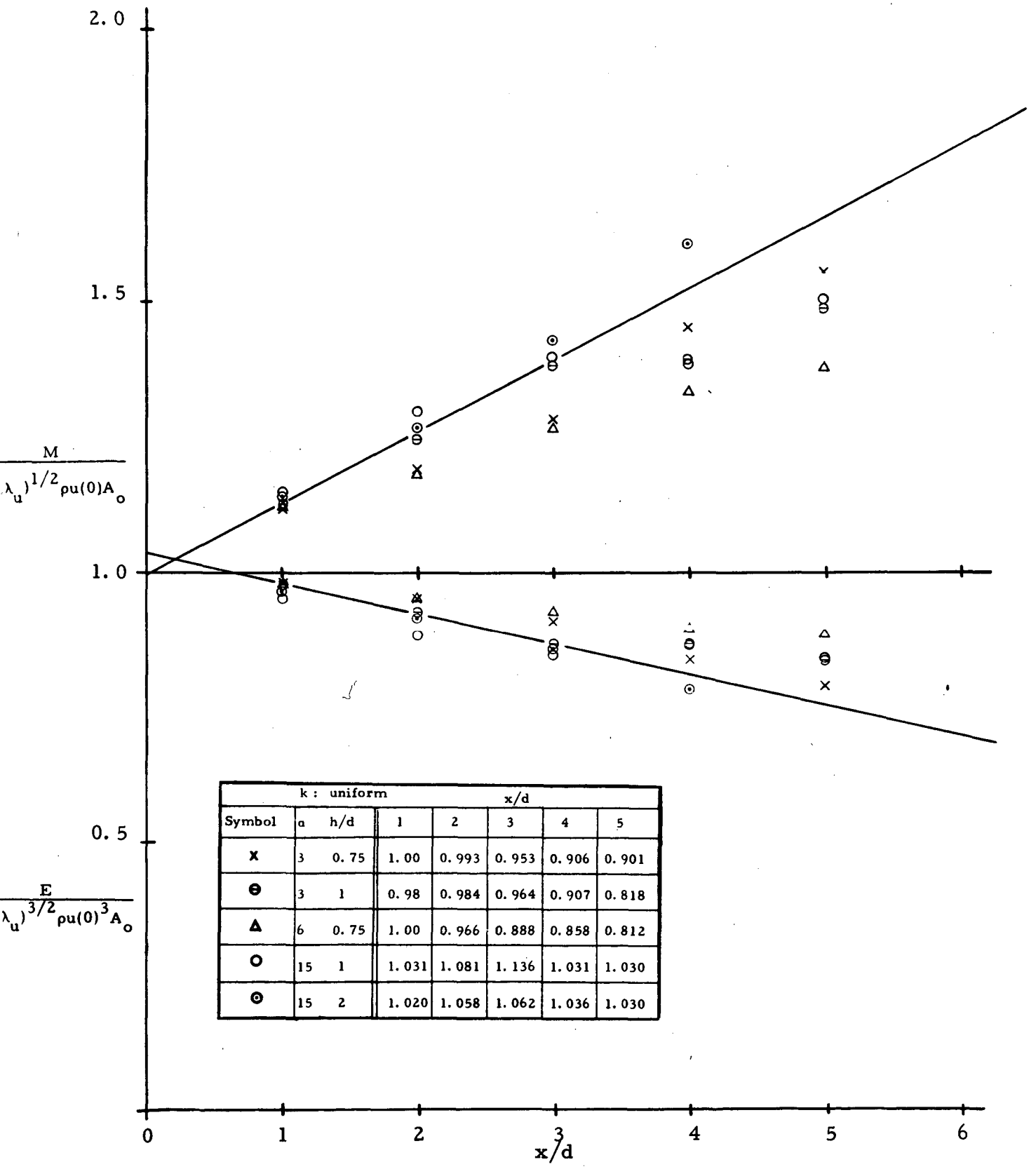

k : uniform			x/d				
Symbol	a	h/d	1	2	3	4	5
x	3	0.75	1.00	0.993	0.953	0.906	0.901
⊖	3	1	0.98	0.984	0.964	0.907	0.818
△	6	0.75	1.00	0.966	0.888	0.858	0.812
○	15	1	1.031	1.081	1.136	1.031	1.030
⊙	15	2	1.020	1.058	1.062	1.036	1.030

Figure 31. Normalized mass and energy flux values, uniform, $|k - 1| > 0.03$.

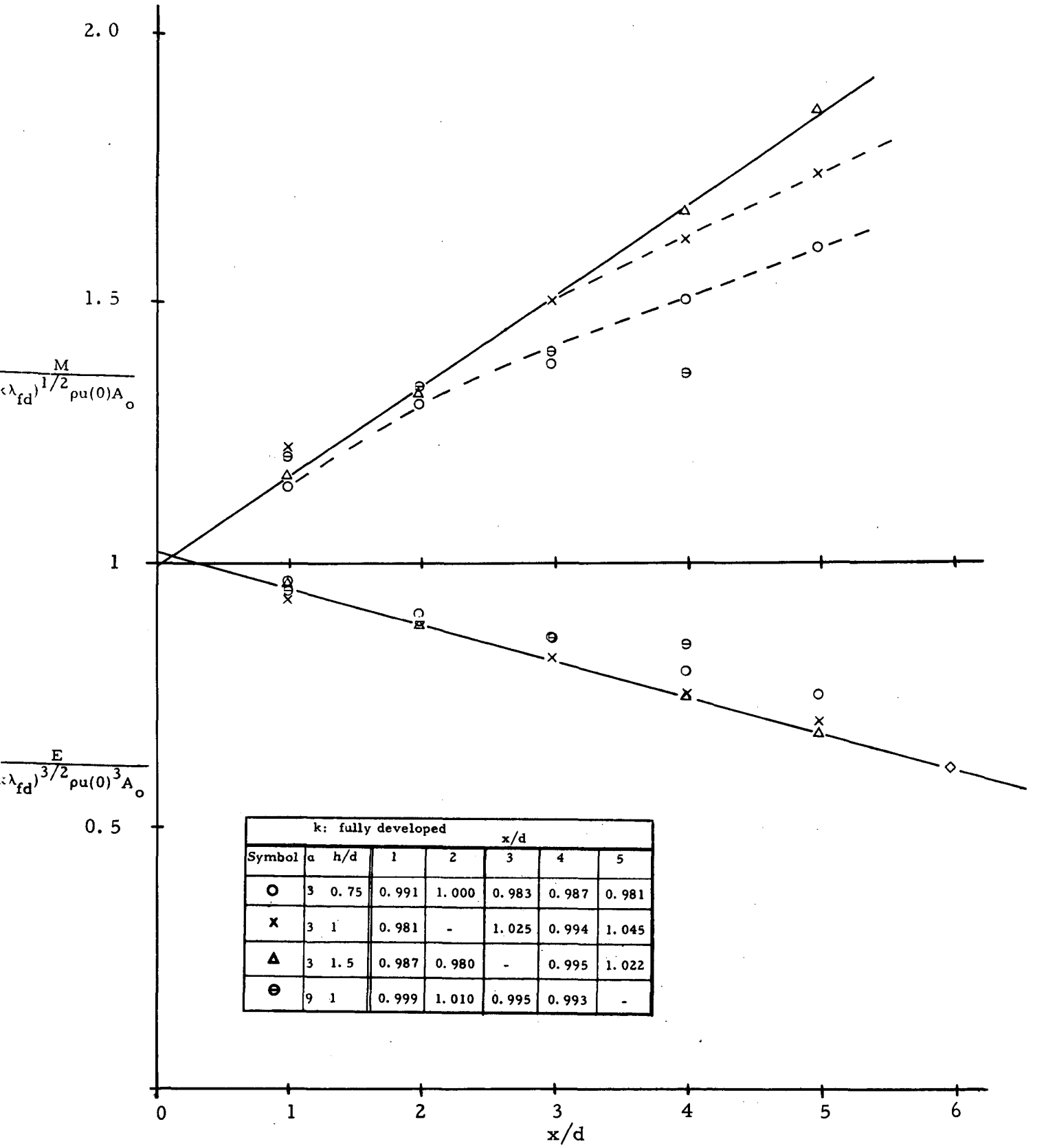

k: fully developed			x/d				
Symbol	α	h/d	1	2	3	4	5
O	3	0.75	0.991	1.000	0.983	0.987	0.981
X	3	1	0.981	-	1.025	0.994	1.045
Δ	3	1.5	0.987	0.980	-	0.995	1.022
Θ	9	1	0.999	1.010	0.995	0.993	-

Figure 32. Normalized mass and energy flux values, fully developed, $0 \leq |k - 1| \leq 0.03$.

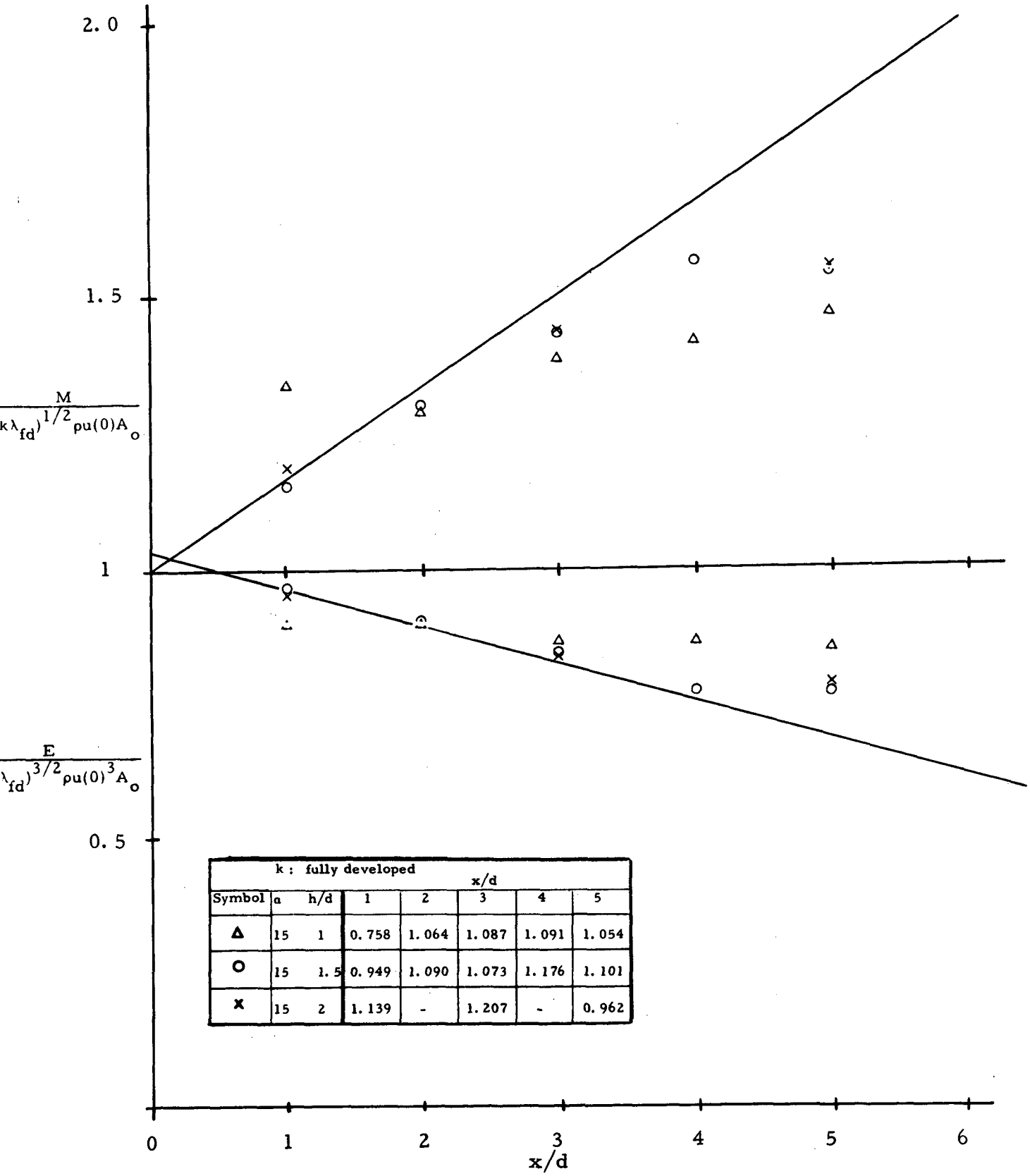

k : fully developed			x/d				
Symbol	a	h/d	1	2	3	4	5
Δ	15	1	0.758	1.064	1.087	1.091	1.054
O	15	1.5	0.949	1.090	1.073	1.176	1.101
×	15	2	1.139	-	1.207	-	0.962

Figure 33. Normalized mass and energy flux values, fully developed, $|k - 1| > 0.03$.

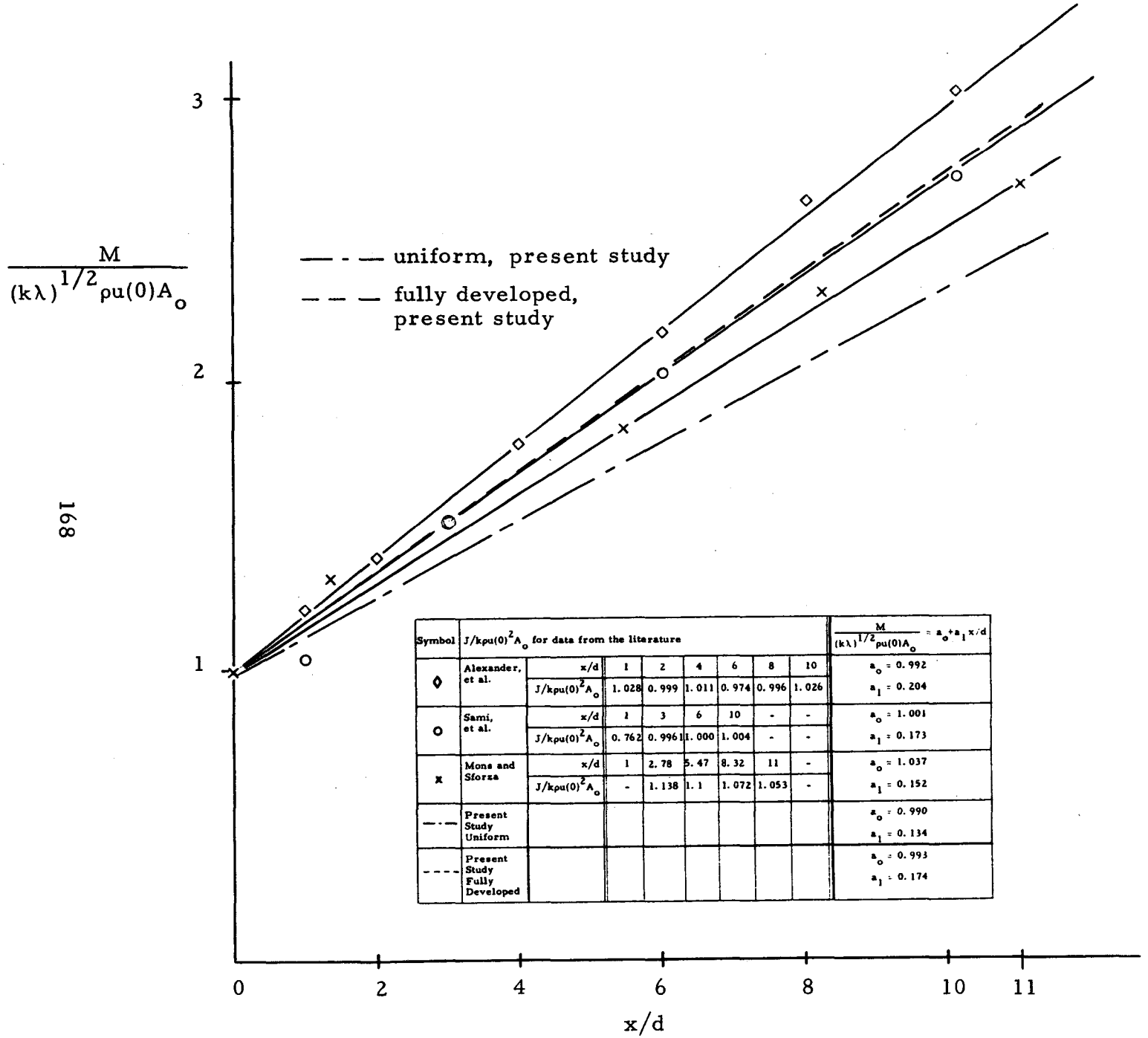

Symbol	$J/k\rho u(0)^2A_o$ for data from the literature							$\frac{M}{(k\lambda)^{1/2}\rho u(0)A_o} = a_o + a_1 x/d$
◊	Alexander, et al.	x/d	1	2	4	6	8	10	$a_o = 0.992$
		$J/k\rho u(0)^2A_o$	1.028	0.999	1.011	0.974	0.996	1.026	$a_1 = 0.204$
o	Sami, et al.	x/d	1	3	6	10	-	-	$a_o = 1.001$
		$J/k\rho u(0)^2A_o$	0.762	0.996	1.000	1.004	-	-	$a_1 = 0.173$
x	Mons and Sforza	x/d	1	2.78	5.47	8.32	11	-	$a_o = 1.037$
		$J/k\rho u(0)^2A_o$	-	1.138	1.1	1.072	1.053	-	$a_1 = 0.152$
—·—	Present Study Uniform								$a_o = 0.990$
									$a_1 = 0.134$
----	Present Study Fully Developed								$a_o = 0.993$
									$a_1 = 0.174$

Figure 34. Normalized mass flux values as evaluated from references [12], [14] and [21]. (Data for Crow and Champagne [11] not shown, $a_1 = 0.136$ for $0 \leq x/d \leq 2$; $a_1 = 0.292$ for $x/d > 6$.)

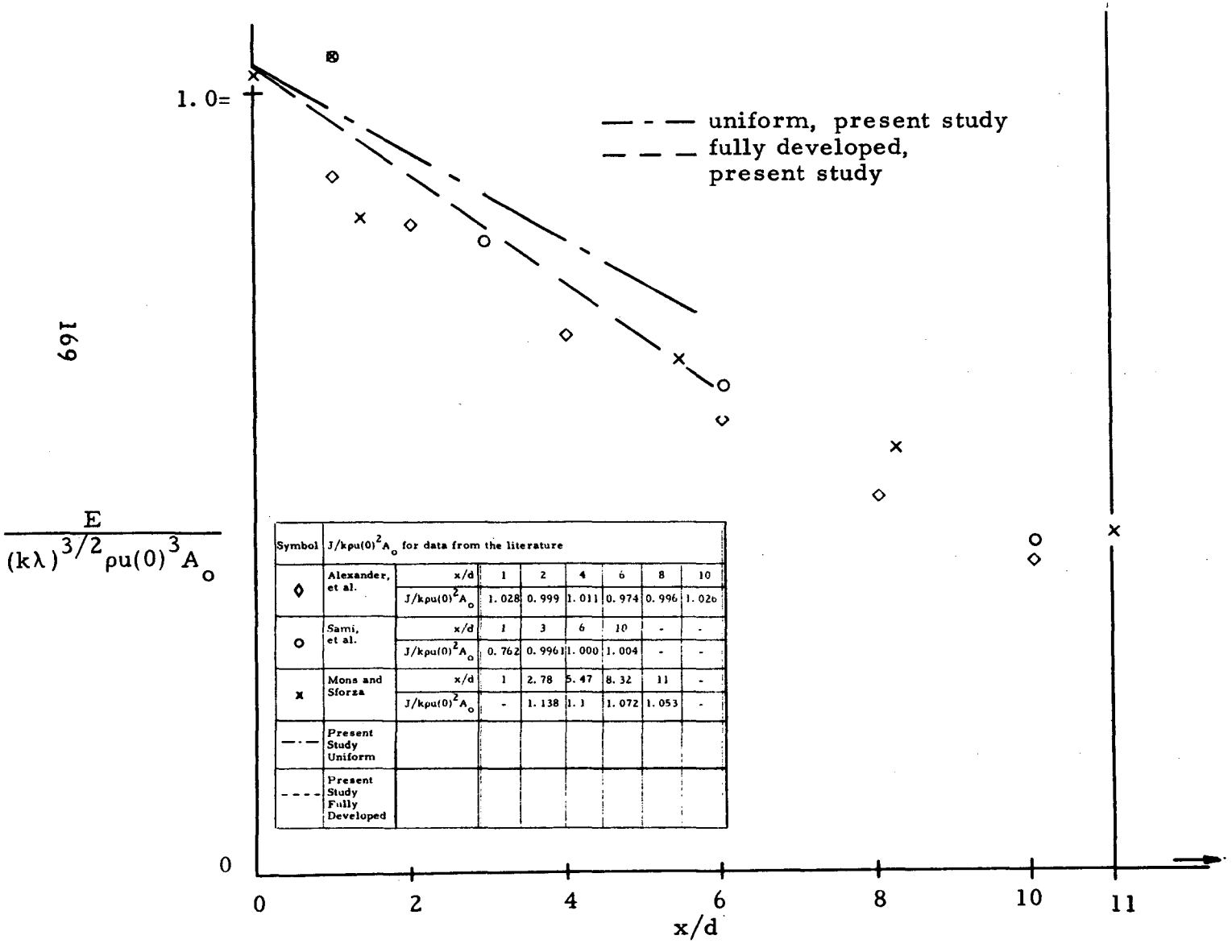

Symbol	$J/k\rho u(0)^2 A_o$ for data from the literature						
◇	Alexander, et al.	x/d	1	2	4	6	8	10
		$J/k\rho u(0)^2 A_o$	1.028	0.999	1.011	0.974	0.996	1.026
○	Sami, et al.	x/d	1	3	6	10	-	-
		$J/k\rho u(0)^2 A_o$	0.762	0.9961	1.000	1.004	-	-
×	Mons and Sforza	x/d	1	2.78	5.47	8.32	11	-
		$J/k\rho u(0)^2 A_o$	-	1.138	1.1	1.072	1.053	-
—·—	Present Study Uniform							
- - - -	Present Study Fully Developed							

Figure 35. Normalized energy flux values as evaluated from references [12], [14] and [21].

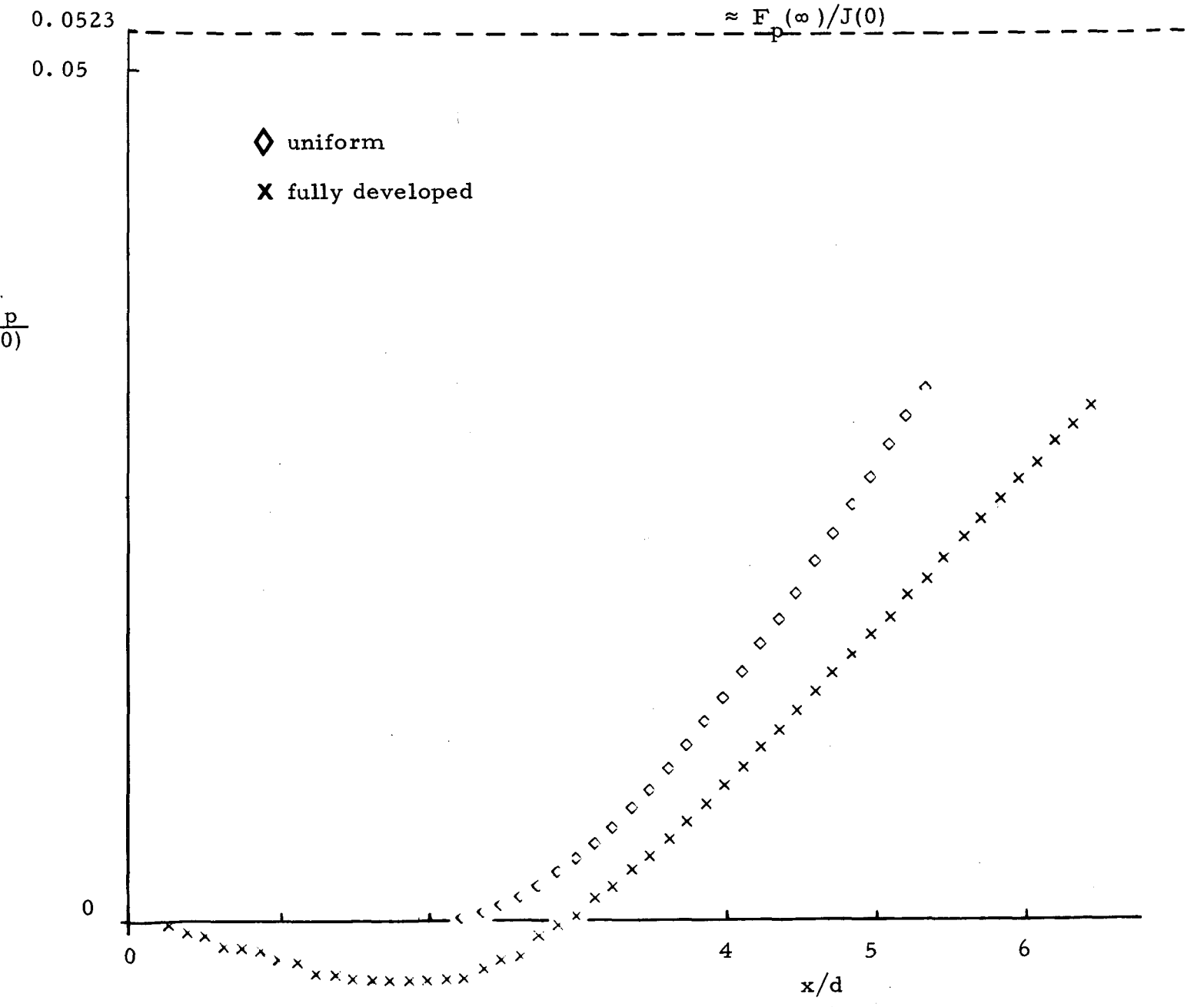

Figure 36. $F_p/J(0)$ vs. x/d, a = 3, h/d = 0.75.

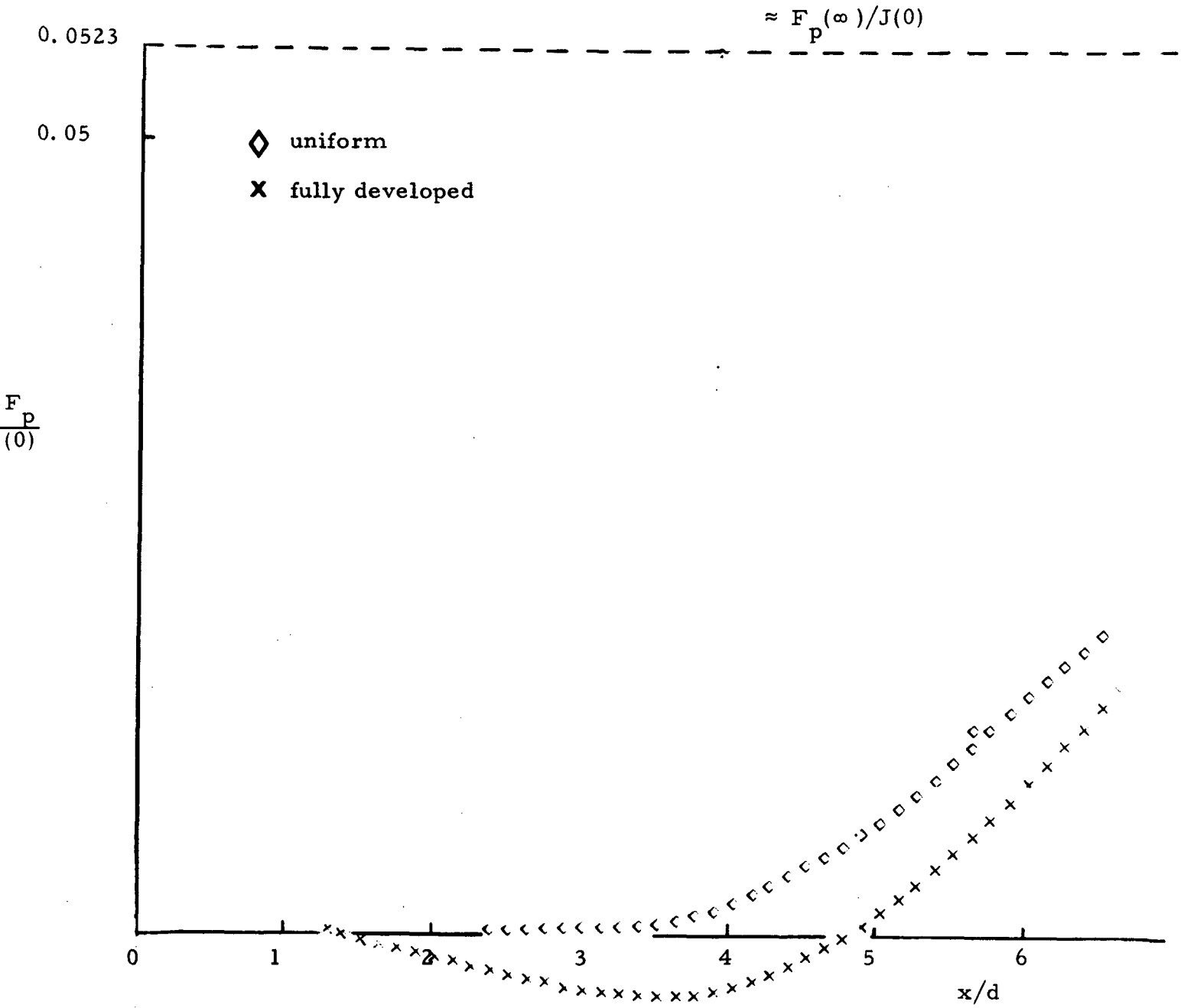

Figure 37. $F_p/J(0)$ vs. x/d, a = 3, h/d = 1.

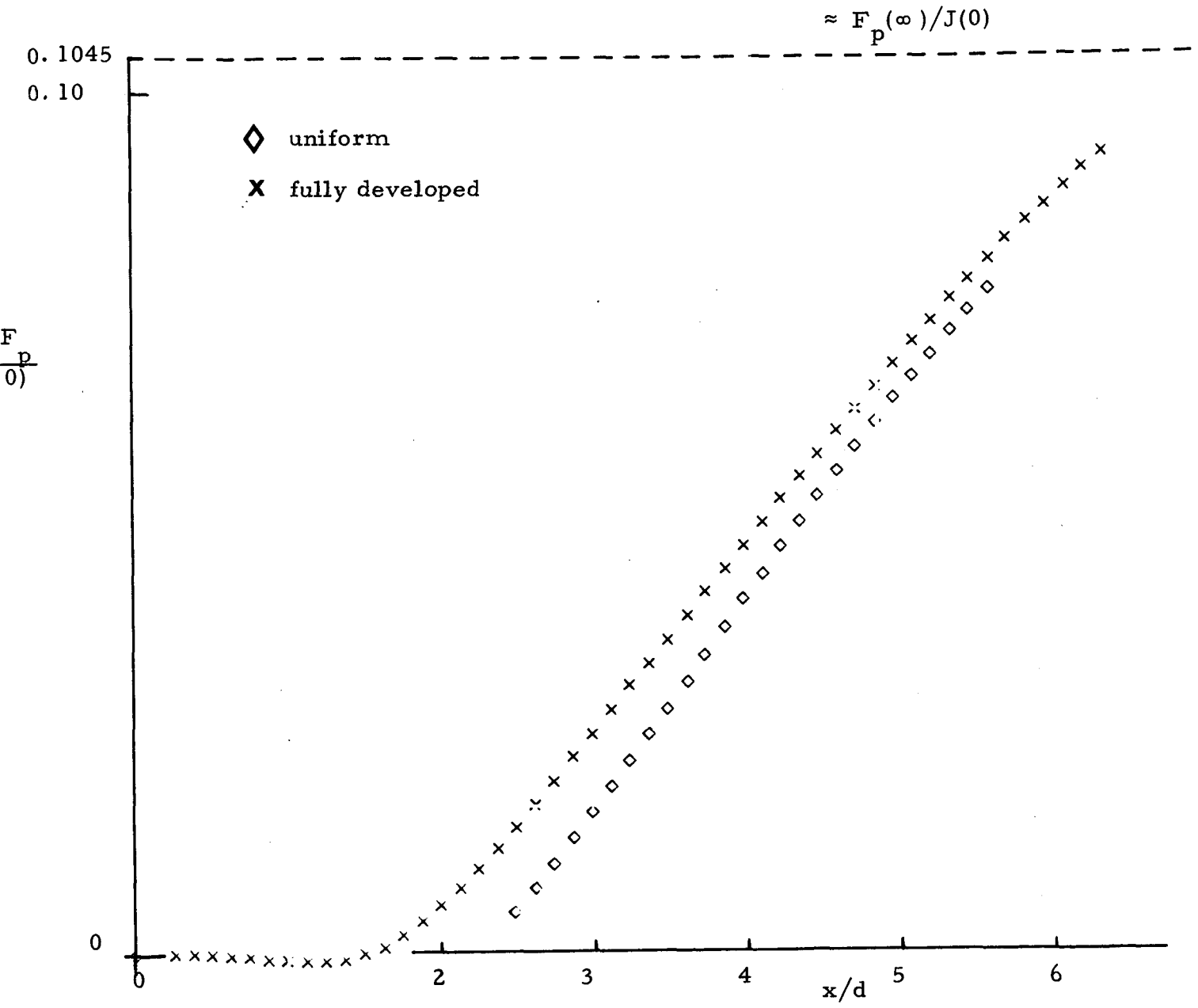

Figure 38. $F_p/J(0)$ vs. x/d, a = 6, h/d = 0.75.

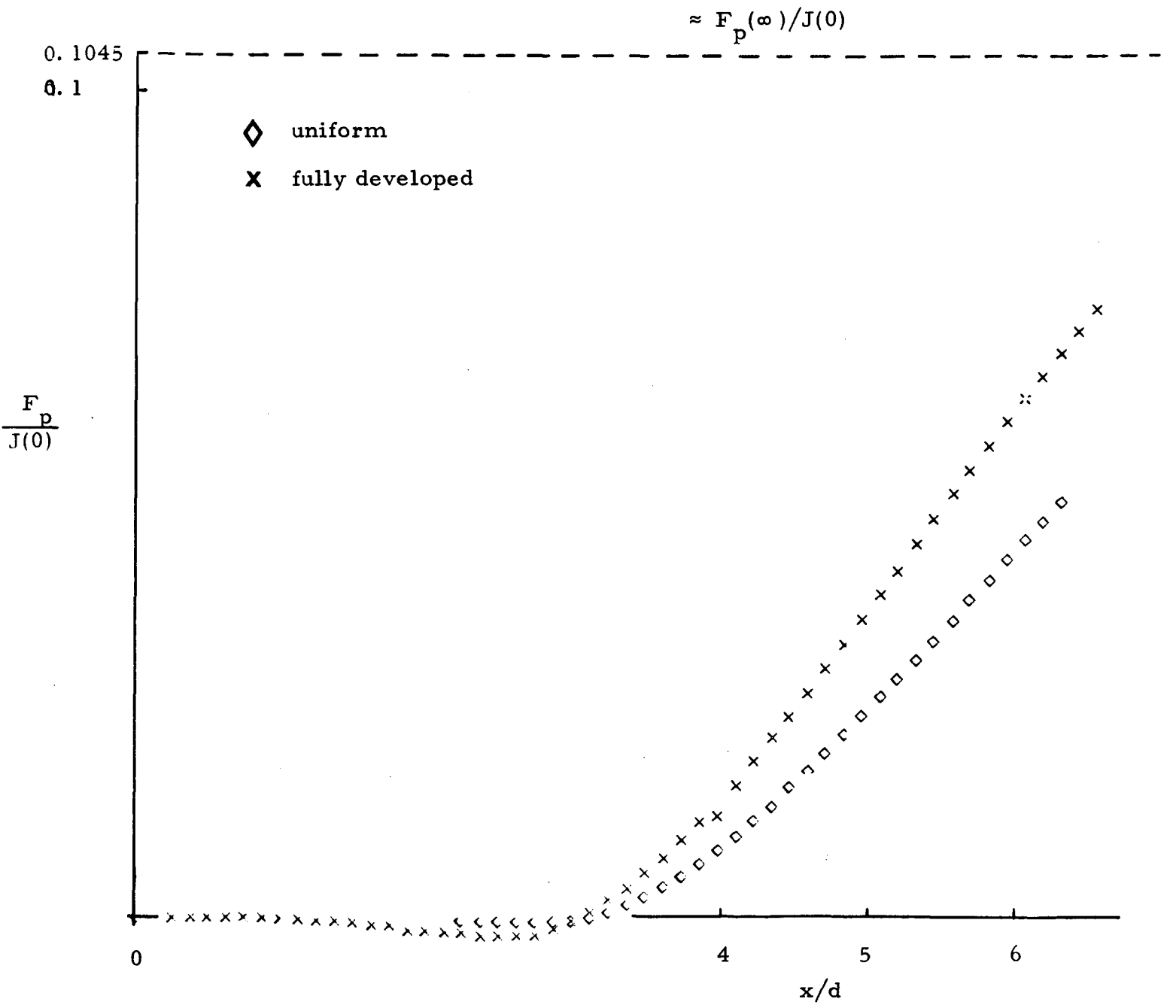

Figure 39. $F_p/J(0)$ vs. x/d, $\alpha = 6$, $h/d = 1$.

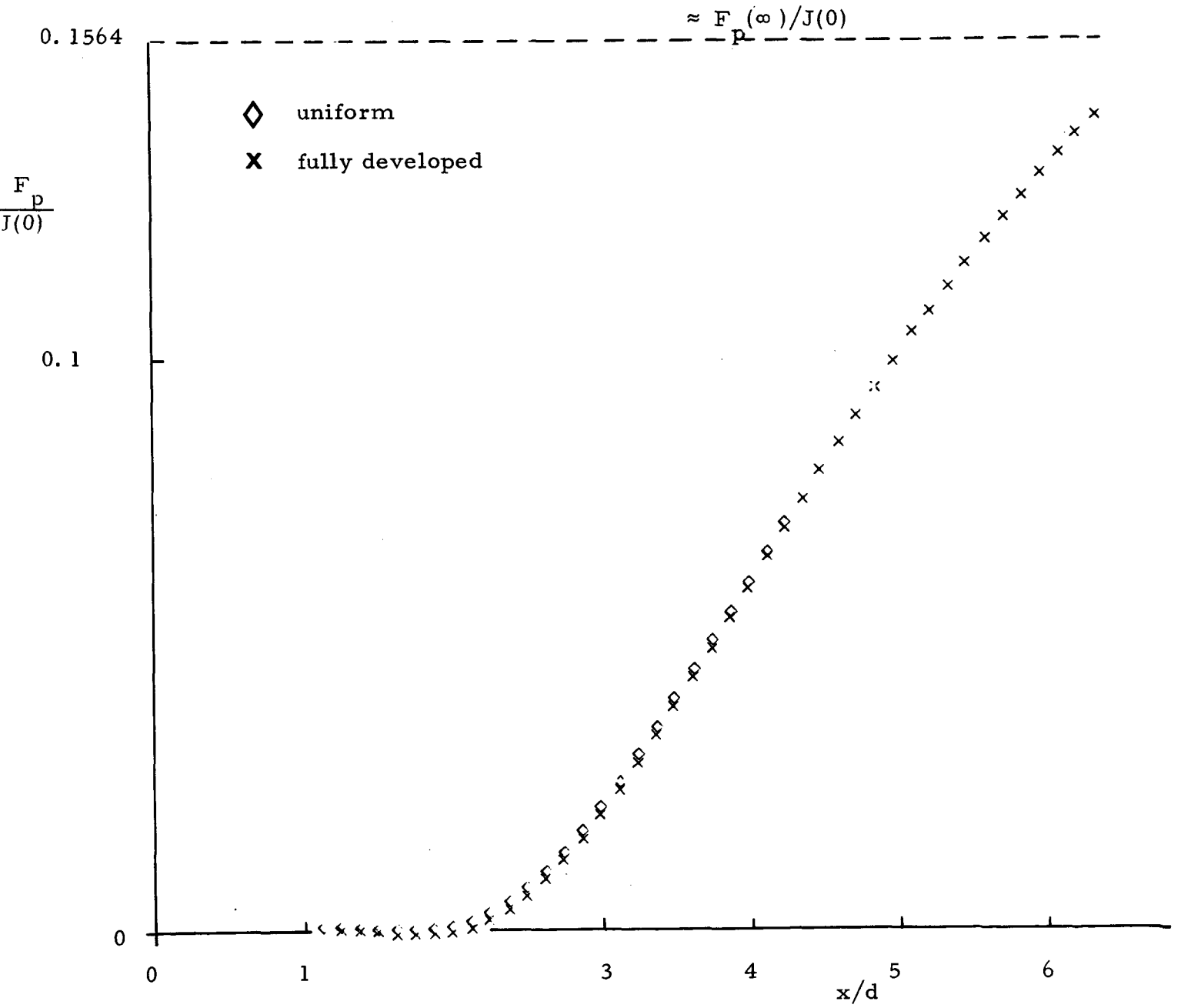

Figure 40. $F_p/J(0)$ vs. x/d, $\alpha = 9$, $h/d = 1$.

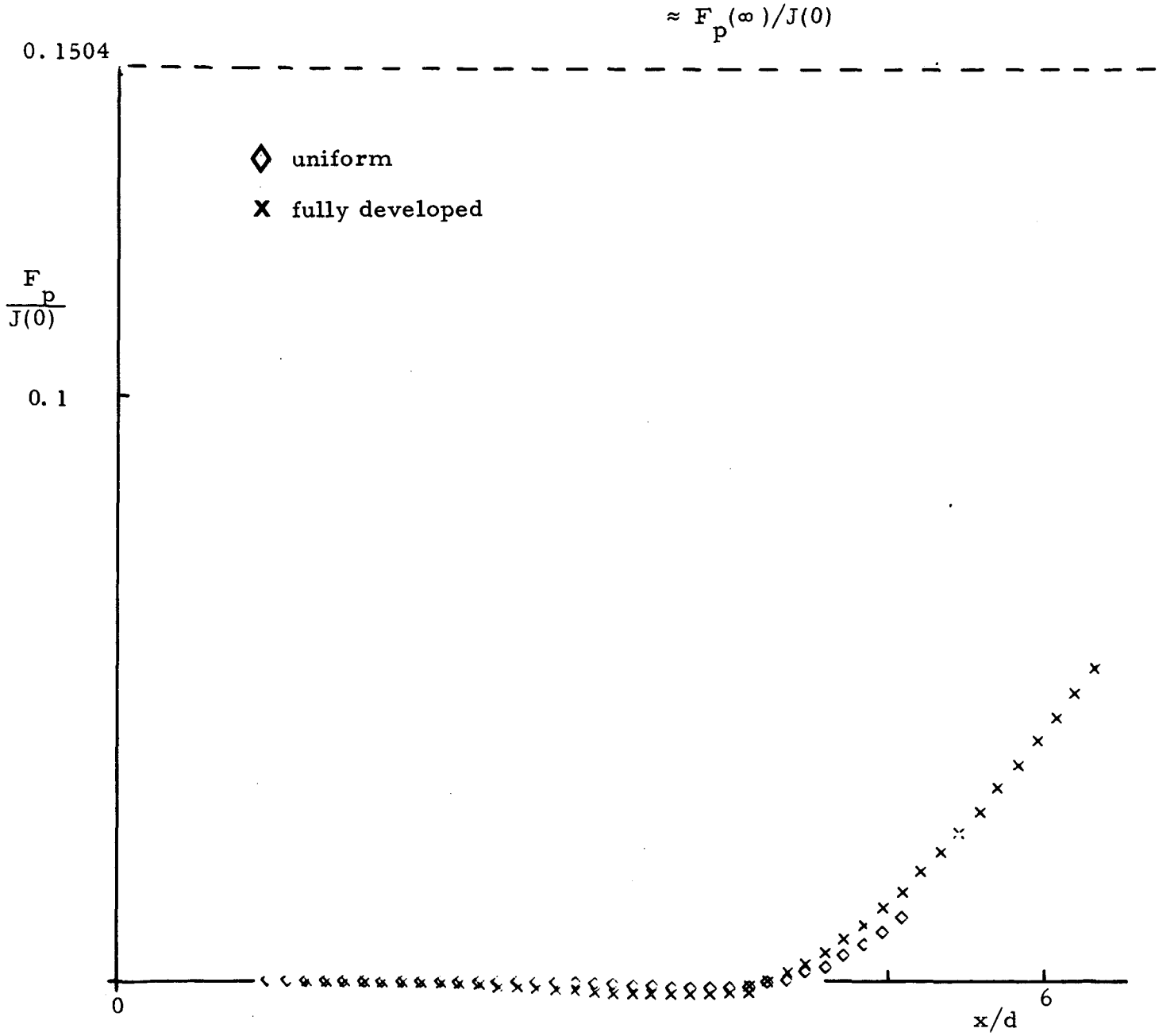

Figure 41. $F_p/J(0)$ vs. x/d, $\alpha = 9$, $h/d = 1.5$.

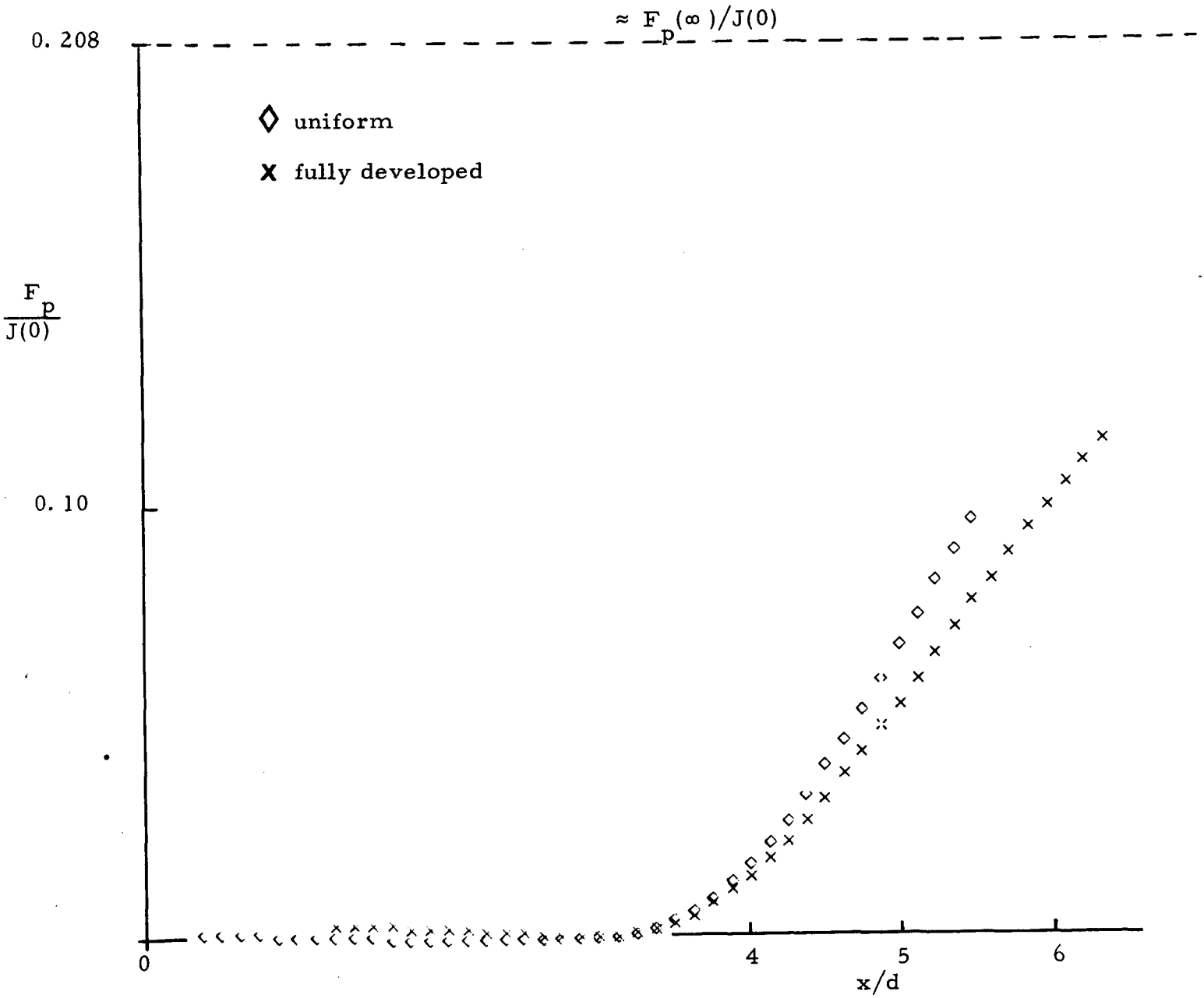

Figure 42. $F_p/J(0)$ vs. x/d, a = 12, h/d = 1.5.

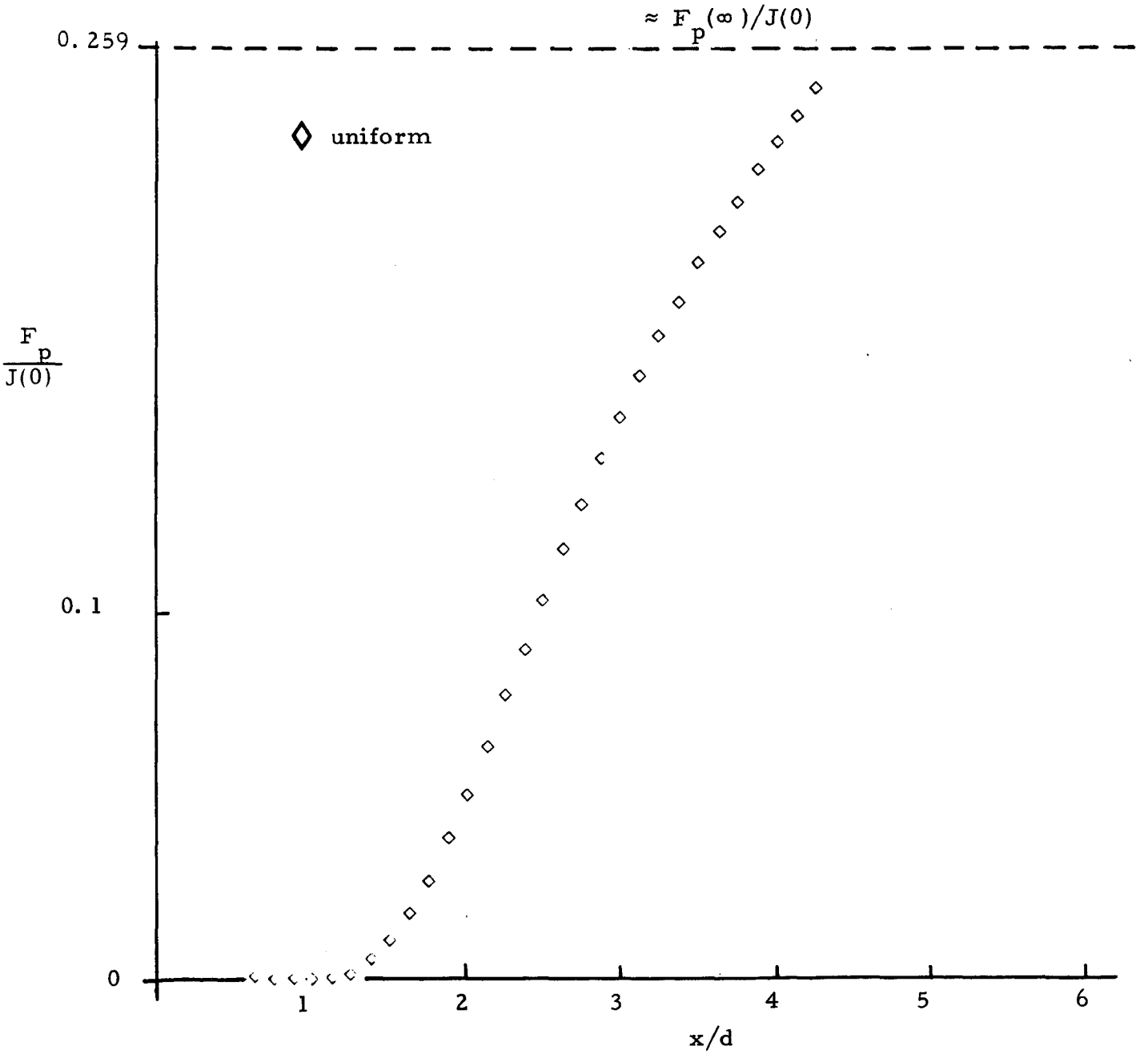

Figure 43. $F_p/J(0)$ vs. x/d, $\alpha = 15$, $h/d = 1$.

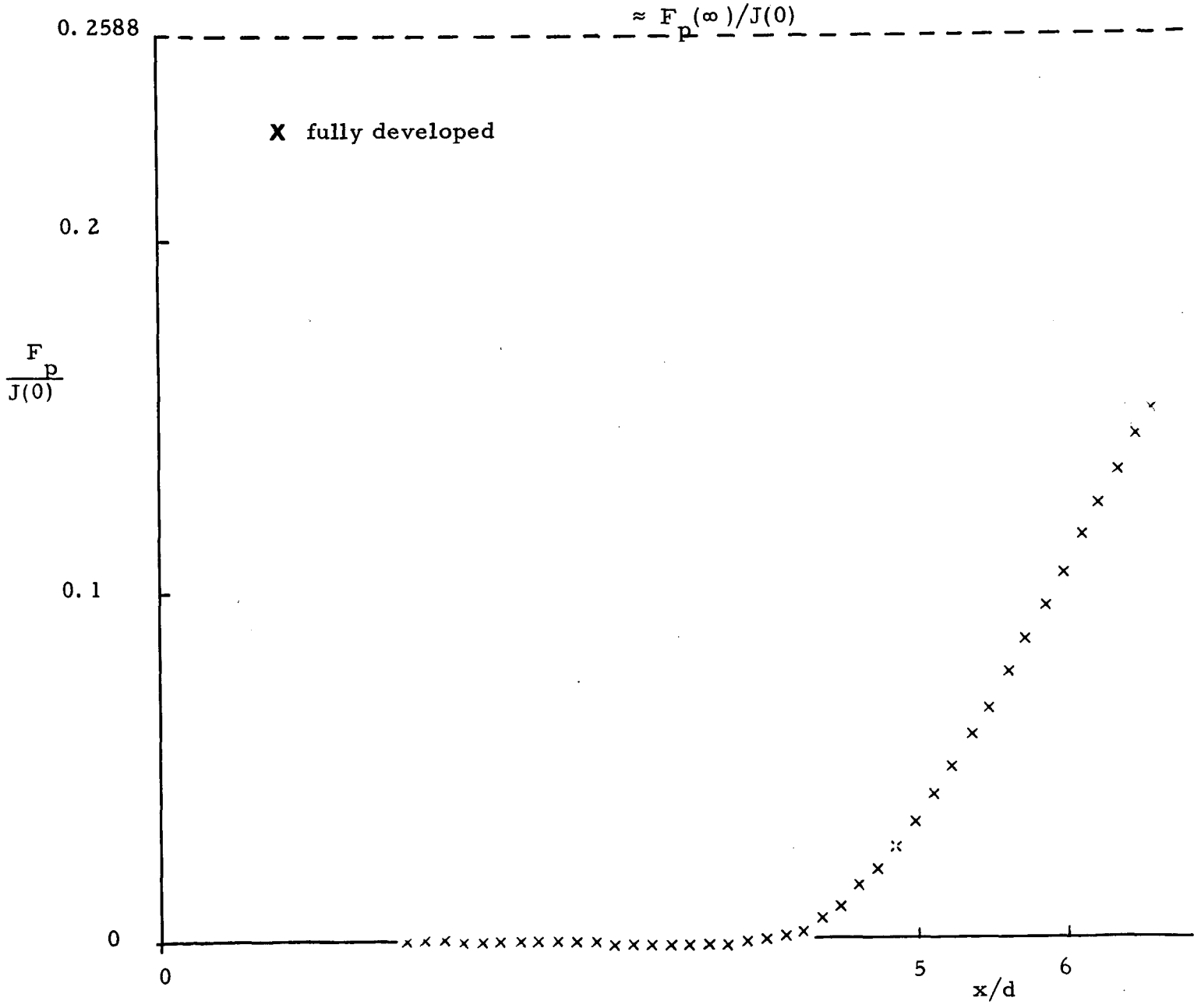

Figure 44. $F_p/J(0)$ vs. x/d, $\alpha = 15$, $h/d = 2$.

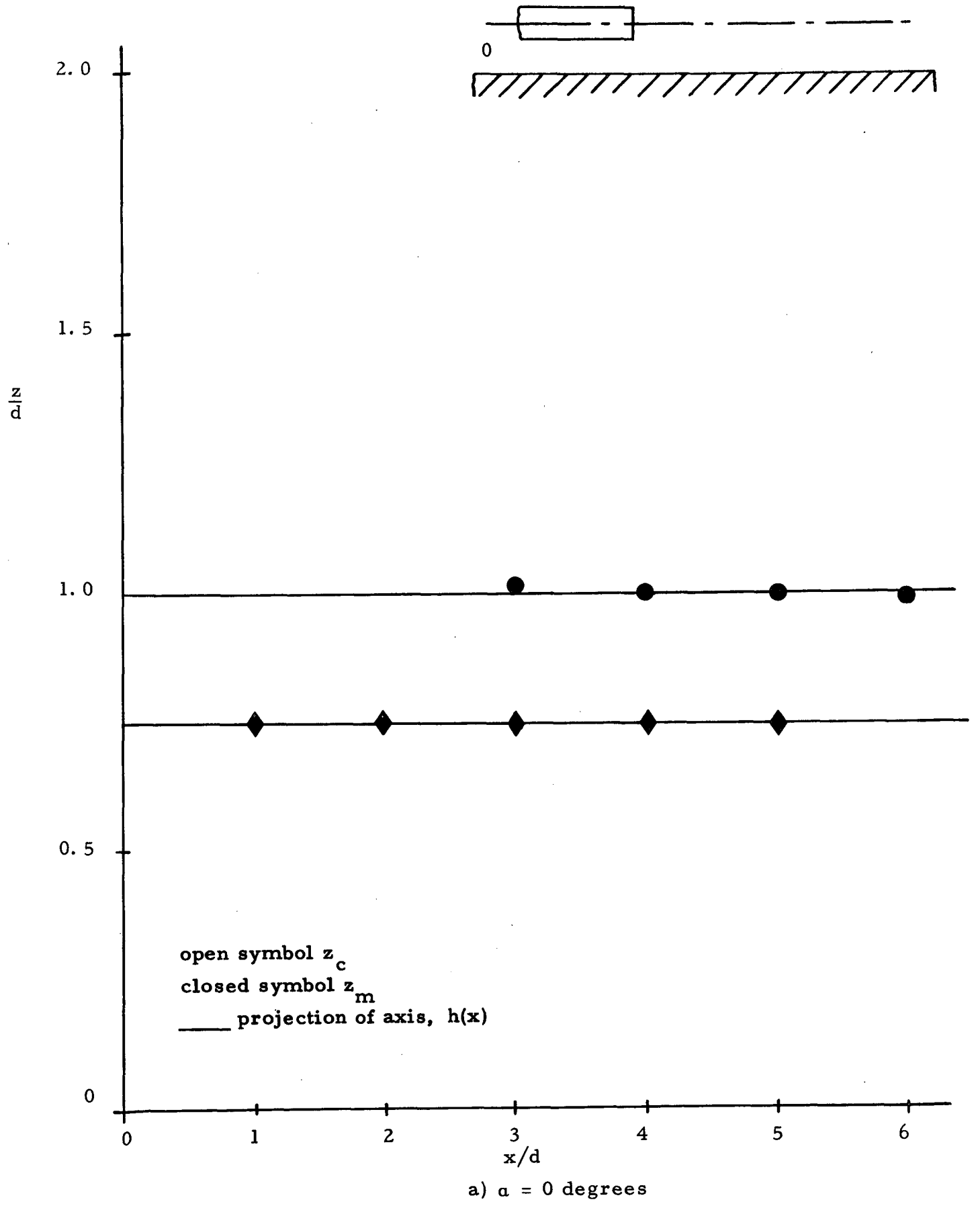

Figure 45. z_c and z_m vs. x/d, uniform.

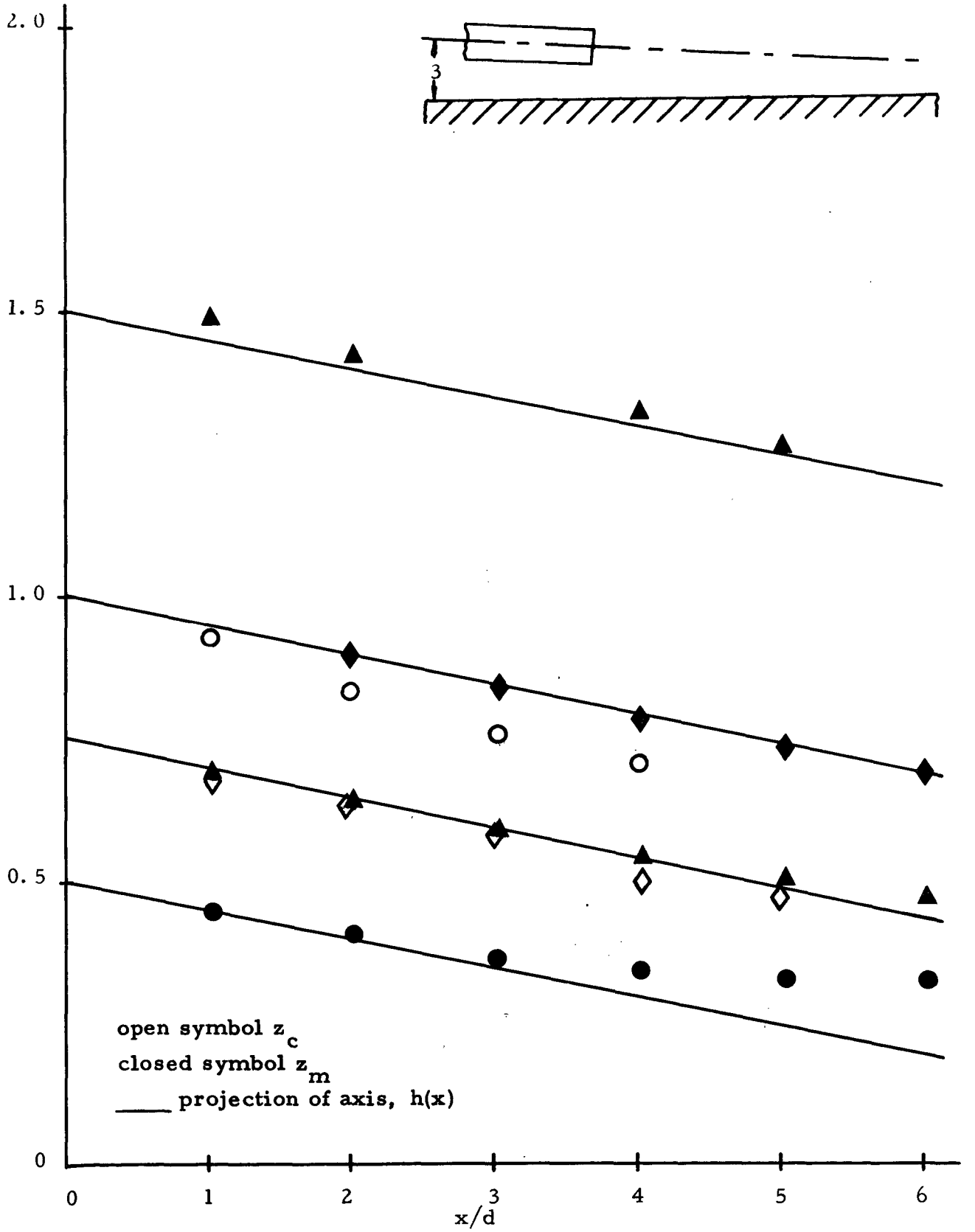

b) α = 3 degrees

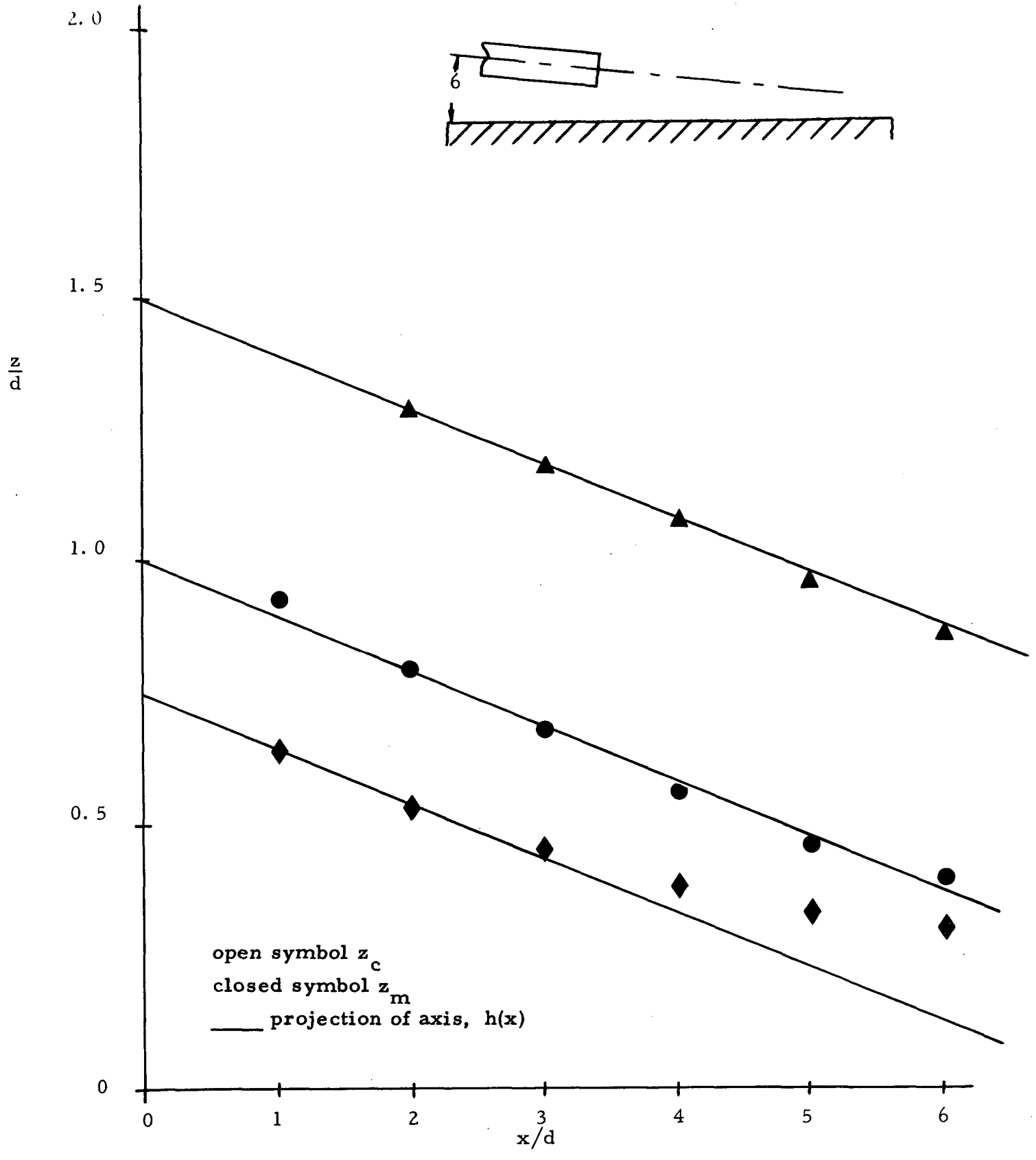

c) α = 6 degrees

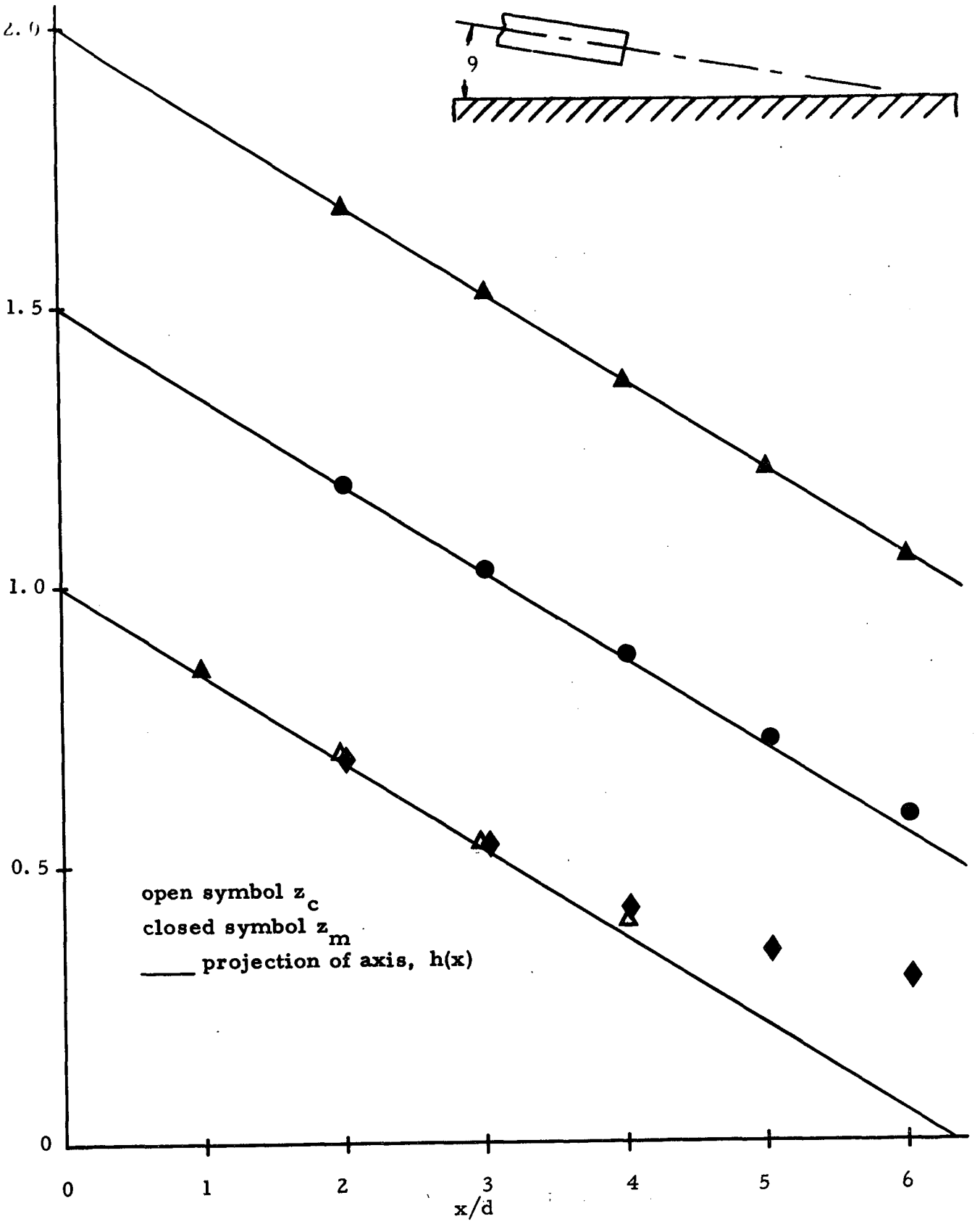

d) α = 9 degrees

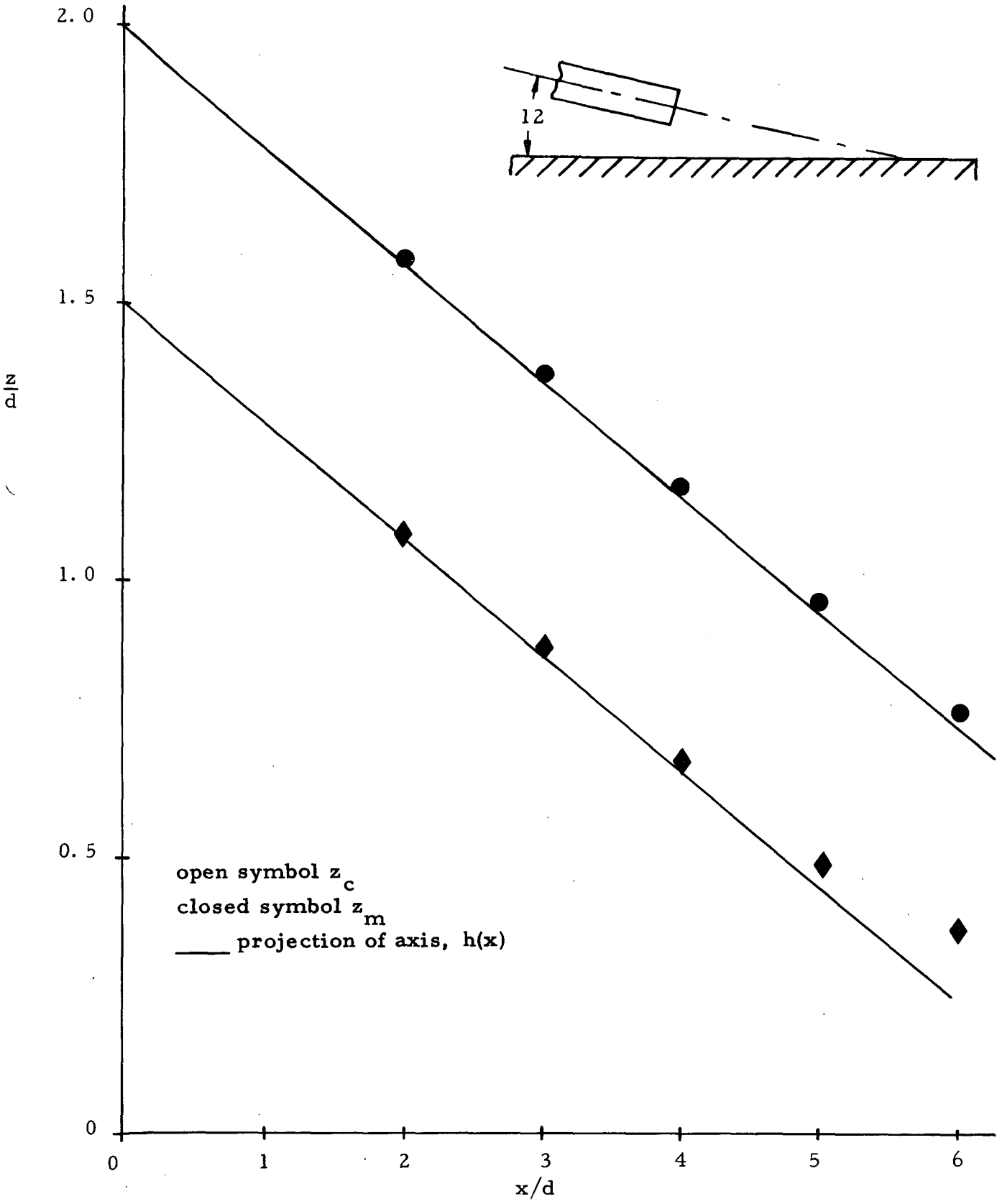

e) α = 12 degrees

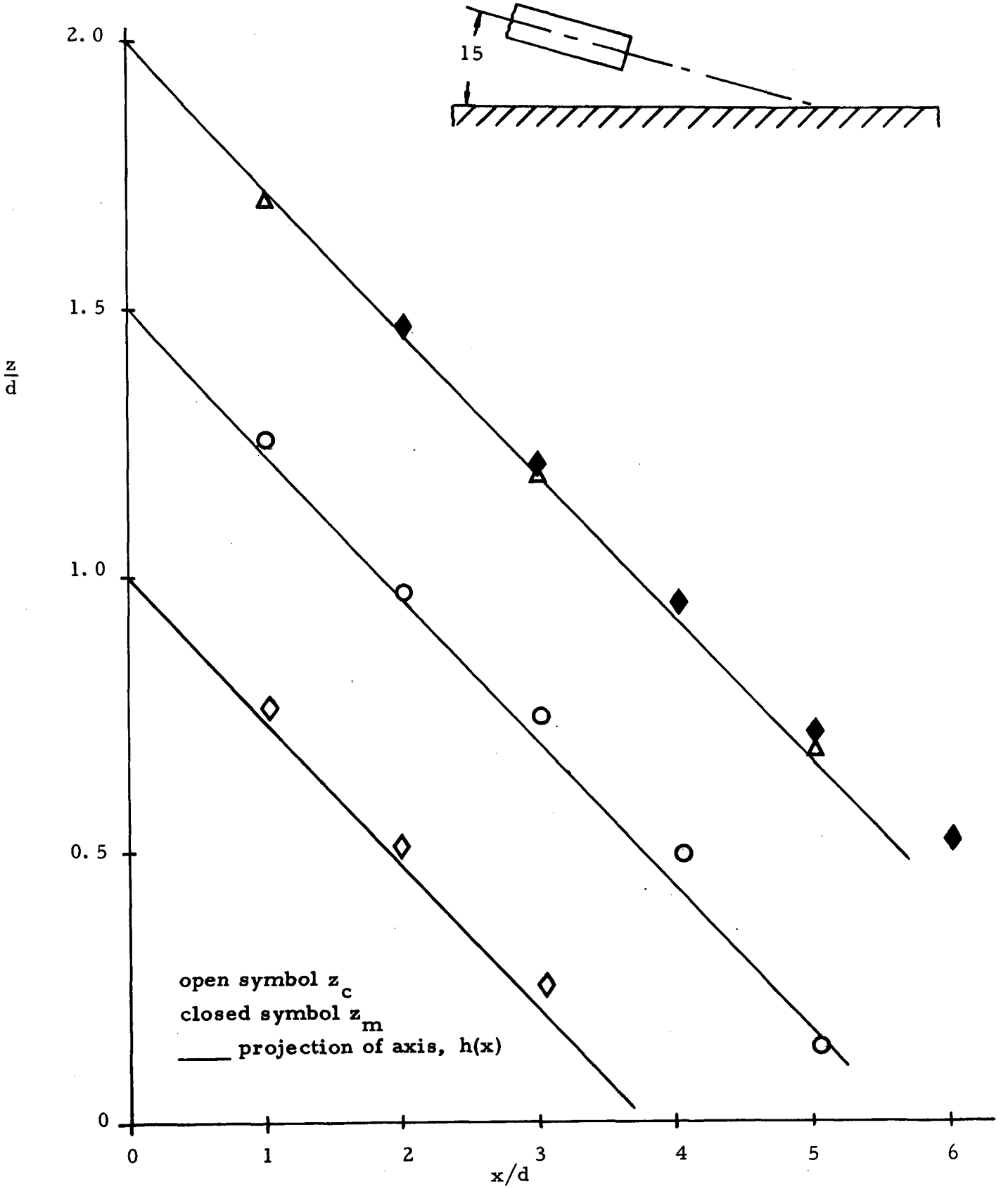

f) α = 15 degrees

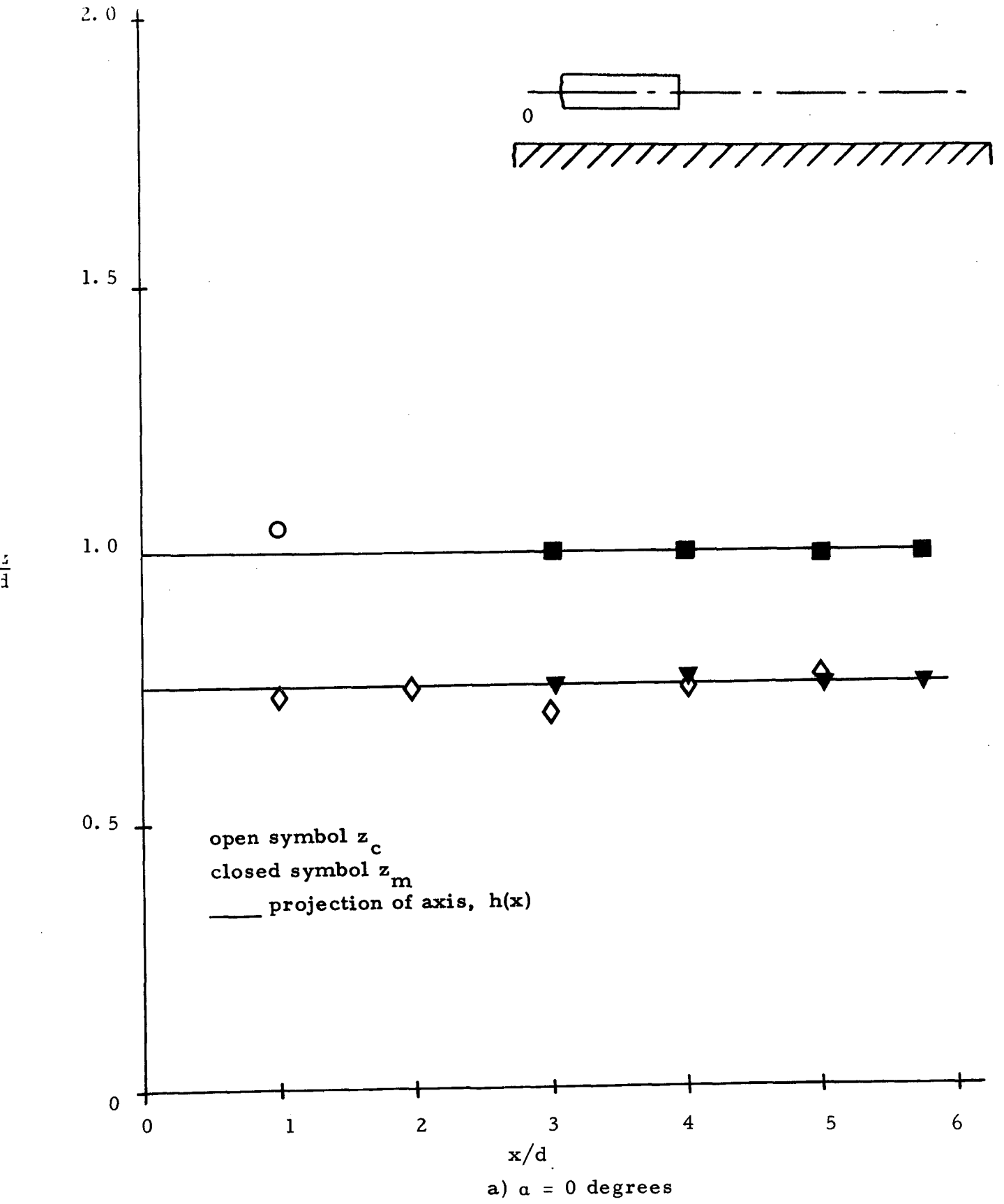

a) α = 0 degrees

Figure 46. z_c and z_m vs. x/d, fully developed.

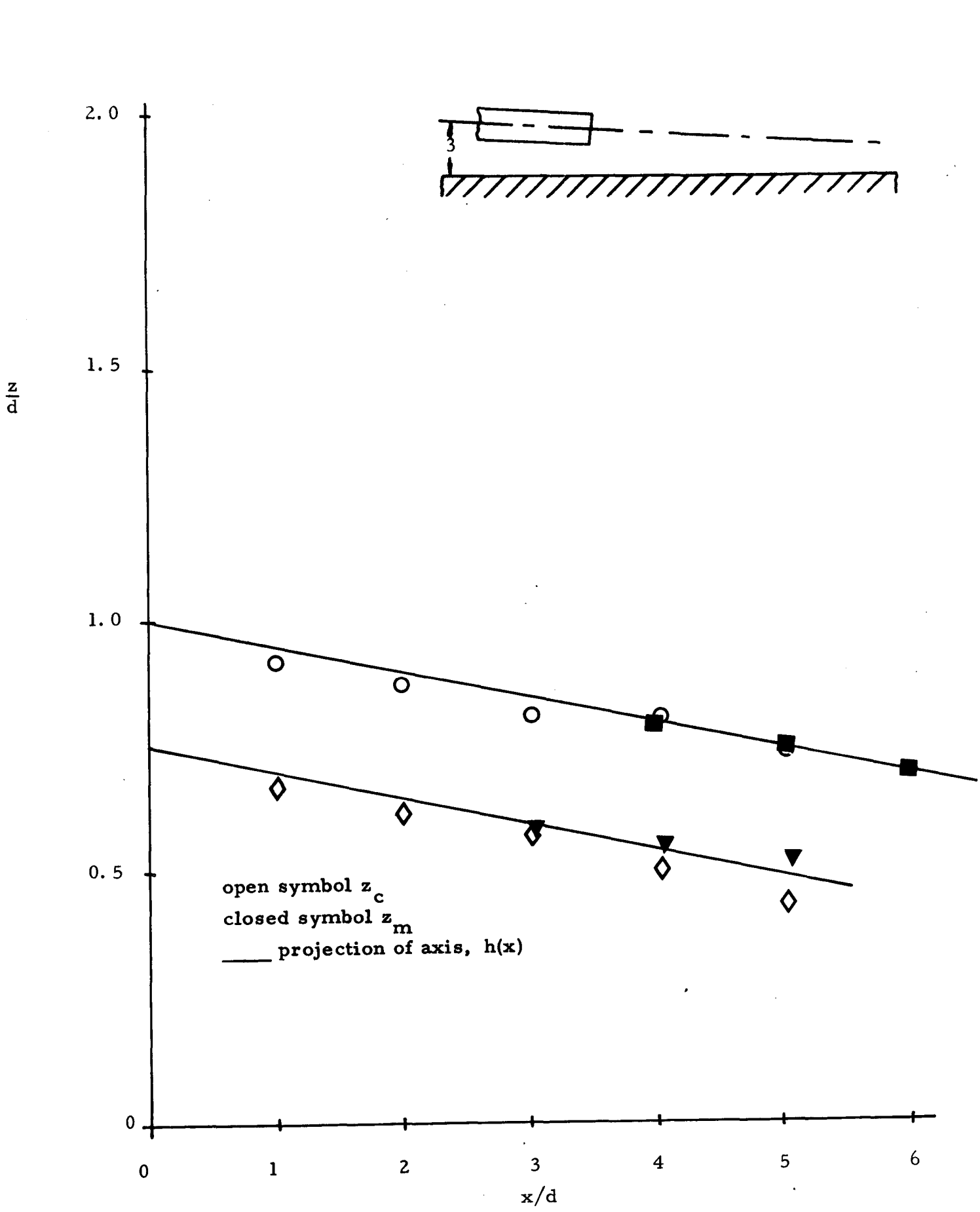

b) α = 3 degrees

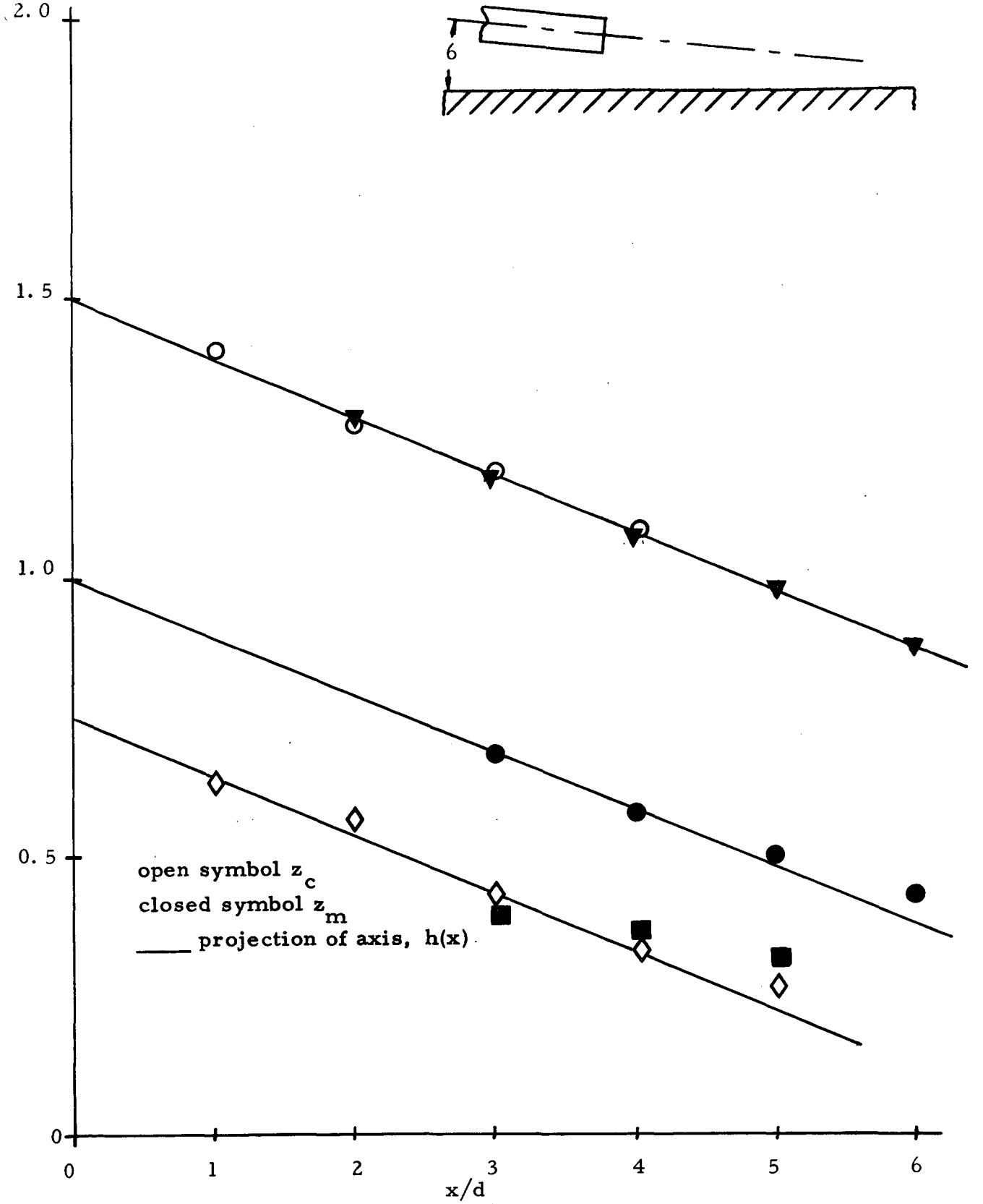

c) α = 6 degrees

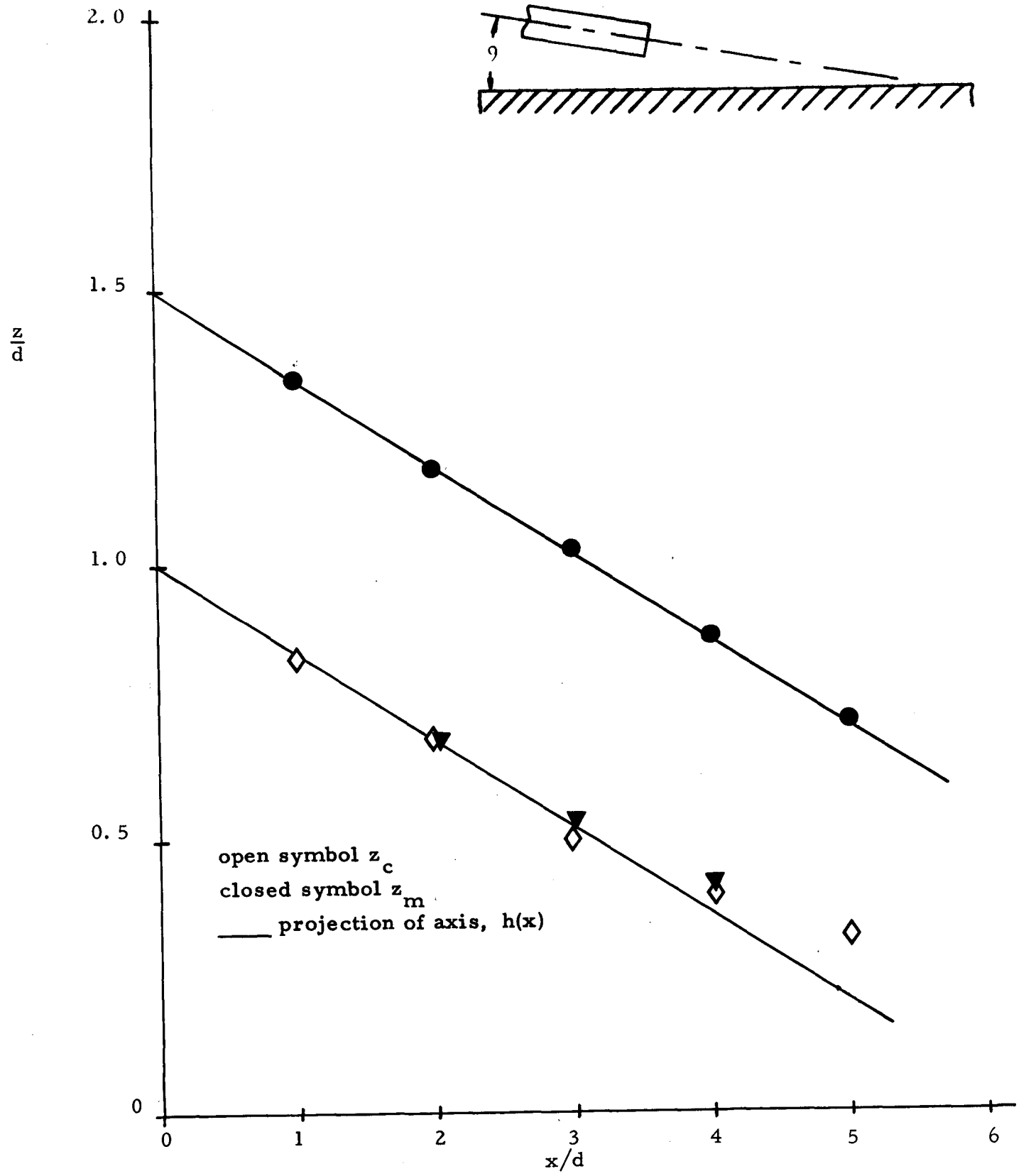

d) α = 9 degrees

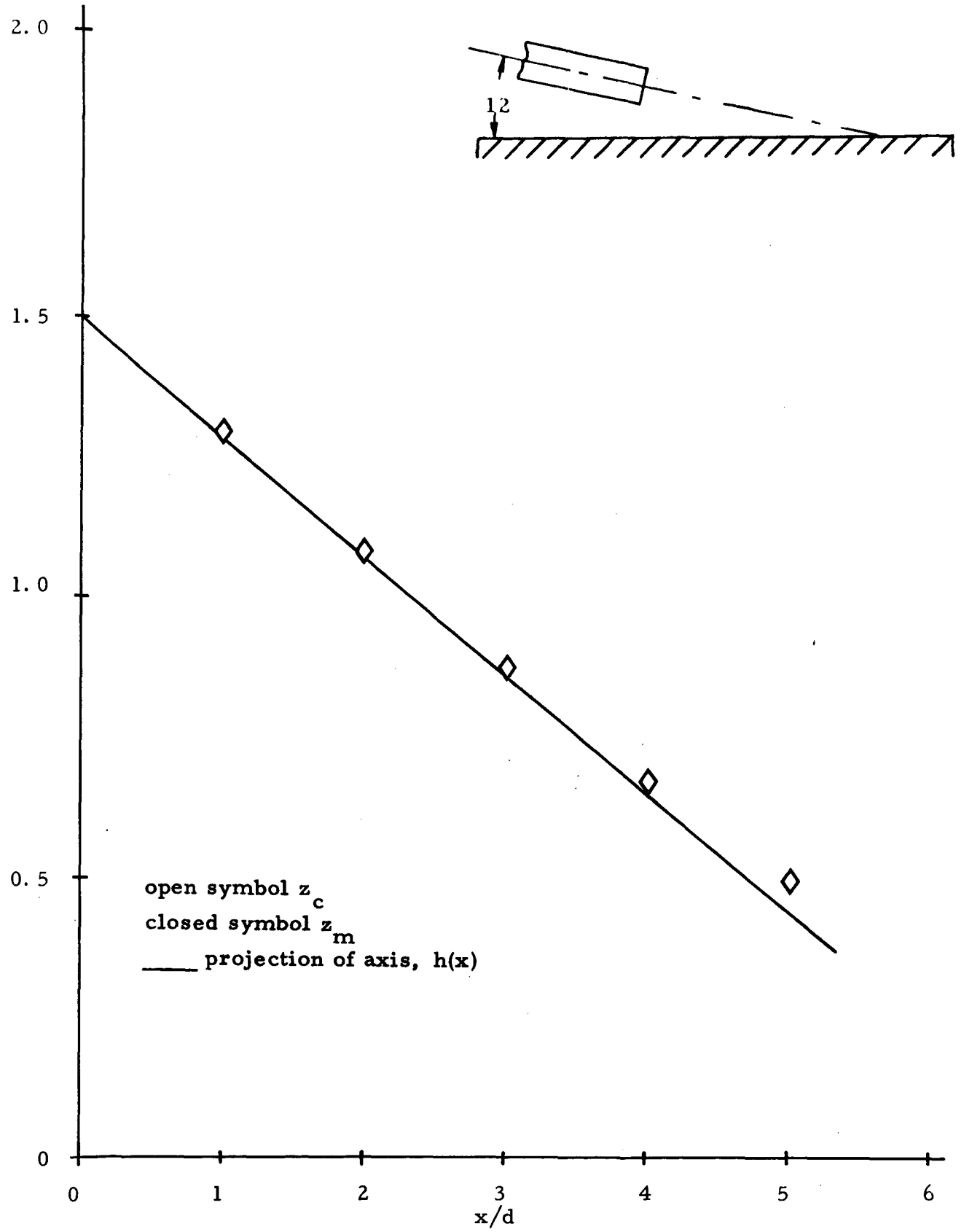

e) α = 12 degrees

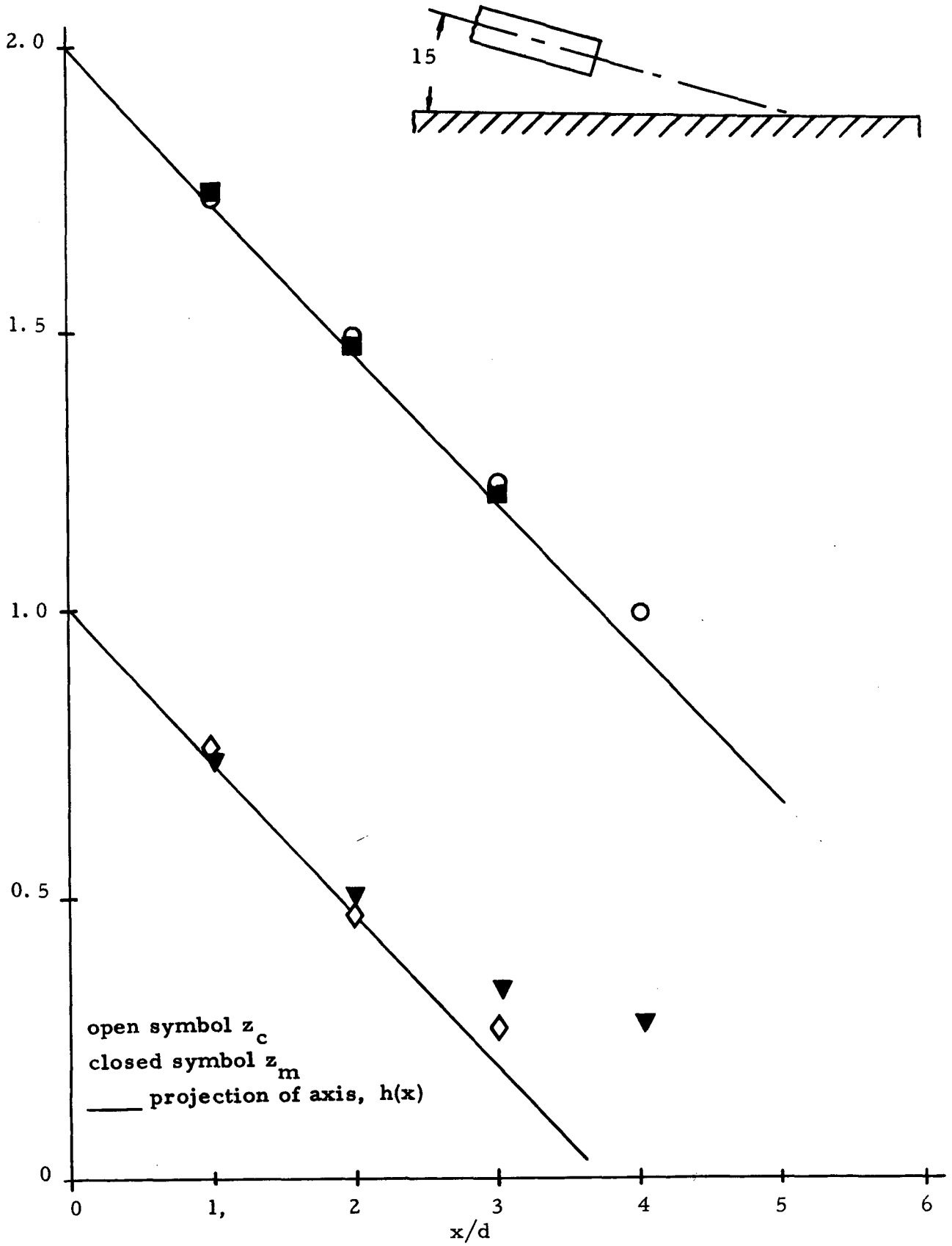

f) α = 15 degrees

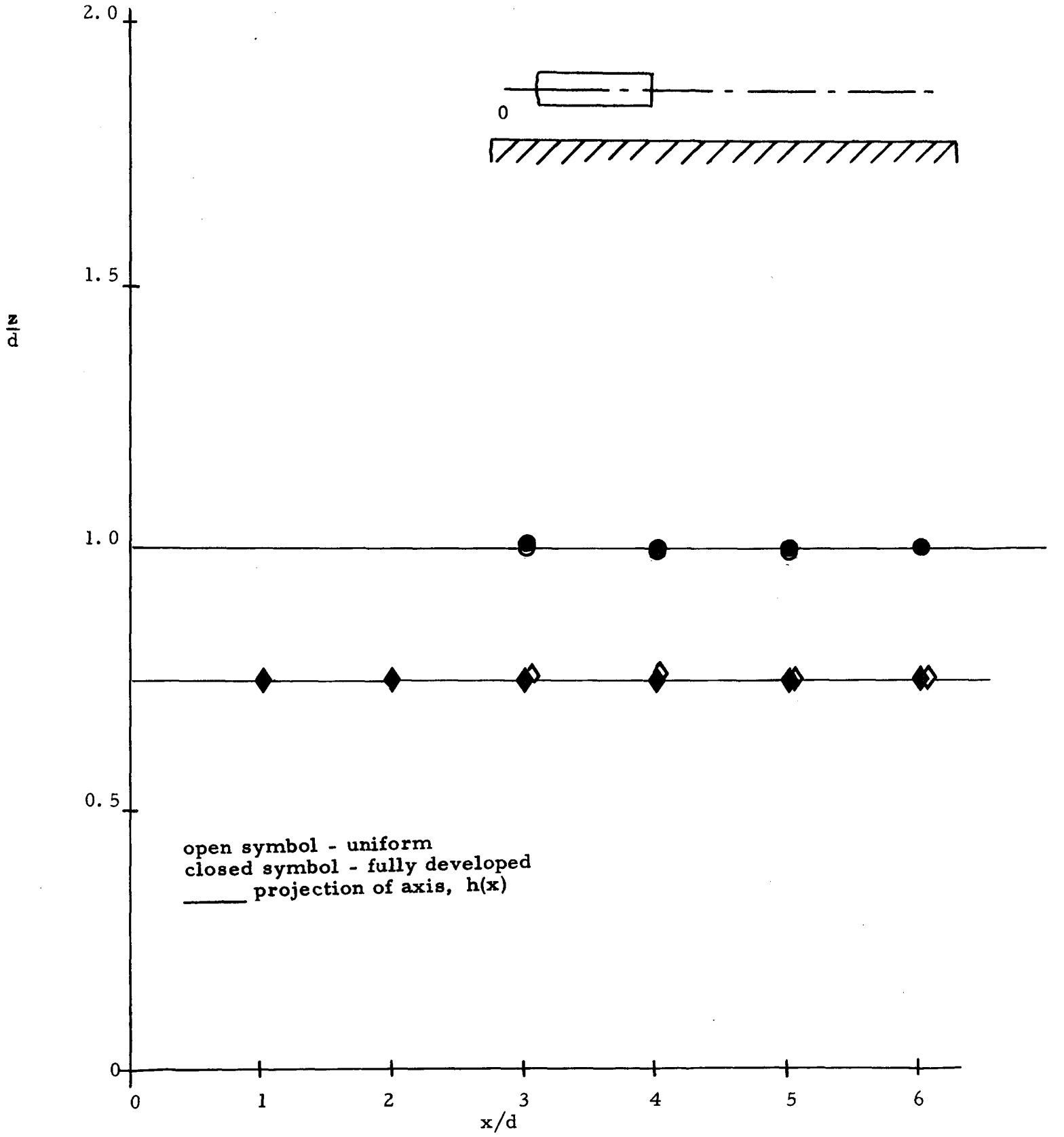

a) α = 0 degrees

Figure 47. z_m - uniform and z_m - fully developed vs. x/d.

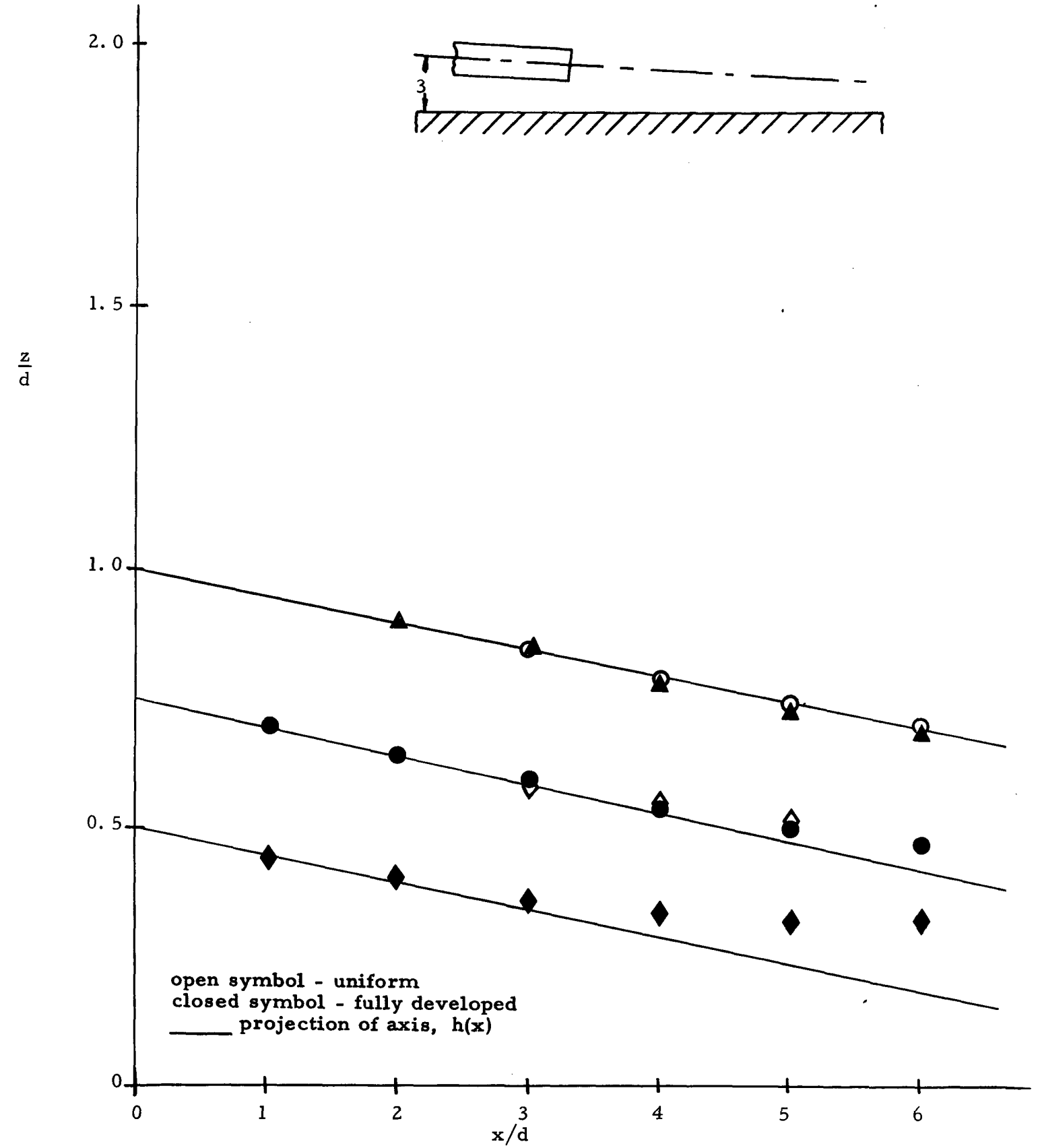

b) α = 3 degrees

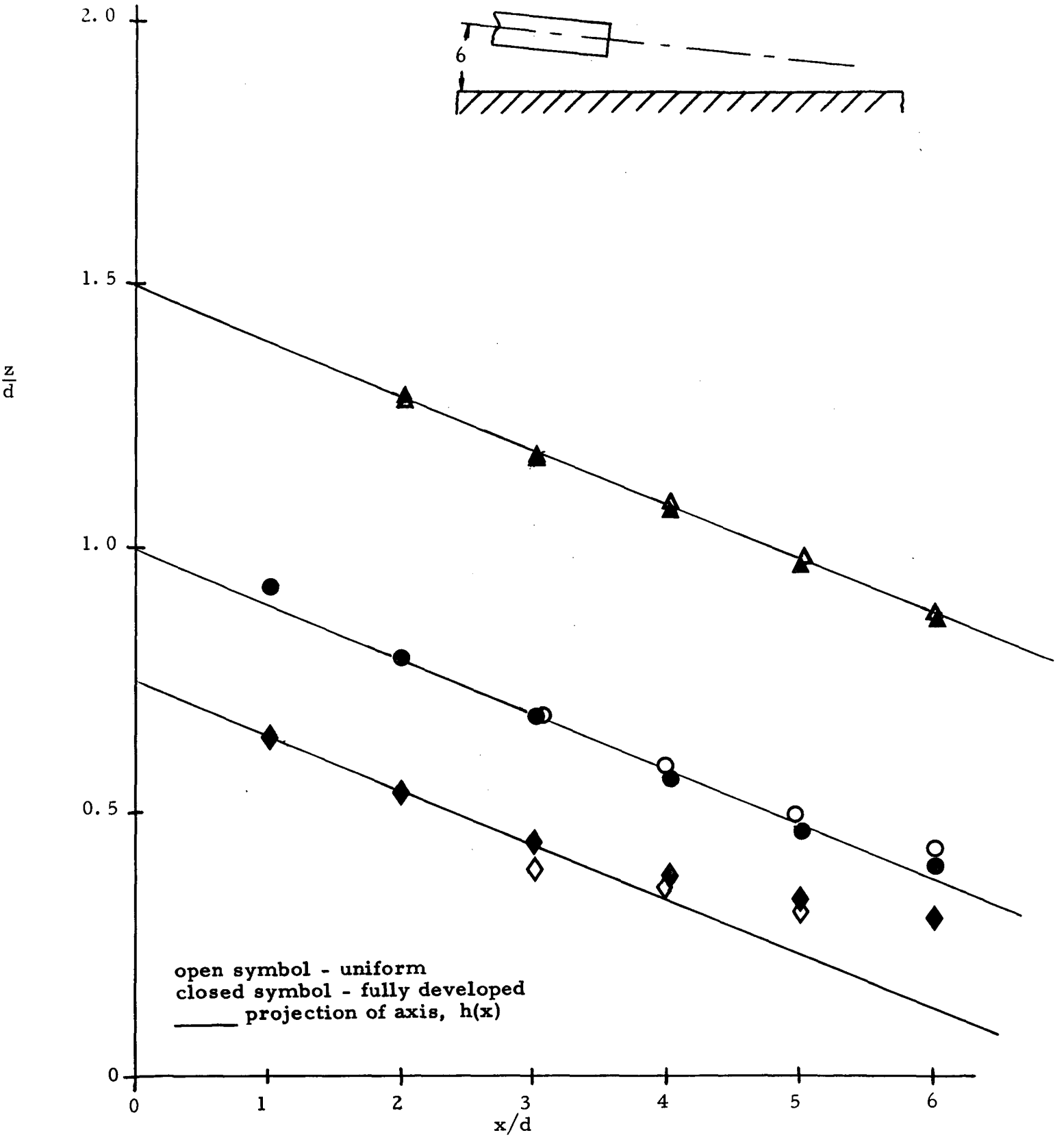

c) α = 6 degrees

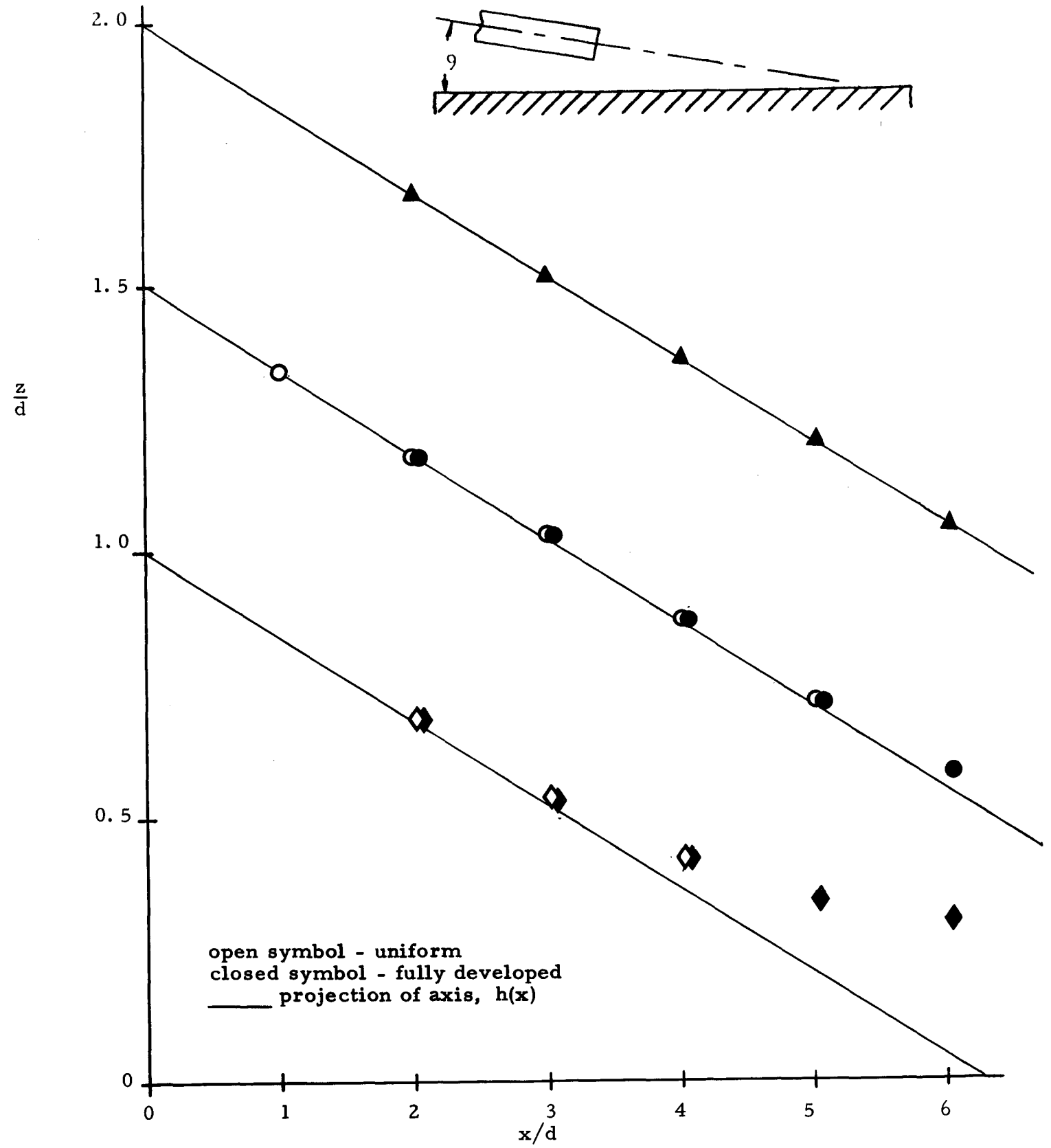

d) α = 9 degrees

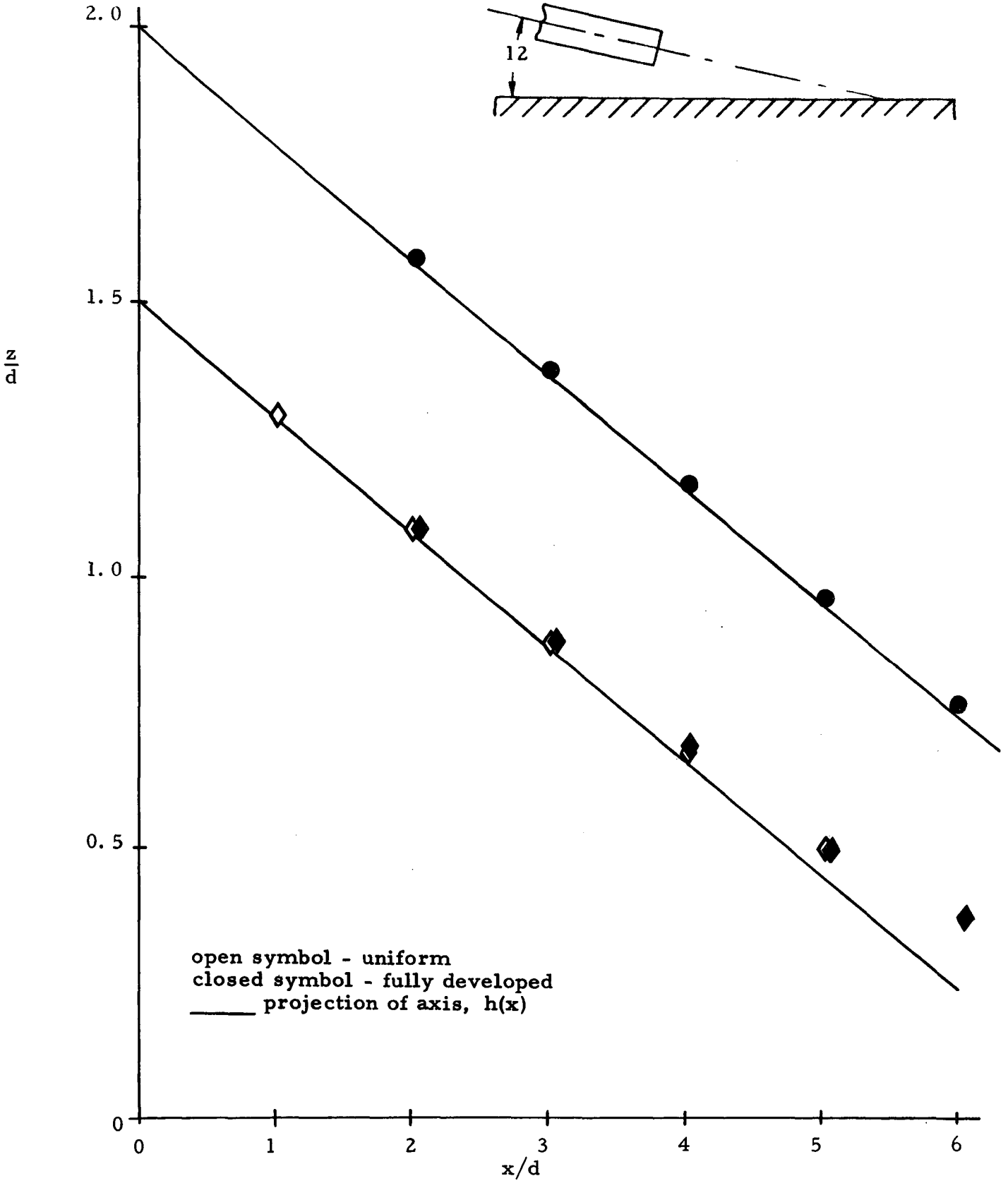

e) α = 12 degrees

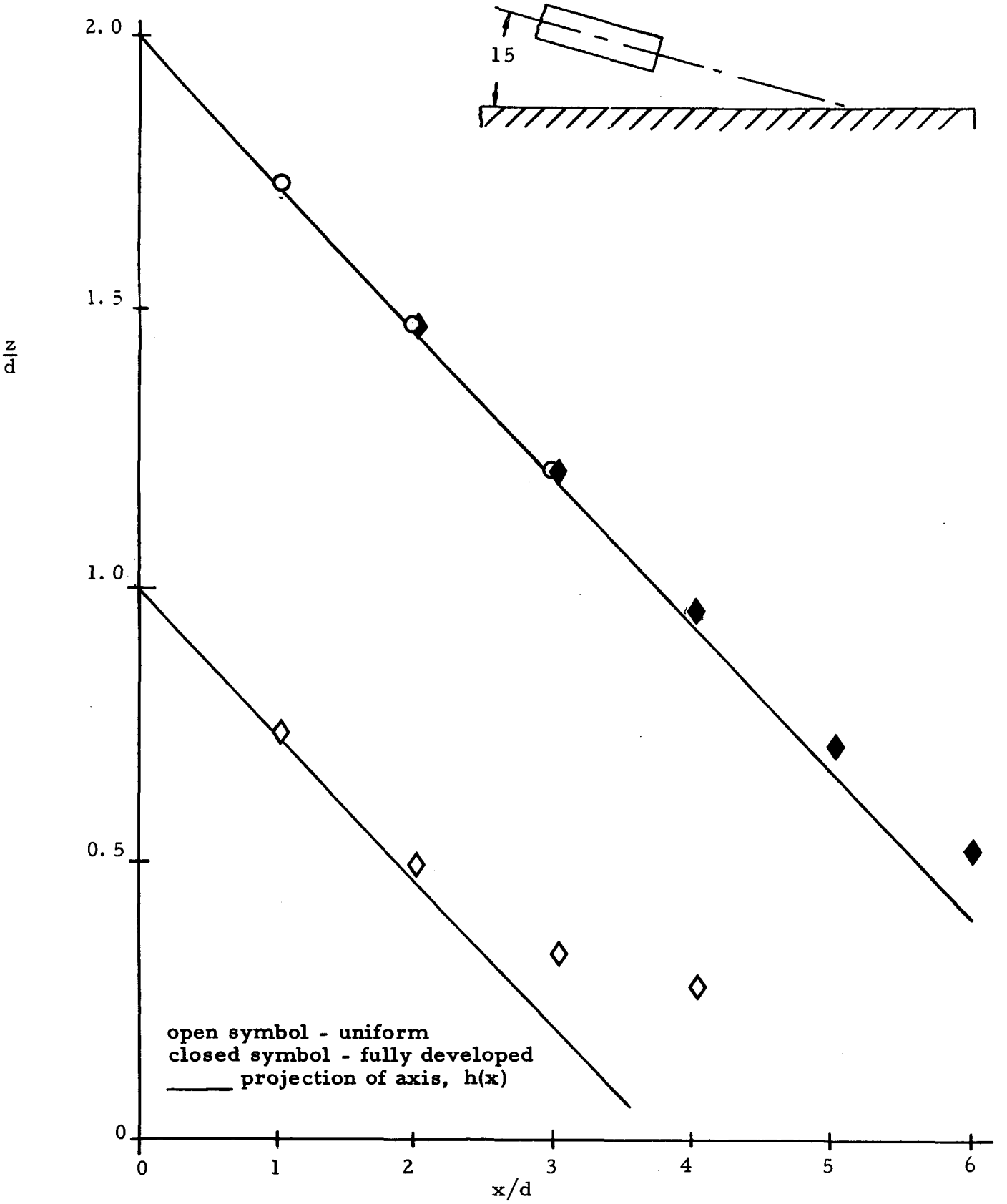

f) α = 15 degrees